Stability of Magnetohydrodynamic Shear Flow Boundaries: Kelvin-Helmholtz Instabilities and Emission of Magnetosonic Waves

by

Hava Turkakin

A thesis submitted in partial fulfillment of the requirements for the degree of

Doctor of Philosophy

Department of Physics

University of Alberta

Abstract

In this thesis, the stability of the Magnetohydrodynamic (MHD) shear flow boundaries for the Kelvin-Helmholtz Instability (KHI) is investigated. We have focused our attention on the emission of magnetosonic waves from the Kelvin-Helmholtz (K-H) unstable shear flow boundaries of MHD plasmas. We have shown for the first time that the Kelvin-Helmholtz Instability is a mechanism for fast and slow MHD wave, i.e. magnetosonic wave, generation along MHD shear flow boundaries. Our results is significant in showing that the emission of MHD waves from an unstable MHD shear flow boundary is possible and these waves may provide a efficient mean of energy transportation in between two MHD media. The Kelvin - Helmholtz generated fast/slow waves are introduced in the context of the primary/secondary KHI.

First, the primary and secondary K-H surface wave modes on the Earth's magnetopause are studied. The primary KHI is caused by fast MHD waves while the secondary KHI is caused slow MHD waves. The secondary KHI usually is possible at smaller shear flow speeds and have smaller growth rates than the primary KHI. The Earth's magnetopause is considered as an infinitely thin MHD shear flow boundary. Phase velocity diagrams are presented that allow us to identify the excited MHD waves that correspond to growing modes of the KHI under different conditions of the regions on both sides of the magnetopause boundary. The relation between the primary and the secondary KHI to magnetosonic wave interactions under different solar wind conditions is revealed through these diagrams. Using the observational values of the KHI relevant waves and the results of our study, general behavior of the primary and the secondary KHI relevant waves along the K-H unstable magnetopause is provided. A relation between the KHI waves and Negative Energy Waves (NEWs) is also shown.

Following, the KHI of the Earth's magnetotail flow channels associated with bursty bulk flows (BBFs) is investigated. The BBF channel boundary is also considered as an infinitely thin MHD shear flow boundary and an inner boundary is assumed in the middle

of the channel. MHD oscillations of the BBF channels in both kink and sausage modes are investigated for the KHI. Both the primary and the secondary KHI are found to cause the emission of magnetosonic waves along these boundaries. These instabilities are shown to be important for stopping the BBFs where the KHI removes energy from the flow. We have provided a model that can explain, for the first time, the generation mechanism for the observations of waves propagating towards both flanks of the Earth's magnetopause and emitted from BBF channels in the central magnetotail. Results shown in this section was published in Geophysical Research Letters and the paper was chosen as a spotlight paper with innovative ideas by American Geophysical Union.

Then a finite width boundary layer is added and emission of magnetosonic waves due to KHI from superfast relative flows across MHD plasma boundaries are investigated. While previous studies have focused their attention on the most unstable KHI waves, we have shown that the most significant modes are not the fastest growing modes. In contrast, the KHI wave growth resulting in emission of magnetosonic waves, which usually does not efficiently take place for the fastest growing modes, is the main source of energy transport. With the results obtained, the processes of the KHI and magnetosonic wave emission along various MHD shear flow boundaries in the Earth's magnetosphere and the solar corona is discussed. We have concluded that while the KHI would be more favorable on the day-side magnetopause and Coronal Mass Ejection (CME) boundaries, emission of magnetosound would dominate along the nightside magnetopause, BBFs in the inner plasmasheet and Supra-Arcade Downflows (SADs) in the solar corona.

Finally, nonlinear evolution of the KHI and emission of magnetosound due to the action of the KHI are investigated using the FLASH code which is provided by Flash Center at the University of Chicago. The same parameter space as the linear calculations for finite transition thickness is used to study the nonlinear KHI along MHD shear flow boundaries. Results obtained from the FLASH code were in very good agreement with the linear results. Emission of magnetosound from MHD shear flow boundaries in the linear stages of the KHI is confirmed.

Preface

Chapter 3 of this thesis has been published as H. Turkakin, R. Rankin, and I.R. Mann, "Primary and Secondary Compressible Kelvin-Helmholtz Surface Wave Instabilities on the Earth's Magnetopause", *Journal of Geophysical Research*, Vol. 118, 4161-4175, doi:10.1002/jgra.50394, 2013. I was responsible for the physical formulations, computational analysis as well as the manuscript composition. R. Rankin and I.R. Mann were supervisory authors and were involved with concept formation and manuscript composition.

Chapter 4 has been published as H.Turkakin, I.R. Mann, and R. Rankin, "Kelvin-Helmholtz Unstable Magnetotail flow Channels: Deceleration and Radiation of MHD Waves", *Geophysical Research Letters*, Vol. 41, doi:10.1002/2104GL060450. I was responsible for the physical formulations, computational analysis as well as the manuscript composition. R. Rankin and I.R. Mann were supervisory authors and were involved with concept formation and manuscript composition.

Chapter 5 thesis has been submitted as H.Turkakin, R. Rankin, and I.R. Mann, "Emission of Magnetosound from MHD-Unstable Shear Flow Boundaries" *Journal of Geophysical Research* , 2014 I was responsible for the physical formulations, computational analysis as well as the manuscript composition. R. Rankin and I.R. Mann were supervisory authors and were involved with concept formation and manuscript composition.

To

My husband and my children

Acknowledgements

I thank my supervisors who were extremely supportive in pursuing my goals during my work. I also would like to thank them for being supportive during my challenging family situations and for understanding my difficulties and helping me making progress. I would like to thank all of my friends who have supported me morally and helped me throughout difficulties I have encountered during my research.

Table of Contents

List of Tables

List of Figures

Chapter 1

Introduction

1.1 Overview

In this chapter I introduce some basic facts concerning the KHI. These topics include a description of plasmas, the solar wind as a plasma and the interaction of the solar wind with the Earth's magnetic field lines. The formation and the regions of the Earth's magnetosphere and coordinate systems used in magnetospheric studies are also described. We have provided a detailed description of plasmas as magnetohydrodynamics (MHD) fluids and MHD waves in plasmas which is closely related to KHI studies on MHD shear flow boundaries. Geomagnetic pulsations and geomagnetic field line resonances are also introduced which are suggested to be generated by the KHI.

In chapter 2, a detailed description of the KHI and plasma instabilities are given. The MHD theory and derivations of KHI waves dispersion relations are shown and models used in the thesis are described. Negative energy waves (NEWs) are also described as a related subject to the KHI.

In chapter 3 we show the results obtained and the paper published [*Turkakin et al.*, 2013] on the KHI of the Earth's magnetopause using the derivations and models described in chapter 2 and section 2.3.1. Results showing a relation between KHI waves and NEWs

are also shown in this chapter.

Chapter 4 shows the results obtained and the paper published [*Turkakin et al.*, 2014] on the KHI and the emission of the magnetosound along Bursty Bulk Flow (BBF) boundaries in the central plasmasheet of the Earth. In this chapter the derivations and models described in chapter 2 and section 2.3.1 are used.

In chapter 5, the KHI and emission of magnetosound from MHD shear flow boundaries with finite transition thickness is investigated. The possible applications to the shear flow regions in the Earth's magnetosphere and the solar corona are discussed. The results obtained using the derivations and model described in chapter 2 and section 2.3.2 are shown. The contents of this chapter is submitted to the Journal of Geophysical research for publication.

In chapter 6 nonlinear evolution of the KHI on MHD shear flow boundaries with finite thickness is studied using the FLASH code. Linear and nonlinear results are compared and nonlinear effects on the emission of magnetosound are discussed.

In chapter 7 conclusions are given and possible future work is discussed.

1.2   Definition of a Plasma

The fourth state of the matter, which is the plasma, is not commonly known although a large fraction of our visible universe is in the plasma state. Plasma is a gas of charged particles which are, on average, electrically neutral [*Kivelson and Russell*, 1995; *Baumjohann and Treumann*, 1999]. Microscopic space charge fields of the individual charge carriers must cancel each other in each volume element to provide macroscopic charge neutrality. The Coulomb potential field of any charge is shielded by other charges in the plasma, which is called Debye shielding [*Gurnett and Bhattacharjee*, 2004].

The Coulomb potential of a charged particle with charge q is

$$\phi_C = \frac{q}{4\pi\epsilon_0 r},$$

(1.1)

and Debye potential is

$$\phi_D = \frac{q}{4\pi\epsilon_0 r} e^{-r/\lambda_D}, \tag{1.2}$$

where, $\epsilon_0 \simeq 8.85^{-12}$ C^2/Nm^2 is the free space permittivity, r is the distance from the particle, and λ_D is the characteristic distance called Debye length. The Debye length is defined as,

$$\lambda_D = \left(\frac{\epsilon_0 k_B T}{ne^2}\right)^{1/2}, \tag{1.3}$$

where, $k_B \simeq 1.38 \times 10^{-23}$ J/K is the Boltzmann constant, T is temperature, n is number density, and e is electron charge. The exponential function in the Debye potential cuts off the potential at distances $r > \lambda_D$.

In order for a plasma to be quasineutral, the physical dimension of the system, L, must be large compared to the Debye length,

$$L \gg \lambda_D \tag{1.4}$$

which marks the first criterion for an ionized medium to behave as plasma. The average physical values of the Debye length in the inner magnetosphere is $\simeq 2.3^1$ m, in the outer magnetosphere is $\simeq 1.7^2$ m and in the solar corona is $\simeq 4^{-3}$ m.

Collective behavior inside the Debye sphere of radius λ_D is the cause of the shielding. Therefore, for Debye shielding to take effect, the number of particles inside the Debye sphere must be large enough, which is the second criterion for the plasma. The number of particles inside such a sphere will be $\frac{4\pi}{3} n_e \lambda_D^3$ and thus for a plasma the condition

$$n_e \lambda_D^3 \gg 1 \tag{1.5}$$

must hold. The term $n_e \lambda_D^3$ is called the plasma parameter and referred to as, Λ. The average physical values of the number of particle in the Debye sphere is $\simeq 5.4^1 2$ in the inner magnetosphere, $\simeq 1.9^1 3$ in the outer magnetosphere and $\simeq 3.6^2$ in the solar corona.

When an external force disturbs the quasineutrality of a plasma, the electrons will be accelerated to restore charge neutrality. Since the ions are much heavier, they will stay relatively stationary and electrons will oscillate. The typical oscillation frequency of electrons in a fully ionized plasma is the electron plasma frequency, ω_{pe} which is expressed as

$$\omega_{pe} = \left(\frac{n_e e^2}{\epsilon_0 m_e} \right)^{1/2}.$$ (1.6)

If the plasma is not fully ionized and has a substantial number of neutral particles, these particles will collide with electrons during their oscillations with frequency ω_{pe}. If these collisions are too frequent, the electrons will be forced into equilibrium with neutrals and the medium will become a neutral gas. Therefore, for electrons to stay unaffected by the collisions with the neutrals, the collision frequency should be smaller then their oscillation frequency around the ions, i.e. ω_{pe}. In other words the average time between two collisions, τ_n, must be larger than the inverse of the ω_{pe}

$$\omega_{pe}\tau_n \gg 1.$$ (1.7)

This is the third criterion for an ionized gas to behave as a plasma [*Gurnett and Bhattacharjee*, 2004].

1.3 Space Plasmas and Solar Wind

In our solar system, plasmas are abundant even in the neighborhood of the Earth. Above approximately 80 km of altitude, the atmosphere gradually turns into the ionosphere and the magnetosphere which are to be described in terms of plasma physics. The source of energy and plasma in the near-Earth space environment is the solar wind. The solar wind is a flow of ionized solar plasma and solar magnetic field that is released into interplanetary space at speeds ranging between $\sim 300 - 1400$ km/s. The solar wind is produced as a result of the expansion of the solar corona due to the strong pressure

difference between the solar corona and interplanetary space. Solar wind is strongly influenced by the solar activity and transmits these effects into the interplanetary space, planets, comets and moons [*Kivelson and Russell*, 1995; *Baumjohann and Treumann*, 1999]. It consists of electrons and protons, i.e. ionized hydrogen, a low percentage of helium and a few ions of heavier elements [*Kivelson and Russell*, 1995]. An image of solar wind is shown in Figure 1.1.
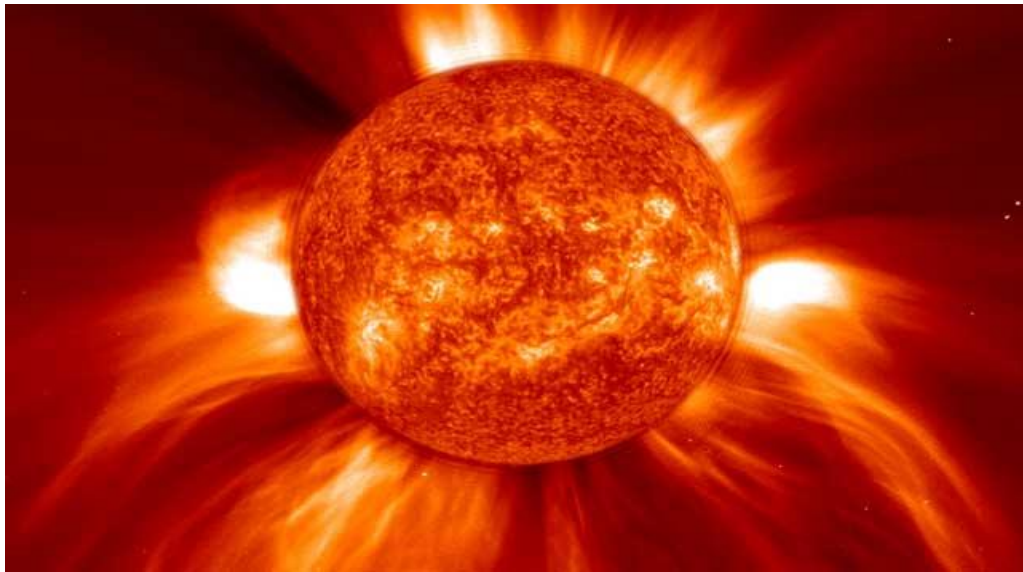
Figure 1.1: A picture showing the solar coronal eruption.
(from *http://naturalwondernl.weebly.com/how-do-the-northern-lights-work.html*)

1.4 Solar Wind's Interaction with the Earth - a Magnetized Planet

The Earth's magnetic field, a nearly perfect dipole at distances $\sim 2R_E$ (Earth radii) [*Kivelson and Russell*, 1995], is an obstacle to and deflects the solar wind around the Earth leading to the formation of a cavity called magnetosphere (see Figure 1.2). The solar wind hits the Earth's magnetic field with supersonic speeds and a bow shock wave is generated. At this point the plasma is slowed down and the kinetic energy of the particles
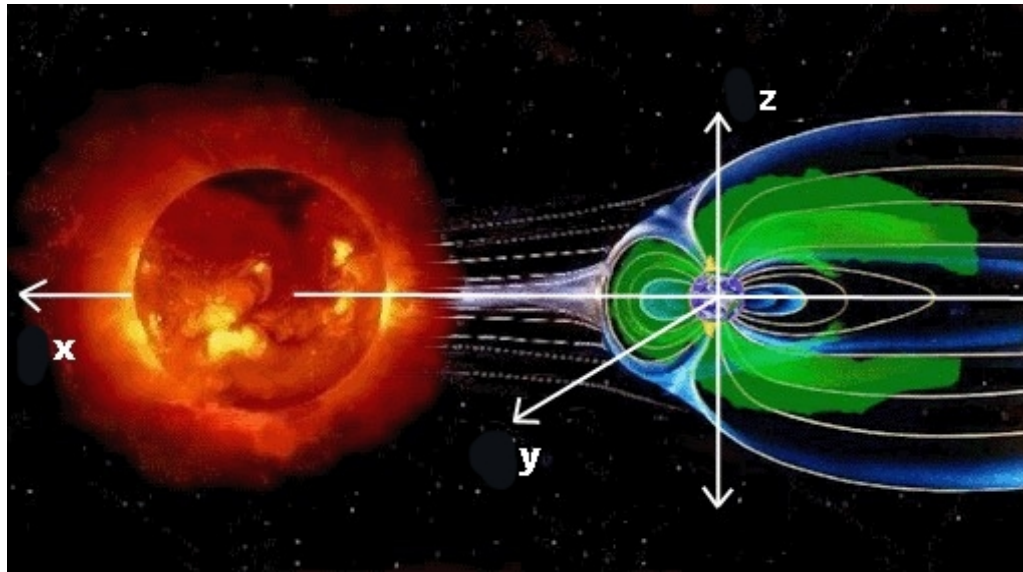
Figure 1.2: Deflection of the solar wind around the Earth , i.e. formation of the magne-
tosphere.
(from *http://www.davidreneke.com/solar-wind-could-affect-earths-magnetosphere*)

are converted into thermal energy, forming the magnetosheath with hotter and denser

plasma and with higher magnetic field strength compared to that of the solar wind. The

solar wind is a highly conducting plasma which results in the solar magnetic field's being

frozen in with it. This magnetic field is called interplanetary magnetic field (IMF) and

has a strength typically of the order of 5 nT. As a result of being frozen-in, or captive of

the solar wind, the IMF cannot penetrate the terrestrial field lines and thus a boundary

called magnetopause is formed. The Magnetopause separates the magnetosheath region,

the region of flowing solar wind plasma, from the region of geomagnetic field lines - the

magnetosphere.

In the following sections, an overview of the regions of the Earth's magnetosphere is

given. Magnetohydrodynamic (MHD) treatment of plasmas and MHD waves in homoge-

neous plasmas are then introduced which are strongly related to the current study. To aid

with the understanding of the studies done in this thesis, we will also briefly describe the

box model of the Earth's magnetosphere, GSM coordinate system as one of the various co-

ordinate system commonly used in the magnetospheric studies and Ultra-Low-Frequency (ULF) waves observed in the Earth's magnetosphere.

1.5   Structure of the Earth's Magnetosphere
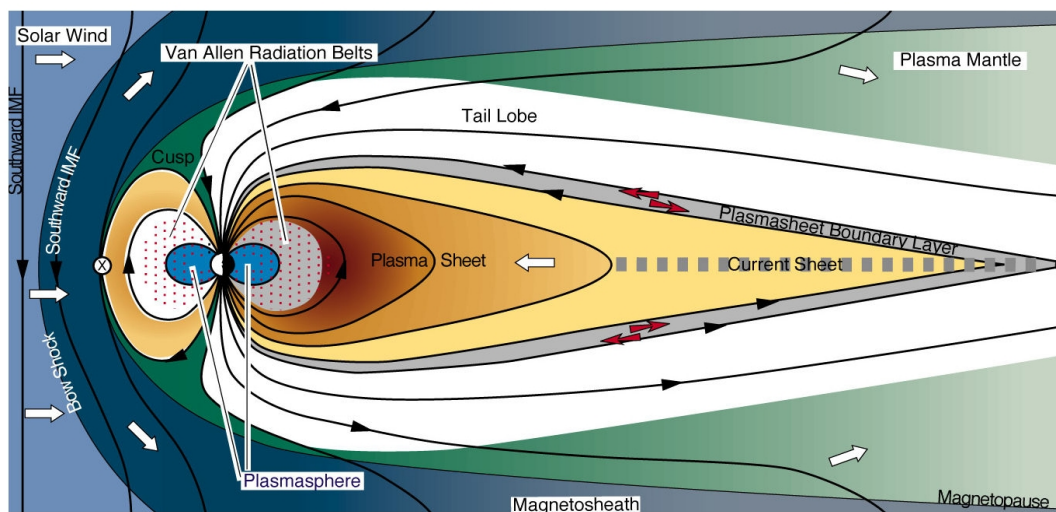
Figure 1.3: Plasma regions of the Earth's magnetosphere.
(from *http://survive2012.com/news/2011/02/sun-moon-earth-936.html*)

The outer part of the terrestrial dipole magnetic field is distorted by the solar wind, with kinetic pressure stretching the nightside and compressing the dayside. As a result, a tail-like structure is formed on the nightside called the magnetotail extending beyond the lunar orbit. The position of the magnetopause extends up to approximately $\sim 10 R_E$ on the dayside and $\sim 200 R_E$ on the nightside (1 R_E = 6371 km) [*Kivelson and Russell*, 1995]. The plasma in the magnetosphere mainly consists of electrons, protons and small fractions of He^+, He^{++} and O^+ [*Baumjohann and Treumann*, 1999]. The Earth's magnetosphere has complicated dynamics and different plasma regions with different densities and temperatures. The plasma regions of the Earth's magnetosphere are illustrated in Figure 1.3. The main components are the magnetotail lobe, the plasma sheet boundary

layer, and the plasma sheet. Closer to the Earth are the radiation belts and the plasma-sphere [*Kivelson and Russell*, 1995].

The magnetotail lobe is the outer part of the magnetotail with low-density plasma, ≤ 0.1 cm^{-3}. The ions in the tail lobe are believed to be of ionospheric origin. Tail lobes are named as North and South lobes which are magnetically connected to the polar regions of the Earth [*Kivelson and Russell*, 1995].

The plasma sheet boundary layer is generally observed as a transition region between magnetotail lobes and the hot plasma sheet. It is the distant part of the plasma sheet in which the ion flow velocity is high with densities of order ~ 0.1 cm^{-3}.

Most of the plasma in the magnetotail is contained in the plasma sheet, at $\sim 10~R_E$ in the tail mid-plane. The plasma sheet consists of hot particles with densities of $\sim 0.1 - 1$ cm^{-3} [*Kivelson and Russell*, 1995]. The plasma sheet is populated mainly by solar wind particles during quiet times and particles originating from the ionosphere during active times. A current sheet, also called neutral sheet, lies in the center of the tail embedded within the plasma sheet.

The radiation belts, also called Van Allen belts, are structures that lie between $\sim 2 - 6~R_E$ with the energetic particles oscillating between two hemispheres. These particles drift azimuthally around the earth due to the magnetic field gradient, thus forming the ring current. The number density and the energy density of the particles are more intense near the equatorial plane and less intense at low latitudes since they interact with the neutral atmosphere and become lost. There are two radiation belts namely the inner radiation belt and the outer radiation belt. The characteristic electron density in the radiation belts is ~ 1 cm^{-3}, the temperature is $\sim 5 \times 10^7$ K, and the magnetic field strength varies between $\sim$100 and 1000 nT [*Kivelson and Russell*, 1995; *Baumjohann and Treumann*, 1999].

The plasmasphere coexists in approximately the same region as the radiation belts [*Kivelson and Russell*, 1995]. It contains cold dense plasma of ionospheric origin with densities $\sim 10^3 cm^{-3}$ and temperatures $\sim 1eV$. The plasmasphere corotates with the

Earth and extends up to $\sim 4 - 6R_E$ in the equatorial plane.

The ionosphere is also an important region forming the inner edge of the magnetosphere. It is formed by the photo-ionization of high altitude atmospheric molecules by UV and X ray radiation from the sun. At high latitudes, it is also produced by the solar wind impinging on the Earth and ionizing part of the neutral atmosphere. A typical electron density in the ionosphere is $\sim 10^5$ cm^{-3} and temperatures are of order $\sim 10^3$ K and the magnetic field strength is of order $\sim 10^4$ nT. The ionosphere merges into the plasmasphere at low and mid-latitudes.

The plasma in the magnetosphere can also sustain currents that feed back and affect the shape of the magnetosphere. Electrons and ions move in different directions producing electric current which affects the dynamics of the magnetosphere significantly by transporting charge, mass, momentum and energy, and producing magnetic fields. For instance, the magnetopause current, the current flowing across the magnetopause surface, affects the compression of the terrestrial field lines on the dayside magnetosphere. There is also magnetotail current in the tailside. Different types of currents in the Earth's magnetosphere is shown in Figure 1.4. In Figure 1.4, the ring current which is caused by particles in the Van Allen belts is also seen. The ring current flows around the Earth in the westward direction and it affects the inner configuration of the magnetosphere. Although electrons drift around the Earth eastward they do not have a significant effect on the net westward current, due to their relatively low mass, compared to ion masses. There are also field aligned currents mainly carried by the electrons and they have strong effects on the exchange of energy and momentum between different current regions. At altitudes of $100 - 150$ km, some currents exist in the conducting layers of the ionosphere such as the auroral electrojets, and the equatorial electrojet [*Kivelson and Russell*, 1995; *Baumjohann and Treumann*, 1999].
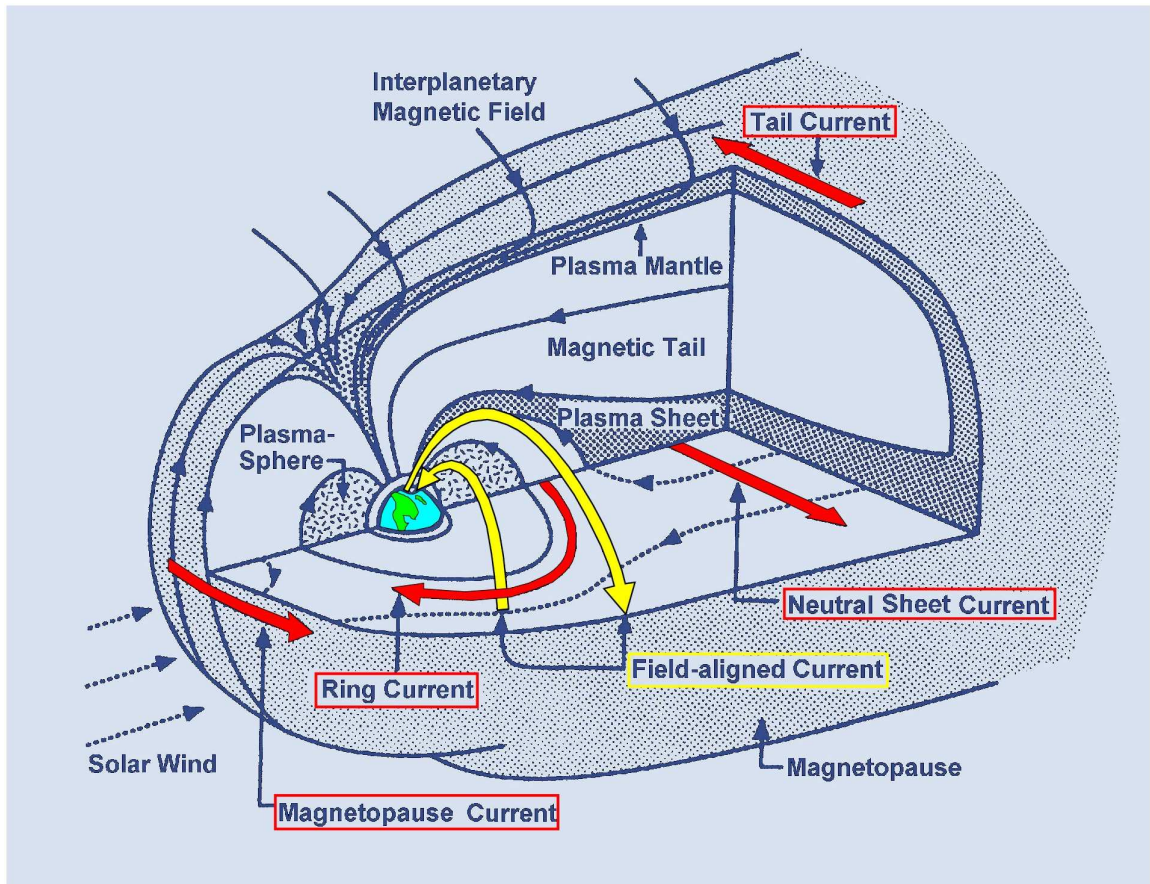
Figure 1.4: Synopsis of the magnetospheric currents. (from *www.ngdc.gov/seg/geomag*)

1.6   Coordinate Systems in Space

In this section, we describe the dipole coordinate system which is the best to define the properties of the geomagnetic field lines. We introduce the box model of the magneto-sphere as an approximation to describe geomagnetic field lines in the regions close to the equatorial plane of the magnetosphere. We also describe the GSM coordinate system, one of many coordinate systems used in the solar-terrestrial environment [c.f., *Kivelson and Russell*, 1995]. The box model approximation and GSM coordinate systems are used in our calculations throughout the thesis.

1.6.1 Dipole Coordinates

At distances not very far from the Earth's surface, the geomagnetic field can be approximated as a dipole field. The Earth's dipole magnetic field is presented with parameters: λ and r, where λ is the magnetic latitude and r is the distance to a magnetic field line at a certain magnetic latitude. A dipolar coordinate system and field lines are displayed in Figure 1.5. The strength of the geomagnetic field at a particular location can be described as,

$$B = \frac{\mu_0}{4\pi} \frac{M_E}{r^3} (1 + 3sin^2\lambda)^{1/2} \tag{1.8}$$

where, $\mu_0 = 4\pi \times 10^{-7}$ N/A^2 is the permeability of free space and $M_E = 8.05 \times 10^{22}$ Am^2 is the Earth's dipole moment. The locus of a point on a particular field line is described
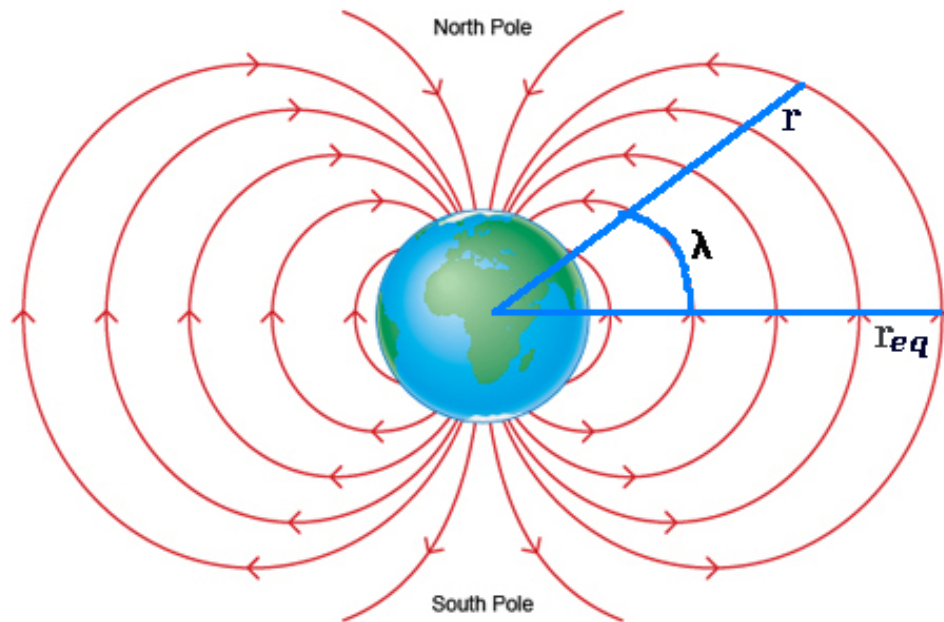
Figure 1.5: Dipolar magnetic field lines, λ is the magnetic latitude and r is the radial distance to a field line at a particular magnetic latitude.(from *http://www.bbc.co.uk/schools/gcsebitesize/science/*)

as;

$$r = r_{eq} \cos^2 \lambda,$$

where r_{eq} is the equatorial distance of a field line (see Figure 1.5). If the radius of the Earth is used as a unit of distance the L-shell parameter can be introduced, $L = r_{eq}/R_E$, and the above field line equation can be written as,

$$r = LR_E cos^2 \lambda.$$

The value of the equatorial geomagnetic field, $B_E = \mu_0 M_E/(4\pi R_E^3)$, together with the L parameter can be inserted in the Equation 1.8 resulting a new equation for the strength of a geomagnetic field as,

$$B = \frac{B_E}{L^3} \frac{(1 + 3sin^2\lambda)^{1/2}}{cos^6\lambda}. \tag{1.9}$$

1.6.2 Box Model of the Magnetosphere

The box model of the magnetosphere is a common approximation used in the context of magnetospheric dynamics. In this approximation, magnetic field lines are straightened and bounded by the ionosphere at top and bottom *Kivelson and Russell* [1995] (see Figure 1.6). Only the variation of the magnetic field intensity in the perpendicular direction is taken into account. The problem can then be formulated in rectangular geometry, with a choice of **B** oriented along the z coordinate and the magnitude of **B** varying in the x direction. Here x, y, z coordinates correspond to radial, azimuthal and north-south directions. The box model is a valid approximation for low magnetic latitudes, i.e. regions close to the equatorial plane. At higher magnetic latitudes, dipole coordinates provide a better approximation.
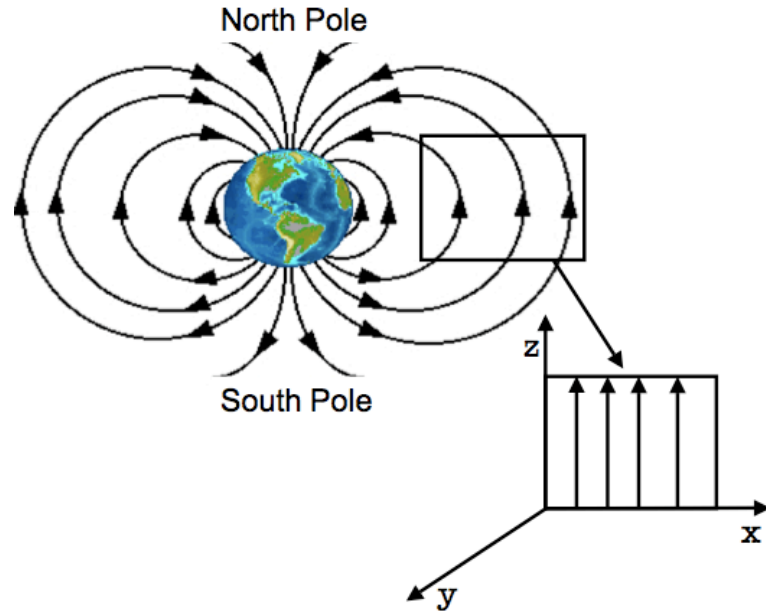
Figure 1.6: Schematic showing the box model and its relation to the dipole field lines. The Cartesian coordinates, x, y, and z are shown as a possible choice of the magnetic field direction for the straightened field lines. (adapted from *http://www.unc.edu/depts/oceanweb/turtles/juvenilemap/EarthMF.html*)

1.6.3   Geocentric Solar Magnetic (GSM) Coordinate System

There are many different coordinate systems used in space physics studies. Here we describe one of them, the Geocentric Solar Magnetic (GSM) coordinate system, since it is used for the results shown in Chapter 4 of this thesis (see [*Kivelson and Russell*, 1995] for a detailed explanation of different coordinate systems). The GSM system of coordinates is based on the center of the Earth, the sun and the geomagnetic field. The GSM system has its origin at the center of the Earth, the positive x axis directed towards the sun, and the positive z axis is in the same direction as the northern magnetic pole in a plane containing the x axis, so that the x-z plane contains the dipole axis [*Kivelson and Russell*, 1995]. The y axis is set such that x,y,z form a right handed system of orthogonal coordinates. Figure 1.2 shows a sample of the GSM coordinates set up together with the Earth-sun system. The GSM system is widely used in magnetopause and shock-boundary

calculations since in this system the orientation of the magnetic dipole is not a problem for the cylindrical symmetry of the solar wind flow [*Kivelson and Russell*, 1995]. In this system the direction of the geomagnetic field lines is well ordered near the nose of the magnetosphere and magnetotail, and thus it is the best system to use when studying the effects of the IMF on the magnetosphere. Longitude is measured in the x-y plane from the x toward the y, and latitude is in the y-z plane from the y toward north. An enormous numbers of particles are involved in the behavior of plasmas, and each of these particles move in the electromagnetic field arising from all the others and from external sources. Thus a statistical approach is the best to describe the collective behavior of the plasmas. This approach is called the kinetic theory [e.g., *Gurnett and Bhattacharjee*, 2004; *Walker*, 2005]. In many cases of plasma studies, however, it is not necessary to know the exact evolution of the particles' collective behavior. In such cases, it is sufficient to describe the spatial and temporal evolution of the macroscopic quantities of plasmas, such as densities and velocities, which are quantities of fluid dynamics [*Walker*, 2005]. Therefore, this approach is known as the fluid theory of plasmas. Since the plasmas are magnetized fluids, this approach is commonly known as magnetohydrodynamic (MHD) theory. In this study the magnetohydrodynamic theory of plasmas is used since the problem investigated is better to be described with this approach. Therefore it is relevant at this point to give a detailed explanation of MHD approach.

The MHD approximation requires that the characteristic frequency of any changes must be smaller than the particle cyclotron frequency, $\omega \ll \Omega_c = qB/m$, and characteristic length scale be longer than the particle cyclotron radius, $L \gg r_c = mv\perp/qB$, where Ω_c and r_c are defined as the particle gyration frequency and radius around the background magnetic field, respectively.

1.6.4 Magnetohydrodynamic Equations

The Magnetohydrodynamic theory investigates the evolution of the basic macroscopic quantities, number density, $n_s(\mathbf{r}, t)$; bulk flow velocity, $\mathbf{V}_s(\mathbf{r}, t)$; pressure tensor, $\mathbf{P}_s(\mathbf{r}, t)$;

and kinetic temperature, $T_s(\mathbf{r}, t)$, of the particle species in plasma [*Baumjohann and Treumann*, 1999; *Walker*, 2005]. Following are the MHD equations,

1. **Continuity equation**

   The continuity equation has the physical meaning that the particle mass density is conserved during the fluid's motion if any interaction process that create or annihilate particles species is absent [*Kivelson and Russell*, 1995]. The continuity equation of the s-component fluid of particles in the plasma is

   $$\frac{\partial n_s}{\partial t} + \nabla \cdot (n_s \mathbf{V}_s) = 0. \tag{1.10}$$

2. **Equation of Motion**

   The equation of motion is the momentum density conservation equation of the s-component fluid of the plasma. This equation relates the fluid velocity to density and electromagnetic force acting on the fluid element. The equation of motion is basically the Navier-Stokes equation with the inclusion of the electromagnetic Lorentz force acting on the charges in plasma and is described as,

   $$\frac{\partial (n_s \mathbf{V}_s)}{\partial t} + \nabla \cdot (n_s \mathbf{V}_s \mathbf{V}_s) = -\frac{1}{m_s} \nabla \cdot \mathbf{P}_s + \frac{q_s}{m_s} n_s (\mathbf{E} + \mathbf{V}_s \times \mathbf{B}). \tag{1.11}$$

   The appearance of the Lorentz force in the equation of motion couples the plasma fluid to the full set of electromagnetic equations and distinguishes magnetohydrodynamics from the conventional hydrodynamics [*Walker*, 2005; *Kivelson and Russell*, 1995].

3. **Equation of State**

   Fluid equations of plasma form a hierarchy of ever-increasing order with each order

containing a next-order quantity. Therefore, they must be closed by a truncation of hierarchy. The most common of truncation methods is assuming an equation of state for the pressure. The form of pressure tensor - isotropic or anisotropic, defines the equation of state. For isotropic and isothermal cases the pressure simply takes the ideal gas equation form,

$$P_s = n_s k_B T_s, \tag{1.12}$$

where, k_B is the Boltzmann constant and T_s is the temperature of the particle species. If the temporal variations are sufficiently slow so that plasma has enough time to redistribute energy in order to maintain a constant heat bath temperature, i.e, isothermal condition applies.

If the time variations are fast and heat exchange can not take place, then plasma evolves adiabatically and the change in temperature is related to the change in density. In this case pressure is defined by adiabatic law,

$$P_s = P_{s0} \left(\frac{n_s}{n_{s0}} \right)^\gamma \tag{1.13}$$

Where, γ, is the ratio of specific heat at constant pressure to specific heat at constant volume and is constant in collisionless isotropic plasmas; $\gamma = 5/3$ for the adiabatic case, $\gamma = 1$ for isothermal - constant temperature - case [*Kivelson and Russell*, 1995; *Walker*, 2005] .

The pressure splits into parallel and perpendicular components for anisotropic plasmas. In this case it is still a good approximation to use the ideal gas law for isotropic, isothermal case for both pressures

$$P_{s\parallel} = n_s k_B T_{s\parallel} \tag{1.14}$$

$$P_{s\perp} = n_s k_B T_{s\perp} \tag{1.15}$$

It is not clear however, if both parallel and perpendicular pressures evolve according

to the same adiabatic law.

1.6.5 One-Fluid Theory

Plasmas consist of electrons, of mass m_e, charge q_e and average velocity V_e, and ions, of mass m_i, charge q_i and average velocity V_i. It is possible to neglect differences between the particle species and consider plasma as a conducting fluid that carries magnetic and electric fields. This approximation is called the one-fluid theory of plasmas where fluid variables are assumed to be combinations of variables such as densities and velocities of the different single components of the plasma. This approximation allows one to define a set of one-fluid MHD variables such that.

- The mass density is the total mass per unit volume,

$$\rho = (m_e n_e + m_i n_i);$$

- The fluid velocity is the mass-weighed velocity,

$$\mathbf{V} = (m_i n_i \mathbf{V}_i + m_e n_e \mathbf{V}_e)/(m_e n_e + m_i n_i);$$

- the charge density is,

$$q = e(n_i - n_e);$$

- The current density is,

$$\mathbf{J} = e(n_i \mathbf{V}_i - n_e \mathbf{V}_e);$$

- The plasma pressure is,

$$P = P_i + P_e.$$

Under this approximation the MHD equations can be written as follows;

$$\frac{\partial \rho}{\partial t} + \nabla \cdot [\rho \mathbf{V}] = 0, \tag{1.16}$$

$$\frac{\partial}{\partial t}[\rho \mathbf{V}] + \nabla \cdot [\rho \mathbf{V}] = -\nabla P + \mathbf{J} \times \mathbf{B}, \tag{1.17}$$

$$\frac{d}{dt}\left(\frac{P}{\rho^{\gamma}}\right) = 0. \tag{1.18}$$

The equations 1.16 - 1.18 describe one fluid version of the continuity equation, the equation of motion and the adiabatic law, where electric field, magnetic field, current density, mass density, and pressure are $\mathbf{E}$ $\mathbf{B}$, $\mathbf{J}$, ρ, and P, respectively. An often used assumption of quasineutrality neglects the term $q\mathbf{E}$ in the equation 1.17 for one-fluid MHD plasmas [*Walker*, 2005; *Baumjohann and Treumann*, 1999].

1.6.6   Additional MHD equations

Since plasma is magnetized, additional electromagnetic equations, i.e. Maxwell equations, are also important in the MHD treatment of the plasmas; namely, Faraday's law,

$$\nabla \times \mathbf{E} = -\frac{\partial \mathbf{B}}{\partial t}, \tag{1.19}$$

Ampere's law

$$\nabla \times \mathbf{B} = \mu_0 \mathbf{J} \tag{1.20}$$

and ideal MHD equation, which is a result of the assumption that plasmas are infinitely conducting.

$$\mathbf{E} = -\mathbf{V} \times \mathbf{B}. \tag{1.21}$$

1.6.7   Magnetic Tension and Magnetic Pressure

The term $\mathbf{J} \times \mathbf{B}$ on the right hand side of equation of motion introduces an effect which is the effect of magnetic tension on a conducting MHD fluid. The second term on the

right hand side of Ampere's law, eq. 1.20, can be neglected if the variations are slow which results in the reduced Ampere's law as,

$$\nabla \times \mathbf{B} = \mu_0 \mathbf{J} \tag{1.22}$$

If we take the cross product of both sides of equation 1.22 with $\mathbf{B}$ we can rewrite

$$\mathbf{J} \times \mathbf{B} = -\frac{1}{\mu_0} \mathbf{B} \times \nabla \times \mathbf{B} \tag{1.23}$$

Applying vector algebra,

$$\mathbf{B} \times (\nabla \times \mathbf{B}) = \frac{1}{2}\nabla(B^2) - \nabla \cdot (\mathbf{BB})$$

the above equation results in

$$\mathbf{J} \times \mathbf{B} = -\nabla \left(\frac{\mathbf{B}^2}{2\mu_0} \right) + \frac{1}{\mu_0}\nabla \cdot (\mathbf{BB}). \tag{1.24}$$

The first term on the right hand side of the above equation is the pressure term and the second term is the divergence of the magnetic stress tensor. Magnetic pressure, $B^2/2\mu_0$ simply adds to the plasma pressure and magnetic stress $\mathbf{BB}/\mu_0$ contributes to the tension and torsion of the plasma.

The plasma pressure P and magnetic pressure, $B^2/2\mu_0$, defines the total pressure of the plasma and can be used to define the plasma beta parameter, β. The plasma beta parameter defines the relative importance of the particle and magnetic field pressures. For an isotropic and quasineutral plasma in equilibrium the plasma beta is expressed as

$$\beta = \frac{P}{B^2/2\mu_0} \tag{1.25}$$

For anisotropic plasmas beta splits into parallel and perpendicular components as for the plasma pressure.

$$\beta_{(\perp,\parallel)} = \frac{P_{(\perp,\parallel)}}{B^2/2\mu_0} \tag{1.26}$$

If $\beta \ll 1$ a plasma is called low-beta plasma and if $\beta \gg 1$ high-beta plasma.

1.6.8 Magnetohydrodynamic Waves in Homogeneous Plasmas

MHD equations, 1.16, 1.17 and 1.18, are nonlinear and complicated. Nevertheless, we can study waves with small amplitudes by expressing the wave amplitudes as small perturbations and linearize the MHD equations by neglecting the second-order terms. In this approach, the dependent variables are assumed to be a superposition of an equilibrium value, F_0, and a perturbed value δf. The following substitutions are made to MHD equations

$$\mathbf{V} = \mathbf{V}_0 + \delta\mathbf{v} \quad \mathbf{E} = \mathbf{E}_0 + \delta\mathbf{E} \quad \mathbf{B} = \mathbf{B}_0 + \delta\mathbf{b}$$

$$\rho = \rho_0 + \delta\rho \quad \mathbf{J} = \mathbf{J}_0 + \delta\mathbf{j} \quad P = P_0 + \delta p$$

where, $\mathbf{V_0}$, $\mathbf{E_0}$, $\mathbf{B_0}$, ρ_0, $\mathbf{J_0}$, and P_0 are unperturbed flow velocity, electric field, magnetic field, mass density, current density and pressure, respectively. $\delta\mathbf{v}$, $\delta\mathbf{e}$, $\delta\mathbf{b}$, $\delta\rho$, $\delta\mathbf{j}$, and δp are perturbations to these background values. After substituting the above values and neglecting the second order terms, linearized MHD equations are obtained as:

$$\frac{\partial \delta\rho}{\partial t} + \nabla \cdot (\rho_0 \delta\mathbf{v}) + \nabla \cdot (\delta\rho \mathbf{V_0}) = 0, \tag{1.27}$$

$$\rho_0 \frac{d\delta\mathbf{v}}{dt} + \delta\rho \frac{d\mathbf{V_0}}{dt} + \rho_0(\delta\mathbf{v} \cdot \nabla)\mathbf{V_0} = -\nabla\delta p + (\delta j \times \mathbf{B_0}) + (\mathbf{J_0} \times \delta\mathbf{b}), \tag{1.28}$$

$$\frac{dP_0\rho_0}{dt} + \frac{d\rho_0\delta p}{dt} = \gamma \frac{dP_0\delta\rho}{dt} - \rho_0(\delta\mathbf{v} \cdot \nabla P_0) - P_0(\delta\mathbf{v} \cdot \nabla\rho_0) \tag{1.29}$$

$$\frac{\partial \delta\mathbf{b}}{\partial t} = -(\nabla \times \delta E). \tag{1.30}$$

Equations 1.33 - 1.34 are the continuity equation, the equation of motion, the adiabatic law and Faraday's law respectively.

Substituting the electric field and current density from the linearized ideal MHD law,

$$\delta \mathbf{E} = -\mathbf{V_0} \times \delta \mathbf{b} - \delta \mathbf{v} \times \mathbf{B_0}, \tag{1.31}$$

and reduced Ampere's law

$$\delta \mathbf{j} = \frac{1}{\mu_0} \nabla \times \delta \mathbf{b} \tag{1.32}$$

and using the vector relations,

$$\nabla \cdot (\phi \mathbf{A}) = \mathbf{A} \cdot \nabla \phi + \phi (\nabla \cdot \mathbf{A})$$

and

$$\mathbf{A} \times (\nabla \times \mathbf{B}) = \nabla (\mathbf{A} \cdot \mathbf{B}) - (\mathbf{A} \cdot \nabla)\mathbf{B} - (\mathbf{B} \cdot \nabla)\mathbf{A} - \mathbf{B} \times (\nabla \times \mathbf{A})$$

we obtain a more useful set of linearized equations as;

$$\frac{d\delta\rho}{dt} + \rho_0 (\nabla \cdot \delta \mathbf{v}) + \delta\rho (\nabla \cdot \mathbf{V_0}) + \delta \mathbf{v} \cdot (\nabla \rho_0) = 0, \tag{1.33}$$

$$\rho_0 \frac{d\delta \mathbf{v}}{dt} + \delta\rho \frac{d\mathbf{V_0}}{dt} + \rho_0 (\delta \mathbf{v} \cdot \nabla)\mathbf{V_0} = -\nabla \delta p_T + \frac{1}{\mu_0} \left[(\mathbf{B_0} \cdot \nabla)\delta \mathbf{b} + (\delta \mathbf{b} \cdot \nabla)\mathbf{B_0} \right], \tag{1.34}$$

$$\frac{dP_0\rho_0}{dt} + \frac{d\rho_0\delta p}{dt} = \gamma \frac{dP_0\delta\rho}{dt} - \rho_0 (\delta \mathbf{v} \cdot \nabla P_0) - P_0 (\delta \mathbf{v} \cdot \nabla \rho_0), \tag{1.35}$$

$$\frac{d\delta \mathbf{b}}{dt} = (\delta \mathbf{b} \cdot \nabla)\mathbf{V_0} - \delta \mathbf{b}(\nabla \cdot \mathbf{V_0}) + (\mathbf{B_0} \cdot \nabla)\delta \mathbf{v} - \mathbf{B_0}(\nabla \cdot \delta \mathbf{v}) - (\delta \mathbf{v} \cdot \nabla)\mathbf{B_0}. \tag{1.36}$$

where, d/dt is the convective derivative,

$$\frac{d}{dt} = \frac{\partial}{\partial t} + \mathbf{V_0} \cdot \nabla \tag{1.37}$$

and, δp_T is the total pressure perturbation or generalized pressure,

$$\delta p_T = \delta p + \frac{B_0 \delta b}{\mu_0}. \tag{1.38}$$

If we assume that all the background values are uniform and V_0 is zero, the normalized MHD equations reduce to,

$$\frac{\partial \delta\rho}{\partial t} + \rho_0(\nabla \cdot \delta\mathbf{v}) = 0, \tag{1.39}$$

$$\rho_0\frac{\partial \delta\mathbf{v}}{\partial t} = -\nabla\left(\delta p + B_0\frac{\delta b}{\mu_0}\right) + \frac{1}{\mu_0}(\mathbf{B_0}\cdot\nabla)\delta\mathbf{b}, \tag{1.40}$$

$$\frac{\partial \delta p}{\partial t} = \gamma\frac{P_0}{\rho_0}\frac{\partial \delta\rho}{\partial t}, \tag{1.41}$$

$$\frac{\partial \delta\mathbf{b}}{\partial t} = (\mathbf{B_0}\cdot\nabla)\delta\mathbf{v} - \mathbf{B_0}(\nabla\cdot\delta\mathbf{v}), \tag{1.42}$$

and the ideal MHD law reduces to,

$$\delta\mathbf{E} = -\delta\mathbf{v}\times\mathbf{B_0}. \tag{1.43}$$

We obtain

$$\frac{\partial \delta\rho}{\partial t} = \frac{1}{C_s^2}\frac{\partial \delta p}{\partial t}$$

from equation 1.41 and substitute into equation 1.39 which yields;

$$\frac{1}{C_S^2}\frac{\partial \delta p}{\partial t} + \rho_0(\nabla\cdot\delta\mathbf{v}) = 0 \tag{1.44}$$

where

$$C_S = \left(\gamma\frac{P_0}{\rho_0}\right)^{1/2} \tag{1.45}$$

is the speed of sound.

If equation 1.40 is differentiated with respect to time and $\partial\delta\mathbf{b}/\partial t$ and $\partial\delta p/\partial t$ are eliminated using 1.42 and 1.44 and the following wave equation is obtained:

$$\frac{\partial^2\delta\mathbf{v}}{\partial t^2} = \nabla(C_S^2 + V_A{}^2)(\nabla\cdot\delta\mathbf{v}) - \nabla(\mathbf{V_A}\cdot\nabla)(\mathbf{V_A}\cdot\delta\mathbf{v})$$

$$- \mathbf{V_A}(\mathbf{V_A}\cdot\nabla)(\nabla\cdot\delta\mathbf{v}) + (\mathbf{V_A}\cdot\nabla)^2\delta\mathbf{v} \tag{1.46}$$

where

$$V_A = \frac{B_0}{\sqrt{\mu_0 \rho_0}} \tag{1.47}$$

is the Alfvén speed. We now assume a harmonic wave solution

$$A e^{i(\mathbf{k} \cdot \mathbf{r} - \omega t)} \tag{1.48}$$

where A is a complex amplitude, $\mathbf{k}$ is the wave number, $\mathbf{r}$ is position, ω is complex frequency and t is time. The physical quantity is the real part of this representation and plane waves advance with a velocity ω / k in the direction of $\hat{\mathbf{k}}$. The phase velocity is defined as

$$\mathbf{V_p} = \hat{\mathbf{k}} \frac{\omega}{k}. \tag{1.49}$$

We replace the operators ∇ and $\partial/\partial t$ by $i\mathbf{k}$ and $i\omega$, respectively. Equation 1.46 then becomes,

$$[\omega^2 - (\mathbf{k} \cdot \mathbf{V_A})^2]\delta\mathbf{v} - \mathbf{k}(C_S^2 + V_A^2)(\mathbf{k} \cdot \delta\mathbf{v}) + (\mathbf{k} \cdot \mathbf{V_A})[\mathbf{k}(\mathbf{V_A} \cdot \delta\mathbf{v}) - \mathbf{V_A}(\mathbf{k} \cdot \delta\mathbf{v})] = 0. \tag{1.50}$$

The above equation can be written by its components in Cartesian coordinate system and arranged as,

$$\begin{pmatrix} d_1 & d_2 & d_3 \\ d_4 & d_5 & d_6 \\ d_7 & d_8 & d_9 \end{pmatrix} \begin{pmatrix} v_x \\ v_y \\ v_z \end{pmatrix} = \begin{pmatrix} 0 \\ 0 \\ 0 \end{pmatrix} \tag{1.51}$$

Where,

$$
\begin{aligned}
d_1 &= \omega^2 - (\mathbf{k} \cdot \mathbf{V_A})^2 + [(\mathbf{k} \cdot \mathbf{V_A})V_{Ax} - (C_s^2 + V_A^2)k_x]k_x - (\mathbf{k} \cdot \mathbf{V_A})k_x V_{Ax}, \\
d_2 &= [(\mathbf{k} \cdot \mathbf{V_A})V_{Ay} - (C_s^2 + V_A^2)k_y]k_x - (\mathbf{k} \cdot \mathbf{V_A})k_y V_{Ax}, \\
d_3 &= [(\mathbf{k} \cdot \mathbf{V_A})V_{Az} - (C_s^2 + V_A^2)k_z]k_x - (\mathbf{k} \cdot \mathbf{V_A})k_z V_{Ax}, \\
d_4 &= [(\mathbf{k} \cdot \mathbf{V_A})V_{Ax} - (C_s^2 + V_A^2)k_x]k_y - (\mathbf{k} \cdot \mathbf{V_A})k_x V_{Ay}, \\
d_5 &= \omega^2 - (\mathbf{k} \cdot \mathbf{V_A})^2 + [(\mathbf{k} \cdot \mathbf{V_A})V_{Ay} - (C_s^2 + V_A^2)k_y]k_y - (\mathbf{k} \cdot \mathbf{V_A})k_y V_{Ay}, \\
d_6 &= [(\mathbf{k} \cdot \mathbf{V_A})V_{Az} - (C_s^2 + V_A^2)k_z]k_y - (\mathbf{k} \cdot \mathbf{V_A})k_z V_{Ay}, \\
d_7 &= [(\mathbf{k} \cdot \mathbf{V_A})V_{Ax} - (C_s^2 + V_A^2)k_x]k_z - (\mathbf{k} \cdot \mathbf{V_A})k_x V_{Az}, \\
d_8 &= [(\mathbf{k} \cdot \mathbf{V_A})V_{Ay} - (C_s^2 + V_A^2)k_y]k_z - (\mathbf{k} \cdot \mathbf{V_A})k_y V_{Az}, \\
d_9 &= \omega^2 - (\mathbf{k} \cdot \mathbf{V_A})^2 + [(\mathbf{k} \cdot \mathbf{V_A})V_{Az} - (C_s^2 + V_A^2)k_z]k_z - (\mathbf{k} \cdot \mathbf{V_A})k_z V_{Az}.
\end{aligned}
$$

For studying MHD waves of a stationary uniform medium, it is appropriate to choose a coordinate system where the plane of incidence is defined as the plane containing the background magnetic field $\mathbf{B}$ and the wavenumber $\mathbf{k}$. This approach is appropriate for such a medium since the properties are cylindrically symmetric. In such a coordinate system we reduce the problem to a two-dimensional problem which makes the wave properties easier to understand [*Walker*, 2005]. Without loss of generality we can set the magnetic field along the z axis and wave number $\mathbf{k}$ in the $x - z$ plane, the equation 2.47 simplifies to

$$
\begin{pmatrix}
\omega^2 - k_z^2 V_A^2 - k_x^2(V_A^2 + C_S^2) & 0 & -k_x k_z C_S^2 \\
0 & \omega^2 - k_z^2 V_A^2 & 0 \\
-k_x k_z C_S^2 & 0 & \omega^2 - k_z^2 C_S^2
\end{pmatrix}
\begin{pmatrix}
\delta \mathbf{v_x} \\
\delta \mathbf{v_y} \\
\delta \mathbf{v_z}
\end{pmatrix}
=
\begin{pmatrix}
0 \\
0 \\
0
\end{pmatrix}
\tag{1.52}
$$

The determinant of the coefficients of the perturbations, $\delta \mathbf{v}_{x,y,z}$, in the equation 1.52 has two factors for perturbations in the y direction and in the $x-z$ plane, the plane containing

k and **B**. The dispersion relation of MHD waves requires that this determinant goes to zero, which yields the dispersion relation as,

$$\omega^2 - k_z^2 V_A^2 = 0 \tag{1.53}$$

$$\omega^4 - \omega^2 k^2 (V_A^2 + C_S^2) + k^2 k_z^2 V_A^2 C_S^2 = 0. \tag{1.54}$$

Equations 1.53 and 1.54 now can easily be converted to an arbitrary coordinate system by replacing the term $k_z V_A$ with $\mathbf{k} \cdot \mathbf{V_A}$. This causes the above equation to be modified to a more general form as,

$$\omega^2 - (\mathbf{k} \cdot \mathbf{V}_A)^2 = 0 \tag{1.55}$$

$$\omega^4 - \omega^2 k^2 (V_A^2 + C_S^2) + k^2 (\mathbf{k} \cdot \mathbf{V_A})^2 C_S^2 = 0. \tag{1.56}$$

Where $k = \sqrt{k_n^2 + k_t^2}$ is the total wave number, k_t is the component along the magnetic field, and k_n is the wave number perpendicular to the magnetic field. The direction of $\mathbf{V}_A$ is the same as the background magnetic field. In equations 1.55 and 1.56, we insert $\mathbf{k} \cdot \mathbf{VA} = k V_A \cos\theta$ and divide the equations by k^2 and k^4 respectively to obtain the phase velocities of MHD waves - Alfvén , fast and slow waves. Here θ is the angle between the background magnetic field and the wave number. The resulting phase velocity equations are,

$$V_{p(Alf)}^2 = V_A^2 \cos^2\theta \tag{1.57}$$

$$V_{p(f,s)}^4 - V p_{f,s}^2 (V_A^2 + C_S^2) + V_A^2 C_S^2 \cos^2\theta = 0. \tag{1.58}$$

Equation 1.57 describes the phase velocity of the Alfvén waves as,

$$V_{p(Alf)} = \pm V_A \cos\theta, \tag{1.59}$$

and equation 1.58 can be solved to give the phase velocities of fast and slow MHD waves as,

$$V_{p(f,s)} = \frac{1}{2} \left((V_A^2 + C_S^2) \pm \sqrt{(V_A^2 + C_S^2)^2 - 4V_A^2 C_S^2 cos^2\theta} \right)^{1/2}. \tag{1.60}$$

Equation 1.59 describes the shear Alfvén wave, which propagates parallel to the ambient magnetic field and is a transverse electromagnetic wave. The shear Alfvén wave perturbs the plasma in the direction perpendicular to the plane containing the background magnetic field and the wave vector **k** [*Kivelson and Russell*, 1995; *Walker*, 2005]. Alfvén waves do not cause any change in either magnetic field magnitude or the plasma density and thus they are also called non-compressional waves.

Equation 1.60 gives the phase velocities of magnetosonic waves, fast and slow waves. The fast wave solution is with the positive sign and the slow wave solution is with the negative sign. The phase velocity of the magnetosonic waves depends on the Alfvén and sound velocities and the angle between the magnetic field and wave number. The magnetosonic wave perturbs the plasma within the plane of wave number and background magnetic field, which implies that the waves of this type change the plasma density and magnetic field magnitude and thus they are named compressional waves [*Kivelson and Russell*, 1995]. Phase relations of magnetic and plasma pressure perturbations for fast and slow compressional MHD waves are shown in Figure 1.7. The thermal or plasma pressure and magnetic pressure are out of phase for slow MHD waves (Figure 1.7 a) and in phase for fast MHD waves (Figure 1.7 b).

Another important property of MHD waves is their group velocity, $\mathbf{V}_g$, the velocity at which the wave packet moves [*Sutherland*, 2010]. The group velocity can be found using

$$V_g = \frac{d\omega}{d\mathbf{k}} = \hat{x}\frac{d\omega}{dk_x} + \hat{y}\frac{d\omega}{dk_y} + \hat{z}\frac{d\omega}{dk_z}, \tag{1.61}$$

and can be obtained from the dispersion relation in Equations 1.55 and 1.56. The group velocity is in the direction of energy transfer by a wave packet that is physically realistic and may contain a spread of wave vectors. The direction and values of the group veloc-
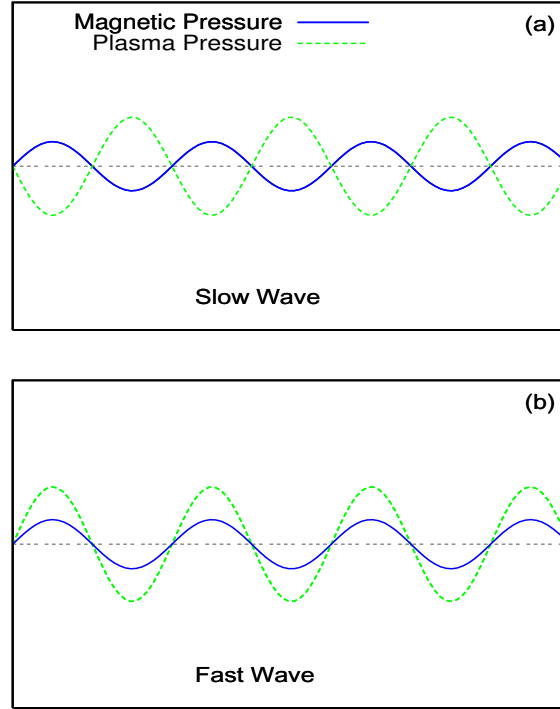
Figure 1.7: Phase relations of the magnetic and plasma pressures for slow and fast waves. Panel (a) shows the slow waves and panel (b) shows the fast waves phase relations.

ity are not necessarily equal to those of the phase velocity [*Walker*, 1977; *Kivelson and Russell*, 1995; *Sutherland*, 2010]. Figure 1.8 displays the distinction between phase and group velocities of a wave. Figure 1.8 (a) shows that phase and group velocities can be obtained using the dispersion relation curve. The phase velocity at certain values of ω and k is equal to the slope of the line drawn to the point from the origin. The group velocity is found using the value of the derivative at the point of interest. Figure 1.8 (b) shows a wave packet and envelope of the wave moving with the group velocity while the planes of constant phase moving with the phase velocity [*Gurnett and Bhattacharjee*, 2004].

The polarization relations of the electric field , velocity, current density and magnetic field perturbations of the MHD waves are shown in Figure 1.9. In Figure 1.9, the back-
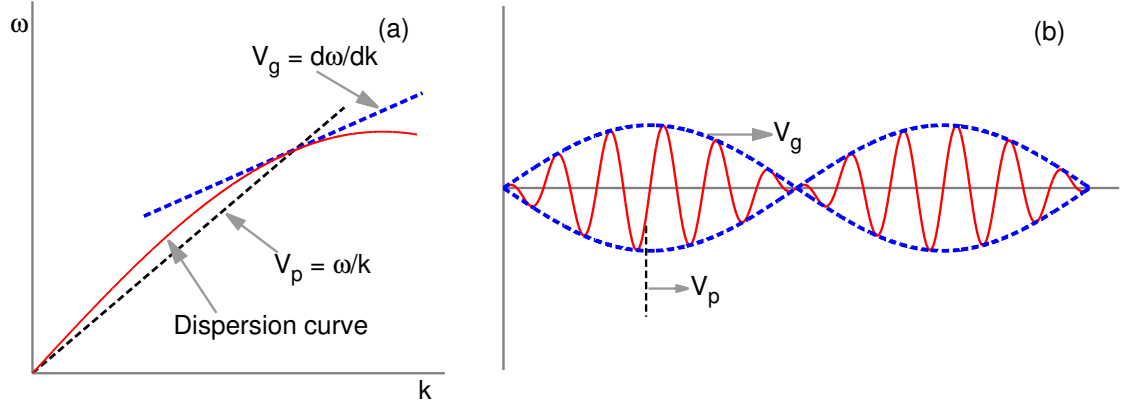
Figure 1.8: Distinction between phase and group velocities. The phase and group velocities of a wave can be determined using its dispersion curve, displayed on panel (a). The difference between the phase and group velocities are shown on panel (b); the envelope of a wave packet moves at the group velocity and the planes of constant phase move at the phase velocity.

ground magnetic field $\mathbf{B_0}$ is assumed to lay on the xz plane and the wave number $\mathbf{k}$ is assumed to be along x. The Poynting vector, $\mathbf{S} = 1/\mu_0 \delta E \times \delta b$, is also added which shows the direction of energy propagation [*Kivelson and Russell*, 1995]. Panel (a) shows the polarization relations for the Alfvén wave and panel (b) shows the polarization relations for the fast and slow compressional waves.

The polar plot of the MHD waves phase velocity with one axis aligned with the background magnetic field is a useful tool for understanding the wave properties. These phase velocity diagrams are known as Friedrichs diagrams, and are shown in Figure 1.10. The angle related to the axis of the magnetic field is the angle between, $\mathbf{k}$ and $\mathbf{B_0}$, and the distance from the origin to a point is the phase velocity value at the referred point. The contours of the phase velocity diagrams change with the relative values of C_s and V_A. Figure 1.10 shows these contours for $V_A > C_S$ on panel (a) and $V_A < C_s$ on panel (b). In both cases, fast wave phase velocity is largest when $\mathbf{k}$ is perpendicular to $\mathbf{B}_0$ and can
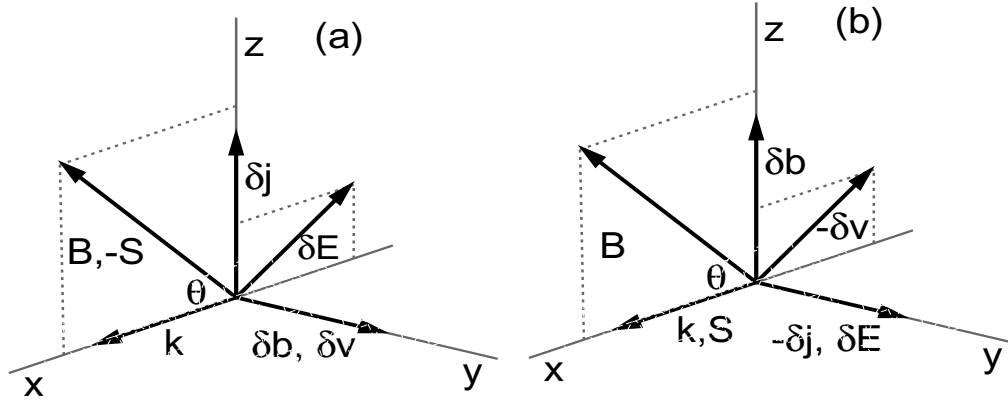
Figure 1.9: Schematic of the electric field, magnetic field, velocity and current polarizations of Alfvén wave, panel (a), and fast and slow waves, panel (b).

propagate in all directions. Slow and Alfvén waves phase velocities are largest at parallel angles and do not propagate in the direction perpendicular to B_0.

Similar to phase velocity diagrams, group velocity diagrams can also be represented in a polar plot with respect to the background magnetic field. Figure 1.11 shows group velocity diagrams of MHD waves; panel (a) is for $V_A > C_S$ and panel (b) is for $V_A < C_S$. The fast MHD wave group velocity is finite in all directions while that of slow and Alfvén waves is mainly along $\mathbf{B}_0$. The Alfvén wave has a group velocity that is along $\pm\mathbf{B}_0$ for all values of $\mathbf{k}$ with amplitude V_A. The slow wave on the other hand, has a group velocity of $\pm C_S$ if $\mathbf{k}$ is along $\mathbf{B}_0$, and increases slightly as the angle between $\mathbf{k}$ and $\mathbf{B}_0$ increases and rotates away. As $\mathbf{k}$ continue to increase the slow wave group velocity decreases aligning more closely to $\mathbf{B}_0$ [*Kivelson and Russell*, 1995]. Group velocities are significant in

(a) $V_A > C_S$ (b) $V_A < C_S$
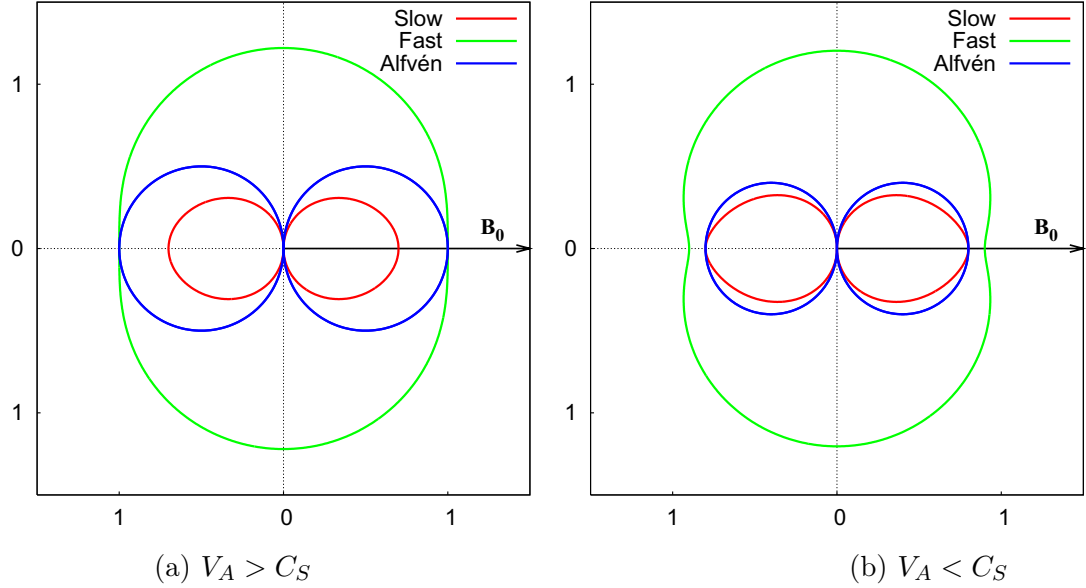
Figure 1.10: Phase velocity, Friedrichs, diagrams of MHD waves, fast, slow and Alfvén waves. The angle relative to the axis of $\mathbf{B_0}$ is the angle between, $\mathbf{B_0}$ and $\mathbf{k}$. The phase velocity value at any point is the distance from the origin to the point. Panel (a) shows the diagrams for $V_A > C_S$ and panel (b) shows the diagrams for $V_A < C_S$.

describing the direction of energy propagation associated with the waves. Therefore, we can conclude from Figures 1.11 (a) and (b) that fast MHD waves can carry energy in any direction while slow waves can carry energy over a relatively narrow range of angles with respect to $\mathbf{B_0}$. Alfvén waves on the other hand, can carry energy only along the background magnetic field even if the phase fronts are arbitrarily oriented [*Kivelson and Russell*, 1995]. The direction of the Poynting flux which also shows the direction of the energy propagation, agrees with the conclusions drawn from group velocity diagrams (see Figure 1.9).

1.7 Geomagnetic Pulsations

The existence of oscillations of the Earth's surface magnetic field or geomagnetic pulsations has been known for centuries [*Kivelson and Russell*, 1995; *Walker*, 2005]. Here
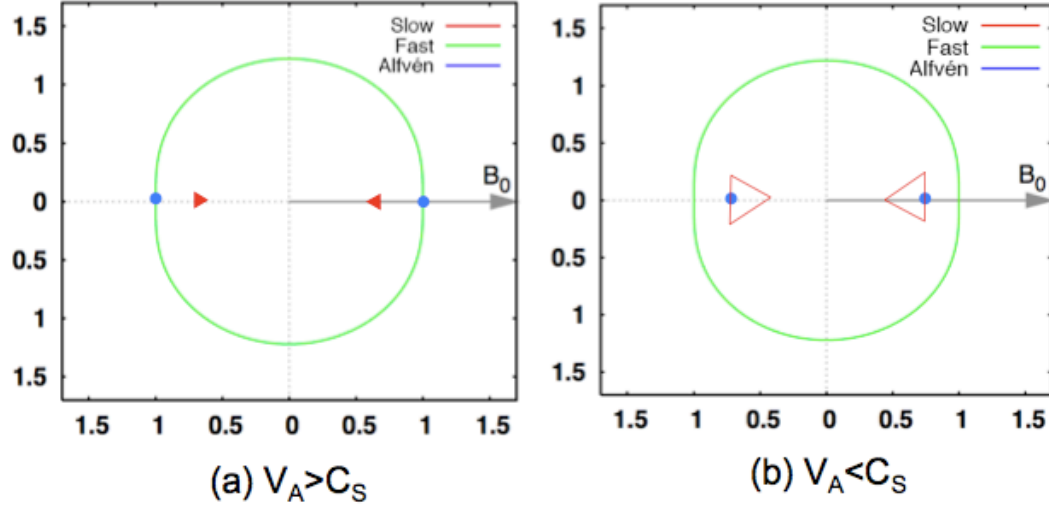
Figure 1.11: Group velocity diagrams of MHD waves. The background magnetic field, $\mathbf{B_0}$, is aligned along x axis. Panel (a) shows the diagrams for $V_A > C_S$ and panel (b) shows the diagrams for $V_A < C_S$.

we consider long period waves with scales comparable to the size of the magnetosphere, namely Ultra Low Frequency (ULF) waves, and ignore the shorter periods oscillations that are the result of processes out of the MHD limit [*Walker*, 2005]. These oscillations are actually MHD waves and they are classified according to their frequency range, which is divided into five intervals, $Pc1 - Pc5$ for continuous pulsations and two intervals, $Pi1 - Pi2$ for irregular pulsations [e.g., *Kivelson and Russell*, 1995; *Baumjohann and Treumann*, 1999; *Walker*, 2005]. Table 1.1 shows frequency and period range of the ULF pulsations.

Name	Pc-1	Pc-2	Pc-3	Pc-4	Pc-5	Pi-1	Pi-2
T (s)	0.2-5	5-10	10-45	45-150	150-600	1-40	40-150
f	0.2-5 Hz	0.1-0.2 Hz	22-100 mHz	7-22 mHz	2-7 mHz	0.025-1 Hz	2-25 mHz

Table 1.1: Period and frequency ranges of ULF waves observed in the magnetosphere.

ULF fluctuations were observed long before their connection to space plasmas were found. They were suggested as originating from MHD waves in the outer atmosphere

about a century after their first observations [*Kivelson and Russell*, 1995]. Continuous oscillations (Pc) are quasi-sinusoidal and have longer durations while irregular oscillations (Pi) are shorter lived and do not have a well defined spectral peak. Pi pulsations are also more localized in latitude and longitude than the Pc pulsations. Geomagnetic pulsations can inject a significant amount of energy into the magnetosphere [*Taroyan and Ruderman*, 2011]. In many cases, the pulsating disturbances observed are associated with Alfvén waves.

Boundary conditions are important for frequencies of the ULF waves that can be excited. The high latitude ionosphere forms boundaries at the ends of most field lines and the near-equatorial ionosphere forms the inner boundary while the magnetopause forms the outer boundary. If conductivity is very high, the ionosphere will reflect back the waves that are incident on it. Like waves on a string, Alfvén waves can satisfy reflection conditions for only a certain range of wavelengths and thus only certain frequencies can be resonant. These frequencies are controlled by the length of the field lines between two ionospheres, the plasma density and the strength of the magnetic field [*Kivelson and Russell*, 1995].

Pc5 pulsations are usually referred as Field Line Resonances (FLRs) and they represent a resonant Alfvén wave standing on the geomagnetic field lines [*Walker*, 2005; *Taroyan and Ruderman*, 2011; *Baumjohann and Treumann*, 1999]. FLRs are caused by the oscillations of the geomagnetic field lines often as a mixture of poloidal and toroidal oscillations [*Baumjohann and Treumann*, 1999]. The energy source of FLRs or Pc5 pulsations is thought to be near magnetopause since they are usually observed close to the magnetopause flanks. [*Taroyan and Ruderman*, 2011].

There are several possible driving mechanisms for the FLRs. One possible mechanism is the Kelvin Helmholtz Instability (KHI) generated surface waves excited on the magnetopause. These KHI surface waves can set the inner magnetosphere into oscillations which can become resonant with a certain geomagnetic field line [*Southwood*, 1974; *Chen and Hasegawa*, 1993]. It is found that there is a strong correlation between the solar

wind speed and the FLRs which is a strong indicator that the energy source of the FLRs can be KHI [*Mills and Wright*, 1999].

Other possible excitation mechanisms of FLRs are suggested to be the compressional waves generated by solar wind entering into the magnetosphere directly from high latitudes [*Baumjohann and Treumann*, 1999; *Walker*, 2005] and magnetospheric waveguide modes [*Mann et al.*, 1999; *Mills et al.*, 1999; *Mills and Wright*, 1999].

Southwood [1974] proposed a model that illustrates fast waves coupling to the observed FLRs. Their model however did not fully describe the mechanism which drive the fast waves. In this thesis we have shown for the first time that the Kelvin-Helmholtz Instability is a mechanism for fast and slow MHD waves generation along MHD shear flow boundaries. The KHI generated MHD waves may propagate into the regions on either side of the boundary and provide a significant mechanism for energy transport. MHD waves generation due to KHI on the magnetopause boundary could explain the unknown generation mechanism of fast waves coupling to FLRs suggested by *Southwood* [1974]. The Kelvin - Helmholtz (K-H) generated fast/slow waves are introduced in the context of the primary/secondary KHI.

Chapter 2

Kelvin-Helmholtz Instability on MHD Shear Flow Boundaries: Background and Theory

2.1 Introduction

Shear flows of magnetized plasmas are observed in the solar atmosphere, in interplanetary space and planetary magnetospheres. They are also important elements of remote astrophysical objects such as accretion disks, black holes and neutron stars. Understanding physical processes such as plasma mixing, energy and momentum transport between two media on both sides of these flow boundaries is strongly related to their stability conditions [*Ruderman and Belov*, 2010]. The Kelvin-Helmholtz Instability (KHI) which is the subject of study in this thesis, is a type of instability often observed along such shear flow boundaries.

On the Earth's magnetopause, the KHI is generated due the velocity shear between magnetosheath and magnetosphere flows and it plays momentous roles in many magnetospheric phenomena. Such are generation of geomagnetic pulsations [*Agapitov et al.*,

2009; *Villante*, 2007; *Rae et al.*, 2005; *Chen and Hasegawa*, 1993; *Miura and Pritchett*, 1982; *Walker*, 1981; *Southwood*, 1974], inducing magnetic reconnection and plasma mixing at the magnetopause during northward Interplanetary Magnetic Field(IMF) [*Nakai and Ueno*, 2011; *Pegoraro et al.*, 2008; *Nakamura et al.*, 2006; *Fairfield et al.*, 2000], and causing momentum and energy transport across the magnetopause [*Hasegawa et al.*, 2006; *Kivelson and Chen*, 1995; *Miura*, 1984; *Pu and Kivelson*, 1983b]. Kelvin-Helmholtz(K-H) driven surface waves can couple to the cavity modes in the magnetosphere and initiate field line resonances [*Mann et al.*, 1999; *Mills and Wright*, 2000]. The KHI generated surface waves on the shear flow boundaries in the inner magnetosphere may also be a possible motive for the substorm expansion onsets which are key elements for solar wind interaction with the Earth's magnetosphere and the ionosphere [*Uberoi*, 2006; *Lui*, 2004; *Yoon et al.*, 1996; *Rae et al.*, 2005].

The KHI on MHD shear flow boundaries is also a significant tool for understanding many physical processes in solar atmospheres [*Andries et al.*, 2000; *Andries and Goossens*, 2001; *Foullon et al.*, 2011, 2013; *Nykyri and Foullon*, 2013; *Möstl et al.*, 2013; *Cécere et al.*, 2014] and remote astrophysical objects such as accretion disks [*Michikoshi and Inutsuka*, 2006; *Johansen et al.*, 2006; *Barranco*, 2009; *Pessah*, 2010; *Guillochon et al.*, 2010; *Lee et al.*, 2010a, b], galactic centers [*Anninos et al.*, 2012; *Kamaya*, 1998; *Roediger et al.*, 2012, 2013], molecular clouds [*Berné and Matsumoto*, 2012] and cometary tails [*Ershcovich and Chernikov*, 1973; *Ershkovich*, 1979; *Ray*, 1982; *Niedner et al.*, 1983; *Ershkovich and Mendis*, 1986]. In the solar atmosphere for instance, the KHI is a process that could lead to plume/interplume mixing, provide a source for Alfvénic fluctuations [*Andries and Goossens*, 2001; *Andries et al.*, 2000] and mixing of Coronal Mass Ejection (CME) regions with the outside region of the solar corona [*Foullon et al.*, 2011, 2013; *Nykyri and Foullon*, 2013; *Möstl et al.*, 2013]. The heliopause, the boundary between the solar system and interstellar wind, is also a type of MHD shear flow boundary and subject to the KHI which can enhance the energy transport from the interstellar medium into the solar system [*Ruderman and Fahr*, 1993, 1995; *Taroyan and Ruderman*, 2011].

Negative energy waves (NEWs) are also supported by plasmas with relative motion [*Andries and Goossens*, 2002; *Walker*, 2000; *Ruderman and Wright*, 1998; *Ruderman and Goossens*, 1995; *McKenzie*, 1970; *Fejer*, 1963]. Existence of NEWs in between two media with relative motion is also a prominent physical phenomenon in hydrodynamics [*Ostrovskii et al.*, 1986; *Cairns*, 1979; *Acheson*, 1976], atmospheric sciences [*Lindzen and Rosendhal*, 1982], and solar atmosphere [*Tirry et al.*, 1998; *Joarder et al.*, 1997]. The KHI surface modes are theorized to be related to negative energy waves or over-reflected waves in many studies [*Lashmore-Davies*, 2005; *Taroyan and Erdélyi*, 2003b, a, 2002; *Mann et al.*, 1999; *Mills et al.*, 1999; *Mills and Wright*, 1999; *Lindzen and Rosendhal*, 1982; *Cairns*, 1979; *McKenzie*, 1970; *Ruderman and Belov*, 2010]. The concept of the connection between the KHI and NEWs however, needs further investigation.

In this Chapter we describe governing equations and boundary conditions for various models of the KHI that are used in this thesis and show derivations. The models presented may be applicable to MHD shear flow boundaries in the Earth's magnetospheric regions as well as those of the solar corona or remote astrophysical objects. We will also briefly discuss the possible relation between the KHI and Negative Energy Waves.

The KHI can evolve spatially (grow in space) or temporally (grow in time) or both *Itoh et al.* [2004]. A spatial KHI is called absolute if initiated wave modes grow exponentially with time at any fixed location in space, and it is called convective if they are convected very quickly and decay with time at any fixed spatial position despite increasing amplitude. [*Bers*, 1983]. Only temporal evolution of the KHI is considered in the current study.

2.2   Concept of Instabilities

In Chapter 1 Section 1.6.8, we have obtained wave solutions for which frequency, ω, is purely real. These types of solutions represent waves whose amplitudes are constant in time which implies that plasma neither loses energy to the waves nor gains energy from

the waves [*Kivelson and Russell*, 1995]. If there is energy accumulation or a source of free energy in a plasma, energy exchange between the plasma and the waves will be possible and average wave amplitude will change with time [*Kivelson and Russell*, 1995]. The plasma conditions that lead to wave growth in time are referred as instabilities, or more precisely temporal instabilities [*Kivelson and Russell*, 1995]. Instabilities develop as a way of redistributing the available free energy to reach an equilibrium state [*Kivelson and Russell*, 1995].

If waves described by the equation

$$Ae^{i(\mathbf{k}\cdot\mathbf{r}-\omega t)} \tag{2.1}$$

are to change amplitude with time, ω must have an imaginary part, $\omega = \omega_r + i\omega_i$. For positive values of ω_i the wave amplitude grows and for negative values of ω_i the wave amplitude decays exponentially with time. Therefore ω_i is called the growth rate.

The plasma regions in space and astro-space are not closed systems in thermal equilibrium and are driven by energy and momentum input from outside [*Baumjohann and Treumann*, 2001]. Therefore free energy and instabilities are generally available in these plasma systems. The energy and momentum input from outside produces inhomogeneities and spatial gradients on macroscopic scales which cause the large-scale or macroinstabilities. On the microscopic scale this input causes the deformation and distortion of the local plasma distribution and small scale or microinstabilities [*Baumjohann and Treumann*, 2001]. The scale sizes of macroinstabilities are comparable to the bulk scales of plasma and that of microinstabilities are comparable to the particle inertial lengths and gyroradii [*Baumjohann and Treumann*, 2001]. Therefore, macroinstabilities can be treated within the frame work of fluid plasma (MHD) theory while microinstabilities should be treated with kinetic plasma approach [*Baumjohann and Treumann*, 2001]. The Kelvin-Helmholtz Instability is a macroinstability and therefore is treated with MHD theory in the current study.

2.3 KHI Models and Equations

As mentioned earlier the KHI is a macroscopic instability generated by shear flows in magnetized plasmas, thus the best way to study this phenomenon would be magnetohydrodynamic (MHD) theory which is used in the current study. Since plasma is considered to be collisionless in space, the ideal MHD equations are used where the plasma is assumed to be infinitely conducting and the displacement electric field is zero. A standard approach to the problem of the KHI on MHD shear flows is the use of normal mode analysis, which is based on the linearized MHD equations - shown in Chapter 1 and Section 1.6.8.

KHI can develop on a Tangential Discontinuity (TD) boundary, where normal components of the background magnetic field and plasma flow velocity are absent. Two different shear flow boundary configurations that may lead to KHI on a TD boundary is illustrated on Figure 2.1 (a) and (b). In Figure 2.1 (a) flow velocities, $V_{01,02}$, are in opposite directions and in Figure 2.1 (b) region 2 is stationary, $V_{02} = 0$, while plasma in region 1 has a flow velocity V_{01} in the $-y$ direction. Physically a TD boundary has a finite thickness, Δ_x, as shown in Figure 2.1 (a) and (b). However, it could be assumed to have zero transition thickness if waves with large wavelength are considered.

In this thesis, we first consider a zero boundary thickness approach with infinite plasmas on both sides of the boundary. Following, an inner boundary on one side is included which introduces the effects of the reflected waves. Finally we will consider a finite thickness boundary which provides a wider wavelength regime for the investigation of the KHI waves. For all three models considered, we have assumed warm homogeneous plasmas in two media on both sides the boundary. A TD boundary is assumed to lay in the $y - z$ plane and the x direction is chosen to be the boundary normal. The following sections describe each of the models used and show derivations for the KHI waves dispersion relations.
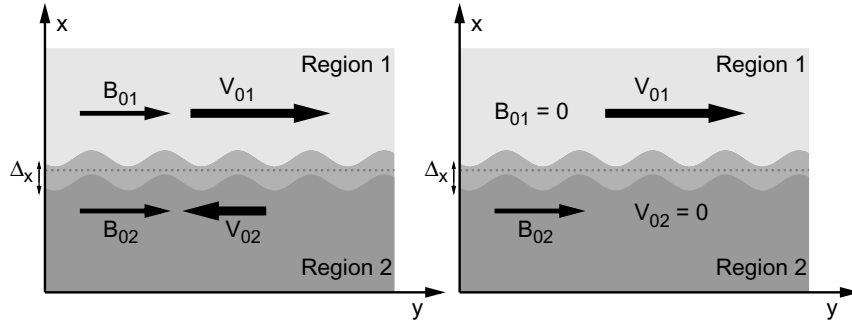
Figure 2.1: Two configurations that may lead to Kelvin-Helmholtz instability. The boundary has a nonzero thickness, Δ_x. However, zero thickness boundary can be assumed if the wavelengths of the considered waves are larger than the thickness of the boundary, $\lambda \gg \Delta_x$.

2.3.1   Thin Boundary Layer Model

In this section, the dispersion relations for the KHI waves are derived corresponding to the zero thickness boundary assumption. Zero transition thickness is suitable if the wavelengths, λ, of the generated waves are considerably larger than the thickness, Δ_x, of the boundary; $\lambda \gg \Delta_x$. A sinusoidal perturbation is assumed, depending on time and space as in equation 2.1, and a Cartesian coordinate system is used. The set up used is displayed in Figure 2.2. Boundary conditions corresponding to a TD boundary, namely continuity of the displacement, δ_x, and total pressure perturbation, δp_T, across the MHD shear flow boundary, are applied.
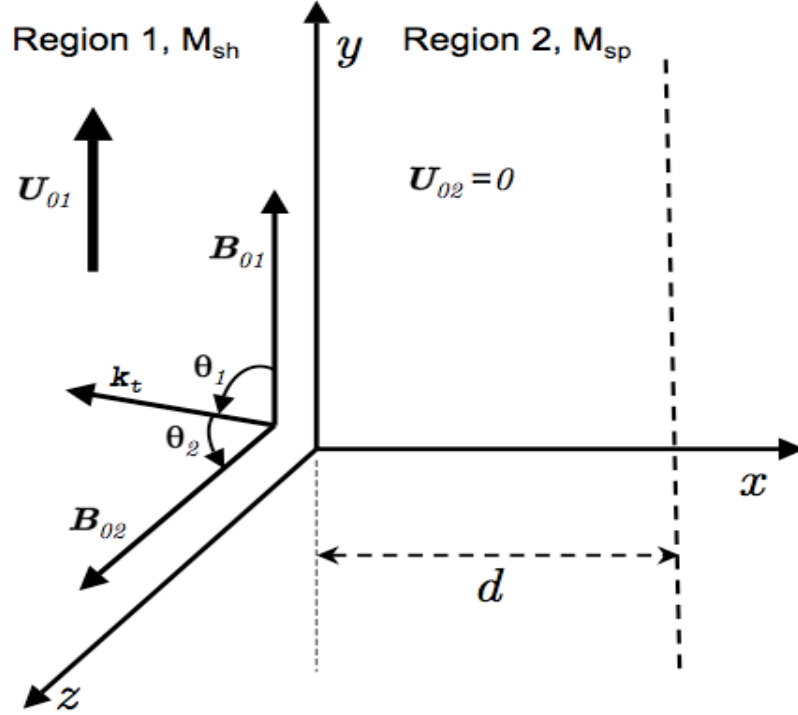
Figure 2.2: Model used for the zero thickness boundary derivations. An inner boundary is set at $x = d$ in region 2 for bounded calculations, and is removed for calculations with semi-infinite plasmas in both regions.

KHI on a Boundary With Infinite Plasmas on Both Sides

Here we consider a shear flow with two semi-infinite plasma media on both sides of the boundary. In this approach, one uses the boundary conditions across the TD boundary as mentioned above and the assumption that the perturbations vanish at $\pm\infty$.

We make use of the linearized one-fluid MHD equations shown in Chapter 1 and Section 1.6.8 (equations 1.33 - 1.36). Considering a plasma with a uniform background flow velocity, magnetic field, electric field, current density, pressure and density as, $\mathbf{V}_0, \mathbf{B}_0, \mathbf{E}_0, \mathbf{J}_0, P$

and ρ_0 respectively we simplify the linear equations to obtain:

$$\frac{d\delta\rho}{dt} \; + \; \rho_0(\nabla \cdot \delta\mathbf{v}) = 0 \qquad\qquad \text{continuity equation,} \qquad (2.2)$$

$$\rho_0\frac{d\delta\mathbf{v}}{dt} \; = \; -\nabla\delta p_T + \frac{1}{\mu_0}\left[(\mathbf{B_0}\cdot\nabla)\delta\mathbf{b}\right] \qquad \text{equation of motion,} \qquad (2.3)$$

$$\frac{d\delta p}{dt} \; = \; C_S^2\frac{d\delta\rho}{dt} \qquad\qquad\qquad \text{adiabatic law,} \qquad (2.4)$$

$$\frac{d\delta\mathbf{b}}{dt} \; = \; (\mathbf{B_0}\cdot\nabla)\delta\mathbf{v} - \mathbf{B_0}(\nabla \cdot \delta\mathbf{v}) \qquad\qquad \text{Faraday's law.} \qquad (2.5)$$

Notice here that d/dt is the convective derivative,

$$\frac{d}{dt} = \frac{\partial}{\partial t} + \mathbf{V_0}\cdot\nabla, \qquad\qquad\qquad (2.6)$$

and δp_T is total pressure perturbation or generalized pressure,

$$\delta p_T = \delta p + \frac{B_0\delta b}{\mu_0}. \qquad\qquad\qquad (2.7)$$

If we assume space and time variation as $Ae^{i(\mathbf{k r}-\omega t)}$ as shown in Equation 2.1 , then we can use the following replacements;

$$\tfrac{\partial}{\partial t} = -i\omega, \quad \nabla = i\mathbf{k},$$

and thus the convective derivative can be replaced by,

$$\frac{d}{dt} = -i\omega + \mathbf{V}_0\cdot\mathbf{k} = -i\omega',$$

where we have introduced the Doppler-shifted frequency,

$$\omega' = w - \mathbf{V}_0\cdot\mathbf{k}. \qquad\qquad\qquad (2.8)$$

Using above the replacements the Equations 2.2 - 2.5 may be written as;

$$-i\omega'\delta\rho \quad + \quad \rho_0(i\mathbf{k}\cdot\delta\mathbf{v}) = 0, \tag{2.9}$$

$$-i\omega'\rho_0\delta\mathbf{v} \quad = \quad -i\mathbf{k}\delta p_T + \frac{1}{\mu_0}\left[(\mathbf{B_0}\cdot i\mathbf{k})\delta\mathbf{b}\right], \tag{2.10}$$

$$-i\omega'\delta p \quad = \quad -i\omega'C_S^2\delta\rho, \tag{2.11}$$

$$-i\omega'\delta\mathbf{b} \quad = \quad (\mathbf{B}_0\cdot i\mathbf{k})\delta\mathbf{v} - \mathbf{B_0}(i\mathbf{k}\cdot\delta\mathbf{v}). \tag{2.12}$$

We now substitute $\delta\mathbf{b}$ from Equation 2.12 and $\delta\rho$ from Equation 2.11, in Equation 2.10 and 2.9 reducing the above equations to two;

$$-\omega'\frac{1}{C_S^2}\delta p \quad + \quad \rho_0(\mathbf{k}\cdot\delta\mathbf{v}) = 0, \tag{2.13}$$

$$-\omega'\rho_0\delta\mathbf{v} \quad = \quad -\mathbf{k}\delta p_T + \frac{1}{\mu_0\omega'}(\mathbf{B_0}\cdot\mathbf{k})\left[-(\mathbf{B_0}\cdot\mathbf{k})\delta\mathbf{v} + \mathbf{B}_0(\mathbf{k}\cdot\delta\mathbf{v})\right]. \tag{2.14}$$

Let us now adopt the Cartesian coordinate system shown in Figure 2.2, where all the background values are uniform along the y, z coordinates and change sharply at $x = 0$. Using Tangential Discontinuity (TD) boundary conditions such that the normal components of the $\mathbf{B}_0, \mathbf{V}_0$ are zero and taking the x component of equation 2.14 we obtain:

$$-\omega'\rho_0\delta v_x = -k_x\delta p_T - \frac{1}{\mu_0\omega'}(\mathbf{B}_0\cdot\mathbf{k})^2\delta v_x. \tag{2.15}$$

We choose the total pressure perturbation, δp_T, and the normal displacement, δ_x, as the fundamental quantities to be determined since TD boundary conditions require that they are continuous across the boundary even though the zero order quantities are discontinuous. Therefore we rewrite Equation 2.15 in terms of δp_T and replace $\delta v_x = d\delta x/dt = -i\omega'\delta x$ which yields;

$$ik_x\delta p_T = \rho_0\left[\omega'^2 - \frac{1}{\mu_0\rho_0}(\mathbf{B}_0\cdot\mathbf{k})^2\right]\delta x. \tag{2.16}$$

Now we apply TD boundary conditions to the above equation. Since plasma parameters will change across the boundary we distinguish the quantities for both sides with indices 1 and 2. Therefore we use the following conditions;

$$\delta p_{T1} = \delta p_{T2}, \quad \delta x_1 = \delta x_2 \tag{2.17}$$

to obtain;

$$[(\omega_1')^2 - \frac{(\mathbf{B}_{01} \cdot \mathbf{k}_t)^2}{\rho_{01}\mu_0}]\frac{\rho_{01}}{k_{x1}} + [(\omega_2')^2 - \frac{(\mathbf{B}_{02} \cdot \mathbf{k}_t)^2}{\rho_{02}\mu_0}]\frac{\rho_{02}}{k_{x2}} = 0. \tag{2.18}$$

In deriving equation 2.18, we take into account the fact that the normals on both sides of the TD boundary are directed oppositely.

Rewriting equation 2.18 in terms of background Alfvén velocities, we obtain a more useful form as;

$$[(\omega_1')^2 - (\mathbf{V}_{A1} \cdot \mathbf{k}_t)^2]\frac{\rho_{01}}{k_{x1}} + [(\omega_2')^2 - (\mathbf{V}_{A2} \cdot \mathbf{k}_t)^2]\frac{\rho_{02}}{k_{x2}} = 0, \tag{2.19}$$

where $\omega_{1,2}'$ are Doppler-shifted frequencies, $V_{A1,A2}$ are Alfvén velocities, $C_{S1,S2}$ are sound speeds and $k_{x1,x2}$ are wave numbers normal to the boundary in regions 1 and 2 respectively(see Figure 3.2). Similar derivations can be found in [*Pu and Kivelson*, 1983a]. However, we have considered fully arbitrary values of background parameters and specifically magnetic field directions in our calculations which is not done in the past and results are shown in chapter 3 of this thesis. The equations for the normal wave numbers in each homogeneous plasma region can easily be derived from the equation 1.56 as;

$$k_{x1,x2} = \left(\omega_{1,2}'^4 / \left[\omega_{1,2}'^2 (V_{A1,A2}^2 + C_{s1,s2}^2) - (\mathbf{V}_{A1,A2} \cdot \mathbf{k}_t)^2 C_{s1,s2}^2\right] - k_t^2\right)^{1/2}. \tag{2.20}$$

Equation 2.18 is used in Chapter 3 to find the solutions to the Kelvin-Helmholtz unstable waves on the boundary of the Earth's magnetopause with semi-infinite plasmas on both sides. Allowing $k_{x1,x2}$ to be complex provides solutions that can describe not

only purely oscillatory or evanescent modes, but also modes that have both oscillations and a background growth or decay in x. The arbitrary conditions we have adopted allow us to find modes which decay in time and have a spatially growing nature in either region.

KHI with a Reflecting Boundary in the Region 2

If a perfectly reflecting boundary is added in one of the regions as shown on Figure 2.2, this may cause significant impacts on the evolution of the KHI.

We assume that a perfectly reflecting boundary is added in region 2 at $x = d$. Two types of MHD wave modes with different boundary conditions at $x = d$ become possible namely kink and sausage waves. The sausage modes will oscillate on the shear flow boundary causing expansion and contraction of the plasma while not disturbing the inner boundary. Kink modes on the other hand will cause symmetric oscillations along the shear flow and in the inner boundary giving the plasma a serpentine motion.

In addition to connecting MHD wave solutions in regions 1 and 2 through TD boundary conditions, one also has to match inner boundary conditions at $x = d$. The boundary conditions at $x = d$ are different for the kink and sausage modes, since the kink modes will have an anti-node and sausage modes will have a node at this position. Hence the boundary condition at $x = d$ for the sausage modes is

$$\delta v_{x2} = 0, \tag{2.21}$$

from which it follows that

$$\frac{d\delta p_{t2}}{dx} = 0, \tag{2.22}$$

and those of kink modes are

$$\frac{d\delta v_{x2}}{dx} = 0, \tag{2.23}$$

and

$$\delta p_{T2} = 0, \tag{2.24}$$

where δv_{x2} is the perpendicular velocity perturbation. Connecting the MHD wave solutions across $x = 0$ using TD boundary conditions in Equation 2.17 together with the inner boundary conditions 2.21 and 2.22 at $x = d$, MHD sausage modes are found to be governed by the equation

$$i \tan(k_{x2}d)[(\omega_1')^2 - (\mathbf{V}_{A1} \cdot \mathbf{k}_t)^2]\frac{\rho_{01}}{k_{x1}} - [(\omega_2')^2 - (\mathbf{V}_{A2} \cdot \mathbf{k}_t)^2]\frac{\rho_{02}}{k_{x2}} = 0. \qquad (2.25)$$

Similarly applying the boundary conditions 2.23 and 2.24 at $x = d$ together with TD boundary conditions, MHD kink modes are found to be governed by the equation

$$i \cot(k_{x2}d)[(\omega_1')^2 - (\mathbf{V}_{A1} \cdot \mathbf{k}_t)^2]\frac{\rho_{01}}{k_{x1}} + [(\omega_2')^2 - (\mathbf{V}_{A2} \cdot \mathbf{k}_t)^2]\frac{\rho_{02}}{k_{x2}} = 0. \qquad (2.26)$$

Equation 2.25 is used in Chapter 3 to find the solutions to the Kelvin-Helmholtz unstable waves on the boundary of the Earth's magnetopause with an inner boundary added in the magnetosphere at $x = d$. Additionally Equations 2.26 and 2.25 are used in Chapter 4 for finding solutions to the KHI kink and sausage modes along the Bursty Bulk Flow (BBF) channels in the central plasmasheet. The coordinate system used in Chapter 4 is modified to represent Geocentric Solar Magnetic (GSM) coordinate system and boundary is assumed to be at the half channel position, $y = 0$. A change of coordinate system or the position of inner boundary does not alter the derivations shown above for the kink and sausage modes.

2.3.2 Finite Width Boundary Layer Model

In this section we derive the KHI wave dispersion relation for a finite thickness MHD shear-flow boundary.

Assume a plane geometry where all the zero order quantities are dependent only on x. In this case, the perturbations to background plasma parameters should be of the

form,

$$\delta g(\mathbf{r}, t) = g(x)e^{i(\mathbf{k_t} \cdot \mathbf{r} - \omega t)}, \tag{2.27}$$

where g is any perturbed quantity, $g(x)$ is the corresponding amplitude, ω is the complex frequency and $\mathbf{k_t} = (0, k_y, k_z)$ is the tangential wave number. With the type of perturbation shown in Equation 2.27 the following replacement can be used

$$\frac{d}{dt} = -i\omega', \quad \nabla = \hat{x}\frac{\partial}{\partial x} + i\mathbf{k_t},$$

and the linearized MHD equations, equations 2.2 - 2.5, can be written as

$$-i\omega'\delta\rho + i\rho_0(\mathbf{k_t} \cdot \delta\mathbf{v}) + \rho_0\frac{\partial \delta v_x}{\partial x} + \delta v_x\frac{\partial \rho_0}{\partial x} = 0, \tag{2.28}$$

$$-i\omega'\rho_0\delta\mathbf{v} + \rho_0\delta v_x\frac{\partial \mathbf{V_0}}{\partial x} = -i\mathbf{k_t}\delta p_T - \hat{x}\frac{\partial \delta p_T}{\partial x} + \frac{1}{\mu_0}\left(i[\mathbf{B_0} \cdot \mathbf{k_t}]\delta\mathbf{b} + \delta B_x\frac{\partial \mathbf{B_0}}{\partial x}\right), \tag{2.29}$$

$$-i\omega'(\delta p - C_S^2\delta\rho) + \left(\frac{\partial P_0}{\partial x} + \frac{C_S^2}{\gamma}\frac{\partial \delta\rho_0}{\partial x}\right)\delta v_x = 0, \tag{2.30}$$

$$i\omega'\delta\mathbf{b} = \mathbf{B_0}\left(\frac{\partial \delta v_x}{\partial x} + i(\mathbf{k_t} \cdot \delta\mathbf{v})\right) + \delta v_x\frac{\partial \mathbf{B_0}}{\partial x} - \delta b_x\frac{\partial \mathbf{V_0}}{\partial x} - i(\mathbf{B_0} \cdot \mathbf{k_t})\delta\mathbf{v}. \tag{2.31}$$

First we take the x component of equation 2.31 and replace $\delta v_x = \partial\delta x/\partial x = -i\omega'\delta x$ to obtain

$$\delta b_x = i(\mathbf{k_t} \cdot \mathbf{B_0})\delta x. \tag{2.32}$$

Then we take the x component of equation 2.29, and replace $\delta v_x = -i\omega'\delta x$ and δb_x from 2.32. Applying these steps provides a general equation connecting two important parameters $\delta p_T = \delta p + (\mathbf{B_0} \cdot \delta b)/\mu_0$ and δx;

$$\frac{\partial \delta p_T}{\partial x} - \Omega\delta x = 0. \tag{2.33}$$

where

$$\Omega = \rho_0[\omega'^2 - (\mathbf{V}_A \cdot \mathbf{k_t})^2]. \tag{2.34}$$

In order to find a solution to equation 2.33, we need to find a second equation involving these variables. We will next find an expression describing δp_T in terms of δx and replace it in equation 2.33. This will provide us with a solvable equation for δx only.

First take the scalar product of both sides of equation 2.31 with $\mathbf{k}_t$ and replace $\delta v_x = -i\omega'\delta x$ to obtain an equation for the term $\mathbf{k}_t \cdot \delta\mathbf{b}$ as,

$$\mathbf{k}_t \cdot \delta\mathbf{b} = -(\mathbf{k}_t \cdot \mathbf{B}_0)\frac{\partial\delta x}{\partial x} - \frac{\partial(\mathbf{k}_t \cdot \mathbf{B}_0)}{\partial x}\delta x. \tag{2.35}$$

Next take the scalar product of equation 2.29 with $\mathbf{k}_t$ and replace $\mathbf{k}_t \cdot \delta\mathbf{b}$ from equation 2.35 to obtain,

$$\mathbf{k}_t \cdot \delta\mathbf{v} = \frac{(\mathbf{k}_t \cdot \mathbf{V}_A)^2}{\omega'}\frac{\partial\delta x}{\partial x} - \frac{\partial(\mathbf{k}_t \cdot \mathbf{V}_0)}{\partial x}\delta x + \frac{k_t^2}{\omega'\rho_0}\delta p_T. \tag{2.36}$$

Insert $\delta\rho$ from the equation 2.30 into the equation 2.28 and replace $\delta v_x = -i\omega'\delta x$ to write an expression for δp as,

$$\delta p = \frac{1}{2\mu_0}\frac{\partial\mathbf{B}_0^2}{\partial x}\delta x - \frac{\rho_0 C_S^2}{\omega'^2}[\omega'^2 - (\mathbf{k}_t \cdot \mathbf{V}_A)^2]\frac{\partial\delta x}{\partial x} - C_S^2\left(1 + \frac{1}{\gamma}\right)\frac{\partial\rho_0}{\partial x}\delta x + \frac{k_t^2 C_S^2}{\omega'^2}\delta p_T. \tag{2.37}$$

Take the scalar product of $\mathbf{B}_0$ with equation 2.29 and arrange the results in terms of the magnetic pressure perturbation $\mathbf{B}_0 \cdot \delta b/\mu_0$ to obtain,

$$(\mathbf{k}_t \cdot \mathbf{B}_0)\left[\frac{\mathbf{B}_0 \cdot \delta b}{\mu_0} + \frac{\delta x}{\mu_0}\frac{\partial\mathbf{B}_0^2}{\partial x}\right] = (\mathbf{k}_t \cdot \mathbf{B}_0)\delta p_T - \omega'\rho_0(\mathbf{B}_0 \cdot \delta\mathbf{v}) - \omega'\rho_0\frac{\partial(\mathbf{B}_0 \cdot \mathbf{V}_0)}{\partial x}\delta x. \tag{2.38}$$

Take the scalar product of $\mathbf{B}_0$ with both sides of equation 2.31 and arrange in terms of $\mathbf{B}_0 \cdot \delta\mathbf{v}$ to obtain,

$$\mathbf{B}_0 \cdot \delta\mathbf{v} = \frac{1}{\mathbf{B}_0 \cdot \mathbf{k}_t}\left(\frac{B_0^2 k_t^2}{\omega'\rho_0}\delta p_T - \frac{B_0^2}{\omega'}[\omega'^2 - (\mathbf{k}_t \cdot \mathbf{V}_A)^2]\frac{\partial\delta x}{\partial x} - \omega'\frac{\partial B_0^2}{\partial x}\delta x \right. \tag{2.39}$$
$$\left. -\frac{\partial(\mathbf{B}_0 \cdot \mathbf{V}_0)}{\partial x}\delta x - \omega'(\mathbf{B}_0 \cdot \delta b)\right).$$
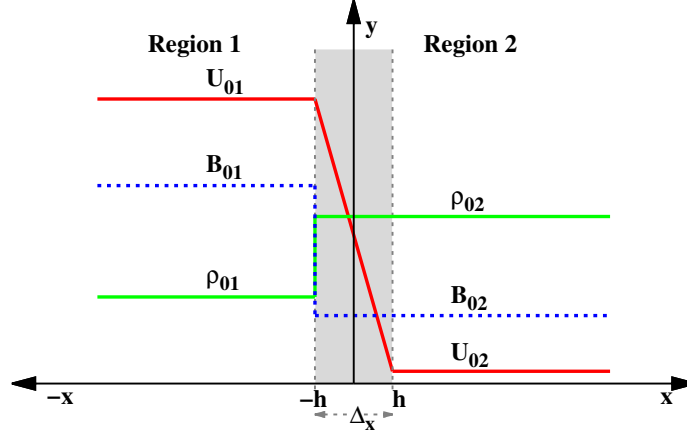
Figure 2.3: Schematic of the MHD boundary layer model used for the finite with boundary thickness. $\Delta_x = 2h$ is the boundary layer thickness.

Then insert equation 2.39 in equation 2.38 to obtain a more simplified equation for magnetic pressure perturbation as,

$$\frac{\mathbf{B}_0 \cdot \delta b}{\mu_0} = -\rho_0 V_A^2 \frac{\partial \delta x}{\partial x} - \frac{\delta x}{\mu_0} \frac{\partial B_0^2}{\partial x} - \frac{(\mathbf{k}_t \cdot \mathbf{V}_A)^2 - k_t^2 V_A^2}{\omega'^2 - (\mathbf{k}_t \cdot \mathbf{V}_A)^2} \delta p_T \tag{2.40}$$

Finally add equations 2.37 and 2.40 to obtain an expression for δp_T as,

$$\delta p_T = \chi \frac{\partial \delta x}{\partial x} - \frac{1}{\mathfrak{L}} \frac{\delta x}{2\mu_0} \frac{\partial B_0^2}{\partial x} - C_S^2 \frac{1}{\mathfrak{L}} \left(\frac{\gamma + 1}{\gamma} \right) \frac{\partial \rho_0}{\partial x}. \tag{2.41}$$

Where $\chi = -\Omega/k_x^2$, $\mathfrak{L} = [\omega'^4 - \omega'^2 k_t^2 (C_S^2 + V_A^2) + k_t^2 C_S^2 (\mathbf{k}_t \cdot \mathbf{V}_A)^2]/[\omega'^4 - \omega'^2 (\mathbf{k}_t \cdot \mathbf{V}_A)^2]$, and k_x is the complex wave number normal to the boundary which is described in the equation 2.20.

We now assume that only the plasma flow velocity varies along x and all the other background values are constant. The boundary layer is set as an additional region between $x = -h$ and $x = h$ which makes the thickness $\Delta_x = 2h$. The variation of the flow velocity across the boundary is chosen as $V_0(x) = \frac{V_{01}}{2} \left(1 - \frac{x}{h} \right) + \frac{V_{02}}{2} \left(1 + \frac{x}{h} \right)$ (this set up is shown in Figure 2.3). When we apply these assumptions, the last two terms in equation 2.41

are cancelled and a simpler equation for δp_T is obtained,

$$\delta p_T = \chi \frac{\partial \delta x}{\partial x}. \tag{2.42}$$

Finally we substitute δp_T from equation 2.42 into equation 2.33 to obtain the following equation for the amplitude of the plasma displacement, δx;

$$\frac{\partial}{\partial x} \left(\chi \frac{\partial \delta x}{\partial x} \right) - \Omega \delta x = 0, \tag{2.43}$$

Equation 2.43 is applied to the boundary regions described above. We will now have three regions, region 1, region 2 and the boundary layer region. Thus four boundary conditions are to be matched. Following the standard approach in previous studies [*Chandrasekhar*, 1961; *Lee and Olson*, 1980; *Roberts*, 1991; *Farrugia et al.*, 1998; *Gratton et al.*, 2004], solutions to equation 2.43 in these three regions are chosen as;

$$
\begin{aligned}
\delta x_1 &= A_1 e^{ik_{x1}x}, & x \leq -h \\
\delta x_{bl} &= A_2 e^{ik_{xbl}x} + A_3 e^{-ik_{xbl}x}, & -h < x < h \\
\delta x_2 &= A_4 e^{ik_{x2}x}. & x \geq h
\end{aligned}
\tag{2.44}
$$

The subscripts 1 and 2 corresponds to regions 1 and 2, respectively. The boundary layer region values are symbolized as δx_{bl} and k_{xbl}. The solutions in region 1/2 have been so chosen that perturbations vanish at $-\infty / +\infty$. Therefore, the imaginary parts of the perpendicular wave numbers are chosen as, negative in region 1, $k_{x1i} < 0$, and positive in region 2, $k_{x2i} > 0$. Boundary conditions corresponding to a tangential discontinuity, namely continuity of the displacement and total pressure is applied to the boundaries at

$x = \pm h$, resulting in the following matching conditions;

$$\chi_1 \frac{\partial \delta x_1}{\partial x} = \chi_{bl} \frac{\partial \delta x_{bl}}{\partial x}, \qquad \delta x_1 = \delta x_{bl}, \qquad x = -h \tag{2.45}$$

$$\chi_{bl} \frac{\partial \delta x_{bl}}{\partial x} = \chi_2 \frac{\partial \delta x_2}{\partial x}, \qquad \delta x_{bl} = \delta x_2, \qquad x = h \tag{2.46}$$

Applying matching conditions in equations 2.45 and 2.46, we obtain four linear equations for four unknown constants, A_1, A_2, A_3, and A_4 which can be written in matrix form as;

$$\begin{pmatrix} e^{-ik_{x1}h} & e^{-ik_{xbl}h} & e^{ik_{xbl}h} & 0 \\ i\chi_1 k_{x1}e^{-ik_{x1}h} & i\chi_{bl}\zeta_1 e^{-ik_{xbl}h} & -i\chi_{bl}\zeta_1 e^{ik_{xbl}h} & 0 \\ 0 & e^{ik_{xbl}h} & e^{-ik_{xbl}h} & e^{ik_{x2}h} \\ 0 & i\chi_{bl}\zeta_{bl}e^{ik_{xbl}h} & -i\chi_{bl}\zeta_{bl}e^{-ik_{xbl}h} & i\chi_2 k_{x2}e^{ik_{x2}h} \end{pmatrix} \begin{pmatrix} A_1 \\ A_2 \\ A_3 \\ A_4 \end{pmatrix} = \begin{pmatrix} 0 \\ 0 \\ 0 \\ 0 \end{pmatrix} \tag{2.47}$$

The compatibility of these equations requires that the determinant of the matrix multiplying constants A_1, A_2, A_3 and A_4 must be equal to zero which leads to the dispersion relation,

$$\chi_1 k_{x1}\left(\kappa e^{i(k_{x2}+k_{xbl})\Delta_x} + \xi\right) + \zeta\chi_{bl}\left(\kappa e^{i(k_{x2}+k_{xbl})\Delta_x} - \xi\right). \tag{2.48}$$

The following notation applies:

$$\chi_1 = \frac{-\Omega_1}{k_{x1}^2},$$

$$\chi_{bl} = \frac{-\Omega_{bl}}{k_{xbl}^2},$$

$$\zeta = k_{xbl} - k_t \cos\alpha \frac{(V_{01} - V_{02})}{4k_{xbl}} \frac{(G_{bl}H_{bl} - F_{bl})}{G_{bl}^2},$$

$$\kappa = k_t \cos\alpha \frac{(V_{01} - V_{02})}{4k_{x2}} \frac{(G_2 H_2 - F_2)}{G_2^2},$$

$$\xi = 2k_{x2} + \kappa,$$

$$G_{bl,2} = \omega_{bl,2}'^2(C_{Sbl,S2}^2 + V_{Abl,A2}^2) - (\mathbf{V}_{Abl,A2} \cdot \mathbf{k}_t)^2 C_{Sbl,S2}^2,$$

$$H_{bl,2} = 4\omega_{bl,2}'^3 - 2k_t^2 \omega_{bl,2}'(C_{Sbl,S2}^2 + V_{Abl,A2}^2),$$

$$F_{bl,2} = 2\omega_{bl,2}'(C_{Sbl,S2}^2 + V_{Abl,A2}^2)(\omega_{bl,2}'^4 - k_t^2 G_{bl,2}).$$

Here α represents the angle between the tangential wave number, $\boldsymbol{k}_t$, and flow velocity, $\boldsymbol{V}_{01,02}$. Equation 2.48 is used in Chapter 5 to find the solutions to the Kelvin-Helmholtz unstable waves on an MHD shear flow boundary with finite thickness. This approach allows us to investigate the effect of finite thickness on the KHI growth rates and MHD wave emission due to the KHI. Moreover, with this approach we were able to consider waves with wavelengths comparable to the size of the boundary thickness.

2.4   KHI and Negative Energy Waves

There is an ongoing discussion on the possibility of a relation between KHI and Negative Energy Waves (NEWs). Negative energy waves, when incident on a non-rigid boundary such as magnetopause, can extract energy from it and reflect back with enhanced amplitude and energy [*Walker*, 2000; *McKenzie*, 1970]; then the transmitted wave should be assumed to have negative energy in order to keep energy conservation of the wave [*Mann et al.*, 1999; *McKenzie*, 1970; *Fejer*, 1963]. Negative energy waves are also called over-reflected waves and they can better be defined by an active boundary method where instead of assigning negative energy to the transmitted waves, an energy exchange between the waves and the boundary is considered [*Walker*, 2000]. Interaction of a negative and a positive energy wave is suggested to be a initiator for the onset of the linear KHI [*Taroyan and Erdélyi*, 2003a, 2002; *Cairns*, 1979]. The KHI is proposed to start when a negative and a positive energy wave coalesce [*Taroyan and Erdélyi*, 2002; *Mills et al.*, 1999; *Mills and Wright*, 1999; *Cairns*, 1979]. *Mann et al.* [1999] have studied K-H unstable and waveguide modes in connection with the over-reflection and propagation of negative energy waves in the Earth's magnetosphere. They have postulated that the KHI-generated waves are always over-reflected at the magnetopause, a fact implied ear-

lier by *Pu and Kivelson* [1983a], and thus K-H waves are possible through NEW. *Mills and Wright* [1999] have employed the theory of over-reflection to study the K-H excited waveguide modes and their impacts on driving field line resonances. In Chapter 3 we show results confirming that the KHI waves are always over-reflected.

Chapter 3

Primary and Secondary Kelvin-Helmholtz Instabilities on the Earth's Magnetopause

3.1 Introduction

Numerous studies are conducted on KHI of the Earth's magnetopause and physical facts on this instability have been found in the past. There are, however, a number of ambiguous features that remain to be solved. In this chapter of the thesis we provide a complete investigation of the Kelvin-Helmholtz instability along the Earth's magnetopause. We show a clear distinction between the two types of KHI, primary and secondary, on the Earth's magnetopause. We also demonstrate the characteristics of the primary and secondary KHI waves for the dayside and nightside magnetopause with the comparison of two different approaches where either plasmas on both sides of the boundary are assumed to be semi-infinite or a reflecting boundary is included in the magnetospheric side. All of the results shown in this chapter are our contributions to the area of research on the KHI of the Earth's magnetopause and published in the Journal of Geophysical Research,

2013. We have provided a brief explanation of the derivations used for the equations in the paper and refer the reader to chapter 2 section 2.3.1 for the detailed derivations. Detailed explanations to the box model of the magnetosphere used in this study can also be found in chapter 1, section 1.6.2 (see also Figure 1.6). The following section provides the details of the published paper:[1]

3.2 Paper 1: "Primary and Secondary Compressible Kelvin-Helmholtz Surface Wave Instabilities on the Earth's Magnetopause"

3.2.1 Abstract

Primary and secondary Kelvin-Helmholtz surface wave modes on the Earth's magnetopause are studied within the framework of warm plasma ideal magnetohydrodynamics (MHD) across an infinitely thin magnetopause tangential discontinuity (TD). With the increase of background flow velocity, a KHI unstable boundary separating two uniform semi-infinite plasma regions is always ultimately stabilized to KHI growth at an upper cut-off while inclusion of an inner boundary in one plasma region removes this stabilization. Phase velocity Friedrichs diagrams are presented that allow us to identify unstable fast and slow modes that correspond to growing modes of the KHI under different magnetosphere and magnetosheath conditions. For a TD on the near Earth flanks unstable fast and slow surface modes are created. On the deeper flank, and into the magnetotail, where the magnetosheath and magnetosphere fields become more aligned, new KH unstable intermediate-fast modes are created which can have phase speeds above the Alfvén speed but which cannot propagate exactly perpendicular to the magnetic field. In the plasma frame, primary unstable KH waves show fast/fast, while secondary KH

waves show slow/fast mode behavior in the magnetosphere/magnetosheath. Secondary KHI occurs at slower flow speeds than the primary KHI and grows more slowly and at a narrow range of propagation angles. Our analysis is placed in the context of in-situ satellite observations of the phase speed of KHI-related waves in the magnetosheath and magnetosphere in the long wavelength regime where our analysis applies. We conclude that KH unstable surface waves on the near-Earth magnetopause flanks are likely to be secondary KHI waves, while those further down the flanks and on the night-side magnetopause are likely to be primary KHI waves - the latter being the most important for energy transport at the magnetopause.

3.2.2 Introduction

The Kelvin-Helmholtz Instability (KHI) can arise when the equilibrium of a stratified heterogeneous fluid with relative motion in different layers is considered [*Chandrasekhar*, 1961]. It evolves temporally and/or spatially corresponding to whether wave modes grow with time and space, respectively [e.g., *Itoh et al.*, 2004]. The velocity shear between the magnetospheric and magnetosheath plasma in the Earth's magnetosphere generates a magnetohydrodynamic KHI, which plays an important role in many magnetospheric phenomena, such as the generation of geomagnetic pulsations [*Southwood*, 1974; *Walker*, 1981; *Miura and Pritchett*, 1982; *Chen and Hasegawa*, 1993; *Rae et al.*, 2005; *Villante*, 2007; *Agapitov et al.*, 2009], magnetic reconnection and plasma mixing at the magnetopause especially during northward Interplanetary Magnetic Field (IMF) [*Otto and Fairfield*, 2000; *Fairfield et al.*, 2000; *Nakamura et al.*, 2006; *Pegoraro et al.*, 2008; *Nakai and Ueno*, 2011], and as an agent for momentum and energy transfer across the magnetopause [*Pu and Kivelson*, 1983b; *Miura*, 1984; *Kivelson and Chen*, 1995; *Hasegawa et al.*, 2006]. It has also been proposed that the surface waves generated by the KHI may have an influence on substorm expansion phase onset in the plasmasheet [e.g., *Rostoker and Eastman*, 1987; *Yoon et al.*, 1996; *Lui*, 2004; *Uberoi*, 2006]. All of these are key elements for solar wind interactions with the Earth's magnetosphere and ionosphere. In

the solar atmosphere KHI is also a process that can lead to plume/interplume mixing and may be a source for Alfvénic fluctuations in the solar wind [e.g., *Andries et al.*, 2000; *Andries and Goossens*, 2001].

Due to the significant effects it has on the magnetosheath-magnetosphere boundary, understanding the KHI and the behavior of the waves related to it is an active area of research in magnetospheric physics. Several early works shed light on this subject for incompressible [*Sen*, 1963] and compressible [*Fejer*, 1964; *Sen*, 1964, 1965; *Lerche*, 1966] plasmas. *Sen* [1965] identified the regions of the day-side/night-side magnetopause and magnetotail that may be KH unstable. *Southwood* [1968] studied the magnetospheric boundary allowing different magnetic fields on both sides of the magnetopause and discovered that the maximum growth rate occurs when shear flow is perpendicular to the background magnetic field.

In the KHI studies, the magnetopause boundary is often assumed to have zero thickness [*Pu and Kivelson*, 1983a, b; *Mann et al.*, 1999; *Mills et al.*, 1999; *Mills and Wright*, 1999]; this assumption is valid for waves with wavelengths bigger than the thickness of the boundary layer. Under this assumption the growth rates of the KH unstable waves increase without limit as the tangential wave number increases [*Southwood*, 1968; *Ong and Roderick*, 1972; *Mann et al.*, 1999]. Study of KHI with the finite transition thickness was first done by *Ong and Roderick* [1972] employing both incompressible and compressible flow analysis. They found that the finite thickness of the transition layer stabilizes the boundary for short wavelength perturbations. They also noted that the component of the background magnetic field parallel to the shear flow reduces the growth rate of the instability and confirmed the fact that the compressibility has a stabilizing effect as well, which was suggested earlier by *Sen* [1964]. It is also found that when a boundary finite thickness is included, growth rates have a maximum value for a finite wave number and tends towards to zero growth as the wave number tends to infinity [*Ong and Roderick*, 1972; *Walker*, 1981; *Miura and Pritchett*, 1982; *Allan and Wright*, 1997].

Although the KHI of the magnetopause has been investigated extensively in the past,

there are still a number of features that remain to be fully explained. For instance, it is well known that there is an upper and a lower cut-off velocity for the onset of the KHI surface wave when the plasmas on both sides of the magnetopause are unbounded [*Pu and Kivelson*, 1983a, b; *Mills and Wright*, 1999; *Mills et al.*, 1999; *Mann et al.*, 1999; *Taroyan and Erdélyi*, 2002, 2003a, b]. It is also known that the upper cut-off velocity is removed when an inner boundary is included in the magnetosphere [*Fujita et al.*, 1996; *Mann et al.*, 1999; *Mills et al.*, 1999; *Mills and Wright*, 1999]. A lower cut-off velocity below which the boundary is stable exists due to magnetic tension on the boundary [*Pu and Kivelson*, 1983a, b; *Miura*, 1995; *Mann et al.*, 1999]. The upper cut off velocity is typically explained as the point where KHI generated surface waves turn into oscillatory modes and propagate into the magnetosphere and magnetosheath stabilizing the KHI [*Fujita et al.*, 1996; *Pu and Kivelson*, 1983a; *Mann et al.*, 1999; *Mills et al.*, 1999]. However, in the bounded case there can be an influence of the inner boundary on the shear flow boundary and this has not been fully examined.

Less well-known is the fact that in a compressible plasma there can be two KH unstable, often distinct flow speed regions, which allow for the existence of a primary as well as a less intense secondary KHI interval, depending on the ambient plasma parameters [*González and Gratton*, 1994; *González et al.*, 2002; *Taroyan and Erdélyi*, 2002, 2003a]. This secondary instability region occurs for flow speeds typically below the primary KHI and with usually smaller growth rates. Nevertheless, the secondary instability should not be ignored since it could be the only active instability under certain physical conditions [e.g., *González et al.*, 2002] and might hence be the only means of energy propagation at the boundary. We examine the generation of the primary and secondary KHI in the context of the magnetopause KHI in this paper.

When waves are incident on a non-rigid boundary such as the magnetopause, they can extract energy from the boundary and be reflected back with an enhanced amplitude and energy [e.g., *McKenzie*, 1970; *Walker*, 2000]. In this case, the transmitted wave can be considered to have negative energy in order to maintain energy conservation [*Fe-*

jer, 1963; *McKenzie*, 1970; *Mann et al.*, 1999]. However, for the more realistic scenario where wave-packets have finite length, causality suggests that the interactions can better be described by an active boundary where, instead of assigning negative energy to the transmitted waves, energy exchange between the waves and the flow is described in terms of the work done by Reynolds and Maxwell stresses at the boundary [*Walker*, 2000]. The interaction of a negative and a positive energy wave has also previously been theorized to be an initiator of the onset of the KHI [*Cairns*, 1979; *Mills et al.*, 1999; *Taroyan and Erdélyi*, 2002, 2003a], however, we revisit this conclusion here.

In the current study, the behavior of MHD modes in a bounded and unbounded magnetosphere and magnetosheath separated by a shear flow across a tangential discontinuity (TD) are explored and compared. An analysis of a bounded magnetosphere is more applicable to the dayside magnetosphere and the near-Earth flank night-side magnetosphere where the plasmapause may represent an inner boundary. Further down the magnetotail, the two regions on both sides of the magnetopause can be assumed to be semi-infinite, since the average value of the diameter of the magnetotail can reach up to $\sim 50 - 60 R_E$ [*Pertinec and Russell*, 1996]. In this latter case the boundary is far away from the shear layer to the extent that any waves reflected from the distant boundary may have little or no impact on the dynamics of the magnetopause.

We describe the primary and secondary KHI and their relevance to excited MHD wave modes using the physical framework of linear mode interactions. A strong correlation between the linear interactions of MHD waves and the onset and stabilization of primary and secondary KHI is revealed. Similar studies have been performed in the past, but a clear explanation of the relationship between the wave-wave interactions and the properties of the primary and secondary KHI was not provided [e.g., *Mills et al.*, 1999; *Taroyan and Erdélyi*, 2002, 2003a, b]. This framework also reveals some physics of the upper cut-off. Finally, we examine the fast and slow mode characteristics of the primary and secondary KHI waves, showing that the modes can have different characteristics of slow or fast on either side of the magnetopause. We further examine the observational

implications of this in the magnetospheric context.

3.2.3 KHI Dispersion Relation and Numerical Method

Observations have demonstrated that the region of the magnetopause which is most susceptible to the KHI is the low latitude boundary layer in the equatorial plane on the flanks starting from the dayside flanks and extending into the magnetotail [e.g., *Hasegawa et al.*, 2004, 2006; *Foullon et al.*, 2008, 2010]. In the present study, the dayside
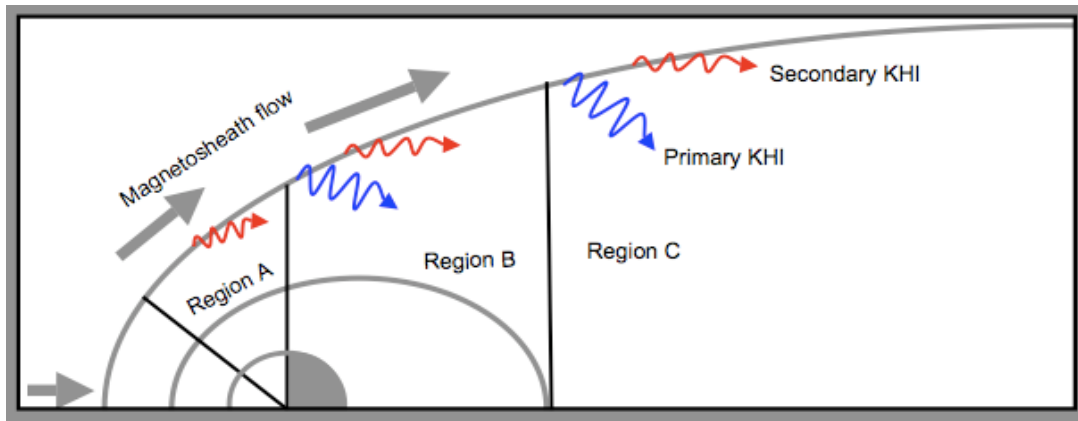
Figure 3.1: Regions of the magnetosphere investigated. Region A corresponds to the dayside flanks, region B corresponds to the night-side flanks, and region C corresponds to the far down the magnetotail. A representative position of the plasmapause is shown as the inner boundary for a bounded magnetosphere calculations of regions A and B. The size of the Earth is exaggerated for clarity.

and night-side flanks of the magnetosphere, and the magnetotail, will all be probed along the equatorial plane for the onset of the KHI. These regions are labelled as region A, B, and C respectively for clarity throughout the rest of this paper (see Figure 3.1). Region A corresponds to the dayside flanks of the magnetosphere, region B corresponds to the night-side flanks until distances $\simeq 10 - 15R_E$ downtail from the terminator where the plasmapause remains as a possible inner boundary, and region C is even further down the magnetotail where the shear-flow boundary is effectively unbounded on either side.

In the analysis presented here, a tangential discontinuity (TD) boundary with zero

thickness is assumed. At a TD, the normal components of the background magnetic field and plasma flow velocity are zero. We have assumed a zero transition thickness which is suitable if the wavelengths, λ, of the generated waves are considerably larger than the thickness, l, of the boundary. Observations have revealed that the magnetopause boundary thickness typically varies between $\sim 0.1 - 1R_E$ [e.g., *Gnavi et al.*, 2009; *Nakai and Ueno*, 2011; *Hwang et al.*, 2011], while wavelengths of long period KHI relevant waves can vary between $\sim 2 - 15R_E$ [e.g., *Chen and Kivelson*, 1993; *Kivelson and Chen*, 1995; *Owen et al.*, 2004; *Hasegawa et al.*, 2006; *Foullon et al.*, 2008; *Agapitov et al.*, 2009; *Gnavi et al.*, 2009; *Foullon et al.*, 2010; *Nakai and Ueno*, 2011; *Hwang et al.*, 2011], indicating that $\lambda \gg l$ in most cases. Therefore, a zero transition thickness can be assumed to be a valid model for the magnetopause when these long period KHI waves with long wavelengths are under investigation. Shorter period waves which will have shorter wavelengths are better explored with a model magnetopause of finite thickness [e.g., *Walker*, 1981; *Miura*, 1984; *Taroyan and Erdélyi*, 2002, 2003a, b]

In region A, the magnetic fields on both sides of the boundary are chosen to be perpendicular to each other. In regions B and C, the magnetic fields are set parallel (or anti-parallel - the dispersion relations are symmetrical) to each other. The flow velocity is set parallel to the background magnetic field in the magnetosheath in all the regions, A, B and C. A box model is used that corresponds to a Cartesian coordinate system with a zero transition thickness shear flow boundary, as displayed in Figure 3.2. In Figure 3.2, region 1 represents the magnetosheath, and region 2 represents the magnetosphere. $B_{01,02}$ are the background magnetic fields and d is the distance to the inner boundary in the bounded magnetosphere cases (A and B) expressed in units of the Earth's radius, R_E; d is set to ∞ for the isolated unbounded shear flow boundary in case C. $U_{01,02}$ are the background flow velocities in regions 1 and 2, where U_{01} is assumed to be directed along y and U_{02} is set to zero.

The KHI is a macroscopic instability where the scale length of the generated waves is comparable to the bulk scales of the plasma [*Baumjohann and Treumann*, 2001]. Thus
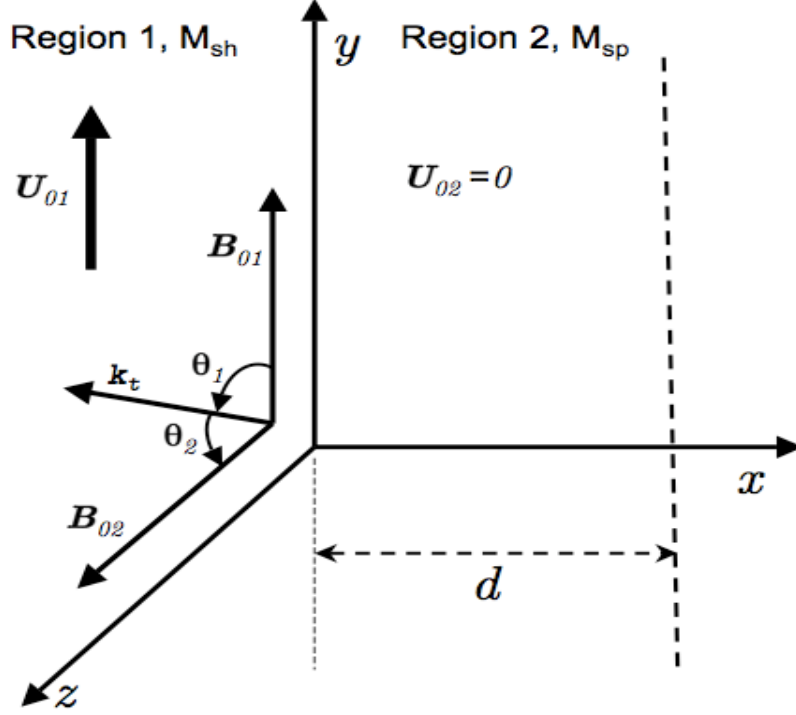
Figure 3.2: Model used for the bounded magnetosphere; region 1 is the magnetosheath, M_{sh}, and region 2 is the magnetosphere, M_{sp}. The magnetosheath has a uniform flow in the y direction and the magnetosphere has zero flow velocity. Both regions have background magnetic fields at arbitrary directions with respect to the direction of wave propagation. An inner boundary is set at $x = d$ in the magnetosphere for bounded magnetosphere calculations, and is removed for the unbounded magnetosphere calculations.

an appropriate approach for studying this phenomenon is to use magnetohydrodynamics (MHD), and ideal MHD is the approach used in the current study. We follow the standard approach where the ideal MHD equations are linearized under a small amplitude approximation for compressible warm homogeneous plasmas on both sides of the boundary. The dependent variables are assumed to be a superposition of an equilibrium value, g_0, and a perturbed value δg; $g(\mathbf{r}, t) = g_0(\mathbf{r}, t) + \delta g(\mathbf{r}, t)$, where g represents the dependent variable. A sinusoidal perturbation is assumed, depending on time and space as $\delta g(\mathbf{r}, t) = D e^{i(\mathbf{k}.\mathbf{r} - \omega t)}$, where ω is the complex frequency, $\mathbf{k} = \mathbf{k_t} + \mathbf{k_x}$ is the wave num-

ber - $\mathbf{k_t}$ is the tangential wave number and $\mathbf{k_x}$ is the complex wave number normal to the boundary - and D is a constant amplitude. The setup displayed in figure 3.2 is used, and boundary conditions corresponding to a tangential discontinuity, namely continuity of the displacement and total pressure perturbation across the magnetopause boundary, are applied to the dispersion relation:

$$[(\omega_1')^2 - \frac{(\mathbf{B}_{01} \cdot \mathbf{k}_t)^2}{\rho_{01}\mu_0}]\frac{\rho_{01}}{k_{x1}} + [(\omega_2')^2 - \frac{(\mathbf{B}_{02} \cdot \mathbf{k}_t)^2}{\rho_{02}\mu_0}]\frac{\rho_{02}}{k_{x2}} = 0. \tag{3.1}$$

Here, $\rho_{01,02}$ are the background mass densities and μ_0 is the permeability of free space. Rewriting equation 3.1 in terms of background Alfvén velocities, we obtain;

$$[(\omega_1')^2 - (\mathbf{V}_{A1} \cdot \mathbf{k}_t)^2]\frac{\rho_{01}}{k_{x1}} + [(\omega_2')^2 - (\mathbf{V}_{A2} \cdot \mathbf{k}_t)^2]\frac{\rho_{02}}{k_{x2}} = 0, \tag{3.2}$$

where

$$\omega_{1,2}' = \omega - \mathbf{U}_{01,02} \cdot \mathbf{k}_t, \tag{3.3}$$

$$\mathbf{V}_{A1,A2}^2 = (\mathbf{B}_{01,02})^2 / (\rho_{01,02}\mu_0), \tag{3.4}$$

$$k_{x1,x2}^2 = \left((\omega_{1,2}')^4 / \left[(\omega_{1,2}')^2 \left(V_{A1,A2}^2 + C_{S1,S2}^2\right) - (\mathbf{V}_{A1,A2} \cdot \mathbf{k}_t)^2 C_{S1,S2}^2\right]\right) - k_t^2, \tag{3.5}$$

$$C_{S1,S2}^2 = \gamma P_{01,02}/\rho_{01,02}. \tag{3.6}$$

In equations 3-6, ω is the frequency in the stationary frame, $\omega_{1,2}'$ are Doppler shifted frequencies, $V_{A1,A2}$ are Alfvén velocities, $k_{x1,x2}$ are wave numbers normal to the boundary, and $C_{S1,S2}$ are the sound speeds in regions 1 and 2, respectively. The adiabatic index γ is taken as 5/3. When a perfectly reflecting boundary is included in the magnetosphere,

equation 3.2 becomes

$$i\tan(k_{x2}d)[(\omega_1')^2 - (\mathbf{V}_{A1} \cdot \mathbf{k}_t)^2]\frac{\rho_{01}}{k_{x1}} - [(\omega_2')^2 - (\mathbf{V}_{A2} \cdot \mathbf{k}_t)^2]\frac{\rho_{02}}{k_{x2}} = 0. \qquad (3.7)$$

Eigenfrequencies of equations 3.2 and 3.7, representing an unbounded and a bounded magnetosphere respectively, are computed numerically using a Newton-Raphson scheme. The growth rates and real frequencies of KHI unstable surface waves are determined for different sets of parameters applied to three different regions: regions A, B and C (see Figure 3.1). Stable and unstable waveguide modes are also possible in the bounded magnetosphere case [*Mann et al.*, 1999], however they are not examined in the current study. Phase velocity Friedrichs diagrams are plotted as an aid to understanding wave-wave interactions and their connection to the KHI. Group velocity diagrams are also plotted in order to investigate the direction of energy propagation of the KH unstable waves.

In the following sections of the paper normalized flow velocities $V_{01,02}$ are used such that $V_{01,02} = U_{01,02}/V_{A2}$ with normalization with respect to the Alfvén speed, V_{A2}, in the magnetosphere. The distance, d, is normalized by R_E, and wavenumbers, k, are normalized by $1/d$. Normalized frequencies are; real frequencies, $\omega_r d/V_{A2}$, growth rates, $\omega_i d/V_{A2}$, and Doppler shifted frequencies, $\omega_r d/V_{A2} - \mathbf{V_{01}}.\mathbf{k}_t d$. The background physical parameters are set such that $\beta_1 = 2.5$, $\beta_2 = 0.64$, $B_{01}/B_{02} = 2/3$, $\rho_{01}/\rho_{02} = 10$, $k_t d = 2.82$, with V_{01} in the range of 1-10, and $V_{02} = 0$. These are characteristic values across the magnetopause [e.g., *Pu and Kivelson*, 1983a, b; *Taroyan and Erdélyi*, 2003b]. Here, $\beta_{1,2} = (P_{01,02}) / (B_{01,02}^2/2\mu_0)$, such that the parameters chosen represent realistic values of the plasma beta on each side of the boundary. We set $B_{01} \perp B_{02}$ in region A, $B_{01} \parallel B_{02}$ in regions B and C. We have investigated unbounded magnetospheric cases applicable to regions A, B and C. We also examined cases of a bounded magnetosphere, for regions A and B, where the inner boundary is set at $d = 9R_E$ in region A, and at $d = 17R_E$ in

region B. Note that the results of unbounded region B also apply to unbounded region C since the magnetic field and the background flow velocity configurations are the same for these two regions. All the physical values are calculated in the stationary frame of the plasmas on either side of the magnetopause. Since the background flow is set to zero in region 2, the stationary plasma frame is also the magnetospheric stationary frame such that $\omega_2' = \omega$.

3.2.4   Results

In this section, KH surface modes excited by the shear flow TDs with five different wave propagation directions with respect to the background magnetic fields will be considered in regions A, B and C of the magnetosphere. The magnetic field orientations are summarized in Table 3.1. All of the generated MHD modes have been investigated, and

Regions								
A			**B**			**C**		
θ_1	θ_2	**d**	θ_1	θ_2	**d**	θ_1	θ_2	**d**
0°	90°		0°	0°		0°	0°	
30°	60°		30°	30°		30°	30°	
45°	45°	9	45°	45°	17	45°	45°	∞
60°	30°		60°	60°		60°	60°	
90°	0°		90°	90°		90°	90°	

Table 3.1:   Magnetic field configurations for regions A, B, and C; θ_1 and θ_2 represent the direction of wave propagation with respect to the background magnetic fields in the magnetosheath and the magnetosphere, respectively, and d is the distance to the inner boundary, where appropriate.

the KHI - related modes examined in the context of wave-wave interactions and their relation to the primary and secondary KHI and to negative energy waves. The MHD waves will be classified as slow and fast modes based on their phase velocity with respect to the Alfvén speed using phase velocity diagrams, i.e., Friedrichs diagrams, and the effect of the background flow on the phase velocity in the magnetosheath will be displayed through these diagrams as well. Significantly, the importance of the primary and secondary KHI waves under different conditions along the magnetopause in regions A, B and C, will be

summarized and compared to previous satellite observations.

1. Growth Rates and Frequencies

For the case of an unbounded shear flow interface, the KHI can be understood through the linear mode interactions that can occur when the waves have equal frequencies and wave numbers, i.e., when they have equal phase velocities [e.g., *Swanson*, 1989; *Shiryeava*, 2001]. Across our warm plasma interface, four physically distinct modes (numbered from 1-4 for clarity) associated with the KHI are obtained with the set of the parameters listed in Table 3.1. The real frequencies and growth rates corresponding to $\theta_1 = 0°, \theta_2 = 90°$ (left panels (a) and (c)) and $\theta_1 = 60°, \theta_2 = 30°$ (right panels (b) and (d)) for an unbounded magnetosphere are shown in Figure 3.3 as examples illustrating the characteristics and physical aspects of the interacting MHD modes. This is equivalent to an unbounded case of region A. Here θ_1 and θ_2 are the angles of propagation with respect to the background magnetic field in regions 1 and 2, respectively. In Figure 3.3 the real frequencies (top row) are shown with solid lines and the growth rates (bottom row) are shown with symbols; the growth rate of a specific mode is shown with the same color as its real frequency. Since magnetic tension was present for all the cases presented in Figure 3.3, a lower cut-off velocity, that is a background flow velocity value above which KHI onset occurs, always existed. The primary and the secondary KHI intervals are marked with vertical lines and corresponding labels. For this unbounded case, mode interaction regions are observable when two modes have equal real frequencies, ω_r, and growth rates, ω_i, in complex conjugate pairs. For each unbounded configuration, KH instability occurs when two linear wave modes can be considered to interact; in Figure 3.3a modes 3 and 4 are interacting, while in Figure 3.3b modes 3 and 2 are interacting throughout the primary KHI interval. It is also seen in Figure 3.3c and 3.3d that these interacting modes have complex frequencies in complex conjugate pairs as expected.

The secondary KHI does not exist in Figure 3.3 for $\theta_1 = 0°, \theta_2 = 90°$, but is present for the configuration of $\theta_1 = 60°, \theta_2 = 30°$ in the interval of instability with lower V_{01}. Figure 3.3b shows that the secondary KH instability occurs when mode 1 and mode 2 are

interacting, again in complex conjugate pairs. The phase velocity of these wave modes are also calculated and found to be equal to each other, as expected, throughout intervals of the primary and secondary KHI. In this unbounded case, there is an upper cut-off speed for both the primary and secondary KHI. The real frequencies and growth rates of the surface wave modes obtained for the unbounded $(d \rightarrow \infty)$ cases of the night-side and the magnetotail configurations in regions B and C display similar characteristics to those in Figure 3.3.

When an inner boundary is included, however, the KH unstable modes no longer occur in complex conjugate pairs and can have different frequencies. Therefore, the concept of linear wave-wave interactions are not valid in the case of a bounded magnetosphere. This fact is illustrated in Figures 3.4a and 3.4c for a bounded dayside magnetosphere for $\theta_1 = 90°, \theta_2 = 0°$ (region A) and in Figures 3.4b and 3.4d for a bounded night-side magnetosphere for $\theta_1 = \theta_2 = 60°$ (region B). It is seen in Figures 3.4c and 3.4d that the KHI still exists in the bounded case, but with the exclusion of an upper cut-off velocity, i.e, once a mode becomes unstable it remains unstable even though the growth rate decreases as the background flow speed increases. Physically, this can be understood to arise from the fact that waves can now be reflected from the bounded magnetosphere and influence the instability conditions at the shear flow magnetopause boundary. As in the semi-infinite magnetosphere case, stable non-growing waves are present before the onset of the primary and secondary KHI. Such stable MHD surface wave modes could potentially still be excited on the magnetopause by processes such as solar wind dynamic pressure perturbations at flow speeds below the onset of the KHI. Figure 3.4c displays the additional feature that for the configuration $\theta_1 = 90°, \theta_2 = 0°$, the magnetic tension is not strong enough to quench the KHI so that mode 2 has a small growth rate even for

(a) $\theta_1 = 0°, \theta_2 = 90°$

(b) $\theta_1 = 60°, \theta_2 = 30°$

(c) $\theta_1 = 0°, \theta_2 = 90°$

(d) $\theta_1 = 60°, \theta_2 = 30°$
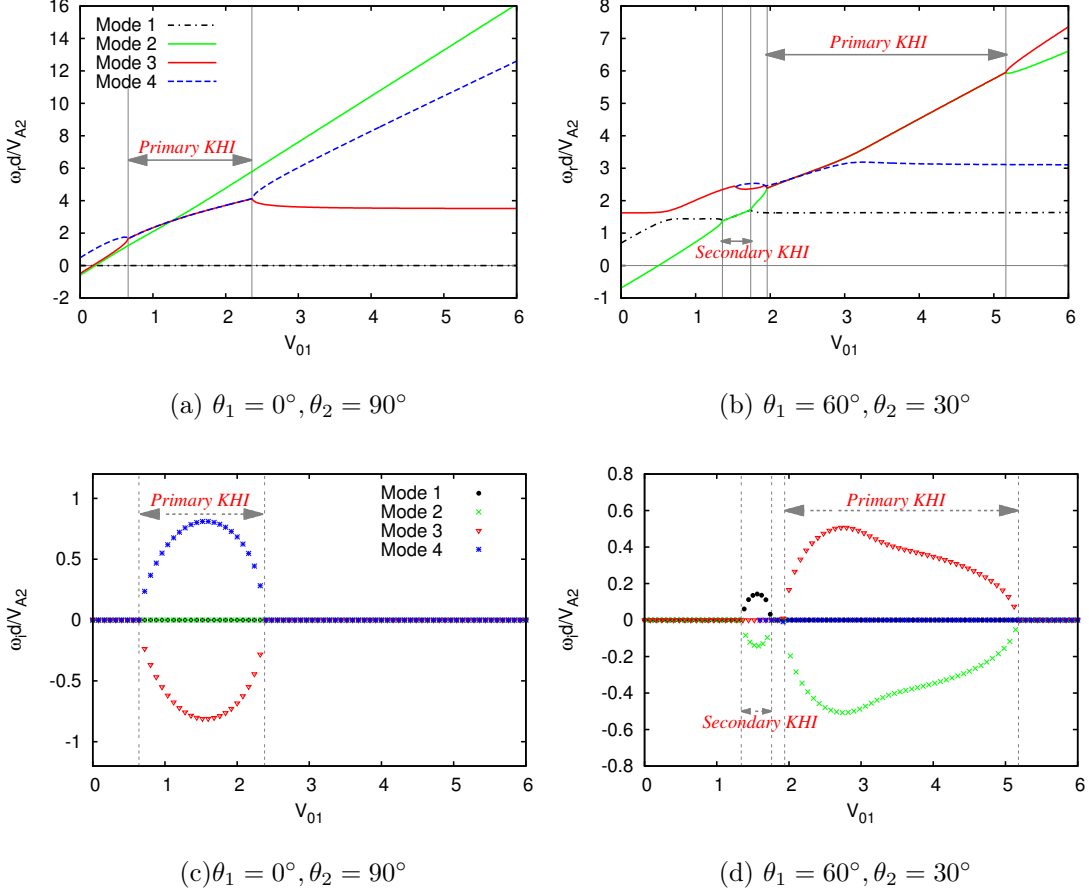
Figure 3.3: Real frequencies, (a) and (b), and growth rates, (c) and (d), of two different configurations of regions A for the case of unbounded magnetopause. Modes are labelled 1-4 for clarity. For each configuration, where different modes have equal real frequencies and are in complex conjugate pairs, this implies the presence of linear wave-wave interactions and the possibility of instability. Positions of KHI onsets and upper cut-off velocities are marked with vertical lines and primary and secondary KHI intervals are labelled.

very small flow speed. For the bounded case, it seems likely that the effects of magnetospherically reflected waves can cause the waves to become KH unstable even at very low background flow speeds.

In the semi-infinite magnetosphere case, complex conjugate pair wave-wave interactions are possible throughout the primary and the secondary KHI intervals and for flow

speeds above the unstable region all the modes have different frequencies and are purely propagating with zero growth rates (see Figure 3.3 as an example). For the bounded

(a) $\theta_1 = 60°, \theta_2 = 30°$, Dayside

(b) $\theta_1 = 60°, \theta_2 = 60°$, Nightside

(c) $\theta_1 = 60°, \theta_2 = 30°$, Dayside

(d) $\theta_1 = 60°, \theta_2 = 60°$, Nightside
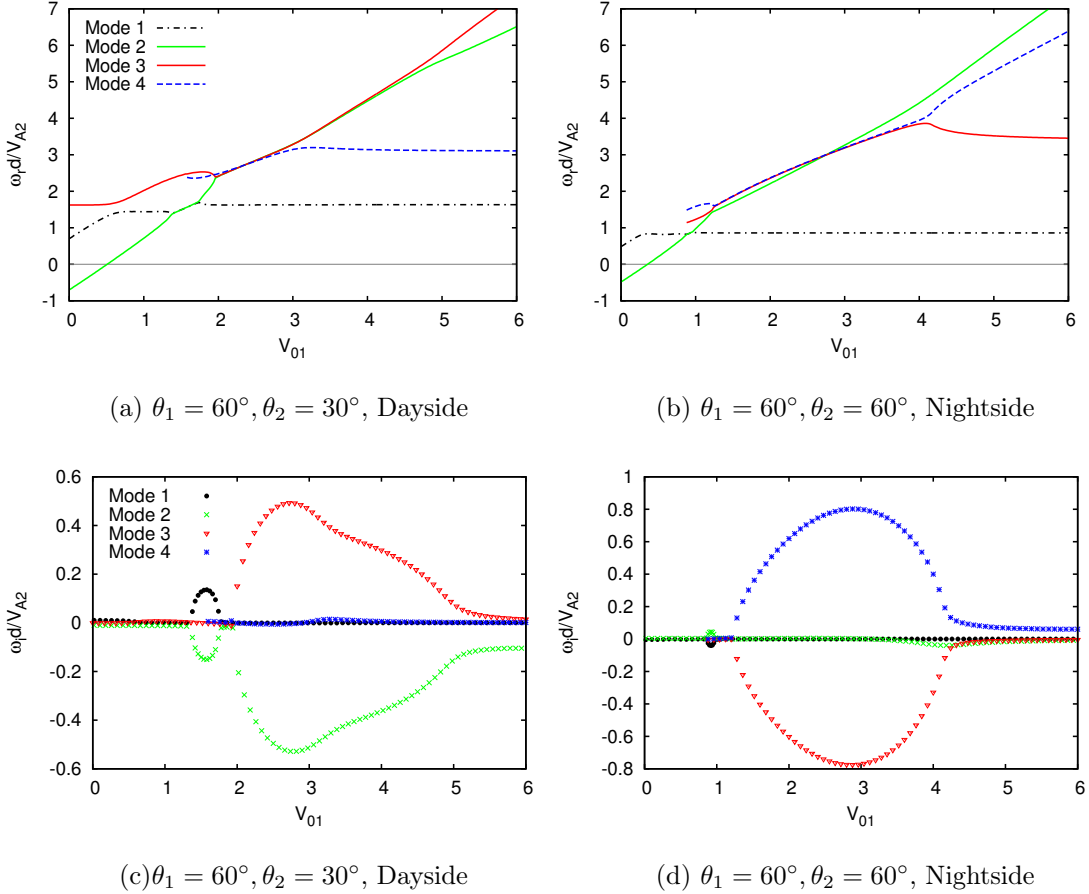
Figure 3.4: Growth rates and real frequencies for a bounded magnetosphere. Panels (a) and (c) show results for bounded dayside flanks, region A, and panels (b) and (d) show results for bounded night-side flanks, region B. It is clearly seen that the unstable modes are no longer characterized by complex conjugate pairs, and the real frequencies of the stable and unstable branches are not exactly equal.

magnetosphere, however, the wave modes are not in complex conjugate pairs anymore and don't have equal real frequencies, implying that the two mode complex conjugate wave-wave interaction does not hold anymore and thus the upper cut-off speed does not exist (see Figure 3.4 as examples from our results). We suggest that the absence of complex conjugate pairs, and thus symmetric wave-wave interactions, are the reason for the

removal of the upper cut-off speed in the bounded magnetosphere case. The fact that the KHI occurs in the bounded magnetosphere case, although there are no symmetric wave-wave interactions, also indicates that the onset of the KHI is not related to the two wave interactions in contrast to what has been previously suggested [*Taroyan and Erdélyi*, 2003a, b, 2002; *Mills et al.*, 1999; *Cairns*, 1979].

All of the other configurations in Table 3.1 demonstrate a similar distinction between the unbounded magnetosphere and bounded magnetosphere.

2. Doppler Shifted Frequencies: Are KHI Relevant Waves Negative Energy Waves?

Negative energy waves or over-reflected waves have been suggested to have negative Doppler shifted frequencies [e.g., *Mann et al.*, 1999; *McKenzie*, 1970]. Our results show that the Doppler shifted frequencies of unstable wave modes have negative values after the onset of the primary and secondary KHI, implying that they are negative energy waves. This result agrees with the previous results by *Pu and Kivelson* [1983a] and *Mann et al.* [1999] that the KHI waves always have negative energy. This fact is displayed in Figure 3.5a for an unbounded magnetosphere with magnetic field configuration $\theta_1 = 60, \theta_2 = 30°$, and in Figure 3.5b for a bounded magnetosphere with magnetic field configuration $\theta_1 = \theta_2 = 30°$, representative of regions A and B, respectively. In Figure 5 normalized Doppler shifted frequencies are shown such that, $\omega_{doppler} = \omega_r d/V_{A2} - \mathbf{V_{01}}.\mathbf{k_t}d$. In the unbounded case, for flow speed above the upper cut-off speed, previously KH unstable modes still have a negative Doppler shifted frequency (see Figure 3.5a). Therefore a negative Doppler shifted frequency (and negative energy waves) is a necessary but not sufficient condition for the KHI to be unstable. However, extraction of energy from the background flow by the waves remains responsible for the onset of the KHI.

Walker [2000] offers an attractive alternative approach, where energy exchange between the waves and the background flow is considered instead of emphasizing the negative energy of the waves. In *Walker* [2000], the energy extraction is also shown to

(a) $\theta_1 = 60°, \theta_2 = 30°$, Day-side.　　　　(b) $\theta_1 = 30°, \theta_2 = 30°$, Night-side
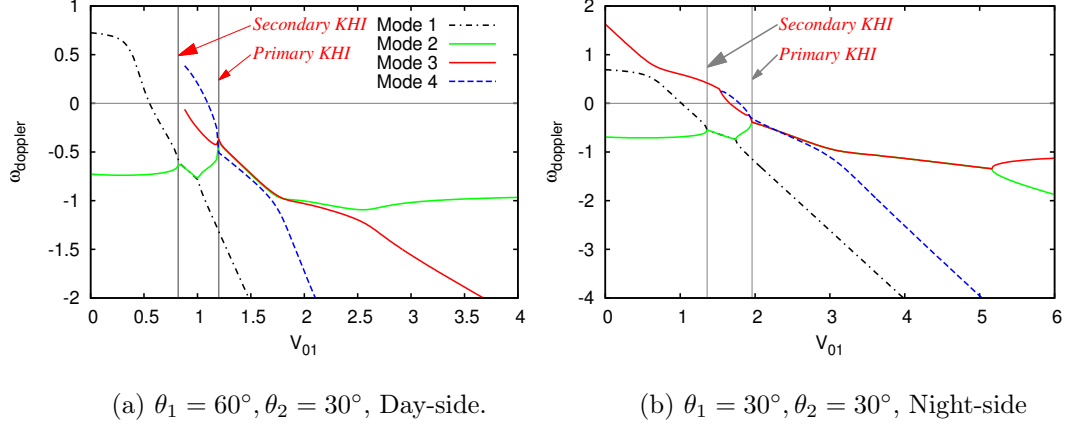
Figure 3.5: Normalized Doppler shifted frequencies, $\omega_{doppler} = \omega_r d / V_{A2} - \mathbf{V_{01}}.\mathbf{k_t}d$, (a) for region A for an unbounded magnetosphere with $\theta_1 = 60°, \theta_2 = 30°$, and (b) for region B for a bounded magnetosphere with $\theta_1 = 30°$ and $\theta_2 = 30°$. All the modes have negative Doppler shifted frequencies after the onsets of the primary and secondary KHI. Vertical lines mark the flow speed for the onset of the primary and secondary KHI.

be possible through the work done on the wave by the background flow which can be explained and is dependant on the Reynolds and Maxwell stresses on the boundary. Following *Walker* [2000]'s idea, we believe that the K-H unstable waves also extract energy from the background flow through the work done by the Maxwell and Reynolds stresses. In order to fully explain the relationship between the KHI, negative energy waves and work done by the stresses at the boundary, further work is needed using the approach suggested by *Walker* [2000] and this is left as a future work.

3. Characteristics of KH Unstable MHD Modes: Dependence on the Angle of Propagation

(a) Phase Velocity Diagrams

In this section, the angles of propagation, θ_1 and θ_2, in the two media are varied from 0 to 2π while the magnetic field and flow velocity orientations are maintained constant. This allows the classification of the wave modes as fast and slow by comparing their phase velocities with the Alfvén speed using phase velocity diagrams. The total phase velocity of the modes are plotted in a polar coordinate system with their magnitude along

k with respect to the background field direction (i.e., in the form of Friedrichs diagrams). For each different value of propagation angle, the total phase velocity is calculated using the solution for the frequencies and wave numbers from the dispersion relation, with the equation

$$\mathbf{U_P} = \frac{\omega_r}{(k_t^2 + k_x^2)}\mathbf{k}. \tag{3.8}$$

Normalized phase velocity, $V_p = U_p/V_{A2}$, diagrams of KHI relevant MHD modes for the dayside magnetosheath and magnetosphere, region A, are shown in Figure 3.6 at flow velocity value $V_{01} = 2.3$. The phase speeds for decoupled Alfvén modes propagating at the Alfvén speed in each medium are shown in each diagram both for comparison and for classifying modes as slow or fast. These Friedrichs diagrams aid with understanding the behavior of the MHD modes in the magnetosheath and magnetosphere which are coupled across the magnetopause under the influence of background plasma flow. Figures 3.6a show that in the magnetosheath, the phase velocity of the modes is distorted due to the effects of the background flow and coupling to the modes in the magnetosphere.

Figures 3.6b displays that in the magnetosphere, only mode 1 is a slow mode for all propagation angles and all the other modes have fast mode characteristics. Interestingly, for the same flow speed Figure 3.6b also shows that mode 2 and 4 become slow modes at values of $\theta_2 \lesssim 30°$. The intervals of the primary KHI are highlighted with grey colors and those of the secondary KHI are highlighted with yellow colors. The primary KHI which holds for the propagation angles $\theta_2 \simeq 26° - 90°$ for the first quadrant of Figure 3.6b; the other three quadrants are symmetric with respect to the first quadrant. Throughout this interval, mode 3 is the unstable mode at $\theta_2 \simeq 26° - 32°$ and is interacting with mode 2, and mode 4 is unstable at $\theta_2 \simeq 33° - 90°$ and is interacting with mode 3. The secondary KHI holds for propagation angles $\theta_2 \simeq 19° - 24°$, where mode 1 is unstable and is interacting with mode 2. Remembering the result found in section 1 that in an infinite unbounded medium the wave-wave interaction is related to both primary and secondary KHI, Figure 3.6b shows that in region A of a semi-infinite dayside magnetosphere, the

(a) $V_{01} = 2.3$, Magnetosheath modes   (b) $V_{01} = 2.3$, Magnetosphere modes
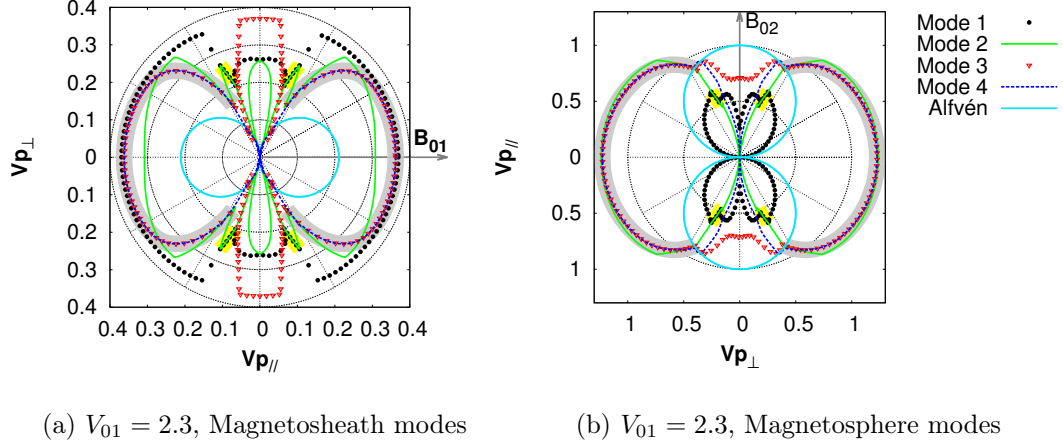
Figure 3.6: Friedrichs phase speed (normalized by V_{A2}) diagrams at flow velocity value 2.3 for dayside unbounded region A, (a) in the magnetosheath, and (b) in the magnetosphere. Wave mode 3 is a fast mode in the magnetosphere at angles of propagation $\theta_2 \simeq 30° - 90°$, and its phase velocity is smaller than the Alfvén wave at angles $\theta_2 \simeq 0° - 30°$. Modes 2 and 4 are fast for $\theta_2 \gtrsim 30°$ and slow for $\theta_2 \lesssim 30°$ angle of propagation. In the magnetosheath, all the modes are fast modes at all values of θ_1. Yellow shaded areas mark the secondary KHI zones and grey shaded areas mark the primary KHI zones.

primary KHI is related to a fast-fast mode interaction and the secondary KHI is related to a slow-slow mode interaction in the magnetosphere. Of course the mode interaction (overlap) is seen in both the magnetosphere and magnetosheath on either side of the shear flow boundary.

Interestingly, of course, the modes can have different fast or slow characteristics on either side of the magnetopause. For example the secondary KHI wave seen in Figure 3.6a and 3.6b (at low θ_2) is a slow mode in the magnetosphere, but a fast in the magnetosheath. For the primary KHI it is a fast mode in both magnetosphere and magnetosheath.

The results for the bounded dayside magnetosphere are morphologically similar to the unbounded cases shown in Figure 3.6, despite the fact that perfect wave-wave interactions do not occur in the bounded case. To illustrate this point, phase velocity diagrams for unbounded and bounded dayside magnetosphere flanks, with other parameters from region A, are shown in Figures 3.7a and 3.7b, respectively, for $V_{01} = 1.6$. The primary

and secondary KHI zones are again marked with grey and yellow highlights. In Figure 3.7a (the unbounded case), mode 4 is unstable to the primary KHI for $\theta_2 \simeq 32° - 90°$ and it has a phase velocity equal to that of mode 3 throughout this interval. Whereas,

(a) Unbounded   (b) Bounded
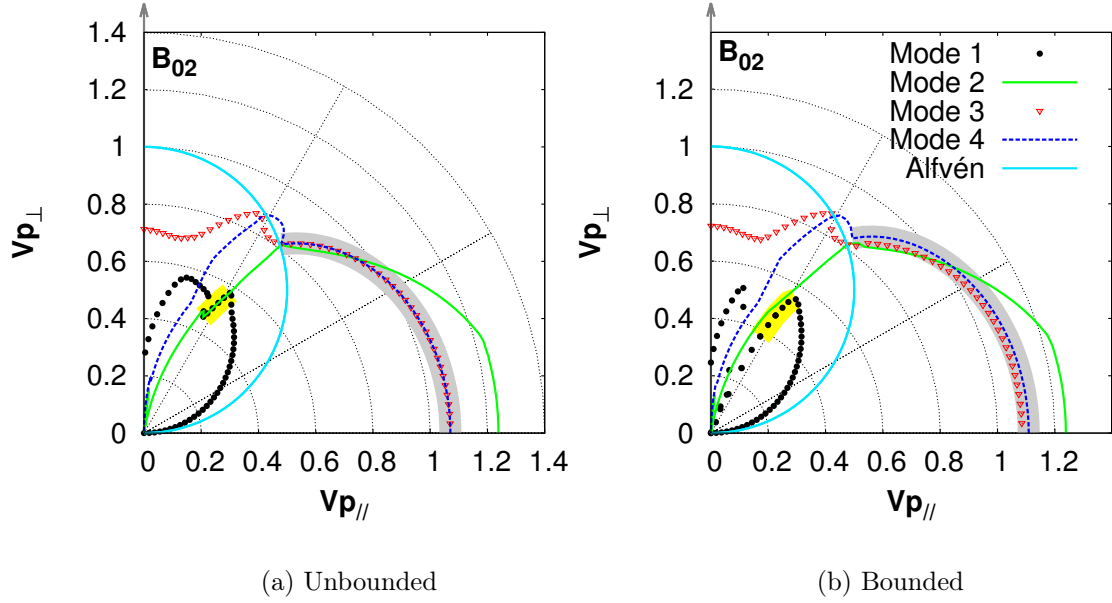
Figure 3.7:   Friedrichs (normalized) phase speed diagrams at flow velocity value $V_{01} = 1.6$, on the magnetosphere side of region A, (a) semi-infinite, and (b) bounded magnetosphere respectively, displaying the presence/absence of linear wave-wave mode interaction in each case. Throughout the primary and secondary KHI intervals, grey and yellow shaded areas, mode 3 and 4 and mode 1 and 2 have exactly equal phase velocity for a semi-infinite magnetosphere while they are propagating at different phase velocities for a bounded magnetosphere.

in Figure 3.7b, these two modes propagate at different phase velocities although mode 4 is still unstable to the primary KHI at about the same range of angles as in Figure 3.7a. Similarly, mode 1 is unstable to the secondary KHI for $\theta_2 \simeq 26° - 32°$ in both unbounded and bounded magnetosphere cases and it has equal phase velocity to that of mode 2 only in the unbounded case. Despite the fact that symmetric complex conjugate wave-wave interactions do not occur in the bounded case, there remains regions of primary and secondary KHI. Therefore, in the bounded magnetosphere, the upper cut-off velocity is removed and the boundary is never again perfectly stabilized with increasing flow speed

once it becomes unstable.

Example Friedrichs diagrams of MHD modes for the unbounded magnetotail, region C, are shown in Figures 3.8 for the magnetosheath and the magnetosphere at magnetosheath flow velocity values $V_{01} = 1$ and 2.3, respectively. A new result shown in Figure 3.8 is that none of the modes propagate perpendicular to the background magnetic fields, and hence also perpendicular to the magnetopause boundary. Hence the MHD waves in the magnetotail cannot have $\mathbf{k}$ exactly perpendicular to $\mathbf{B}_{01,02}$, such that they must propagate either sun-ward or anti-sunward with a component of phase speed parallel or anti-parallel to $\mathbf{B}_{01,02}$. These type of surface modes have been obtained in the past when a background plasma flow is present [e.g., *Tajiri*, 1967; *Kato et al.*, 1966; *Namikawa and Hamabata*, 1981]. These wave modes are considered to be a type of mixed fast-slow mode which we call intermediate-fast mode following the terminology of *Namikawa and Hamabata* [1981]. Intermediate-fast modes are defined in this paper as the modes that have phase velocity values in the expected range of fast mode waves but do not propagate exactly perpendicular to the background magnetic field.

Figures 3.8a and 3.8c show that, on the magnetosheath side, mode 3 and mode 4 converts to intermediate-fast from slow modes as flow velocity increases, while mode 1 and 2 stay as intermediate-fast. Mode 4 is also a slow mode for flow velocity values $V_{01} < 1$ and converts to intermediate-fast at larger flow speeds. On the magnetosphere side, mode 2, mode 3 and mode 4 are generated as slow modes and converted to intermediate-fast modes as the flow velocity increases, while mode 1 is generated and remains as a slow mode in Figures 3.8b and 3.8d. Mode interaction zones match with the intervals of the primary and secondary KHI, grey and yellow shaded areas, and are similar to those shown for the dayside magnetosphere flanks, region A, in Figure 3.6. Figure 3.8b shows that in the magnetosphere, at flow velocity $V_{01} = 1$, both mode 1 and mode 2 are slow modes and are interacting with each other during the secondary KHI interval. Again these same modes show a fast-fast interaction on the magnetosheath side.

(a) $V_{01} = 1$, Magnetosheath modes

(b) $V_{01} = 1$, Magnetosphere modes

(c) $V_{01} = 2.3$, Magnetosheath modes

(d) $V_{01} = 2.3$, Magnetosphere modes
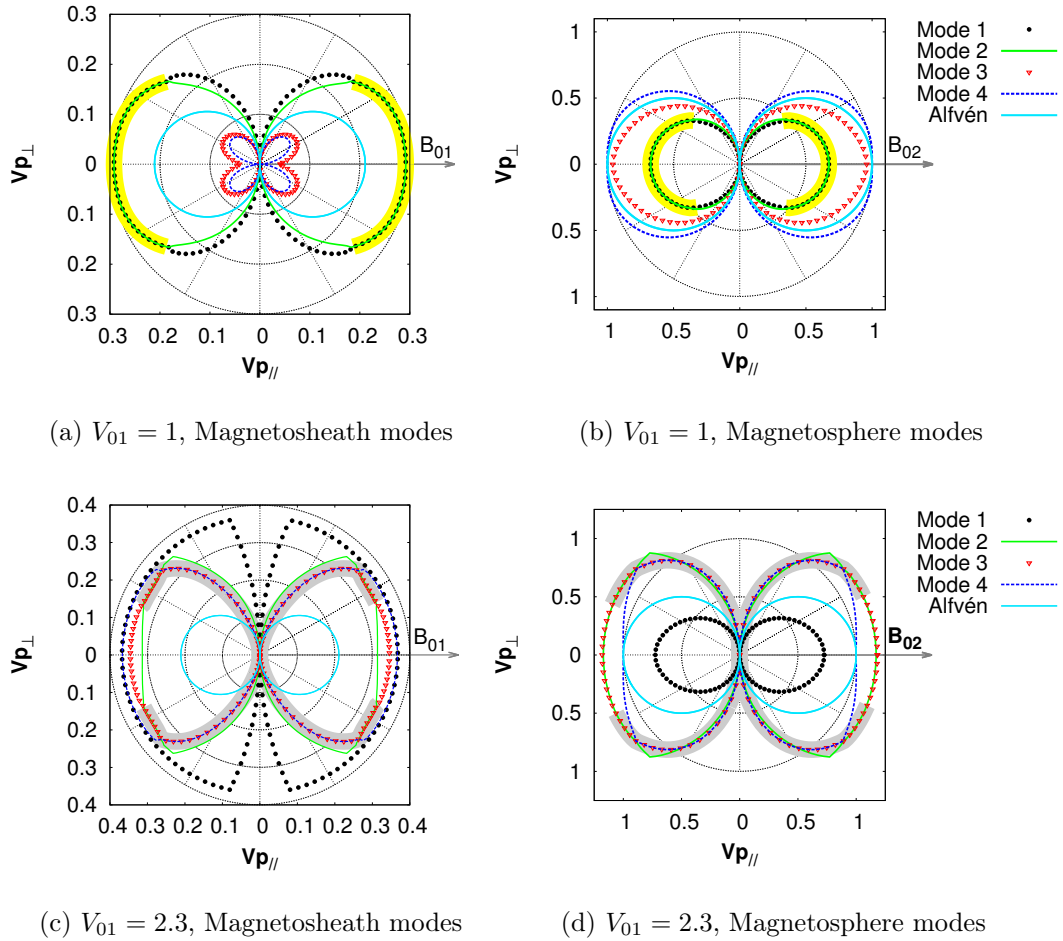
Figure 3.8: Normalized phase velocity diagrams at two different flow velocity values for region C, for the magnetosheath (panels (a) and (c)), and the magnetosphere (panels (b) and (d)). Only secondary KHI is obtained on panels (a) and (b), yellow shaded areas, and only primary KHI is obtained on panels (c) and (d), grey shaded areas. Characteristics of the wave propagation are significantly different than region A; specifically perpendicular propagation of the modes does not occur on either side of the magnetopause, which introduces a new type of modes labelled intermediate-fast modes in this paper (see text for details).

Friedrichs diagrams of the MHD modes obtained on the bounded night-side magnetosphere flanks, region B, show similar characteristics to those in region C in the magnetotail. However, due to the presence of the inner boundary for bounded region B, perfect linear two wave-wave interactions are not obtained in regions of instability due to the impact of reflected modes and their interaction at the shear flow boundary. Figures 3.9 shows the Friedrichs diagrams for wave modes in the magnetosheath, for regions C and B, to enable a comparison of wave-wave interaction in the unbounded and bounded magnetotail similar to that shown for region A in Figure 3.7. In Figure 3.9, only secondary KHI holds and intervals are highlighted with yellow colors as well. In Figure 3.9a, mode 1 is unstable for the propagation angles of $\simeq 0° - 80°$ and is interacting with mode 2 throughout this interval, i.e, has equal phase velocity. While in Figure 3.9b, although mode 2 is unstable for the propagation angles $\simeq 0° - 88°$, it does not show linear wave-wave interactions with mode 1 or with any other existing modes. Figures 3.9c and 3.9d also show similar characteristics for the case where the background flow value $V_{01} = 1$, where mode 1 is unstable for $\theta_1 = 0° - 42°$ in Figure 3.9c, and mode 2 is unstable for $\theta_1 = 0° - 45°$ in Figure 3.9d. Again there are no wave-wave interactions in the bounded case of Figure 3.9d, while mode 1 and mode 2 are linearly interacting through complex conjugate pairs throughout the secondary KHI zone in Figure 3.9c. Note that while mode 1 and mode 2 are intermediate fast waves at these flow velocity values on the magnetosheath, they are slow waves on the magnetosphere side at the background flow speeds shown in Figure 3.9 (see Figure 3.8b for $V_{01} = 1$ as an example). Figure 3.9a also shows that the phase speed of mode 3 diminishes at $\theta_1 \simeq 30°$, on the magnetosheath side, where the phase velocity is either zero or purely imaginary and the wave propagation direction changes from upstream to downstream.

(b). Growth Rates Dependence on the Angle of Propagation

A polar plot of the growth rates of the unstable modes with respect to the propagation angle is shown in Figure 3.10 for the semi-infinite magnetosphere case with B_{01} perpendicular to B_{02} as in region A with $V_{01} = 2.3$.

(a) Unbounded, $V_{01} = 0.9$

(b) Bounded $V_{01} = 0.9$

(c) Unbounded $V_{01} = 1$
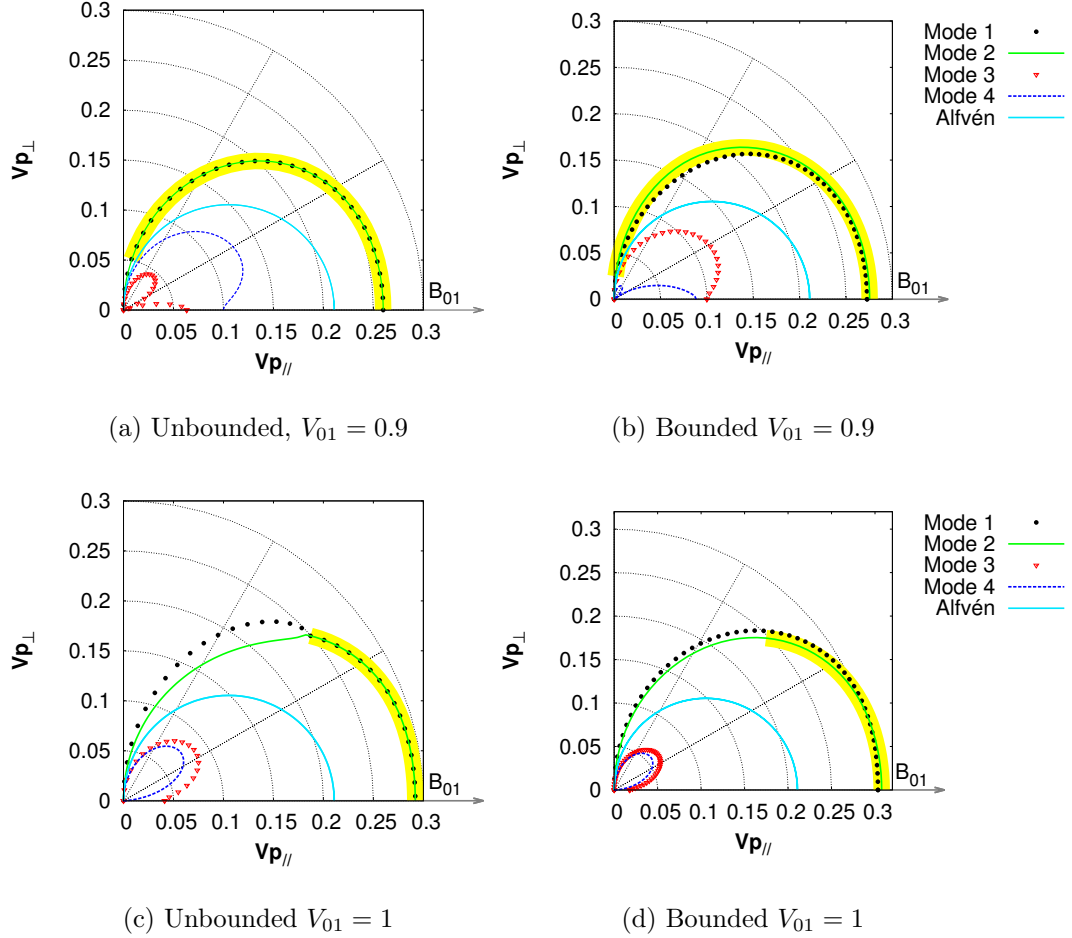
(d) Bounded $V_{01} = 1$

Figure 3.9: Friedrichs (normalized) phase speed diagrams in the magnetosheath at two background flow values: (a) and (b) $V_{01} = 0.9$, and (c) and (d) $V_{01} = 1$. Left column shows region C (unbounded) and right column shows region B (bounded). Secondary KHI regions, which is the only present instability at these flow speeds, are highlighted with yellow colors. The presence/absence of the linear wave-wave interactions in the semi-infinite/bounded case representing region C/B are clearly seen (see text for details).

At this value of the background flow both the primary and the secondary KHI are possible at different values of the angle of propagation. Figure 3.10 shows that at this value of the background flow velocity the primary KHI is generated by mode 3 for $\theta_2 \simeq 26° - 32°$ and by mode 4 for $\theta_2 \simeq 33° - 90°$ in the first quadrant. The secondary KHI is generated purely by mode 1 at $\theta_2 \simeq 19° - 23°$. It is also visible on Figure 3.10 that the growth rates of the primary KHI peak around $\theta_2 = 45°$, and that of the secondary KHI peak at $\theta_2 = 22°$, where θ_2 is the angle of propagation with respect to the magnetic field in the magnetosphere, B_{02}. Exactly the opposite holds for propagation angles (θ_1) with respect to the magnetic field in the magnetosheath, B_{01}. The bounded magnetosphere case for region A (not shown) displayed very similar characteristics as the unbounded magnetosphere case presented in Figure 3.10.

For regions B and C there is not a single flow velocity at which both the primary and secondary KHI are obtained simultaneously. Therefore, the primary KHI growth rate is calculated at the background flow velocity value $V_{01} = 2.3$ and the secondary KHI growth rates are calculated at $V_{01} = 1$. Both are plotted for clarity in Figure 3.11 for region C. The primary KHI growth rates are caused partially by mode 3 and partially by mode 4 similar to Figure 3.10; mode 3 is unstable at $\theta_1 = \theta_2 \simeq 23° - 40°$ and mode 4 is unstable at $\theta_1 = \theta_2 \simeq 40° - 90°$. Figure 3.11 shows that the primary KHI growth rates peak at $\theta_1 = \theta_2 \simeq 56°$, and secondary KHI growth rates peak at $\theta_1 = \theta_2 \simeq 0°$. There is no unstable mode at $\theta_1 = \theta_2 = 90°$ which is expected since there is no propagating mode at this direction for region C. The growth rate characteristics for region B (not shown) displayed similar characteristics to those for region C shown in Figure 3.11.

(c). Energy Propagation into the Magnetosphere with the Primary and Secondary KHI waves

The direction of energy propagation resulting from KH unstable modes can be understood using polar group velocity Friedrichs diagrams. Group velocities are calculated
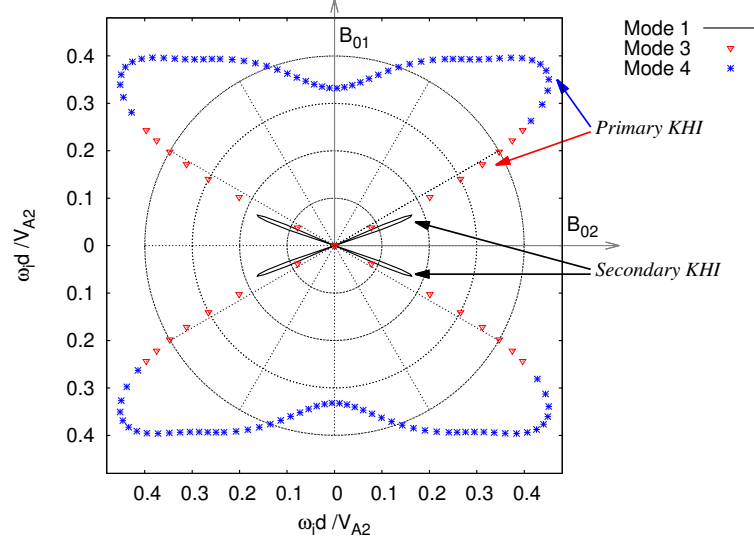
Figure 3.10: Growth rate dependence on the angle of propagation for $V_{01} = 2.3$, in region A for a semi-infinite magnetosphere. Primary and secondary KHI regions are labeled and the background magnetic field orientations in the magnetosheath and magnetosphere are shown with arrows. At this flow velocity, the primary KH instability is caused by mode 3 and mode 4, shown with red triangles and blue points, at different propagation angles. Secondary KHI is caused by mode 1 and is shown with black lines. Primary instability growth rate peaks at orientation angles $\simeq 45°$, and secondary growth rate peaks at $\simeq 22°$, with respect to B_{02} on the magnetosphere side, while exactly the opposite holds with respect to the B_{01} on the magnetosheath side. Primary KHI is possible at a wide range of angles $\simeq 30° - 90°$, while secondary KHI only occurs at $\simeq 19° - 23°$.

using the equation;

$$U_{gr} = \frac{d\omega}{dk},$$

and normalized group velocities are plotted, which is $V_{gr} = U_{gr}/V_{A2}$. These are shown in Figure 3.12 for region A for a semi-infinite magnetosphere with the same value of background flow speed from Figure 3.6. Since our primary interest is investigating energy propagation into the magnetosphere from the magnetosheath, the group velocities are calculated only for the magnetosphere. In Figure 3.12 the primary KH unstable mode consists partially of mode 3 and partially of mode 4, depending on the angle of **k**, while the secondary KH unstable mode is mode 1(see Figure 3.6 and the text related to it
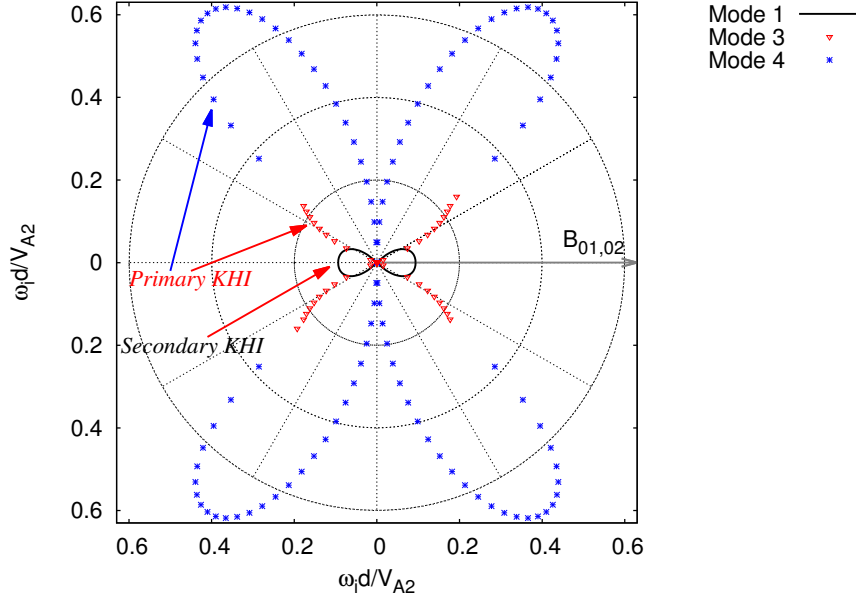
Figure 3.11: Growth rate dependence on the angle of propagation in the magnetotail, region C, for the primary and secondary KHI. The results for the primary KHI were obtained at flow velocity value $V_{01} = 2.3$, and for the secondary KHI were obtained with $V_{01} = 1$. The growth rate of the secondary KHI peaks about $0°$, and the growth rate of the primary KHI peaks at about $56°$, with respect to the direction of the background magnetic fields, B_{01} and B_{02}. Growth rates are zero at $90°$ propagation angle for both the primary and the secondary KHI.

for details). Normalized group velocity diagrams of primary KHI modes in Figures 3.12 shows that modes 3 and 4 are able to propagate energy perpendicular to the background magnetic field in region A. However, these modes have zero group velocity at a small range of angles $\theta_2 \simeq 0°$, and thus cannot propagate energy along this direction. The secondary KHI is only obtained in Figure 3.12 for θ_2 between $19° - 23°$ and is caused by mode 1. The Figure 3.12 hence shows that secondary KH modes can propagate energy into the magnetosphere only at a very narrow range of angles of propagation.

In regions B and C, although the phase velocity diagrams have shown that the primary and the secondary KHI waves are not able to propagate purely perpendicular to the background magnetic field and the phase velocity values become comparably small as
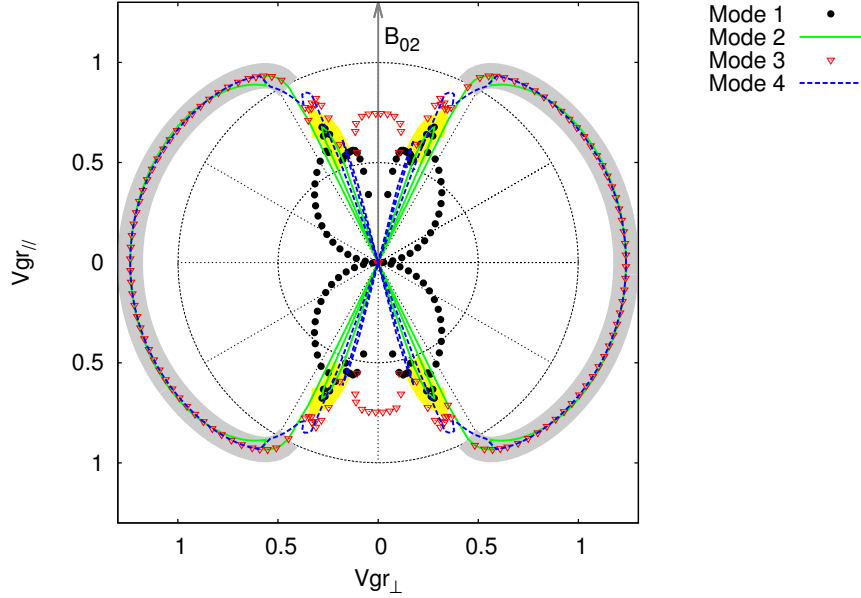
Figure 3.12: Group velocity (normalized by V_{A2}) diagrams at flow velocity value $V_{01} = 2.3$ in region A for a semi-infinite magnetosphere. The yellow and grey shaded areas mark the secondary and primary KHI intervals, the same as in the corresponding phase velocity diagrams shown on Figure 3.6.

the propagation angles approach to $90°$, the group velocity diagrams do not show the same characteristics due to the behavior of the intermediate-fast modes, in this case and discussed earlier. Figure 3.13 shows an example of this for region C. In Figure 3.13a, the secondary KH unstable mode is mode 1 and the primary KHI is not obtained for this background flow at all. Figure 3.13a shows that for $V_{01} = 1$, mode 1 has a group velocity comparable to its phase velocity across a wide-range of angles of propagation, and can propagate energy in these directions. The primary KHI is obtained once the flow speed is fast enough and at $V_{01} = 2.3$ it is seen to be caused partially by mode 3 and partially by mode 4 as shown in Figure 3.13b (see also section 3.2.4 Figure 3.8, and the text related to it). The group velocities of mode 3 and mode 4 have high values at all angles of propagation except for a very narrow range of angles close to $90°$, which shows that the energy transport is very efficient by these modes at these highly oblique angles despite

the small values of phase speed. Exactly at $\theta_2 = 90°$, where intermediate-fast modes have zero phase speed, the group speed is undefined.   We have also investigated the normal
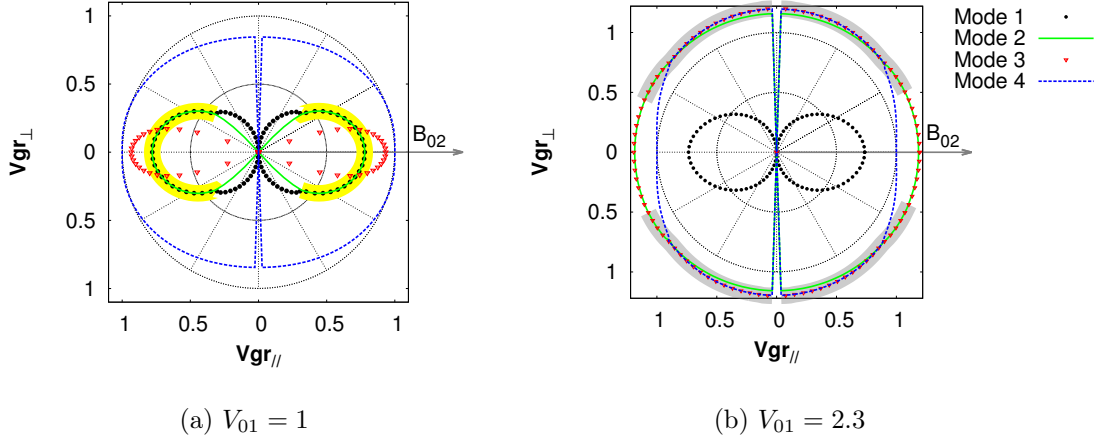
(a) $V_{01} = 1$ (b) $V_{01} = 2.3$

Figure 3.13:   Normalized group velocity diagrams for (a) $V_{01} = 1.0$, and (b) $V_{01} = 2.3$ in region C for a semi-infinite magnetosphere. The same as in the corresponding phase velocity diagrams (see Figure 3.8) the primary and secondary KHI intervals are marked with grey and yellow colors, respectively.

and the parallel phase velocities of the modes in order to investigate the energy transport by the primary and secondary KHI modes as flow velocity increases. All of the modes have zero normal components of phase speeds at low shear flow velocity where neither secondary nor primary KHI lower cut-off velocities have been reached. The modes start to pick up finite perpendicular phase speeds at the onsets of the primary and secondary KHI. This fact is displayed in Figure 3.14a for $\theta_1 = 30°, \theta_2 = 60°$ representing region A, and Figure 3.14b for $\theta_1 = 30°, \theta_2 = 30°$, representing region C, for a semi-infinite magnetosphere. The primary KH instability is caused by mode 4 in Figure 3.14a, and by mode 3 in Figure 3.14b. Both of these modes have zero normal phase speeds before, and they pick up large normal speeds after, the onset of the KHI. After the upper cut-off velocity is reached the normal phase velocity of mode 4 decreases to a constant value while that of mode 3 continue to increase. This result suggests that propagation and energy transport away from the magnetopause may be efficient due to the waves excited

by the primary KHI.

The secondary KHI is caused by mode 1 in Figures 3.14a and 3.14b and it also picks up a finite normal phase speed after the KHI onset, however it is significantly smaller than the normal speed of the primary KHI waves. After the upper cut-off velocity is reached, the normal phase speed of the secondary KHI mode decreases to zero, suggesting that energy transport due to the secondary KHI is mainly possible only during the narrow KHI unstable interval. Nevertheless, since under certain slow values of the background magnetosheath flow the secondary KHI may be the only active instability it could be the only means of extracting energy from the flow and thus it could still be dynamically important. With the difference between the perpendicular phase speeds it is possible that such characteristics may provide a diagnostic mechanism for distinguishing between the primary and secondary KHI waves. The wave propagation characteristics of the primary and the secondary KHI wave on the magnetopause are examined in detail in the following section.
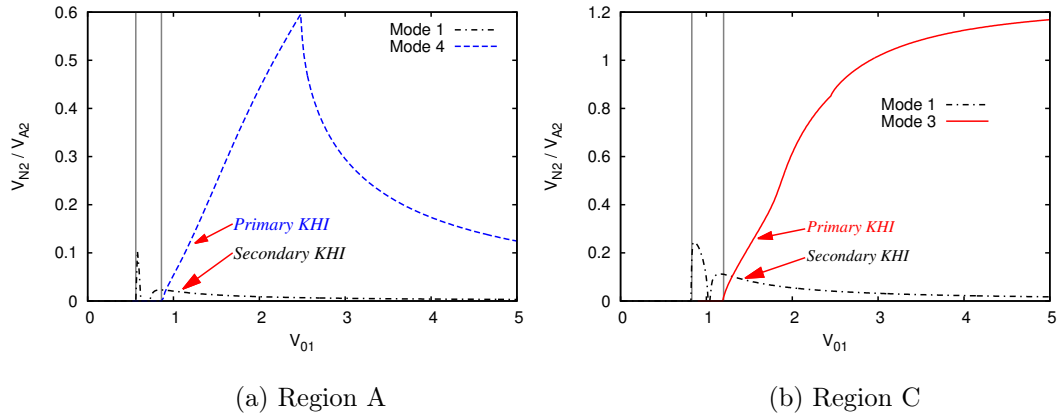
(a) Region A (b) Region C

Figure 3.14: Normal phase velocities of the primary and secondary K-H unstable modes for semi-infinite magnetosphere with magnetic fields orientations (a) $\theta_1 = 30°, \theta_2 = 60°$, corresponding to region A, and (b) $\theta_1 = 30°, \theta_2 = 30°$, corresponding to region C. Onsets of the primary and the secondary KHI are marked with vertical lines. Primary KHI is caused by mode 4 in panel (a) and mode 3 in panel (b), and the secondary KHI is caused by mode 1 in both panels.

4. Comparison to Observations

In this section we compare our results to KHI observations from the literature. Specifically we inspected various papers where KHI waves are observed in-situ at the magnetopause, and identified them with the three regions of the magnetosphere we have considered throughout this study, namely regions A, B and C in Figure 3.1. The observed phase velocities of the waves and the Alfvén speed in the magnetosphere are calculated in km/s using the observed values reported in the papers. Background flow velocities at which the KHI waves are observed, and the phase velocities of these waves are normalized using the observed Alfvén speed in the magnetosphere in the same way as in this paper. The observational KHI papers examined and the values deduced from these observations are summarized in Table 3.2.

Paper	Region	U_{01}	V_{A2}	V_p	V_p/V_{A2}	U_{01}/V_{A2}
[*Agapitov et al.*, 2009]	A	300	264	$190 - 240$	$0.7 - 0.9$	$1.1 - 1.2$
[*Hasegawa et al.*, 2006]	A	250	500	150	0.3	0.5
[*Gnavi et al.*, 2009]	B	300	308	200	0.7	1
[*Owen et al.*, 2004]	B	150	163	65	0.4	$0.6 - 1.2$
[*Chen and Kivelson*, 1993]	B	200	327	106	0.3	0.6
[*Hwang et al.*, 2011]	C	538	436	$322 - 400$	$0.7 - 0.9$	1.2
[*Nakai and Ueno*, 2011]	C	330	308	$50 - 250$	$0.1 - 0.8$	1.07
[*Gnavi et al.*, 2009]	C	300	436	200	0.5	0.7
[*Foullon et al.*, 2008]	C	200	165	$36 - 95$	$0.3 - 0.6$	1.2
[*Hasegawa et al.*, 2006]	C	300	155	200	1.3	1.9
[*Fairfield et al.*, 2000]	C	338	209	$230 - 250$	$1.1 - 1.2$	1.6
[*Kivelson and Chen*, 1995]	C	560	655	320	0.4	0.9

Table 3.2: In-Situ Satellite Observations of KH Surface Waves. U_{01} is the background flow velocity in the magnetosheath, and $V_{01} = U_{01}/V_{A2}$ is the normalized value of U_{01} with respect to the background Alfvén speed in the magnetosphere. V_p is the phase velocity of the KHI waves, in units of km/s , which are either directly given in the inspected papers or calculated using the given wavelengths and frequencies. Each published observation from the literature is also identified with one of regions, A, B and C.

Normalized phase velocity values from our results varied between $\simeq 0.3 - 1.2$ in the magnetosheath, and $\simeq 0.5 - 1.3$ in the magnetosphere, which are in general agreement with the observed phase velocity values of KHI waves summarized in Table 3.2. Com-

bining the results of observations from Table 3.2 and global MHD simulation results from *Lavraud et al.* [2007] and *Lavraud and Borovsky* [2008] we can highlight a range of expected values of the normalized magnetosheath flow speed to generally vary between $0.5 - 1.3$ in region A, $0.6 - 2.6$ in region B, and $0.7 - 4$ in region C. From our dispersion relation, which has a number of limitations including uniform plasma assumptions and an infinitely thin magnetopause, we can nonetheless identify that the intervals of the secondary KHI happens at normalized magnetosheath flow speed values of $\sim 0.7 - 1.8$, and the intervals of the primary KHI happens at flow speed values of $\sim 0.8 - 4$. This suggests that observed KHI waves in region A are mostly secondary KHI waves and in regions B and C they could be primary or secondary KHI waves. The peak values of the growth rates happen at background flow speeds $\sim 0.8 - 1.5$ for the secondary KHI waves and at $\sim 1.5 - 2.9$ for the primary KHI waves. These results suggest that if KH surface waves are seen on the near-Earth magnetopause then the secondary KHI is a prime candidate, although secondary KHI is possible elsewhere too. Since the flow speed is usually smaller in region A, the primary KHI would be expected to be mainly observed in regions B and C. This could be the reason for relatively fewer observations of KHI waves in region A [*Hasegawa et al.*, 2006] than regions B and C. Since the secondary KHI waves have relatively small growth rates and wave amplitudes in comparison to the primary KHI waves, they could also be detected less frequently. However, they can remain important since at low flow speeds they are the only KH unstable waves and thus perhaps might be the only cause of energy transport via KHI in region A.

Energy transport at the magnetopause might be mainly caused by the primary KHI in regions B and C since the magnetosheath flow may reach the lower cut-off for the primary KHI, and the peak values of the primary KH growth rates are typically larger than those of the secondary KHI. Overall, this suggests that the energy transport due to the KHI are likely more efficient in regions B and C, since waves which grow to larger amplitudes can carry more energy into the magnetosphere. We have also compared the new result we found on the direction of KHI wave propagation in regions B and C; namely

that propagation at angles exactly perpendicular to the background magnetic field, which in our case are exactly perpendicular to the magnetopause, is not possible. This agrees with observations of KHI wave propagation shown by *Foullon et al.* [2008], where the direction of observed KHI waves in region C varied between $50° - 86°$ either propagating sunward or anti-sunward (see table 5 in their paper). We summarize in the form of a schematic, the general behavior of unstable primary and secondary KHI surface waves along the magnetopause in Figure 3.1. overhere

3.2.5   Discussion and Conclusions

In this paper, we have investigated the primary and secondary KHI surface wave phenomena in a warm homogeneous plasma in three regions of the magnetosphere, regions A, B and C as shown in Figure 3.1. Our results show that the exclusion of the KH upper cut-off speed in a bounded magnetosphere is due to the interaction of magnetospherically reflected waves with the shear flow magnetopause boundary. In this case, unlike for an unbounded semi-infinite shear flow region, the unstable KH surface modes no longer occur in complex conjugate pairs. In the semi-infinite magnetosphere, wave-wave interactions between the two complex conjugate pairs of modes, an exponentially growing and a decaying mode, are always allowed. These wave pairs have equal phase velocities and thus they can interact with each other throughout the KH unstable intervals. Since the linear and symmetric two wave mode interactions are not present in the bounded magnetosphere case due to the effects of the waves reflected from the inner boundary, the upper cut-off stabilization does not take place anymore.

We identified the MHD surface waves as fast and slow waves by comparing their phase speed to the Alfvén speed through Friedrichs diagrams, i.e, phase velocity diagrams with respect to the direction of the background magnetic fields. On the dayside magnetosphere flanks, MHD waves are allowed to propagate in all directions. On the night-side magnetosphere flanks and in the magnetotail, waves cannot propagate exactly perpendicular to the magnetic field. They propagate in either sunward or anti-sunward directions and and have the general characteristics of a fast mode but which cannot propagate exactly perpendicular to the background magnetic field and which we have

described as intermediate-fast.

The Doppler shifted frequencies of the primary and the secondary KH unstable surface waves are found to always have negative values. However, in contrast with [*Cairns*, 1979; *Mills et al.*, 1999; *Taroyan and Erdélyi*, 2002, 2003a, b], our results indicated that linear interaction of a negative energy wave with a positive energy wave is not a necessary condition for the onset of the KHI. This is consistent with our suggestion that the onset of the KHI in the general case is not related to wave-wave interactions between complex conjugate pairs but to the extraction of energy by the wave from the background flow. This supports the suggestion by *Walker* [2000] that interestingly, the process of energy extraction from the shear flow is better described using the concept of work done by Maxwell and Reynolds stresses rather that in terms of negative energy waves. Further investigation of the relation between KH unstable MHD modes and energy exchange between the MHD wave modes and the background flow arising from work done by Maxwell and Reynolds stresses is left as a future work.

The behavior of the primary and the secondary KHI unstable surface waves on the magnetopause is summarized in Figure 3.1. The phase velocity of the primary unstable KH waves have a large component perpendicular to the magnetopause once they become unstable. The group velocities show that energy propagation by unstable primary KHI wave modes is possible at all propagation angles, except for a very narrow range of the propagation angles close to 90° in regions B and C. Therefore this wide range of the energy propagation angles shows that the energy propagation is likely to be more efficient when the primary KHI is active on the magnetopause. Regions B and C generally have background flow in the magnetosheath above the lower cut-off speed of the primary KHI, such that these regions are more liable to the primary KHI than region A. Energy transport into the magnetosphere from the magnetosheath are hence likely to be more efficient in regions B and C than in region A. The secondary unstable KH modes also have a finite but smaller perpendicular phase speed after the onset of the KHI. However, the value of this perpendicular component decreases with increasing flow speed above the peak value of the growth rate. Since the flow velocity in the magnetosheath in region A is mostly in the range of the lower cut-off velocity for the secondary KHI, the energy propagation via KHI in this region is mostly possible only with the secondary

KHI waves. Comparison of our results to previously published in-situ observations of the KHI surface waves also shows that the primary KHI is mostly possible on the night-side flanks and in the magnetotail, i.e, in regions B and C in Figure 3.1. In contrast, likely only the secondary KHI is possible in region A. Therefore, the energy transport into the magnetosphere from the magnetosheath is more efficient on the night-side flanks and in the magnetotail, in regions B and C, than in the nearer noon dayside flanks, in region A.

Overall, the energy transport arising from the primary KH unstable surface wave is found to be more efficient than the secondary KHI, since the primary KHI waves have larger growth rates and larger phase speeds perpendicular to the magnetopause than the secondary KHI waves. On the magnetospheric side of the magnetopause, the primary KHI is caused by a fast wave and the secondary KHI is caused by a slow wave which is consistent with our results showing that the secondary KH unstable surface wave generally propagates energy at a smaller range of propagation angles than the primary KHI surface wave.

Future studies could examine the evolution of the KHI including the effects of a finite transition thickness layer at the magnetopause boundary, which would allow one to look at the waves at shorter wavelengths. This would help to develop a better understanding of the KHI phenomenon of magnetopause surface waves across a wider range of wavelengths. Allowing inhomogeneities in the magnetosphere would also provide better physical information on characteristics of the wave propagation into the magnetosphere, and an examination of the efficiency of the primary and secondary KHI in driving field line resonances in the magnetosphere. Finally, as discussed by *Mann et al.* [1999], the KHI may also be able to excite body (waveguide) modes in a bounded magnetosphere in addition to the surface waves examined here. The role of primary and secondary KHI in exciting KH unstable waveguide modes remains a subject for further study.

Chapter 4

Kelvin-Helmholtz Unstable Magnetotail Flow Channels

4.1 Introduction

Kelvin-Helmholtz Instability is possible in different regions of the magnetosphere where shear flow boundaries exist. In the plasmasheet region for instance, it is possible to obtain Earthward flow of plasmas reaching up to 1500 km/s called Bursty Bulk Flows (BBFs) [c.f., *Angelopoulos et al.*, 1997; *Shiokawa et al.*, 1997]. The (BBFs) occur in narrow regions, $\simeq 2 - 3R_E$ along y_{GSM} and $\simeq 1.5 - 2R_E$ along z_{GSM}, of the central plasmasheet which are called BBF channels [c.f., *Angelopoulos et al.*, 1992, 1994; *Nakamura et al.*, 2004]. Outside of these flow channels there is relatively slow plasma flow ($\simeq 10 - 100$ km/s) which provides a very efficient shear flow boundary for the KHI growth. These BBFs are usually generated at distances $\simeq -20R_E$ x_{GSM} and stopped closer to the Earth, $\simeq -6R_E$ x_{GSM}, and the reason of this stopping is not clearly explained [c.f., *Shiokawa et al.*, 1997; *McPherron et al.*, 2011]. There are also observations of waves emitted from these BBF shear flow boundaries [*Sergeev et al.*, 2006; *Zhang et al.*, 2002, 2005; *Runov et al.*, 2003; *Volwerk et al.*, 2003, 2005] which are suggested to be possibly related to KHI [*Volwerk et al.*, 2007, 2008]. We refer the reader to chapter 1 section 1.5 for general properties of the plasmasheet region and section 1.6.3 for description of GSM coordinate system (see also Figures 1.2 and 1.3).

In this chapter, the KHI of the magnetotail BBF channels is investigated with compressible warm plasma approach. Two types of possible MHD oscillations, kink and sausage, are investigated for the KHI. The primary and secondary KHI are shown to be possible at sufficiently high flow speeds for both kink and sausage type oscillations. The primary and secondary kink and sausage KHI waves are shown to be fast and slow MHD waves respectively. These MHD waves are shown to be propagating out of the flow channel boundary at sufficiently large flow speeds and carry the flow energy out of the channel. We conclude that this mechanism is a situation of spontaneous emission of magnetosonic waves from a shear flow boundary in the magnetotail and could be a reason for the flow breaking in the near Earth region. The results shown in this chapter contribute to the area of research as the first theoretical study demonstrating the existence of the KHI and magnetosonic (MHD) wave emissions as a result of the KHI on the BBF channel boundaries in the Earth's plasmasheet and is published in Geophysical Research Letters, 2014.

Brief descriptions of derivations can be found in this chapter, however detailed derivations are shown in chapter 2 and section 2.3.1. The following section provides the details of the published paper which was chosen as a spotlight paper with innovative ideas by American Geophysical Union: [1]

4.2   Paper 2: "Kelvin-Helmholtz Unstable Magnetotail Flow Channels: Deceleration and Radiation of MHD Waves"

4.2.1   Abstract

The Kelvin-Helmholtz Instability (KHI) of magnetotail flow channels associated with bursty bulk flows (BBFs) is investigated. MHD oscillations of the channel in both kink and sausage modes are investigated for KHI and both the primary and secondary KHI are found to drive MHD waves. These instabilities are likely to be important for flow channel braking where the KHI removes energy from the flow. At flow speeds above the peak growth rate, the MHD modes excited by KHI develop from surface modes into propagating modes leading to the radiation of

MHD waves from the flow channel. The coupling of BBF driven shear-flow instabilities to MHD waves presented here represents a new paradigm to explain BBF excitation of tail flapping. Our model can also explain, for the first time, the generation mechanism for the observations of waves propagating towards both flanks and emitted from BBF channels in the magnetotail.

4.2.2 Introduction

Earthward Bursty Bulk Flows (BBFs) with flow speeds varying between $200-1500$ km/s have been observed in the central plasmasheet for decades [e.g., *Baumjohann et al.*, 1990; *Angelopoulos et al.*, 1992, 1997; *Shiokawa et al.*, 1997]. These BBFs start at distances $x_{GSM} \lesssim -20R_E$ and are stopped at distances about $x_{GSM} \simeq -6R_E$ [e.g., *McPherron et al.*, 2011]. The details of the braking mechanism of these Earthward BBFs remains unclear with deceleration due to magnetic field dipolarization [e.g., *Shiokawa et al.*, 1997] or due to Kelvin-Helmholtz instabilities [e.g., *Volwerk et al.*, 2007] both having been postulated. Both kink and sausage type oscillations of the current sheet, propagating either along the magnetotail or towards the tail flanks, are also often observed; these flankward waves having been suggested as being driven by a poorly understood emission process in the central part of the magnetotail [e.g., *Sergeev et al.*, 2004]. Observations have suggested that such oscillations may be initiated by Earthward BBFs in the central plasmasheet [e.g., *Volwerk et al.*, 2005] and the boundaries of the BBFs may possibly be Kelvin-Helmholtz unstable [e.g., *Volwerk et al.*, 2007]. However, theoretical details of the relationship between the wave excitation, especially those propagating towards both flanks, and the BBFs have not been established.

In this paper we investigate the excitation of MHD waves by the Kelvin-Helmholtz Instability (KHI) on flow channels in the plasmasheet, such as Earthward BBFs, following the suggestion by *Volwerk et al.* [2007, 2008]. Our results show that both slow and fast kink and sausage MHD waves may become KH unstable at sufficiently fast flow speeds, resulting in the primary and secondary KHI, respectively [cf. *Turkakin et al.*, 2013]. We further investigate the possibility that the KHI may cause the emission of MHD waves from the shear flow boundary in a similar manner to that suggested by *Mann et al.* [1999] as applied to the magnetopause. Our results are significant as the first numerical results showing not only that the KHI is a plausible physical mechanism for braking BBFs, but also that the emission of MHD waves from the flow channels can be triggered by KHI process. Our results can provide for the first time an explanation for

the observations of flankward propagating waves, sometimes described as tail flapping, which can be emitted from such flow channels in the magnetotail [cf. *Sergeev et al.*, 2004; *Volwerk et al.*, 2005]. Two earlier models of magnetic double gradient and ballooning instability waves in a curved magnetic field were suggested by *Erkaev et al.* [2008] and *Golovchanskaya and Maltsev* [2005] to explain tail flapping modes. However as described by *Forsyth et al.* [2009]: *"Neither of the models considers the generation mechanism for the flapping motion of the plasma sheet, only the mechanism that supports the wave propagation"*. Our paper provides the first theoretical framework which explains the link between BBFs, KHI, and the excitation of wave modes such as tail flapping by tail flows. It is also the first to consider MHD wave emission from the flow channel towards the flanks, excited by shear flow KH instability.

4.2.3   Flow Channel Model Geometry and Boundary Conditions

A simplified 1-D flow channel model is used consisting of a plasmasheet flow channel separated by a thin boundary from a semi-infinite plasmasheet. Since the magnetic field orientation is mainly along x_{GSM} in the magnetotail, this model provides a good approximation to the tail[c.f. *Sergeev et al.*, 2004]. A box model whose coordinates are analogous to GSM, Geocentric Solar Magnetic, coordinate system is used. The y coordinate has flow channel boundaries at $y = \pm d$ as illustrated in Figure 4.1. Region 1 represents the external magnetotail plasmasheet and region 2 represents the flow channel. The background magnetic fields in regions 1 and 2, $B_{01,02}$, are set parallel to the flow channel boundary and the background flow velocity, U_{01}, is set to zero and $U_{02} > 0$ directed along positive x. Since the wave behavior of kink and sausage waves analyzed here is symmetric about $y = 0$, we have considered a domain assumed to be half of the flow channel for $y > 0$. We adopt a symmetric inner boundary in the mid-channel, and half-channel width of d. A tangential discontinuity (TD) with zero transition thickness is assumed at $y = d$ which is a valid model for long-period KHI waves with wavelengths much larger than the thickness of the transition layer.

4.2.4   MHD Wave Model

We follow the standard approach where the ideal MHD equations are linearized under a small amplitude approximation for compressible warm homogeneous plasmas on both sides of the flow channel boundary. We have assumed space and time variation of the form $\simeq De^{i(\mathbf{k}\cdot\mathbf{r}-\omega t)}$, where

ω is the complex frequency, $\mathbf{k}$ is the wave number, and D is a constant.

We consider two types of MHD wave modes, kink and sausage surface waves, that are observed along the plasmasheet flow channel boundaries [e.g., *Sergeev et al.*, 2003; *Volwerk et al.*, 2005]. The sausage modes are characterized by expansion and contraction and the kink modes are characterized by wavy flapping motion of the flow channel [cf., *Roberts*, 1991]. The general oscillation characteristics of the kink and sausage modes are illustrated in the top right corner of Figure 4.1.

MHD wave solutions in regions 1 and 2 are connected through TD boundary conditions namely continuity of normal displacement, δy, and total pressure perturbations, δp_t, across the flow channel boundary. Therefore matching conditions across the boundary between region 1, and 2 are $\delta p_{t1} = \delta p_{t2}$, and $\delta y_1 = \delta y_2$. The inner boundary conditions in the mid-channel, $y = 0$, are different for the kink and sausage modes, since the kink modes will have an anti-node and sausage modes will have a node at this position. Hence the boundary condition at $y = 0$ for the kink modes is $\frac{d\delta v_{y2}}{dy} = 0$, from which it follows that $\delta p_{t2} = 0$, and those of sausage modes are $\delta v_{y2} = 0$, and $\frac{d\delta p_{t2}}{dy} = 0$, where δv_{y2} is the perpendicular velocity perturbation in the flow channel, region 2. With the above boundary conditions MHD kink modes are governed by the equation

$$i \cot(k_{y2} d)[(\omega_1')^2 - (\mathbf{V}_{A1} \cdot \mathbf{k}_t)^2]\frac{\rho_{01}}{k_{y1}} + [(\omega_2')^2 - (\mathbf{V}_{A2} \cdot \mathbf{k}_t)^2]\frac{\rho_{02}}{k_{y2}} = 0, \qquad (4.1)$$

and MHD sausage modes are governed by the equation

$$i \tan(k_{y2} d)[(\omega_1')^2 - (\mathbf{V}_{A1} \cdot \mathbf{k}_t)^2]\frac{\rho_{01}}{k_{y1}} - [(\omega_2')^2 - (\mathbf{V}_{A2} \cdot \mathbf{k}_t)^2]\frac{\rho_{02}}{k_{y2}} = 0. \qquad (4.2)$$

Where $\omega_{1,2}' = \omega - \mathbf{U}_{01,02} \cdot \mathbf{k}_t$ are the Doppler shifted frequencies, $\mathbf{V}_{A1,A2}$ are the Alfvén speeds, and $k_{y1,y2}$ are wave numbers normal to the boundary, in regions 1 and 2, respectively.

The eigenfrequencies of equations 4.1 and 4.2, representing kink and sausage wave modes respectively, are computed numerically using a Newton-Raphson scheme, yielding complex eigenfrequencies for a set of given parameters. In the following sections of the paper normalized flow velocities $V_{01,02}$ are used such that $V_{01,02} = U_{01,02}/V_{A2}$ with normalization with respect to the Alfvén speed, V_{A2}, in the flow channel, region 2. The distance, d, is normalized by R_E, and wavenumbers, k_x, k_y, are normalized by $1/d$. Normalized frequencies are; real frequencies $\omega_r d/V_{A2}$ and growth rates $\omega_i d/V_{A2}$. Assuming hydrogen plasma, the background physical pa-

rameters are set such that densities $\rho_{01}/\rho_{02} = 0.75$, $B_{01}/B_{02} = 1.8$, $V_{A1}/V_{A2} = 2.1$, $\beta_1 = 0.78$,

and $\beta_1 = 4.88$ which are observable values in the plasmasheet regions [e.g., *Angelopoulos et al.*,

1992; *Volwerk et al.*, 2007, 2008]. The adiabatic index γ is taken as $5/3$, and $d = 2R_E$ which is

an appropriate value for flow channel half thickness [c.f., *Nakamura et al.*, 2004]. A normalized

tangential wave number is chosen such that one wavelength would fit in the half flow channel,

$k_t = 2\pi/d$, and directed along $+x$, $k_t = k_x$, and waves propagate in the plane of the tail such

that $k_z = 0$ (see Figure 4.1).
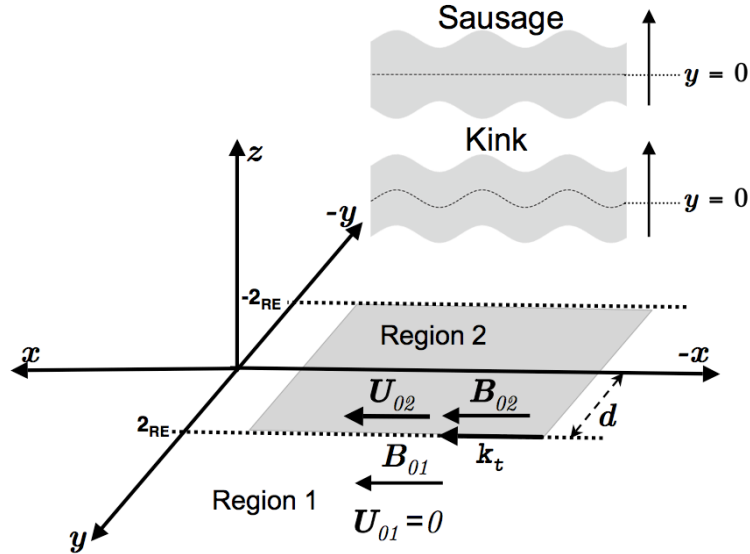
Figure 4.1: Coordinate system considered for calculations of BBF initiated KHI waves. x, y, z coordinate directions are chosen to be analogous to GSM. Region 1 is out of the channel and region 2 is inside the channel. The boundary of the flow channel lies at $y = \pm d = \pm 2R_E$.

4.2.5   Results

The eigenfrequency variation with increasing normalized flow speed, $V_{02} = U_{02}/V_{A2}$, in the

channel is shown in Figures 4.2 (a) and (b), where both kink and sausage modes show two distinct

K-H unstable regions representing primary and secondary KHI [c.f., *Turkakin et al.*, 2013]. The

secondary KHI becomes unstable at lower BBF flows, $V_{02} \simeq 2.8$, than primary KHI, $V_{02} \simeq 3.3$,

which agrees with the results in *Turkakin et al.* [2013]. Figures 4.2 (a) and (b) show that the

primary and secondary sausage modes (red and black solid lines) have slightly larger real fre-
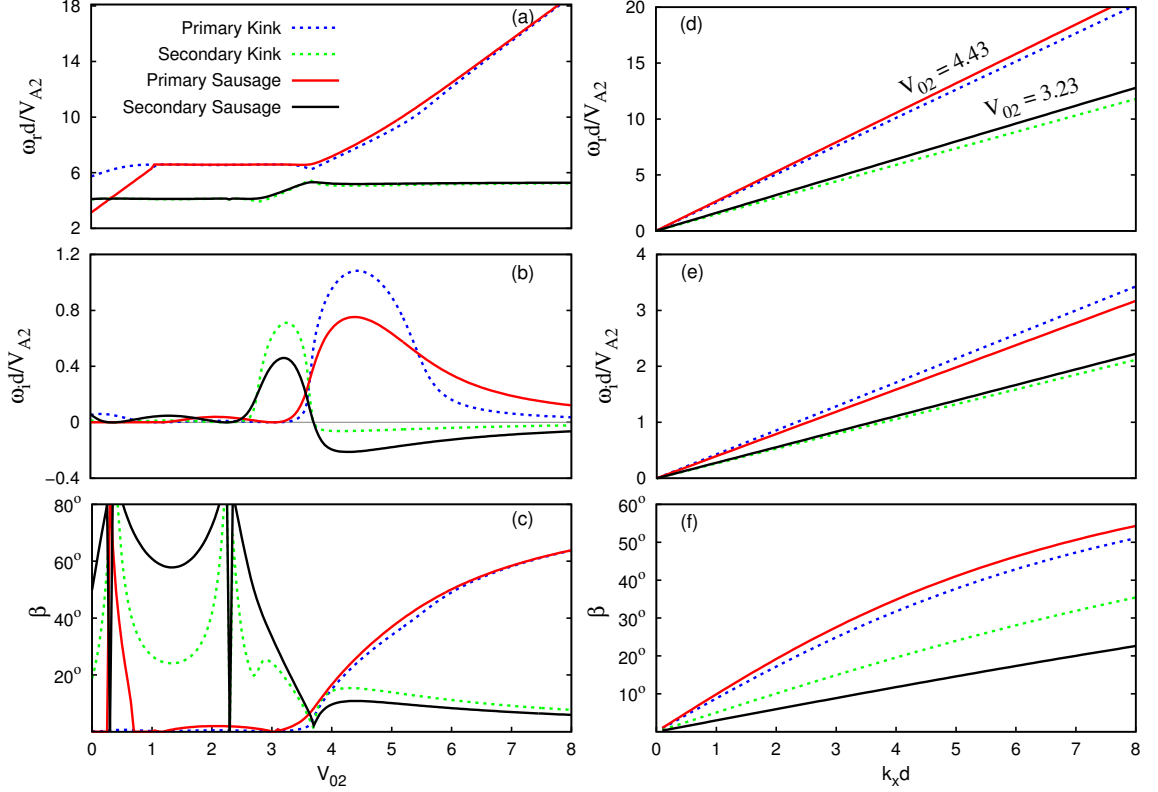
Figure 4.2: The variations of real and imaginary frequencies and the propagation angle as a function of the background flow speed, $V_{02} = U_{02}/V_{A2}$ (panel (a)-(c)) and of the normalized tangential wave number, $k_x d$ (panels (d)-(f)).

quencies and smaller growth rates than the kink modes (blue and green dashed lines). Since the primary KHI onsets occur at larger background flow speeds, V_{02}, it is possible that both primary and secondary KHI may be important during BBF evolution. For example, primary KHI excited kink and sausage modes could be generated during the bursts within the BBFs which can have flow speeds reaching up to 1500 km/s and which last for about 2-4 minutes [c.f., *Angelopoulos et al.*, 1997; *Shiokawa et al.*, 1997]. Secondary KHI kink and sausage modes might be excited more continuously during the core of BBFs where the flow speed can reach up to 700 km/s and last about 10-30 minutes [e.g., *Angelopoulos et al.*, 1992; *Nakamura et al.*, 2004], or at slower speeds during BBF deceleration.

We also calculated the phase velocities, $\mathbf{U_p} = \frac{\omega_r}{(k_x^2 + k_y^2)}\mathbf{k}$, periods, $T_r = 2\pi/\omega_r$, and the propagation angles with respect the background flow, $\beta = \tan^{-1}(k_y/k_x)$ for these modes. Normalized

phase velocities show that the primary kink and sausage modes are fast waves, while the secondary kink and sausage modes are slow waves in the stationary plasma frame in region 1 (not shown here) consistent with the results shown in *Turkakin et al.* [2013]. Variations of propagation angles, β, with background flow are displayed in Figure 4.2 (c) and are found to vary between $\simeq 0° - 64°$ for primary and $\simeq 0° - 40°$ for secondary KHI waves. Sharp peaks in the propagation angles of the secondary KHI waves happen at flow speeds below that for the onset of instability and are the result of a slow resonance [c.f., *Kozlov and Leonovich*, 2011], analysis of which is beyond the scope of this paper. With the use of an appropriate Alfvén speed in the channel as 200 km/s we have calculated the periods and wavelengths of the MHD waves emitted from the BBF boundary. The periods vary between $\simeq 10 - 70$ s and wavelengths vary between $\simeq 2 - 4\ R_E$ for both growing primary and secondary KHI waves. These values are in good agreement with the observed values of the waves along the plasma flow channels [e.g., *Sergeev et al.*, 2003; *Volwerk et al.*, 2004, 2008]. We also investigated the effects of the magnetic tilt along the z_{GSM} direction in the flow channel and found that the growth rates increase with the increasing magnetic tilt (not shown).

We also explored the dependence of the eigenmodes on the normalized tangential wave number, $k_x d$, at a specific BBF speed, selecting $V_{02} = U_{02}/V_{A2} = 4.43$ for primary KHI waves and $V_{02} = U_{02}/V_{A2} = 3.23$ for secondary KHI waves where both kink and sausage modes growth rates are close to maximum (see Figure 4.2 (b)). The results are shown in Figure 4.2 (d)-(f). As expected for a zero thickness boundary, the normalized real frequencies and growth rates of both kink and sausage primary and secondary KHI waves monotonically increase with $k_x d$ [e.g., *Mann et al.*, 1999] (see panel (d) and (e) in Figure 4.2). As $k_x d$ increases, the primary and secondary KHI kink modes propagation direction approach $51°$ and $\simeq 35°$, respectively, while that of the sausage modes approach $\simeq 54°$ and $\simeq 23°$, respectively. This result is in very good agreement with the observed values for the propagation directions of the waves seen in association with BBFs, varying between $\simeq 30° - 48°$ with respect to the flow boundary [e.g., *Sergeev et al.*, 2003; *Volwerk et al.*, 2004, 2008].

Density profiles of the kink and sausage modes reveal that wave propagation away from the flow channel is possible during the KHI process. Figure 4.3 shows eigenmode density profiles for the primary and secondary KHI kink modes, panels (a)-(d), and sausage modes, panels (e)-(g). Panels (a) and (e) display the density profiles of the primary KHI modes at the peak growth

rates, flow speed $V_{02} = 4.45$ for the primary kink mode (panel (a)) and $V_{02} = 4.4$ for the primary sausage mode (panel (e)). Panels (b) and (f) show the profiles at $V_{02} = 5.5$. It is clearly visible
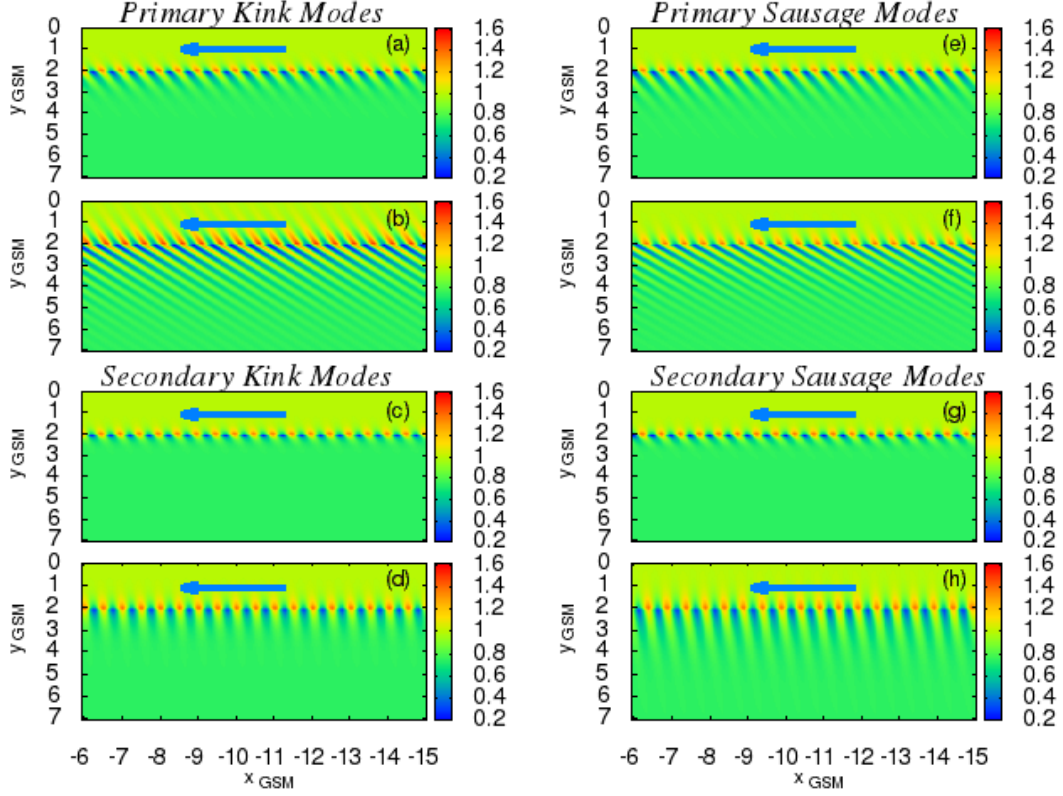
Figure 4.3: Normalized plasma density profiles of the eigenmodes of the primary and secondary kink, panels (a)-(d), and sausage, panels (e)-(h), KHI waves on the flow channel boundary. Panels (a) and (e) show the primary kink and sausage KHI waves at their peak growth rate, $V_{02} = 4.45$ and $V_{02} = 4.4$, respectively. Panels (b) and (f) during MHD wave emission at , $V_{02} = 5.5$. Similarly panels (c) and (g) show the secondary kink and sausage modes at their peak growth rate, $V_{02} = 3.25$ and $V_{02} = 3.2$, respectively, and panels (d) and (h) during period of MHD wave emission for $V_{02} = 3.65$. Emission of MHD waves from the shear flow boundary are visible for $V_{02} \gtrsim 5.5$ for primary KHI and for $V_{02} \gtrsim 3.65$ for secondary KHI.

Figures 4.3 (b) and (f) that both the kink and sausage primary KHI modes excite waves which propagate away from the flow channel at $V_{02} = 5.5$. The secondary kink and sausage mode density profiles are also shown at background flow speeds values at peak growth rates, $V_{02} = 3.25$ for the secondary kink modes (panel (c)) and $V_{02} = 3.2$ for the secondary sausage modes (panel (g)), as well as at a larger flow speed, $V_{02} = 3.65$ (panels (d) and (h)). The secondary KHI modes

are also able to excite waves which propagate out of the flow channel boundary after a certain value of the flow speed is reached. There is a considerable difference however between the flow speed at which the transition from predominantly surface to a propagating mode takes place: $V_{02} = 5.5$ for the primary and $V_{02} = 3.65$ for the secondary KHI. Observations have shown that these normalized flow speed values can be reached during a BBF in the central plasmasheet [c.f. *Angelopoulos et al.*, 1992, and Figure 4 (c) in this paper].

These results illustrate cases of the emission of magnetosonic waves from the boundary of a moving medium [*Landau and Lifshitz*, 1987; *Mann et al.*, 1999] which in the current study are applied to the BBF channel dynamics in the magnetotail and which offer an explanation for the waves observed to be emitted from BBF channels in the central plasmasheet. Our results also suggest that the energy in the BBFs may be fed into primary and secondary KHI kink and sausage modes, including into waves emitted from the flow channels, causing BBF braking in the near-Earth region.

Figure 4.4 displays the spatial variation of the eigenmode profiles across the flow channel boundary at $V_{02} = 5.5$ for the primary KHI modes, and $V_{02} = 3.65$ for the secondary KHI modes where emission of MHD waves from the BBF channel is present (c.f. Figures 4.3 (b), (f), (d) and (h)). What is very clear in Figure 4.4 is that the amplitude of the perturbed velocity and magnetic fields peaks at the shear flow boundary at the edge of the BBF, as expected. Also clear in Figure 4.4 is that there is considerable oscillating eigen-structure as a function of y at constant x for the primary KHI, and not for the secondary KHI, despite propagating MHD waves being emitted from the boundary in both cases. The explanation, of course, relates to the angle of propagation of the phase fronts of the propagating modes outside the BBF in each case. Overall both the primary and secondary KHI kink and sausage modes may be able to extract kinetic energy from the background flow and impact the flow evolution and braking of BBFs as they travel towards the Earth.

We have calculated mode group speeds using the eigenfrequencies and wave numbers obtained above using the equation $U_{gr} = \frac{d\omega}{dk}$. We also calculated the e-folding growth times and distances traveled by wave packets using the group speeds during an e-folding time, i.e. e-folding length, in search of energy dissipation efficiency by the primary and secondary KHI kink and sausage waves.
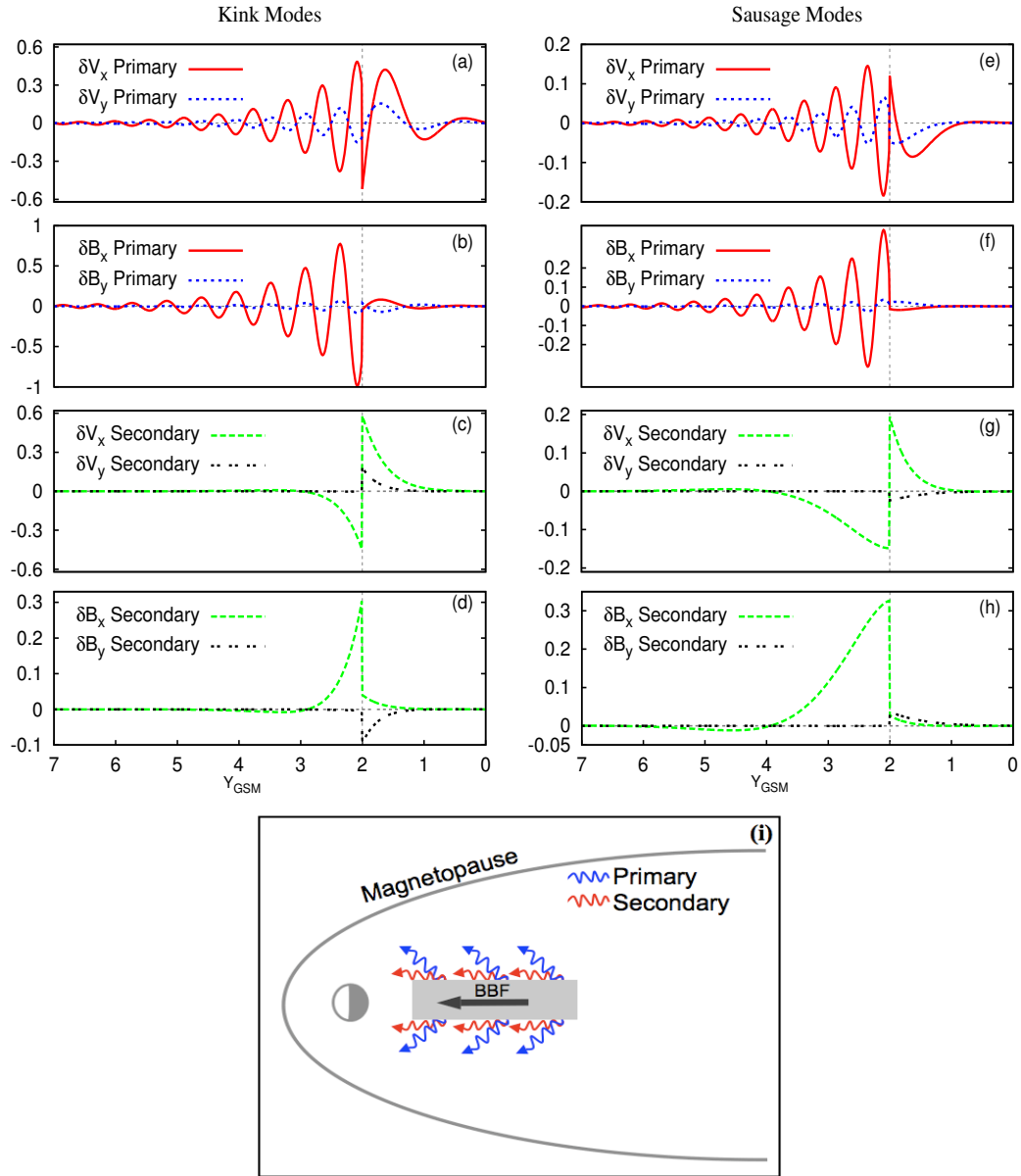
Figure 4.4: The eigenmode profiles of perturbed x and y components of normalized magnetic field and velocity variation across the flow channel boundary for primary and secondary kink (panels (a)-(d)) and sausage modes (panels (e)-(h)). $V_{02} = 5.5$ for the primary modes and $V_{02} = 3.65$ for the secondary modes, with the same parameters as in Figures 4.3 (b) and (f) for the primary, in Figures (d) and (h) for the secondary KHI modes. Panel (i) is the schematic showing the characteristics of the propagation direction of kink and sausage modes which are excited by the KHI at the edges of the BBF channel.

We have again assumed a value of the physical Alfvén speed in the region 2 as 200 km/s and calculated the physical values of e-folding times and e-folding lengths using this Alfvén speed. At the flow speed values for peak growth rates, the primary kink and sausage modes e-folding times are calculated as 58.8 and 84.6 seconds, respectively. Their normalized group speeds, i.e., the speed of energy propagation, $V_{gr} = U_{gr}/V_{A2}$, along the flow are calculated to be 1.84 for the primary kink and 1.82 for the primary sausage waves. With these group speeds the e-folding lengths of the primary kink and sausage wave are calculated to be $\simeq 3.4R_E$ and $\simeq 4.8R_E$, respectively. Therefore, these waves will travel distances $\simeq 7 - 10R_E$ during two e-folding times which is an appropriate distance compared to that which the BBFs generally travel from the tail to the near-Earth region during flow braking. This shows that the primary kink and sausage KHI waves may grow sufficiently fast to be able to dissipate a significant amount of the initially available kinetic energy of the flow causing flow braking in the near-Earth region. The secondary KHI kink and sausage modes are found to have group speeds along the flow as 1.85 and 1.74 at the growth rate peaks and e-folding times of $\simeq 89.5$ and $\simeq 138.4$ seconds resulting e-folding lengths of $\simeq 4.7R_E$ and $\simeq 7.5R_E$, respectively. Therefore, these waves will travel distances $\simeq 10 - 16R_E$ during two e-folding times which could also be appropriate for BBF flow braking. Although not as fast growing as the primary modes, these secondary modes may also grow fast enough to cause flow braking. These results also display the fact that the primary and secondary KHI kink modes can dissipate energy somewhat faster than those of the sausage modes. Since the growth rates increase with increasing angle between the flow and the background magnetic field (not shown), it is possible that as the waves move closer to the Earth, the increase of the magnetic tilt due to the dipolarization might allow strong KHI even in the later stages of BBF evolution. However, at least 2-D simulations would be needed to examine this possibility in detail. Nonetheless, our results strongly suggest that the often observed magnetotail flapping and flankward moving waves can be explained by these primary and secondary KHI radiating MHD waves away from the BBF channels.

4.2.6 Conclusions

In this paper we have presented a theoretical framework for understanding the role of KHI in the evolution and braking of BBF channels in the magnetotail. We have shown for the first time not only that the earthward BBF channels in the central plasmasheet may become unstable

to KHI, but perhaps more importantly proposed an explanation for the observed association between BBFs and MHD waves which propagate towards both flanks. According to our model, this can be explained through the excitation and emission of MHD waves from the BBF shear flow boundaries due to the action of the KHI. At sufficiently high flow speeds these KHI waves may extract kinetic energy from the bulk flow in the BBF channel resulting in the braking of the BBFs closer to the Earth. This is shown schematically in Figure 4.4 panel (i).

Future studies could examine the evolution of the KHI sausage and kink modes along BBF channels including the effects of a finite transition thickness layer at the flow channel boundary, perhaps in 2-D including the effects of the changing magnetic field geometry in the BBF as they approach the Earth, which would help to develop a better understanding of the phenomenon across a wider range of wavelengths. Nonlinear studies of the KHI waves along the flow channel boundary could also shed more light especially on the role of the KHI in the evolution and braking of BBFs in the nightside plasmasheet.

4.3   Appendix

Additional figures that were not included in the paper due length restrictions are included in this section.

Figure 4.5 shows the effect of dipolarization on the KHI along BBFs. In Figure 4.5 the panels (a) and (b) show the real frequency and growth rates for the KHI kink modes and panels (c) and (d) show the real frequency and growth rates for the KHI sausage modes. It is displayed in Figure 4.5 that with the increase of the magnetic field tilt inside the BBF channel the growth rates of both the primary and the secondary kink and sausage KHI waves become larger. The real frequencies, however, do not change significantly.

Figure 4.6 shows the phase velocity values of the primary and the secondary kink and sausage KHI waves. It is displayed in the Figure 4.6 that the primary/secondary kink and sausage KHI modes phase velocities are in the range of the fast/slow MHD wave phase velocities.
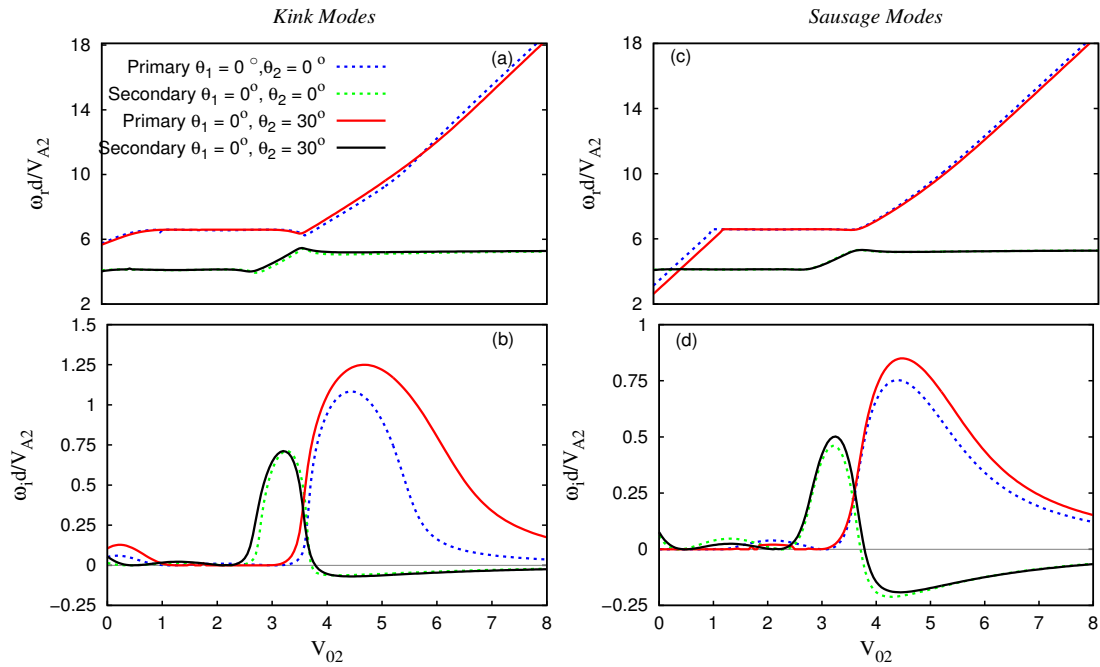
Figure 4.5: Variation of real frequencies and growth rates with the magnetic tilt. Growth rates increase with the magnetic tilt while there is not a significant change in the real frequencies. The change in the real frequencies and the growth rates become more significant with bigger magnetic tilts.
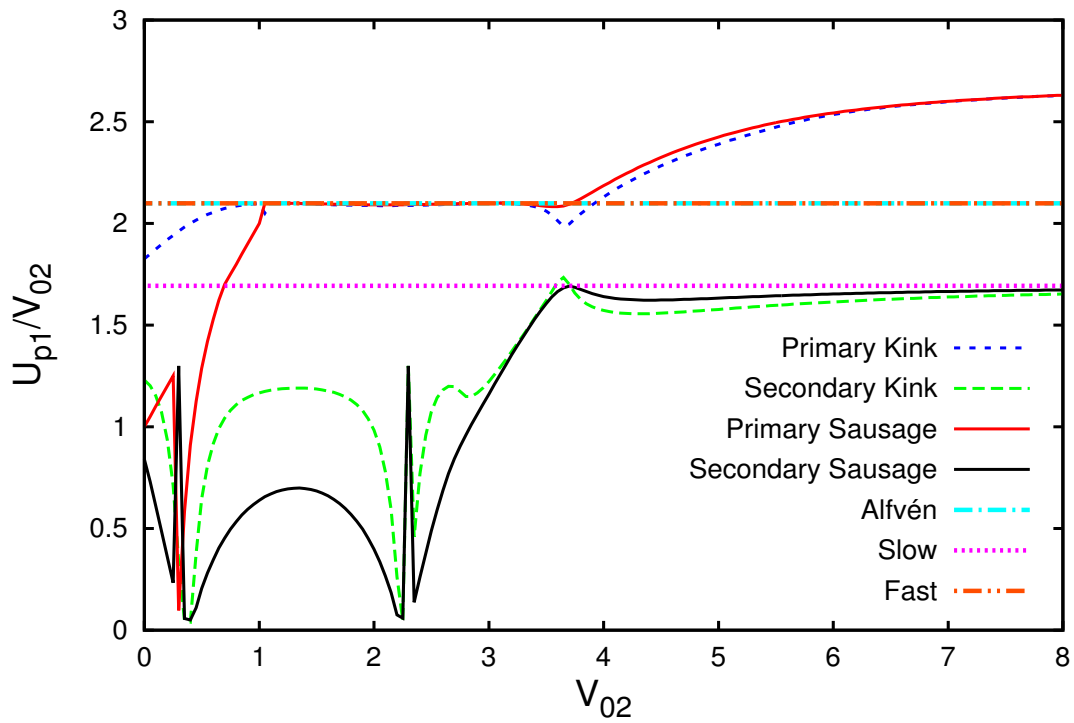
Figure 4.6: Variation of total phase velocity vs. BBF flow speed in the stationary frame of reference, region 1 - out of the flow channel. The primary kink and sausage KHI waves phase velocities are in the range of the fast MHD wave. The secondary kink and sausage KHI waves phase velocities approach to the slow MHD waves. Sharp peaks are due to the slow resonances which are out of the scope of this study.

Chapter 5

Effects of Finite Boundary Thickness on KHI

5.1   Introduction

We have used the zero boundary thickness assumption so far in our calculations. This assumption is valid only for waves with wavelengths considerably larger than the thickness of the boundary. It is possible to obtain waves with wavelengths comparable to the thickness of the shear flow boundaries in which case the boundary should be assigned a finite thickness. In this Chapter we have investigated the effects of a finite thickness boundary on the KHI and MHD wave emission. We give a brief explanation of the equations used and refer the reader to Chapter 2, Section 2.3.2 for a detailed description. Work done in this Chapter is submitted to the Journal of Geophysical Research as a paper. Following Section provides the details of the submitted paper: [1]

---

[1]Turkakin, H., Rankin, R. and Mann, I.R., "Emission of Magnetosound From MHD-Unstable Shear Flow Boundaries, Journal of Geophysical Research, 2014

5.2 Paper 3: "Emission of Magnetosound From MHD-Unstable Shear Flow Boundaries"

5.2.1 Abstract

The emission of propagating MHD waves from flow channels that are unstable to the Kelvin-Helmholtz Instability (KHI) in magnetized plasma is investigated. The KHI and MHD wave emission are found to be two competing processes. It is shown that the fastest growing modes of the KHI surface waves do not coincide with efficient wave energy transport away from a velocity shear boundary. MHD wave emission is found to be inefficient when growth rates of KHI surface waves are maximum, which corresponds to the situation where the ambient magnetic field is perpendicular to the flow channel velocity vector. The efficiency of wave emission increases with increasing magnetic field tension, which in the Earth's magnetosphere dominates along the nightside magnetopause, within Bursty Bulk Flows (BBFs) in the inner plasma sheet, and in the solar corona dominates in Supra-Arcade Downflows (SADs). Our results suggest that efficient emission of propagating MHD waves along BBF and SAD boundaries can contribute to explaining the observed deceleration and stopping of BBFs and SADs.

5.2.2 Introduction

Kelvin-Helmholtz Instability (KHI) is a type of instability that may occur along hydrodynamic and magnetohydrodynamic (MHD) shear flow boundaries. Due to its significant effects on fluid mixing and energy and momentum transfer in-between two different flowing media, the KHI has been studied extensively in both hydrodynamic [e.g., *Lawrence et al.*, 1991; *Malik et al.*, 1994; *Jean and Laurent*, 2000] and magnetohydrodynamic (MHD) [e.g., *Walker*, 1981; *Miura and Pritchett*, 1982; *Pu and Kivelson*, 1983a; *Taroyan and Erdélyi*, 2003a; *Lai and Lyu*, 2006] limits. The evolution of the KHI is more complex in the presence of magnetic fields and ionized media [*Taroyan and Ruderman*, 2011] because magnetic pressure and tension forces act on the flowing plasma in a variety of ways different from the hydrodynamic case. With the inclusion of ambient magnetic fields, magnetic pressure and tension forces combined with non-magnetic forces introduce new types of waves resulting in more complex interactions between the flow and perturbations [*Taroyan and Ruderman*, 2011]. A component of the background magnetic field

parallel to the shear flow boundary inhibits the evolution of KHI. With larger parallel component of the ambient magnetic field, the cut-off speed at which KHI onset occurs increases and the strength of the growth decreases [e.g., *Miura and Pritchett*, 1982; *Pu and Kivelson*, 1983a; *Mann et al.*, 1999].

Studies have been performed on the characteristics of the linear [*Walker*, 1981; *Miura and Pritchett*, 1982; *Pu and Kivelson*, 1983a; *Taroyan and Erdélyi*, 2002] and nonlinear [*Miura*, 1982; *Rankin et al.*, 1997; *Lai and Lyu*, 2006, 2008] evolution of MHD KHI. Several important aspects of the KHI have been discovered, such as the possibility for driving field line resonances [*Southwood*, 1974; *Walker*, 1981], causing magnetic reconnection during northward Interplanetary Magnetic Field (IMF) [*Fairfield et al.*, 2000; *Takagi et al.*, 2006], and carrying energy and momentum across the magnetopause boundary [*Hasegawa et al.*, 2006; *Taroyan and Ruderman*, 2011].

Some studies have assumed a zero thickness boundary, which is appropriate if the wavelengths of the generated waves are significantly larger than the thickness of the boundary [*Pu and Kivelson*, 1983a; *Mann et al.*, 1999; *Turkakin et al.*, 2013, 2014]. The effects of a finite boundary thickness have also been investigated in several studies [*Ong and Roderick*, 1972; *Walker*, 1981; *Farrugia et al.*, 1998; *Contin et al.*, 2003; *Gratton et al.*, 2004]. The main effect of including a finite thickness boundary is that the growth rates become small at finite values of the tangential wavenumber [*Walker*, 1981; *Miura and Pritchett*, 1982; *Gratton et al.*, 2004].

The KHI is also an important process along the interface of the heliopause, in the solar atmosphere and in remote astrophysical objects such as accretion disks near neutron stars and black holes [*Taroyan and Ruderman*, 2011]. The KHI is suggested to be possible in solar plumes leading to the disruption and mixing of plumes with interplume plasma [e.g., *Andries and Goossens*, 2001]. The Atmospheric Imaging Assembly (AIA) on board the Solar Dynamics Observatory (SDO) and the Large Angle and Spectrometric Coronograph Experiment (LASCO) on board the Solar and Heliospheric Observatory (SOHO) have observed occurrences of KHI in the solar corona at velocity shear boundaries including the flanks of high speed Coronal Mass Ejections (CMEs) [*Liu and Ofmann*, 2006; *Foullon et al.*, 2011, 2013; *Möstl et al.*, 2013], solar prominences, and high-corona streamers [*Feng et al.*, 2013]. *Liu and Ofmann* [2006] have also reported observations of KHI and associated waves in the solar corona. Several numerical studies have also investigated the KHI along the boundaries of CMEs [*Foullon et al.*, 2013; *Möstl et al.*, 2013; *Nykyri and Foullon*, 2013], Supra-Arcade Downflows (SADs) [*Cécere et al.*, 2014], coronal plumes

[*Andries and Goossens*, 2001] and coronal streamers [*Feng et al.*, 2013].

Surprisingly, the emission of propagating MHD waves from a shear flow boundary as an effect of the KHI has received little attention. The spontaneous emission of sound waves between two counter-streaming media was first suggested by *Landau and Lifshitz* [1987] as propagating small perturbations in a medium moving with relative supersonic velocities. *Mann et al.* [1999] have suggested that at sufficiently large magnetosheath flow speeds, overreflected surface modes may turn into body modes and carry energy into the magnetosphere. This situation was suggested to be a representation of emission of magnetosound from the boundary of a moving medium. Planar waves moving away from KHI vortices have been reported in a few studies in the past [*Lai and Lyu*, 2006, 2008]. In these studies propagating waves are attributed to nonlinear processes and no connection between them and the linear growth of the KHI was inferred. *Turkakin et al.* [2014] have shown that KHI and MHD wave emission due to KHI may occur along the boundaries of Bursty Bulk Flows (BBFs) in the central plasmasheet of the Earth. These KHI emitted waves are suggested to be a possible means of carrying available energy out of BBF channel boundaries and stopping the BBFs in the near Earth regions.

In the current study, emission of MHD waves from a shear flow boundary is shown to exist during the linear stages of the KHI evolution. The relation between the emission of propagating magnetosonic waves, the growth rates of KHI surface waves, and their wavenumbers is clearly described. Linear MHD theory is used to compute the KHI growth rates of the MHD modes supported by a shear flow boundary with a nonzero thickness. The effects of background magnetic field directions on magnetosonic wave emission is investigated in detail. The results are used to predict the efficiency of MHD wave emission along shear flow boundaries in the magnetospheric regions of Earth - along the magnetopause and the edges of BBF channels. The possibility of spontaneous MHD wave emission due to KHI along shear flow boundaries in the solar corona, such as SADs and CMEs, is also discussed.

5.2.3 Boundary Layer Model and KHI Dispersion Relation

A 1-D simplified model of a shear flow boundary is considered consisting of two semi-infinite plasma regions separated by a boundary layer region of thickness $\Delta_x = 2h$. All zero-order quantities are assumed to vary only along the x-direction. Figure 5.1 shows a schematic of the model, which represents the change of $\rho_0, \mathbf{B_0}$, and P_0 with discontinuous jumps over an interface
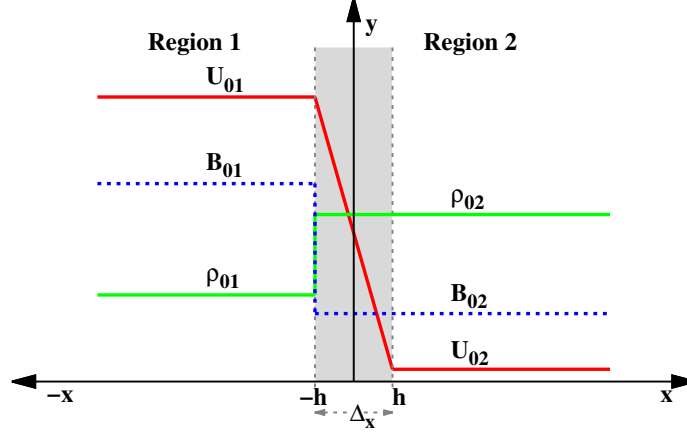
Figure 5.1: Schematic of the MHD boundary layer model used. $\Delta_x = 2h$ is the boundary layer thickness. The background values of magnetic fields, B_{01}, B_{02} and densities, ρ_{01}, ρ_{02} are varied sharply at $x = -h$. Velocity, $U_0(x)$, connects two intervals of constant values U_{01} and U_{02} with a linear function in the transition layer region such that $U_0(x) = \frac{U_{01}}{2}\left(1 - \frac{x}{h}\right) + \frac{U_{02}}{2}\left(1 + \frac{x}{h}\right)$.

of zero thickness at $x = -h$ and a continuous variation of $\mathbf{U}_0$ over a thickness of Δ_x. Here, $\rho_0, P_0, \mathbf{B_0}$, and $\mathbf{U}_0$ are background values of density, plasma pressure, magnetic field, and flow velocity, respectively. The background magnetic field is assumed to lie in the tangent plane of the boundary, i.e., the $y - z$ plane. The zero-order streaming velocity is assumed to have the same direction everywhere. Without loss of generality this is taken as the y direction. The values of U_0 are set to constant values of U_{01} in region 1 and U_{02} in region 2, and vary as $U_0(x) = \frac{U_{01}}{2}\left(1 - \frac{x}{h}\right) + \frac{U_{02}}{2}\left(1 + \frac{x}{h}\right)$ in the transition layer region. This set up is applicable to different MHD shear flow boundaries, such as Earth's magnetopause, BBF channels in the central plasmasheet [e.g., *Turkakin et al.*, 2014] and shear flow boundaries in the solar corona [*Andries and Goossens*, 2001; *Foullon et al.*, 2011; *Ofman and Thompson*, 2011; *Foullon et al.*, 2013; *Nykyri and Foullon*, 2013; *Cécere et al.*, 2014].

The stability of the boundary defined above is studied with linearized ideal MHD assuming small amplitude perturbations in warm compressible homogeneous plasmas in regions 1, 2 and the boundary layer region. Perturbations are assumed to be of the form $\delta g(\mathbf{r}, t) = g(x)e^{i(\mathbf{k}_t \mathbf{r} - \omega t)}$, where g is any perturbed quantity, $g(x)$ is the corresponding amplitude, ω is the complex frequency, and $\mathbf{k}_t = (k_y, k_z)$ is the tangential wavenumber.

Linearization of the warm compressible ideal MHD equations results in the following equation for the amplitude of the plasma displacement, δx;

$$\frac{\partial}{\partial x}\left(\chi\frac{\partial \delta x}{\partial x}\right) - \Omega \delta x = 0. \tag{5.1}$$

The function Ω in Equation 5.1 is defined as $\Omega = \rho_0\left[\omega'^2 - (\mathbf{V}_A \cdot \mathbf{k}_t)^2\right]$, $\chi = -\Omega/k_x^2$. k_x is the complex wavenumber normal to the boundary, defined by,

$$k_x = \left(\omega'^4/[\omega'^2(V_A^2 + C_S^2) - (\mathbf{V}_A \cdot \mathbf{k})^2 C_S^2] - k_t^2\right)^{1/2}. \tag{5.2}$$

Here, $V_A = B_0/\sqrt{\rho_0\mu_0}$ is the Alfvén speed, $C_S = \sqrt{\gamma P_0/\rho_0}$ is the sound speed, and $\omega' = \omega - \mathbf{U}_0 \cdot \mathbf{k}$ is the Doppler shifted frequency. The detailed derivation of equation 5.1 can be found in *Walker* [1981].

Equation 5.1 is applicable to regions 1, and 2, and the boundary layer region. Following the standard approach used in previous studies [cf., *Chandrasekhar*, 1961; *Roberts*, 1991; *Gratton et al.*, 2004], the solution to equation 5.1 in these regions is chosen as;

$$
\begin{aligned}
\delta x_1 &= A_1 e^{ik_{x1}x}, & x \leq -h \\
\delta x_{bl} &= A_2 e^{ik_{xbl}x} + A_3 e^{-ik_{xbl}x}, & -h < x < h \\
\delta x_2 &= A_4 e^{ik_{x2}x}, & x \geq h
\end{aligned}
\tag{5.3}
$$

The subscripts 1 and 2 correspond to regions 1 and 2, respectively. The boundary layer values are symbolized as δx_{bl} and k_{xbl}. The solutions in regions 1 and 2 have been so chosen that perturbations vanish at $+\infty$ and $-\infty$. This brings the choice of the imaginary parts of the perpendicular wavenumbers as negative in region 1, $k_{x1i} < 0$, and positive in region 2, $k_{x2i} > 0$. Boundary conditions corresponding to a tangential discontinuity, namely continuity of the displacement and total pressure are applied to the boundaries at $x = \pm h$, resulting in the following matching conditions;

$$\chi_1 \frac{\partial \delta x_1}{\partial x} = \chi_{bl}\frac{\partial \delta x_{bl}}{\partial x}, \qquad \delta x_1 = \delta x_{bl}, \qquad x = -h \tag{5.4}$$

$$\chi_{bl}\frac{\partial \delta x_{bl}}{\partial x} = \chi_2\frac{\partial \delta x_2}{\partial x}, \qquad \delta x_{bl} = \delta x_2, \qquad x = h \tag{5.5}$$

Applying matching conditions in equations 5.4 and 5.5, we obtain four linear equations for four unknown constants, A_1, A_2, A_3, and A_4. The compatibility of these equations requires that they must be satisfied simultaneously, which leads to the dispersion relation,

$$\chi_1 k_{x1} \left(\kappa e^{i(k_{x2}+k_{xbl})\Delta_x} + \xi \right) + \zeta \chi_{bl} \left(\kappa e^{i(k_{x2}+k_{xbl})\Delta_x} - \xi \right) = 0, \tag{5.6}$$

with the following notation:

$$
\begin{aligned}
\chi_1 &= \frac{-\Omega_1}{k_{x1}^2}, \\
\chi_{bl} &= \frac{-\Omega_{bl}}{k_{xbl}^2}, \\
\zeta &= k_{xbl} - k_t \cos\alpha \frac{(U_{01}-U_{02})}{4k_{xbl}} \frac{(G_{bl}H_{bl}-F_{bl})}{G_{bl}^2}, \\
\kappa &= k_t \cos\alpha \frac{(U_{01}-U_{02})}{4k_{x2}} \frac{(G_2 H_2 - F_2)}{G_2^2}, \\
\xi &= 2k_{x2} + \kappa, \\
G_{bl,2} &= \omega_{bl,2}'^2 (C_{Sbl,S2}^2 + V_{Abl,A2}^2) - (\mathbf{V}_{Abl,A2} \cdot \boldsymbol{k}_{bl,2})^2 C_{Sbl,S2}^2, \\
H_{bl,2} &= 4\omega_{bl,2}'^3 - 2k_t^2 \omega_{bl,2}' (C_{Sbl,S2}^2 + V_{Abl,A2}^2), \\
F_{bl,2} &= 2\omega_{bl,2}' (C_{Sbl,S2}^2 + V_{Abl,A2}^2)(\omega_{bl,2}'^4 - k_t^2 G_{bl,2}).
\end{aligned}
$$

Here, α represents the angle between the tangential wavenumber, k_t, and flow velocity, U_0.

The eigenvectors and eigenvalues of Equation 5.6 are computed numerically for different parameters using a Newton-Raphson iteration scheme. Normalized flow velocities $V_{01,02}$ are used such that $V_{01,02} = U_{01,02}/V_{A2}$, where the normalization is with respect to the Alfvén speed in region 2, V_{A2}. The transition layer thickness Δ_x is normalized by R_E, wavenumbers by $1/\Delta_x$, and frequencies $\omega_{r,i}$ by V_{A2}/Δ_x. The background physical parameters are set such that $B_{01}/B_{02} = 1.25$, $\rho_{01}/\rho_{02} = 1$, $\beta_1 = 0.5$, and $\beta_2 = 1.4$. Here, $\beta_{1,2} = (P_{01,02})/(B_{01,02}^2/2\mu_0)$, such that the parameters chosen represent realistic values of plasma beta on each side of the boundary. These chosen parameters are representative such that they could be considered applicable to the Earth's magnetopause [*Hasegawa et al.*, 2006; *Foullon et al.*, 2010; *Hwang et al.*, 2011], BBF channel boundaries in the central plasmasheet [*Angelopoulos et al.*, 1994; *Grigorenko et al.*, 2012; *Ma et al.*, 2012] and shear flow boundaries in the solar atmosphere [*Andries and Goossens*, 2001;

Foullon et al., 2013; *Ofman and Thompson*, 2011; *Nykyri and Foullon*, 2013; *Cécere et al.*, 2014].
The flow speed in region 2, V_{02}, is set to zero, while several values of the flow speed in region
1, V_{01}, are considered. The normalized tangential wavenumber is set along y - parallel to the
background flow speed direction, $\boldsymbol{k}_t = (k_y, 0)$. The variation of KHI growth rates with $k_y \Delta_x$ is
calculated for different values of V_{01} and background magnetic fields directions.

5.2.4   Results

In this section we present numerical results for cases with and without magnetic stress acting
at the boundary where the KHI is initiated. The ambient parameters were defined in section
2, and only the direction of magnetic fields on either side of the flow boundary, θ_1 and θ_2, and
background flow velocity, V_{01}, remain to be varied. Here θ_1 and θ_2 are the angles between the
tangential wavenumber, k_y, and background magnetic fields, B_{01} and B_{02}, in region 1 and region
2, respectively. Since the tangential wavenumber is chosen along the direction of the background
flow, θ_1 / θ_2 also describes the angles between B_{01}/B_{02} and the background flow velocity, V_{01}.

Particular focus is placed on the effect of magnetic tension on the strength of KHI surface
waves growth rates, and on the initiation of the emission of propagating magnetosonic waves after
the KHI has developed on the boundary. For each configuration, the variation of KHI surface
waves growth rates and the MHD wave emission efficiency as a function of normalized tangential
wave number, $k_y \Delta_x$, is investigated.

Since the focus of this paper is propagating MHD wave emission due to the KHI, we consider
only cases for $M_{F2} > 1$, after which the wave emission is found to be possible. M_{F2} is the fast
mach number defined as $M_{F2} = U_{01}/V_{fast2}$ and

$$V_{fast2} = \left[\frac{1}{2} \left(V_{A2}^2 + C_{S2}^2 + \sqrt{(V_{A2}^2 + C_{S2}^2)^2 - 4V_{A2}^2 C_{S2}^2 cos^2\theta_2} \right) \right]^{1/2},$$

is the fast MHD wave phase speed in region 2. Smaller values of M_{F2} have variations in growth
rates that are similar to cases with $M_{F2} > 1$, but propagating MHD wave emission only possible
for flow speed values of $M_{F2} > 1$.

KHI Surface Waves Growth Rates and MHD Wave Emission in the Absence of Magnetic Tension

The calculations presented in this section show the KHI surface wave growth rates and sponta-neous magnetosonic wave emission process for the case in which B_{01}, B_{02} are perpendicular to the shear flow direction and tangential wavenumber, i.e. $\theta_1 = \theta_2 = 90°$. This removes the effect of magnetic tension on the shear flow boundary, since the tangential components of the magnetic field are zero on either side.

Figure 5.2 shows the growth rates of KHI surface waves as a function of normalized tangen-tial wavenumber, $k_y \Delta_x$. Three different values of the flow speed, V_{01}, are chosen corresponding to $M_{F2} = 1, 1.25$ and 2.25. As displayed in Figure 5.2, normalized growth rates first increase
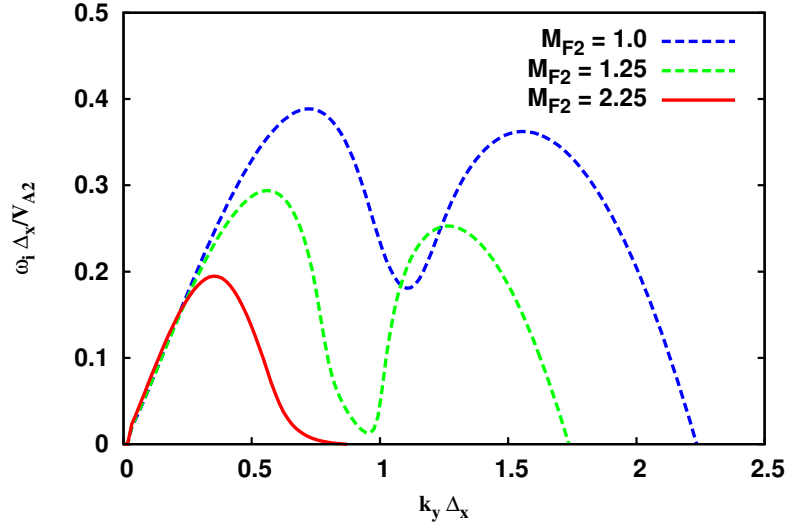
Figure 5.2: KHI surface waves growth rates dependence on the normalized tangential wave number, $k_y \Delta_x$ and fast mach number, $M_{F2} = V_{01}/V_{fast2}$, $\theta_1 = \theta_2 = 90°$. As M_{F2} increases, the growth rates decrease and $k_y \Delta_x$ values corresponding to the fastest growing modes are shifted to the left. The $k_y \Delta_x$ value beyond which all the modes are stable is also shifted to the left. Valleys in the growth rates profiles at $k_y \Delta_x \simeq 1.1$ for $M_{F2} = 1.0$ and $k_y \Delta_x \simeq 0.9$ for $M_{F2} = 1.25$ are possibly due to spontaneous wave emission trying to prevail the KHI growth without success. Wave emission starts at $M_{F2} = 2.25$ for this configuration and is mainly into region 1.

with $k_y \Delta_x$, reach a maximum, and then decrease to zero. Valleys in the growth rates profiles at $k_y \Delta_x = 1.1$ and 0.9 for $M_{F2} = 1.0$ and 1.25 are the consequence of propagating MHD wave

emission prevailing over growth of the KHI surface wave on the shear flow boundary. As M_{F2} increases, KHI surface wave growth rates and tangential wavenumbers corresponding to maximum growth decrease - i.e., the wavelengths of the fastest growing modes increase. The value of the tangential wavenumber beyond which modes are stable also decreases with increasing M_{F2}. These results overall agree with previous studies [e.g., *Walker*, 1981; *Miura and Pritchett*, 1982; *Gratton et al.*, 2004]. In these studies, however, flow speeds up to $M_{F2} = 2$ are considered with the argument that growth rates decrease considerably for values of $M_{F2} > 2$ [e.g., *Miura and Pritchett*, 1982].

Figure 5.3: Density profiles corresponding to Figure 5.2; $M_{F2} = 1.25$ for panel (a) and $M_{F2} = 2.25$ for panel (b). The normalized tangential wavenumber $k_y \Delta_x = 0.6$ for both panels. It is visible that waves propagate mainly into the region 1 on panel (b), while no propagation is observed on panel (a). The flow speed values corresponding to $M_{F2} < 2.25$ did not result wave propagation into either region.
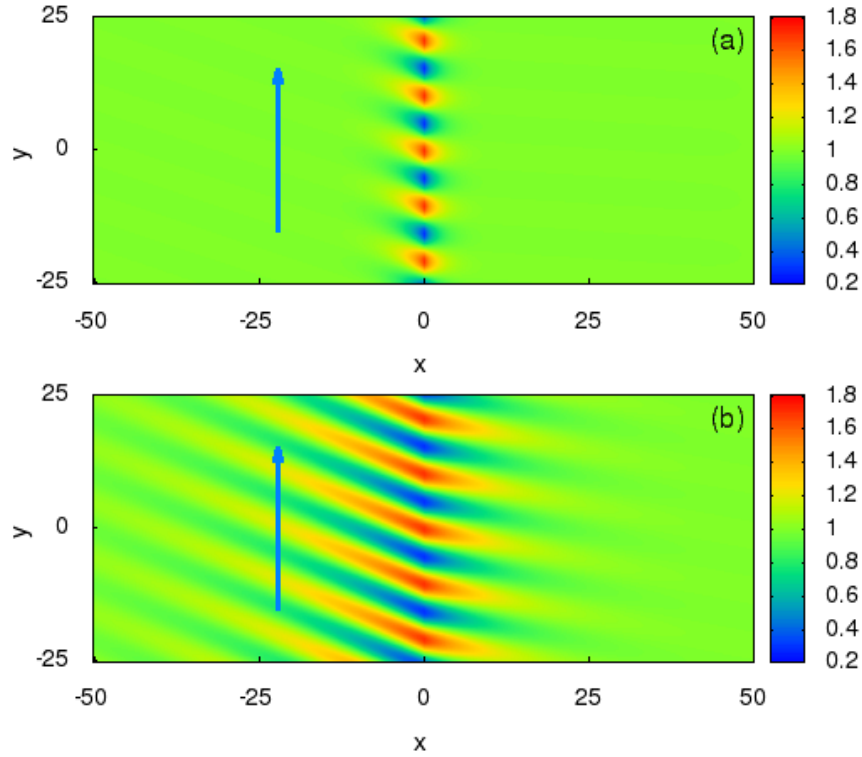
We find that in the absence of magnetic tension, propagating MHD wave emission due to the action of the KHI at the shear flow boundary starts at flow speed values of $M_{F2} \geq 2.25$. Figure 5.3 displays this fact showing density profiles for $V_{01} = 1.25$ (panel (a)) and $V_{01} = 2.25$ (panel (b)); $k_y \Delta_x = 0.6$ for both panels. MHD wave emission is not seen in Figure 5.3 (a) while it is clearly present and directed mainly into region 1 in Figure 5.3 (b). Although growth rates are larger for flow speed values corresponding to $M_{F2} \leq 2.25$ (see Figure 5.2), MHD wave emission is not found. These results suggest that not necessarily the largest growing KHI surface modes are the most significant modes on a K-H unstable boundary. In contrast, growing modes of the KHI characterized by the emission of magnetosound is more important. These magnetosonic waves will propagate into both regions and provide a significant source of energy transport.

To aid with the understanding of the physical reason behind MHD wave emission on a K-H unstable MHD shear flow boundary, real and imaginary wavenumbers perpendicular to the boundary are calculated using Equation 5.2. Figure 5.4 shows normalized values of perpendicular wavenumbers, $k_{xr,xi} \Delta_x$, as a function of $k_y \Delta_x$ for flow speed values corresponding to the M_{F2} values in Figure 5.2. Panel (a) and (b) of Figure 5.4 display the real and imaginary wavenumbers normal to the boundary in region 1, and panels (c) and (d) show real and imaginary wavenumbers normal to the boundary in region 2. The real part of the perpendicular wavenumbers represents the physical wavelength and the imaginary part represents the rate of the spatial decay away from the boundary. As seen in panels (a) and (b) in Figure 5.4, for flow velocity values corresponding to $M_{F2} < 2.25$ the real parts of the perpendicular wavenumbers, k_{x1r}, are small while the imaginary parts, k_{x1i}, are large. This suggests that the waves are mainly surface type and confined to the boundary for $M_{F2} < 2.25$. For flow speed values corresponding to $M_{F2} = 2.25$ however, k_{x1r} picks up large values while k_{x1i} becomes considerably smaller, which suggests that waves change their dominant character into propagating modes and carry energy away from the boundary into region 1. Panels (c) and (d) in Figure 5.4 show that in region 2 the real parts of the perpendicular wavenumbers, k_{x2r}, are always small while imaginary parts, k_{x2i}, are always large. Although for $M_{F2} = 2.25$ there are some regions of small imaginary wavenumber values, wave propagation into region 2 is still insignificant since the real wavenumber in comparison to the imaginary part never becomes large enough for a strong propagation. This is also visible in Figure 5.3 as considerably weaker wave emission into region 2 than into region 1.
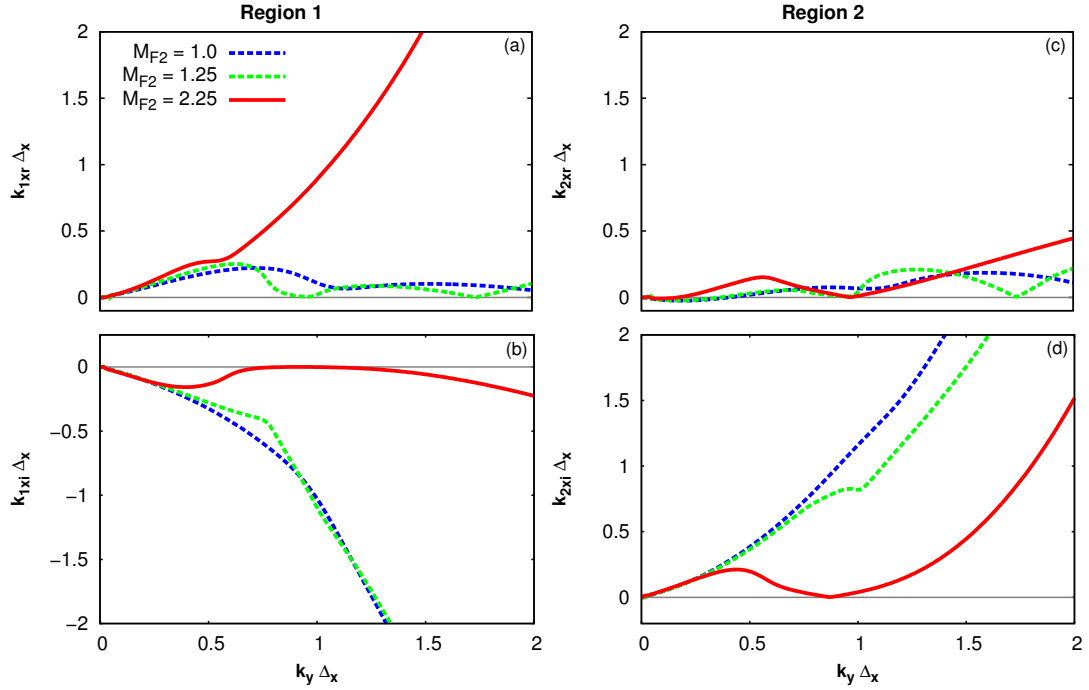
Figure 5.4: Dependence of normalized perpendicular wavenumbers on M_{F2} and $k_y \Delta_x$ - the background parameters are the same as in Figure 5.2. Panel (a)/(b) shows the real/imaginary parts of perpendicular wave numbers in region 1 and panel (c)/(d) shows the real/imaginary parts of perpendicular wave numbers in region 2. For region 1 in panel (a)/(b) we see that the real/imaginary wavenumbers for $M_{F2} = 2.25$ has considerably larger/smaller values than those for $M_{F2} < 2.25$. This means that the KHI waves attain large propagation part and small decay and thus propagate away from the boundary at flow speeds corresponding to $M_{F2} = 2.25$. Panel (c) and (d) show that perpendicular wavenumbers have considerably small real and large imaginary values in region 2 for all the values of M_{F2}. Therefore for $\theta_1 = \theta_2 = 90°$ configuration, the spontaneous emission of MHD waves is mainly possible into region 1 at $M_{F2} \geq 2.25$.

KHI Surface Waves Growth Rates and MHD Wave Emission Under the Effects of Magnetic Tension

Magnetic tension effects are now included by changing the values of θ_1 and θ_2 to $60°$ and $30°$, respectively. This will result in stronger magnetic tension in region 2 due to a larger parallel magnetic field component. Figure 5.5 shows the variation of KHI surface waves growth rates
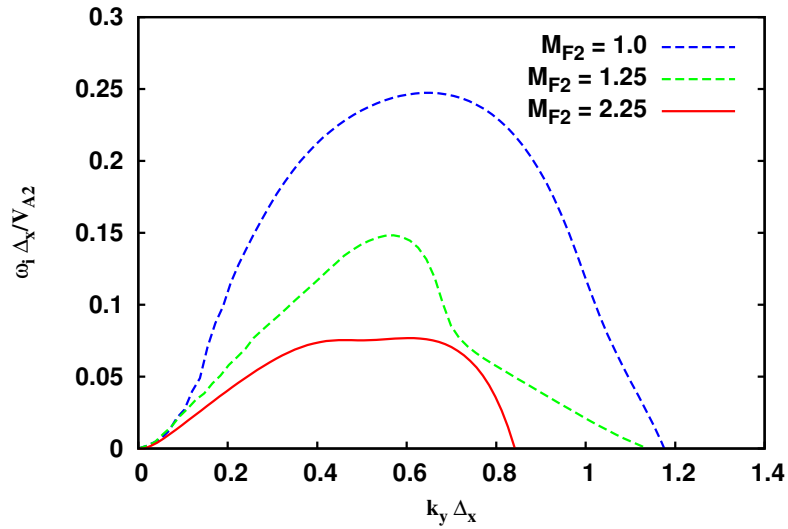
Figure 5.5: Growth rate vs $k_y \Delta_x$ for $\theta_1 = 60°, \theta_2 = 30°$. KHI growth rates and value of $k_y \Delta_x$ where modes stop growing are smaller than the $\theta_1 = \theta_2 = 90°$ case due to the effect of the magnetic tension on the boundary. Spontaneous emission of MHD waves however, starts at considerably smaller flow speed values - for $M_{F2} \geq 1$.

as a function of $k_y \Delta_x$ for this configuration, and for values of M_{F2} that were used to obtain Figure 5.2. As a result of increased magnetic tension, KHI growth rates and critical values of normalized tangential wavenumber at which modes become stable decrease, which agrees with previous results [*Miura and Pritchett*, 1982]. Emission of MHD waves also occurs for flow speeds as low as $M_{F2} \geq 1$.

Density profiles shown in Figure 5.6 (a) and (b) for $\theta_1 = 60°$ and $\theta_2 = 30°$, clearly display the fact that there is strong wave emission into region 2. In Figure 5.6, panel (a) is for $k_y \Delta_x = 0.7$ and $M_{F2} = 1.25$, panel (b) is for $k_y \Delta_x = 0.5$ and $M_{F2} = 2.25$. Although considerably weaker than the $M_{F2} = 1.25$ and 2.25 cases displayed in Figure 5.6, wave emission is also found to be
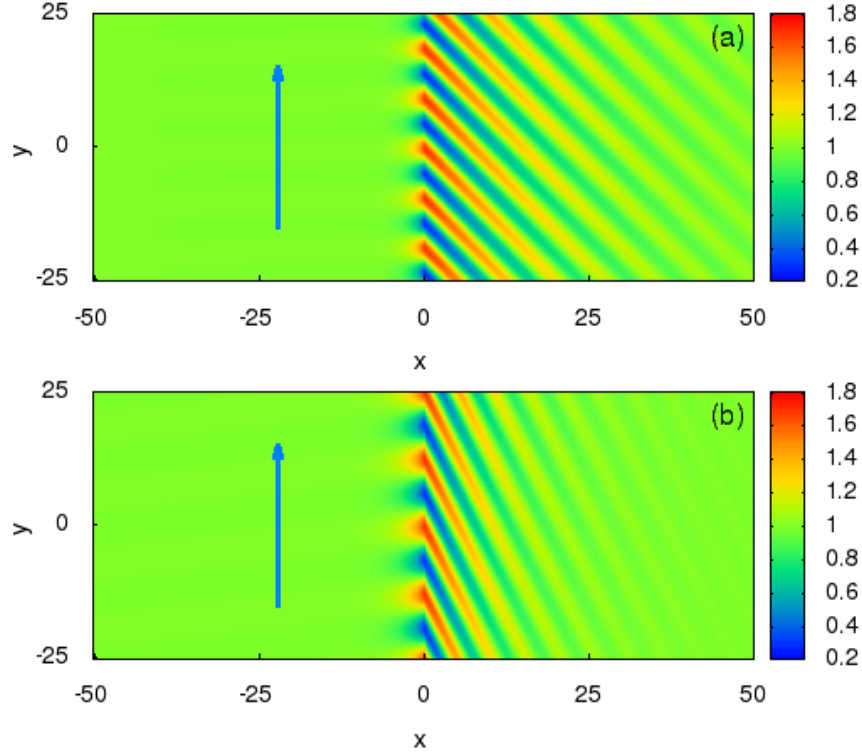
Figure 5.6: Density profiles showing waves propagating into region 2 for $\theta_1 = 60°, \theta_2 = 30°$. Panel (a) is for $M_{F2} = 1.25$ and $k_y\Delta_x = 0.7$, panel (b) is for $M_{F2} = 2.25$ and $k_y\Delta_x = 0.5$. Both panels show spontaneous emission of MHD waves only into region 2. Although weaker, wave emission is also found to be possible at $M_{F2} = 1$.

possible at flow speed values corresponding to $M_{F2} = 1$ for this magnetic field configuration. The results displayed in Figures 5.5 and 5.6 suggest that increased magnetic tension is favorable for spontaneous MHD wave emission due to KHI. Likely the inhibition of KHI surface wave growth rates by the tension may contribute to the increasing dominance of the emitted wave solution for smaller angles between the boundary and the magnetic field direction (larger magnetic tension forces inhibiting the growth rates of the fastest growing surface wave solutions).

Figure 5.7 shows the real and imaginary parts of perpendicular wavenumbers in region 1 (panels (a) and (b)) and region 2 (panels (c) and (d)), for the same M_{F2} values used to obtain Figure 5.5. In Figures 5.7 (a) and (b) perpendicular wavenumbers have small (large) values of real (imaginary) parts in region 1.
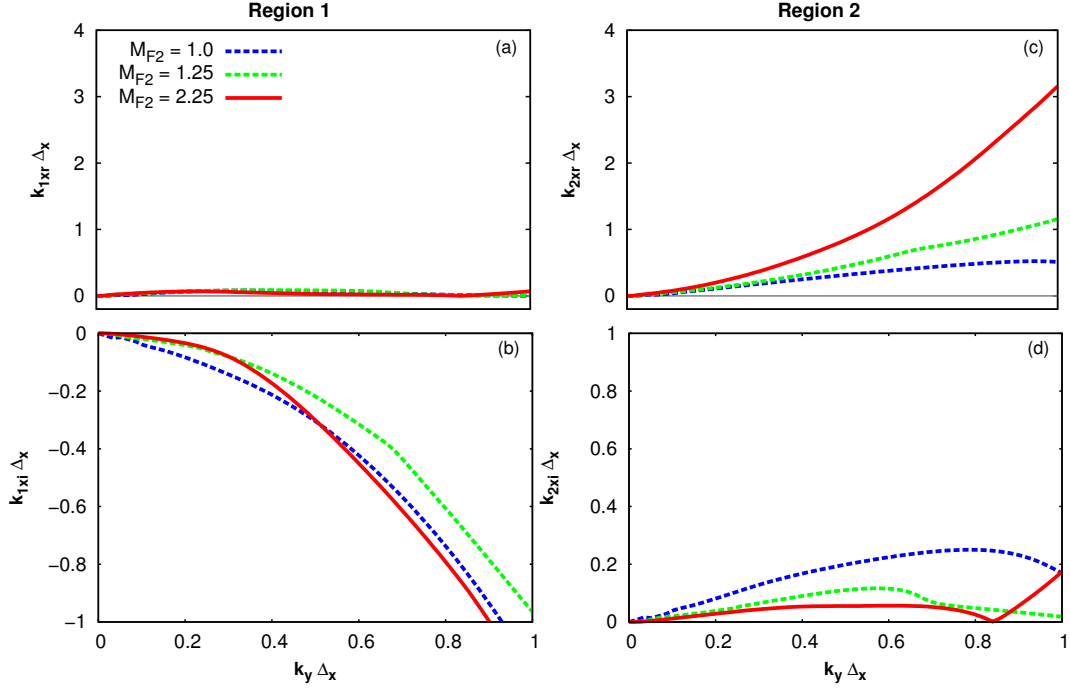
Figure 5.7: Perpendicular wavenumbers vs $k_y \Delta_x$ for $\theta_1 = 60°, \theta_2 = 30°$. Panels (a) an (b) display the perpendicular wavenumbers for region 1, k_{x1r}, k_{x1i}, and panels (c) and (d) display the wavenumbers for region 2, k_{x2r}, k_{x2i}. Very small/large values of real/imaginary wavenumbers on panel (a)/(b) reveals the fact that wave propagation into the region 1 is not present. In contrast, panels (c) and (d) show that waves start to have large real wavenumbers while decay or imaginary wavenumbers becomes very small for $M_{F2} \geq 1.25$ which means strong wave emission into region 2. Due to the strong magnetic tension on the boundary, wave emission into region 2 is possible even at flow speed values corresponding to $M_{F2} = 1$.

In region 2, however, Figures 5.7 (c) and (d) display solutions showing that the modes have perpendicular wavenumbers whose imaginary parts are considerably smaller than their real parts which means that waves propagate into region 2. The variations of real and imaginary perpendicular wave numbers in Figure 5.7 supports the results previously shown in Figure 5.4, i.e., that MHD wave emission from a K-H unstable boundary starts when perpendicular wavenumbers pick up large real values and at the same time have correspondingly small imaginary values. This condition holds only for superfast flow speed values - i.e., flow speed values corresponding to $M_{F2} \geq 1$. These results show that for the magnetic fields configured as $\theta_1 = 60°$ and $\theta_2 = 30°$,

wave propagation is not at all possible into region 1, while it is clearly present into region 2 once $M_{F2} \geq 1$.

MHD Wave Emission Thresholds: Relation to Wavenumbers and Phase Velocities

In this section, the phase speed values of the KHI unstable waves, both those with dominantly surface mode characteristics as well as those demonstrating the emission of magnetosound, are calculated using

$$\mathbf{U}_p = \frac{\omega_r}{(k_t^2 + k_x^2)}\boldsymbol{k}, \tag{5.7}$$

in order to investigate the phase speed values of KHI waves when modes which emit magnetosound occur. Comparison of normalized phase speeds, $V_p = U_p/V_{A2}$, is shown in Figure 5.8 with panels (a) and (b) for $\theta_1 = \theta_2 = 90°$ and panels (c) and (d) for $\theta_1 = 60°, \theta_2 = 30°$. Flow speed values are the same as in Figures 5.2 and 5.5. The normalized phase speed of fast MHD waves, $V_{fast1,2}$, in the absence of flow are also shown by way of comparison (thick grey and brown lines).

Figure 5.8 shows that the phase speed values of the KHI waves is in the range expected of fast MHD waves. This is consistent with the findings of *Turkakin et al.* [2013], who showed that fast MHD waves were responsible for generating the primary KHI. This contrasts with the secondary KHI occurring at lower background flow speeds, which has smaller growth rates and is initiated by slow MHD waves [*Turkakin et al.*, 2013]. The secondary KHI, however, is not investigated in the current study.

Figure 5.8 (a) shows that for the $\theta_1 = \theta_2 = 90°$ case, the phase speeds of KHI surface waves increase to reach the values of fast wave phase speeds in region 1 for $k_y\Delta_x = 0.6$ and $M_{F2} = 2.25$, i.e., where propagating wave emission starts (see Figure 5.3). In region 2, wave emission is considerably weaker for $k_y\Delta_x = 0.6$ and $M_{F2} = 2.25$ (see Figure 5.3). Panel (b) in Figure 5.8 shows that phase speeds of KHI waves are smaller than fast MHD wave phase speeds in region 2. The phase speeds reach background fast wave phase speeds at $k_y\Delta_x > 0.6$, at which point propagating wave emission into both regions is possible. Panel (c) in Figure 5.8 shows that the phase speeds of KHI surface waves do not reach fast MHD wave phase speeds in region 1 for $\theta_1 = 60°$ and $\theta_2 = 30°$. Panel (d) shows that phase speeds exceed the fast MHD wave phase speed in region 2 for $M_{F2} \geq 1$ where strong wave emission is obtained (see Figure 5.6).
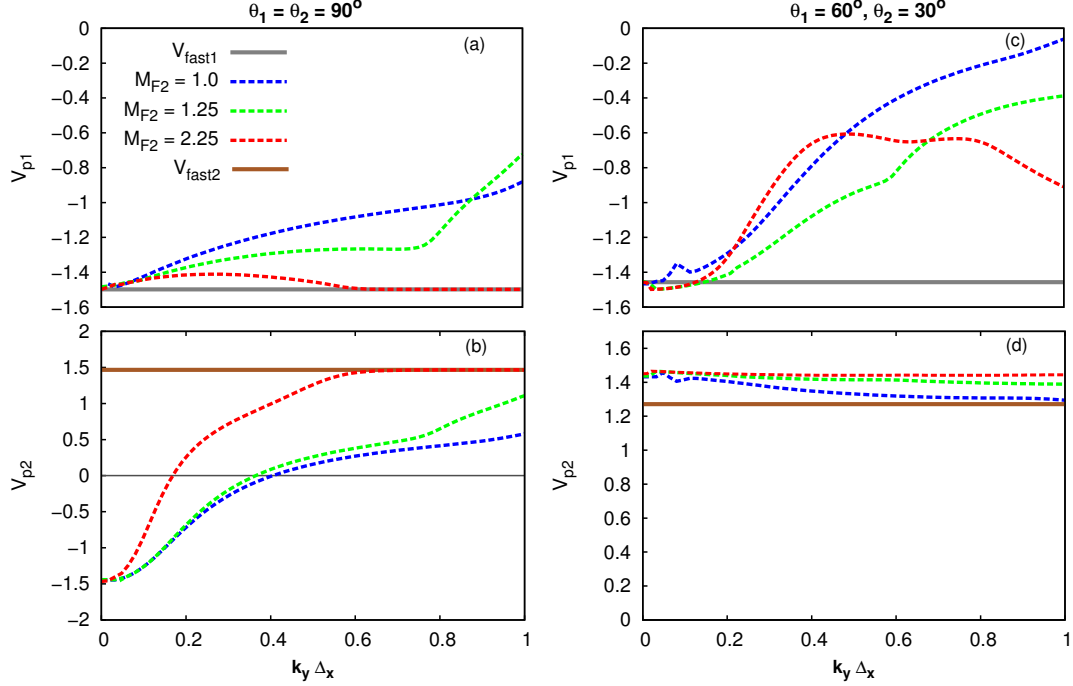
Figure 5.8: Phase velocities vs. $k_y \Delta_x$ for $\theta_1 = \theta_2 = 90°$ (panels (a) and (b)) and $\theta_1 = 60°, \theta_2 = 30°$ (panels (c) and (d)). Flow speed values are the same as in Figures 5.2 and 5.5. Phase speed values of fast MHD waves in the absence of flow, V_{fast1}, V_{fast2}, are shown for comparison (grey and brown thick lines). Wave propagation starts into the flowing side (region 1) for $\theta_1 = \theta_2 = 90°$ at flow velocities $M_{F2} \geq 2.25$ and into the stationary side (region 2) for $\theta_1 = 60°, \theta_2 = 30°$ at flow velocities $M_{F2} \geq 1$. Phase velocity of KHI waves only reach to the fast MHD wave phase speeds for $\theta_1 = \theta_2 = 90°$, while they exceed the fast MHD wave speeds for $\theta_1 = 60°, \theta_2 = 30°$.

The results shown in Figure 5.8 (a) - (d) suggest that propagating MHD wave emission starts at a point where the values of KHI wave phase speeds reach or exceed the fast MHD wave phase speeds in either medium. In the presence of a strong magnetic tension the KHI waves phase speeds exceed the fast wave phase speeds. If magnetic tension is absent, however, they cannot exceed the fast MHD wave phase speed and propagating wave emission is weaker.

Another example showing propagating wave emission driven by KHI at a shear flow boundary is provided in Figures 5.9 and 5.10 for $\theta_1 = \theta_2 = 60°$ and $M_{F2} = 2.5$. Figure 5.9 shows density profiles for this configuration for $k_y \Delta_x = 0.35$ (panel (a)) and $k_y \Delta_x = 0.45$ (panel (b)).
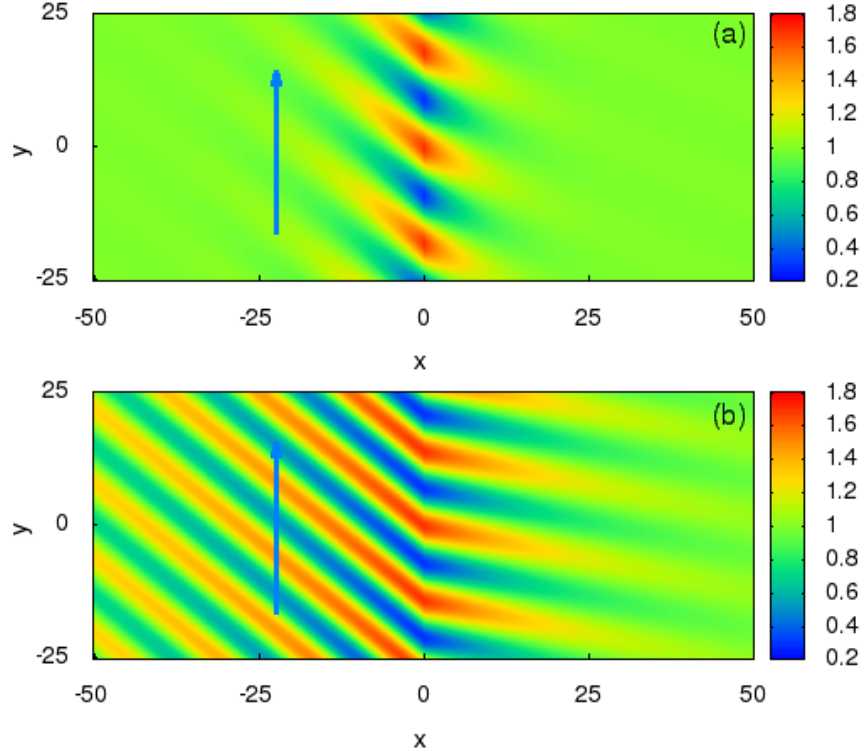
Figure 5.9: Density profiles for magnetic field configuration $\theta_1 = \theta_2 = 60°$. While wave emission is weakly seen on panel (a), waves visibly propagating into region 1 and region 2 in panel (b) - $M_{F2} = 2.5$; $k_y\Delta_x = 0.35$ for panel (a) and $k_y\Delta_x = 0.45$ for panel (b). The above Figure displays the fact that for a specific configuration, not all the wavelengths can be emitted from a K-H unstable boundary. Strong magnetic tension in region 1 cause the KHI waves with bigger wavelengths, i.e. smaller $k_y\Delta_x$, to be emitted from the boundary on panel (a). KHI waves with smaller wavelengths are seen to be emitted into both regions on panel (b) where visible stronger emission into the region 1 is due to the stronger magnetic tension.

Figure 5.9 panel (a) displays the fact that at normalized tangential wavenumber value $k_y\Delta_x = 0.35$, there is very little wave emission into region 1. When the value of $k_y\Delta_x$ increases to 0.45, propagating MHD wave emission becomes possible into both regions, as displayed in Figure 5.9 panel (b). This result suggests that there exists a certain wavelength regime for each region where the KH shear flow instability can excite modes which emit propagating waves from the boundary. Stronger magnetic tension in region 1 initiates propagating emission of MHD waves with larger wavelengths, smaller $k_y\Delta_x$, while emission into region 2 is possible for KHI waves

with smaller wavelengths. Figure 5.9 (b) also displays that due to the stronger magnetic tension, wave emission into region 1 is stronger than wave emission into region 2.
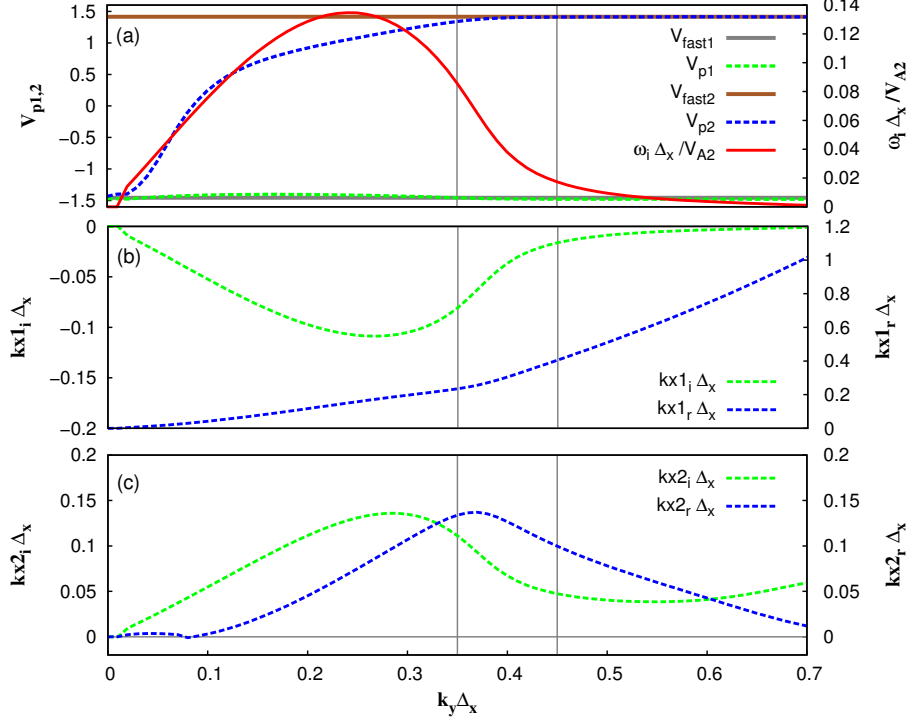
Figure 5.10: Comparison of KHI waves phase velocities, growth rates and real and imaginary perpendicular wave numbers corresponding to Figure 5.9. Vertical grey lines mark the position of $k_y\Delta_x = 0.35$ and $k_y\Delta_x = 0.45$ corresponding to Figure 5.9 (a) and (b). Panel (a) displays the growth rates with phase speed values of KHI waves and panels (b) and (c) shows real and imaginary wavenumbers for region 1 and region 2. Values of fast MHD wave phase speeds in the absence of flow are also shown for region 1 and region 2 (grey and brown lines). Above Figure suggests that there exist a certain wavelength regime for each region where KHI waves are emitted. Spontaneous wave emission into region 1 starts at wavelengths corresponding to $k_y\Delta_x = 0.35$ while wave emission into region 2 could only start at wavelengths corresponding to $k_y\Delta_x = 0.45$.

KHI wave growth rates, phase velocities, and perpendicular wavenumbers corresponding to the values in Figure 5.9 (a) - (b) are shown in Figure 5.10 (a) - (c). Figure 5.10 (a) shows growth rates (red solid line) and phase velocities of the waves in region 1 and 2 (green and blue dashed lines) with the left vertical axis corresponding to phase speed values and the right vertical axis corresponding to growth rates. Background values of the fast MHD wave phase speeds in region 1 and region 2 are also shown for comparison (grey and brown solid lines). Panels (b) and (c)

show real and imaginary perpendicular wavenumbers (blue and green dashed lines) for region 1 and region 2, respectively. In panels (b) and (c) the left (right) vertical axes show imaginary (real) parts of perpendicular wavenumber. Vertical grey lines mark the values of $k_y \Delta_x = 0.35$ and 0.45 corresponding to Figure 5.9 (a) and (b), respectively.

Figure 5.9 (a) shows that propagating wave emission into region 1 starts at wavelengths corresponding to $k_y \Delta_x = 0.35$, while wave emission into region 2 starts at wavelengths corresponding to $k_y \Delta_x = 0.45$. Comparing Figure 5.10 (a) to Figure 5.9 (a), it can be seen that at the start of the region characterized by the emission of propagating magnetosound, the growth rates of these modes are such that they decrease with increasing $k_y \Delta_x$. The fact that wave emission starts at normalized tangential wave number values where growth rates are decreasing is also obtained for the magnetic field configuration $\theta_1 = \theta_2 = 90°$. Only for the configuration $\theta_1 = 60°$ and $\theta_2 = 30°$, is the MHD wave emission found to be possible at the $k_y \Delta_x$ peak in growth rates. In the case of $\theta_1 = 60°$ and $\theta_2 = 30°$, the strong magnetic tension available on the side of region 2 is able to break up the KHI vortices and initiate propagating wave emission near the peak values of the growth rates. This result is very significant in supporting the suggestion that magnetic tension works against KHI surface wave growth and in favor of the excitation of MHD waves characterized by the emission of magnetosound from a KH unstable shear flow boundary. The growth rates start decreasing with $k_y \Delta_x$ after the wave emission starts, since these emitted MHD waves carry energy away from the boundary and weaken the growth of the KHI modes. In other words, KHI surface wave growth and wave emission from a K-H unstable boundary are two processes competing for the control of the physical evolution of the shear flow boundary. Either process may prevail depending on the ambient physical parameters.

The values of KHI waves phase velocities in Figure 5.10 (a) show that at points of spontaneous MHD wave emission (vertical grey lines) the phase speed of the waves reach or exceed background fast MHD wave phase speeds. Figures 5.10 (b) and (c) display that the real parts of perpendicular wave numbers, k_{x1r}, k_{x2r}, become considerably larger than the imaginary parts, k_{x1i}, k_{x2i}, at the value of $k_y \Delta_x$ which characterizes the onset of propagating waves from the boundary. These results support the previously shown results in Figures 5.4, 5.7 and 5.8.

The Effects of Magnetic Field Rotation in the Flowing Region

In this section we investigate the variation of KHI waves growth rates and real and imaginary perpendicular wavenumbers with ambient magnetic field direction in the flowing region 1. The direction of the magnetic field in region 1, θ_1, is varied from $0 - \pi$ while the direction of the magnetic field in region 2, θ_2, is set to a constant value. Resulting values of growth rates and wavenumbers are shown in Figure 5.11 (a)-(c) for four chosen values of the magnetic field direction in region 2 - $\theta_2 = 0°, 30°, 60°$, and $90°$. The flow velocity is chosen such that $M_{F2} = 2.25$ and $k_y \Delta_x = 0.3$.

Figure 5.11 (a) shows that as θ_1 varies from $0 - \pi$ the growth of the KHI surface waves increases to reach a maximum at $\theta_1 = 90°$ and decrease thereafter. The growth rate profiles are similar for all θ_2 values considered, while the magnitudes of growth rates become larger as θ_2 increases. Panels (b) and (c) show the real and imaginary parts of perpendicular wavenumbers in region 1 and region 2, respectively. Left vertical axes on panels (b) and (c) show imaginary parts and right vertical axes show real parts of the perpendicular wave numbers. Imaginary parts, k_{x1i} and k_{x2i}, are shown with solid lines and corresponding real parts, k_{x1r} and k_{x2r}, are shown with dashed lines of the same colors. Similar to how growth rates vary, k_{x1i} and k_{x2i} increase with increasing θ_1, reach to maximum values at $\theta_1 = 90°$ and decrease thereafter. As θ_1 approaches to $90°$, k_{x1r} initially decreases and then slightly increases while k_{x2r} decreases. For $\theta_1 > 90$, k_{x1i} and k_{x2i} decrease, while k_{x1r} first slightly decreases and then increases as k_{x2r} slightly increases. Notice that variations are symmetric for values of $\theta_1 = 0° - 90°$ and $\theta_1 = 90° - 180°$. This is due to the fact that the dispersion relation is symmetric for parallel and anti-parallel configurations of tangential magnetic field components. For $\theta_2 = 90°$, k_{x2r} values are small for all values of θ_1, suggesting that KHI wave emission into region 2 is very weak or not possible. Nevertheless, not much difference is observed in the values of k_{x1r} in region 1.

The results presented in Figure 5.11 overall suggest that while the growth rates of the KHI waves increase to a maximum at $\theta_1 = 90°$, modes that support propagating wave emission is not favorable since they have strong spatial decay, large imaginary parts of perpendicular wavenumbers, k_{x1i}, k_{x2i}. Small values of k_{x1i}, k_{x2i} and large values of k_{x1r}, k_{x2r} for $\theta_1 = 0° - 30°$ and $\theta_1 \simeq 150° - 180°$ suggest that these configurations are more favorable for emission of propagating MHD waves from a KH unstable boundary. This is due to the effect of magnetic tension on the boundary provided by the components of the magnetic fields parallel or anti-

parallel to the flow and the boundary. As the value of θ_2 increase the KHI waves growth rates and imaginary and real parts of the perpendicular wavenumbers also increase, while overall variations with θ_1 stay the same. Results for $\theta_2 = 90°$ marks a special case of very weak or nonexistent modes supporting the emission of propagating MHD waves into the region 2.

Applications to Shear Flow Boundaries in the Earth's Magnetosphere and the Solar Corona

We will now discuss our results in the context of shear flow regions in the Earth's magnetosphere and in the solar corona. Although magnetic fields, densities, and flow velocities are widely different in these cases, certain characteristics hold that are common between them.

If we consider Earth's magnetopause boundary, flow is large in the magnetosheath region while the strengths and directions of the magnetic fields vary depending on the point of observation [*Nakai and Ueno*, 2011; *Hwang et al.*, 2011; *Foullon et al.*, 2008; *Hasegawa et al.*, 2006]. In Figure 5.1, region 1 approximates to the magnetosheath and region 2 to the magnetosphere. Using observational values in [*Nakai and Ueno*, 2011; *Hwang et al.*, 2011; *Fairfield et al.*, 2000; *Hasegawa et al.*, 2006], M_{F2} is between $\simeq 0.5 - 1.2$ in the dayside region and $\simeq 0.5 - 3.5$ in the nightside and magnetotail regions. This implies flow speeds corresponding to $M_{F2} \geq 1$, which means that spontaneous emission of magnetosonic waves is obtainable along the magnetopause boundary. Ambient magnetic fields corresponding to $\theta_1 = \theta_2 = 90°$ are applicable to the dayside magnetopause when the IMF is purely northward or southward. Under these conditions our results suggest that on the dayside magnetopause, the KH surface wave growth is possible with large growth rates. Energy propagation into the magnetosphere from the emission of propagating waves would not be very efficient due to the lack of modes supporting the emission of MHD waves in this configuration. A configuration with $\theta_1 = 60°, \theta_2 = 30°$ however, is also possible on the dayside magnetopause, in which case very efficient spontaneous wave emission into the magnetosphere can occur (see Figure 5.6). On the dawn and dusk flanks and into the nightside magnetopause, the magnetic fields on either side of the boundary are usually parallel or anti-parallel to each other with large tangential components parallel to the magnetopause boundary and flow direction [e.g. *Hasegawa et al.*, 2006; *Nakai and Ueno*, 2011]. The nightside magnetopause and dawn and dusk flanks are therefore favorable for spontaneous emission of MHD waves.
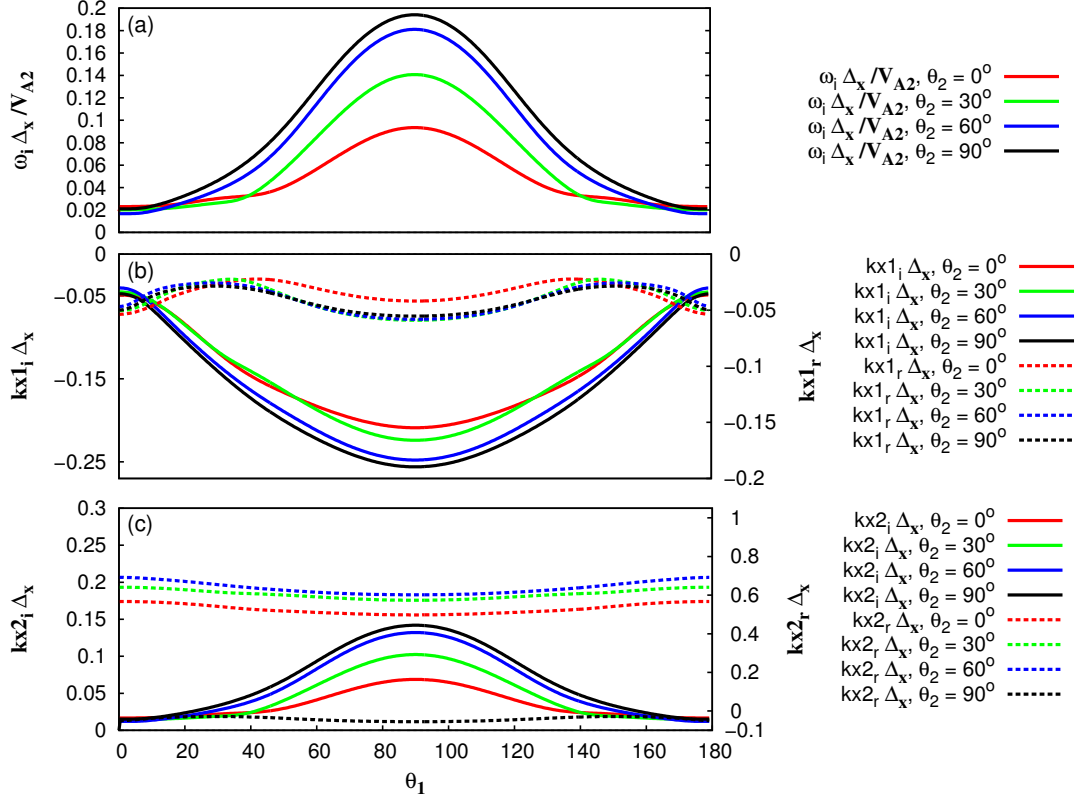
Figure 5.11: Comparison of KHI waves growth rates, real (k_{x1r}, k_{x2r}) and imaginary (k_{x1i}, k_{x2i}) perpendicular wavenumbers in region 1 and region 2 as θ_1 varies from $0 - 2\pi$. $M_{F2} = 2.25$, $k_y\Delta_x = 0.3$ and θ_2 is chosen as $0°, 30°, 60°$, and $90°$. Panel (a) shows that growth rates reach the maximum at $\theta_1 = 90°$ and decreases to their initial values at $\theta_1 = 180°$. Panels (b) and (c) show that as θ_1 approaches to $90°$, k_{x1i} and k_{x2i} considerably increase, showing that KHI waves are strongly evanescent. Therefore, spontaneous MHD wave emission would not be very efficient while KHI growth is the largest at values $\theta_1 \sim 90°$. Wave emission would be most efficient for $\theta_1 = 0° - 30°$ and $\theta_1 = 150° - 180°$ where k_{x1i} and k_{x2i} are small while k_{x1r} and k_{x2r} are large. k_{x2r} values are significantly small for $\theta_2 = 90°$ for all values of θ_1, suggesting that KHI wave emission into region 2 is very weak or not possible. Nevertheless, not much difference is observed in the values of k_{x1r} in region 1 for $\theta_2 = 90°$.

This is due to strong magnetic tension, which enhances wave emission from a KHI unstable flow boundary.

In the central plasmasheet of Earth's magnetotail, Bursty Bulk Flow (BBF) channel boundaries may also be subject to the KHI and spontaneous wave emission [*Turkakin et al.*, 2014]. At the edges of BBF flow channels, region 1 would correspond to inside and region 2 would correspond to outside the channel. Bursty Bulk Flows (BBFs) usually form at $\simeq 19R_E$ in the magnetotail and move towards the Earth decelerating and stopping at $\simeq 6R_E$ [e.g. *McPherron et al.*, 2011]. The flow speed in BBFs varies between 200-1500 km/s [e.g., *Angelopoulos et al.*, 1997; *Shiokawa et al.*, 1997]. Using observations from [*Angelopoulos et al.*, 1992; *Volwerk et al.*, 2007; *Ma et al.*, 2012], BBF speeds normalized by the phase speed of the fast MHD wave in the region outside of the channel are between 0.2 - 2.5, implying that the KHI and modes supporting MHD wave emission can be excited along these shear flow boundaries. Magnetic fields are parallel to the BBF channel boundary in the far magnetotail and change direction due to geomagnetic field dipolarization as BBFs move closer to Earth. In other words θ_1 and θ_2 increase as BBFs move closer to Earth. Results presented in Figure 5.11 then suggest that on BBF channel boundaries, KHI growth is more efficient at positions closer to Earth and wave emission is more efficient further from Earth. Strong emission of MHD waves due KHI at positions further away from Earth may be able to transfer available energy out of BBF channels, resulting in deceleration and stopping of BBFs in near Earth regions. Due to larger values of magnetic fields and thus magnetic tension, propagating MHD wave emission due to KHI would be more observable along BBF channel boundaries than the magnetopause boundary. This can explain often observed kink and sausage wave oscillations emitted from BBF channel boundaries that propagate towards the magnetotail flanks [*Sergeev et al.*, 2004; *Volwerk et al.*, 2005; *Zhang et al.*, 2005].

KHI and shear flow driven propagating MHD wave emission may also be possible on the shear flow boundaries of coronal plumes, Supra-Arcade Downflows (SADs), Coronal Mass Ejections (CMEs) and coronal streamers. Although magnetic field strengths and plasma densities are considerably larger in the solar corona, plasma beta values are of order 1 [*Foullon et al.*, 2013; *Feng et al.*, 2013; *Nykyri and Foullon*, 2013] and normalized values used in this paper are still applicable. Studies performed on the numerical KHI on the boundaries of CMEs [*Foullon et al.*, 2011; *Ofman and Thompson*, 2011; *Nykyri and Foullon*, 2013; *Foullon et al.*, 2013; *Möstl et al.*, 2013], SADs [*Cécere et al.*, 2014], coronal plumes [*Andries and Goossens*, 2001] and coronal

streamers [*Feng et al.*, 2013] have used configurations similar to those used in the current study, and are therefore amendable to analysis.

SADs have strong similarities to BBF channels occurring in Earth's central plasmasheet [*McKenzie and Savage*, 2009; *Cécere et al.*, 2014]. *Cécere et al.* [2014] investigated numerically the occurrence of KHI on the boundaries of SADs, but did not investigate the possibility of the KH driven modes generating the emission of propagating fast magnetosonic modes. Similar to the breaking of BBFs suggested in *Turkakin et al.* [2014], propagating wave emission due to KHI along SAD boundaries is possible and can potentially explain observed deceleration of SADs. Coronal plumes and streamer boundaries have similar characteristics to SADs [*Andries and Goossens*, 2001; *Feng et al.*, 2013] and can thus support MHD wave emission as well. In fact coronal streamer waves, which show very similar characteristics to the waves emitted from BBF channels, have been observed [*Chen et al.*, 2010]

CME boundaries have similarities to the magnetopause boundary [*Foullon et al.*, 2011]. The magnetic field, however, has a helical configuration on one side and is smoothed out on the other side of a CME boundary. With high resolution images provided by the Atmospheric Imaging Assembly (AIA) on-board the Solar Dynamic Observatory (SDO), KHI waves along fast CME ejecta were detected [*Foullon et al.*, 2011; *Ofman and Thompson*, 2011; *Foullon et al.*, 2013] and numerically investigated by [*Ofman and Thompson*, 2011; *Nykyri and Foullon*, 2013; *Möstl et al.*, 2013]. While *Nykyri and Foullon* [2013] and *Ofman and Thompson* [2011] studied the side of the CME boundary where magnetic fields are in a helical configuration, *Möstl et al.* [2013] considered the side where the helical configuration is smoothed. With the flow speed values chosen, they concluded that if there is a parallel component of the magnetic field of strength 20 % of the background field, the KHI is stabilized.

Using observed values in [*Foullon et al.*, 2011, 2013; *Möstl et al.*, 2013; *Cécere et al.*, 2014], we have calculated that values of M_{F2} in solar coronal regions vary between 0.5 - 2.0. The condition of sufficiently fast flow speeds $M_{F2} \geq 1$ implies that along shear flow boundaries in the solar corona the growth of KH modes supporting the emission of magnetosound may be possible. Since background magnetic fields tend to be parallel to the boundary of SADs [*Cécere et al.*, 2014], propagating wave emission due to the KHI will be more probable along these boundaries. In contrast magnetic fields on CME boundaries usually have stronger perpendicular components [*Ofman and Thompson*, 2011; *Foullon et al.*, 2013; *Nykyri and Foullon*, 2013] and thus KHI

surface wave growth will be more favorable than shear flow driven modes supporting the characteristics of propagating wave emission. On the side of the CME boundary where the magnetic field is smoothed, the available strong magnetic tension may support KH modes generating propagating wave emission if flow speeds corresponding to $M_{F2} \geq 1$ are reached. These emitted MHD waves on shear flow boundaries of the solar corona can play a significant role in energy transfer between different regions during solar eruptions.

5.2.5   Discussion and Conclusions

A theory has been developed to investigate the excitation of modes which cause the emission of magnetosonic waves due to the KHI on MHD shear flow boundaries. The parameters chosen are applicable to different shear flow boundaries in Earth's magnetosphere and solar corona. We have determined threshold values of flow speed and tangential wavenumber for modes supporting MHD wave emission under different configurations of the background magnetic fields, $B_{01,02}$. Varying the background magnetic fields allowed us to investigate the effects of magnetic tension on wave emission due to the KHI. The dependence of the modes supporting MHD wave emission on perpendicular wavenumbers and phase velocity of KHI waves has also been investigated.

It is found that for KH modes which generate propagating MHD wave emission from shear flow boundaries, the onset of the wave emission starts at flow speed values corresponding to $M_{F2} = V_{01}/V_{fast2} \geq 1$. As the component of the magnetic field parallel to the MHD shear flow boundary is increased on either side of the boundary, the threshold values of the flow speed where KHI can generate modes which emit magnetosound decreases. Our conclusion is that increasing magnetic tension is supportive of the generation of modes supporting propagating wave emission on shear flow boundaries. While magnetic tension enhances the excitation of modes characterized by propagating wave emission, it hinders the growth of KH surface modes.

Shear flow generation of modes supporting propagating wave emission into either side of an MHD shear flow boundary is possible depending on the strength of magnetic tension. Emission is more efficient into the region where there is a stronger magnetic field component parallel to the boundary, a stronger magnetic tension. Therefore, most of the energy available on the shear flow boundary will be carried into the region with stronger magnetic tension.

The determination of real and imaginary wavenumbers perpendicular to a flow boundary shows that the emission of MHD waves starts when the real parts become larger than the imag-

inary parts. This shows that waves transition from being spatially evanescent surface waves to propagating body waves. When the phase velocity of KHI waves reaches or exceeds background fast MHD wave phase speeds, the perpendicular wavenumber of waves emitted from the flow boundary develops a real part exceeding the imaginary part. In this situation propagating waves carry energy efficiently away from the boundary.

Wave emission usually starts at the point where growth rates are decreasing with $k_y \Delta_x$. However, if there is a strong magnetic field component parallel to the flow on either side of the boundary wave emission may start at peak values of KHI wave growth rates with respect to $k_y \Delta_x$. Our results show that MHD KH modes supporting the propagating wave emission is possible for the fastest growing KH modes only for the $\theta_1 = 60°, \theta_2 = 30°$ configuration. For $\theta_1 = \theta_2 = 90°$ and $\theta_1 = \theta_2 = 60°$ configurations, the KH modes supporting the propagating wave emission are not the fastest growing modes. This supports the suggestion that magnetic tension works in favor of excitation of KH modes supporting MHD wave emission.

We have investigated the effects of varying magnetic field direction in region 1, while the magnetic filed direction in region 2 is kept constant. Four different θ_2 values were considered while θ_1 was varied from $0 - \pi$. For all of the θ_2 values considered we found that the growth rates peak at $\theta_1 = 90°$ while modes supporting propagating wave emission was more probable for $\theta_1 \simeq 0 - 30°$ and $\theta_1 \simeq 150 - 180°$, which corresponds to the situation in which the magnetic field has a strong parallel or anti-parallel component to the background flow. These results confirm that strong magnetic tension enhances MHD wave emission on a KHI unstable boundary.

Applications of the results to shear flow boundaries in the Earth's magnetosphere and in the solar corona is discussed. We have concluded that on the boundaries of the dayside magnetopause and within interplanetary CMEs, KHI surface wave growth dominates the evolution of the boundary. In contrast, on the boundaries of the nightside magnetopause, magnetotail, BBF channels, SAD channels, coronal plumes, and coronal streamers, the shear flow may support the excitation of modes which emit propagating MHD wave disturbances from the boundary. This will also weaken the growth of the KH surface modes as a result of waves carrying energy away from shear flow boundaries of the flow channels. The generation of unstable KH modes which causes the emission of MHD waves can therefore provide a significant source of energy transport between different regions. Propagating KHI driven wave emission and energy transport out of BBF and SAD channels may provide a possible explanation for the deceleration and stopping of

BBFs and SADs.

Chapter 6

Nonlinear Effects on the KHI and Emission of Magnetosound

6.1 Introduction

In the analysis of the KHI waves in previous chapters, we have always assumed that the wave amplitudes were small so that the governing equations can be linearized. This assumption provides remarkably accurate description of small amplitude KHI waves. If the wave amplitude becomes large, which always happens for the KHI waves, the linearization breaks down. Nonlinear effects on the KHI waves then must be taken into account. When the nonlinear stage is reached, the growth of the wave amplitude is stopped due to the nonlinear effects.

The equations used in MHD theory which are described in chapter 1 section 1.6.5 have nonlinear terms. For example, $\rho\mathbf{V}$ term in the continuity equation, $\mathbf{J} \times \mathbf{B}$ term in the equation of motion, and $\mathbf{V}\cdot\nabla\mathbf{V}$ term in convective derivative represent potential sources of non-linear effects. In this chapter the nonlinear effects on KHI and emission of magnetosound are investigated using FLASH code.

6.2 Description of the FLASH Code

FLASH is a publicly available, component based, massively parallel code capable of simulating the compressible, reactive flows in many astrophysical environments. It has been developed primarily at the University of Chicago's ASC/Alliances Flash Center. The FLASH code has a wide user base and is unique among astrophysics application codes [*Dubey et al.*, 2008].

FLASH is a collection of code units and each unit controls a particular aspect of an application. FLASH units are categorized as; infrastructure, physics, driver, monitoring, and simulation. The infrastructure unit is responsible for the management of the runtime environment, the handling of the input and output, and the administration of the solution mesh. It views the physical domain as composed of blocks, where each block covers different fractions of the domain. The physics unit has solvers for hydrodynamics, equations of state, MHD, gravitational fields, cosmology, and particles. The driver unit initializes and finalizes the code, implements the time advancement and controls the connection of units with each other for a specific run. The monitoring unit logs the progress of the simulation. The simulation unit is the most important since it defines the initial, boundary conditions and any other parameters for a particular simulation run[*Dubey et al.*, 2008].

The FLASH code provides MHD solvers included in physics unit. Algorithms are provided to solve the equations of compressible ideal and non-ideal MHD in one, two and three dimensions on Cartesian system. We have used MHD solver for compressible ideal MHD to investigate the KHI and the emission of magnetosound from MHD shear flow boundaries. In simulation unit we have provided a new magnetohydrodynamic KHI unit where we have described our specific problem and defined initial and boundary conditions as well as other plasma parameters such as background flow, plasma density, plasma pressure, and magnetic field. We have used Adaptive Mesh Refinement (AMR) which is implemented with PARAMESH in FLASH. PARAMESH uses a block-structured adaptive mesh refinement scheme in which the fundamental data structure is a block of cells arranged in a logically Cartesian fashion. The complete computational grid consists of a collection of blocks with different physical sizes, which are related to each other in a hierarchical fashion using a tree structures. The blocks at the root of the tree have the largest cells, while their children have smaller cells and are refined.

Assuming the plasma as collisionless and without resistivity we can use the equations of ideal

MHD. The one-fluid MHD equations used in FLASH in normalized form are;

$$\frac{\partial \rho}{\partial t} + \nabla \cdot (\rho \mathbf{V}) = 0, \tag{6.1}$$

$$\frac{\partial (\rho \mathbf{V})}{\partial t} + \nabla \cdot (\rho \mathbf{V} \mathbf{V} - \mathbf{B} \mathbf{B}) = -\nabla (P_T), \tag{6.2}$$

$$\frac{\partial \rho E}{\partial t} + \nabla \cdot (\mathbf{V}(\rho E + P_T) - \mathbf{B}(\mathbf{V} \cdot \mathbf{B})) = 0, \tag{6.3}$$

$$\frac{\partial \mathbf{B}}{\partial t} - \nabla \cdot (\mathbf{V} \mathbf{B} - \mathbf{B} \mathbf{V}) = 0. \tag{6.4}$$

where $\mathbf{V}$ is flow velocity, ρ is the mass density, B is the magnetic field.

$$P_T = P + \frac{B^2}{2}, \tag{6.5}$$

$$E = \frac{V^2}{2} + \frac{P}{\rho(\gamma - 1)} + \frac{B^2}{2\rho} = 0 \tag{6.6}$$

are total pressure and specific total energy. As we described in previous chapters, the total pressure consist of the plasma pressure P and the magnetic pressure $B^2/2$. The three terms in specific energy represent the kinetic energy, the internal energy, and the magnetic energy, respectively.

Normalization in FLASH code is done using a reference velocity, v_0, a reference density ϱ_0, and a reference length $\mathcal{R}_0$. These three factors are then used to scale all quantities in the MHD equations. Letting an overbar indicate the variables in SI units the normalization is done as,

$$r = \frac{\overline{r}}{\mathcal{R}_0} \quad \rho = \frac{\overline{\rho}}{\varrho_0} \quad V = \frac{\overline{V}}{v_0}. \tag{6.7}$$

From above the normalization for the other important parameters becomes,

$$t = \frac{\overline{v_0}}{\mathcal{R}_0}\overline{t} \quad B = \frac{\overline{B}}{v_0\sqrt{\mu_0 \rho_0}} \quad P = \frac{\overline{P}}{\varrho_0 v_0^2}, \tag{6.8}$$

where t is normalized time.

We have used the eight-wave MHD unit in FLASH code which solves the equations 6.1 - 6.4 based on a finite-volume, cell-centered method which was proposed by *Powell et al.* [1999]. The unit uses directional splitting to evolve the MHD equations, making one sweep in each spatial direction to advance equations. In each sweep, the unit uses AMR functionality to fill in com-

putational cells and impose boundary conditions. Then it reconstructs characteristic variables and uses these variables to compute time averaged interface fluxes of the conserved quantities. In order to enforce conservation at jumps in refinement the unit makes flux conservation, calls to AMR, which redistributes affected fluxes using appropriate geometric area factors. Finally, the unit updates the solution and calls EOS (Equation of State) unit to ensure thermodynamical consistency.

EOS unit takes a section of a block and translates it into the data format required by the Eos function, then calls the function. Upon return from the Eos function, the returned data is translated back to the same section of the block. Four implementations of the Eos unit are available: Gamma, which implements a perfect-gas equation of state; Gamma/RHD, which implements a perfect-gas equation taking relativistic effects into account; Multigamma, which implements a perfect-gas equation with multiple fluids with different adiabatic indices (γ), and Helmholtz, which uses a fast Helmholtz free-energy table interpolations to handle degenerate/relativistic electrons/positrons and includes radiation pressure and ions via perfect gas approximation. We have used Gamma unit which is the best applicable approach for ideal MHD solutions. Gamma unit in EOS models a simple ideal gas with a constant adiabatic index γ. The relationship between pressure, density and specific internal energy is $P = (\gamma - 1)\rho\mathfrak{H}$, where $\mathfrak{H}$ is specific internal energy. The expression relating pressure P to temperature T is

$$P = nk_BT, \tag{6.9}$$

Where n is number density of molecules and k_B is the Boltzmann's constant and T is temperature.

After all sweeps are completed, the MHD unit enforces magnetic field divergence cleaning, i.e. $\nabla \cdot \mathbf{B} = 0$ condition, with a truncation error method. In the truncation error method, the solenoidality of the magnetic field is enforced by including several terms proportional to $\nabla \cdot \mathbf{B}$. This removes the effects of unphysical magnetic tension forces and stimulates passive advection of magnetic monopoles, if they are superiously created. This method can effectively bring the superious magnetic monopoles to levels that are sufficiently low, so that generated solutions remain physically consistent. More information on methods used can be found in FLASH user manual at www.flash.uchicago.edu/site/flashcode.

6.3 Code Testing

Validating code against published work is a crucial step in numerical studies in order to prove that code is working properly and providing correct results. This will assure that the new results obtained will be correct and accurate. In this section we provide two tests for the validation of the FLASH code. The Kelvin-Helmholtz Instability is set up and tested against MHD results from *Rankin et al.* [1993] and *Waagan et al.* [2011]. Both tests provided results that are in very good agreement with the results in these papers.

6.3.1 Results Using Parameters in *Rankin et al.* [1993]

We run FLASH code for a 2D MHD shear flow boundary on yz plane and x-direction as normal to the boundary. Using the initial conditions from *Rankin et al.* [1993], we initialized the simulation with velocity profiles as;

$$v_x = V_0 e^{-x^2/\Delta_x^2} \varepsilon cos(k_y y), \tag{6.10}$$

$$v_y = -\frac{V_0}{\Delta_x^2} \frac{2x}{k_{yR}} e^{-x^2/\Delta_x^2}. \tag{6.11}$$

Figure 6.1 shows the velocity profiles of equations 6.10 and 6.11.

Magnetic field is set along z direction and the velocity perturbation is applied to a uniform background plasma. The following parameters taken from *Rankin et al.* [1993] are used: $k_{yR} = 0.3R_E^{-1}$, $k_y = 6.8R_E^{-1}$, $V_A = 280$ km/s, $\sqrt{2}V_0/(e^{1/2}k_{yR}\Delta_x) = 90$ km/s, $\Delta_x = 0.18R_E$, $\varepsilon = 0.02$, $T_0 = 2$ KeV, and $B_0 = 4 \times 10^{-4}$ G. We have chosen background Alfvén velocity as the normalization velocity $v_0 = V_A$, Earth radii as the normalization distance $\mathcal{R}_0 = R_E$, and normalization density as background density $\varrho_0 = \rho_0$. The boundary conditions are set as *periodic*(wrap around) along y, and *outflow*(zero gradient) along x.

The results show very good agreement with *Rankin et al.* [1993]. Figure 6.2 shows the growth in the maximum value of v_x as a function of time. The linear stage of the KHI ends at $\simeq 155s$ where instability saturates. Figure 6.3 shows a log linear fit to the data displayed in Figure 6.2 for the time interval where exponential growth is present. The growth calculated is $\omega_i = 0.033s^{-1}$ which is in excellent agreement with *Rankin et al.* [1993]. These results imply that the FLASH code provides physically correct results. The KHI vortices are shown at $t = 248s$ in Figure 6.4.
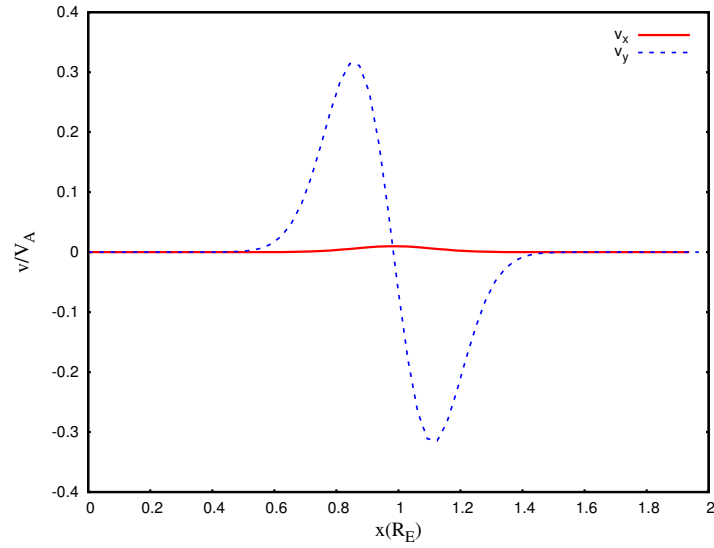
Figure 6.1: Initial velocity profiles used to initialize KHI based on *Rankin et al.* [1993]. Values are normalized with Alfvén velocity, $V_A = 280$ km/s.
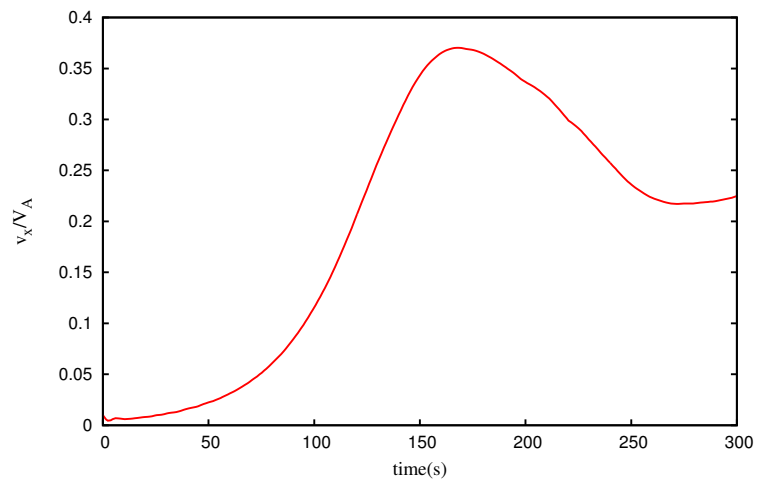
Figure 6.2: Growth of $\max(v_x)$ over the whole simulation time which agrees well with *Rankin et al.* [1993].

Figure 6.3: Log linear fit for the data displayed in Figure 6.2 and value of the calculated growth rate, $\omega_i = 0.033$ s^{-1} which is in perfect agreement with the values predicted by *Rankin et al.* [1993].

Figure 6.4: Vector plot of total velocity at $t = 248$ s from FLASH run with parameters set to same in *Rankin et al.* [1993].

6.3.2 Results using parameters in *Waagan et al.* [2011]

Another test done on the validity of FLASH code is with set up parameters and initial conditions in *Waagan et al.* [2011]. To match the set up conditions used 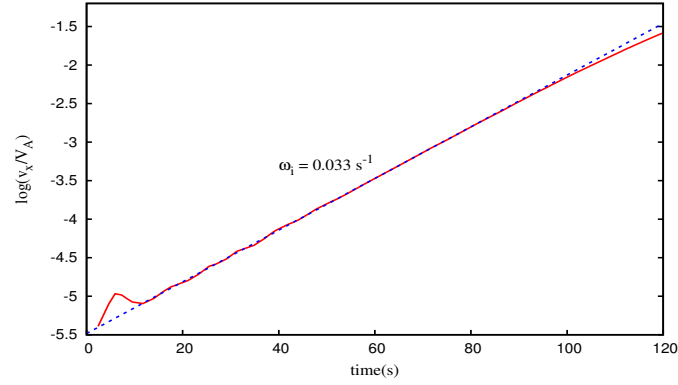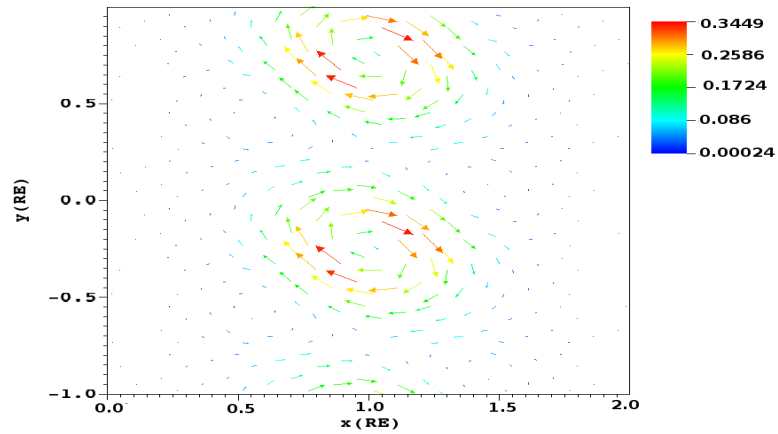in *Waagan et al.* [2011] the boundary normal is chosen along y-direction, and all the background values are set in CGS units. Region 1 corresponds to $y > 0$ and region 2 corresponds to $y < 0$. An initial velocity shear is given along x-direction as, $V_{01} = 0.5$ cm/s and $V_{02} = -0.5$ cm/s. The velocity perturbation is given along y-direction by

$$v_y = 0.0125 sin(2\pi x)e^{-100(y-0.5)^2}.$$

The boundary conditions are set as *periodic* along x-direction and *outflow* along y-direction. The initial parameters are set as; $\rho_{01} = 2$ g/cm^3, $\rho_{02} = 1$ g/cm^3, $B_{01} = 0.5$ G, $B_{02} = -0.5$ G, and $P_{01} = P_{02} = 0.6$ Ba. Magnetic fields are set along x-direction, parallel to the shear flow. These parameters are randomly chosen to test KHI evolution using FLASH code.

Figures 6.5 and 6.6 shows the density profiles for the KHI evolution at times, $t = 1$ s and $t = 9$ s, respectively. These results are in very well agreement with the results shown in *Waagan et al.* [2011] which also implies the FLASH code provides us with correct physical results.
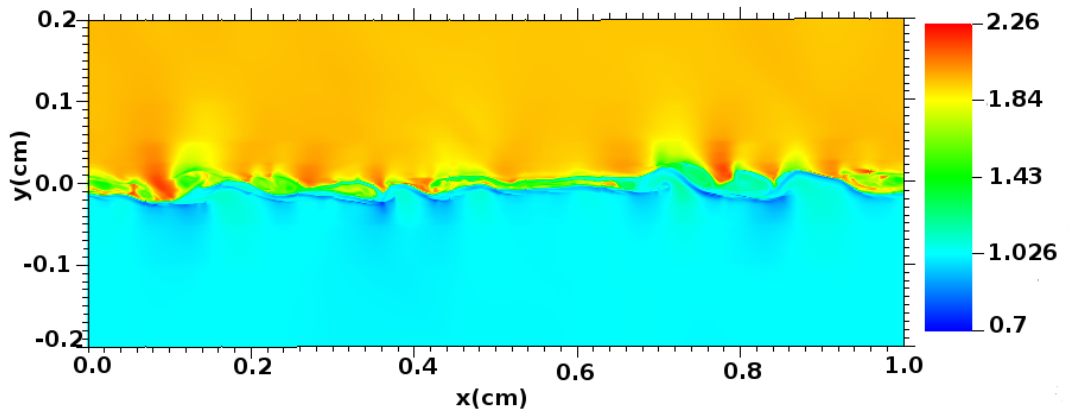
Figure 6.5: Density profile at $t = 1$ s from runs with parameters in *Waagan et al.* [2011].
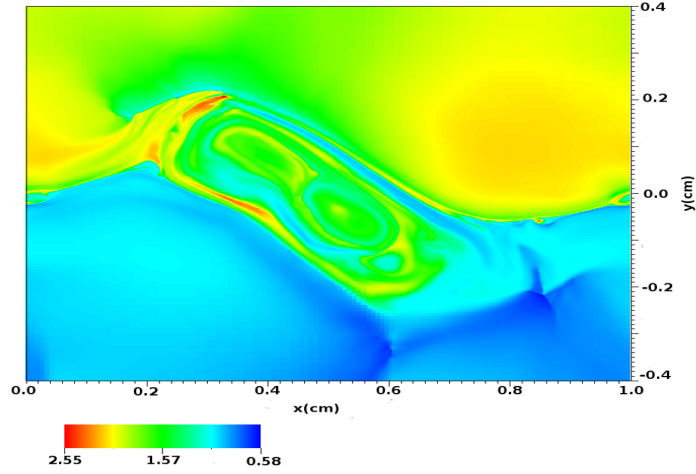
Figure 6.6: Density profile at $t = 9$ s from runs with parameters in *Waagan et al.* [2011].

6.4 Nonlinear KHI and Spontaneous Emission of Magnetosound

6.4.1 Comparing Linear-Nonlinear Results

In this Section the perturbations of linear results obtained in chapter 5 are used as initial perturbations for the KHI growth in FLASH code. KHI growth rate obtained from FLASH code is compared to the linear results. The same set up described in chapter 5 section 5.2.3 with flow velocity corresponding to $M_{F2} = 2.5$ is used. Here, $M_{F2} = V_{01}/V_{fast2}$ is the fast mach number.

KHI growth from linear calculations is displayed in Figure 6.7. The perturbations corresponding to $k_y \Delta_x = 0.42$ is used as initial perturbation for the KHI growth in FLASH code simulation. Normalized growth rate from linear results is calculated as $\omega_i \Delta_x / V_{A2} = 0.056$. Figure 6.8 shows density profile obtained for $k_y \Delta_x = 0.42$ from linear results where wave emission is visible into both regions.
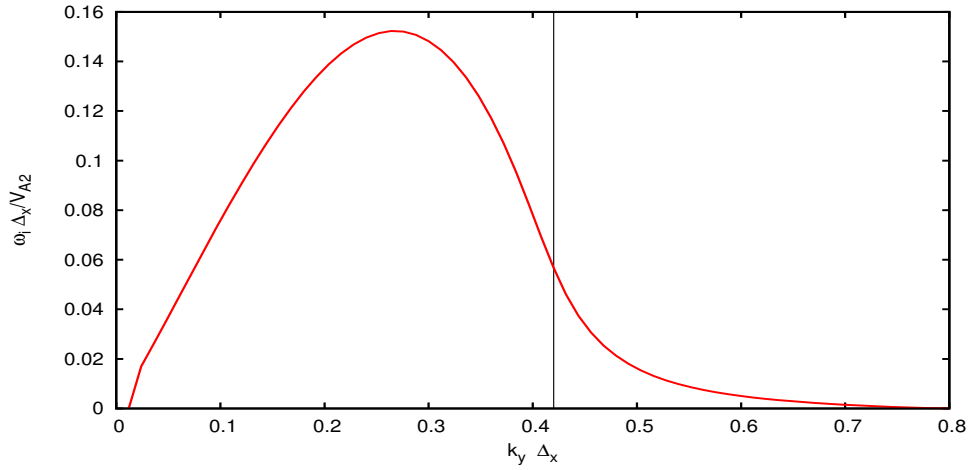
Figure 6.7: KHI growth from linear calculations, $\theta_1 = \theta_2 = 90°$ and $M_{F2} = 2.5$. Perturbations at $k_y \Delta_x = 0.42$, marked by vertical black line, is used as initial perturbation in the FLASH code simulation. At this point normalized growth rate is $\omega_i \Delta_x / V_{A2} = 0.056$.
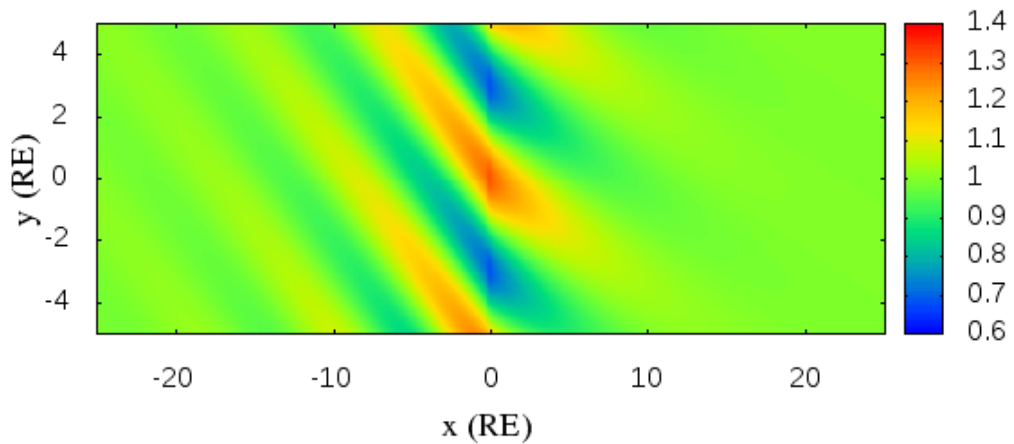
Figure 6.8: Density profile showing wave emission into both regions at $k_y \Delta_x = 0.42$ corresponding the point marked by a vertical line in Figure 6.7.

When the perturbations in above marked point is used in the FLASH code as initial pertur-
bation, obtained results show very well agreement with the linear results. The result showing
growth of v_x with time and log linear fit to data for v_x growth are displayed in Figure 6.9 panels
(a) and (b), respectively. Growth of the v_x velocity saturates at normalized time $t/\tau_{A2} \simeq 15$.
The normalized growth rate, $\omega_i \Delta_x / V_{A2}$, is calculated as 0.054 which is in well agreement with
the linear result of 0.056. Figure 6.10 is a density profile obtained from FLASH simulation results
displaying that wave emission is present into both regions. Since initial perturbations have larger
amplitudes in region 1 than in region 2, superposition of the emitted waves with the initial per-
turbations distorts the shape of the waves. Therefore, the stronger wave emission into region 1 is
not clearly visible. As the amplitude of the waves increase in the nonlinear stages, the stronger
emission into region 1 is more visible.

Figure 6.9: Time evolution of maximum v_x and linear growth rate calculated from FLASH
results for $\theta_1 = \theta_2 = 90°$, $M_{F2} = 2.5$, and $k_y \Delta_x = 0.42$. Calculated growth rate is
$\omega_i V_{A2} / \Delta_x = 0.054$ which is in very good agreement with linear results where normalized
growth rates is calculated as 0.056.
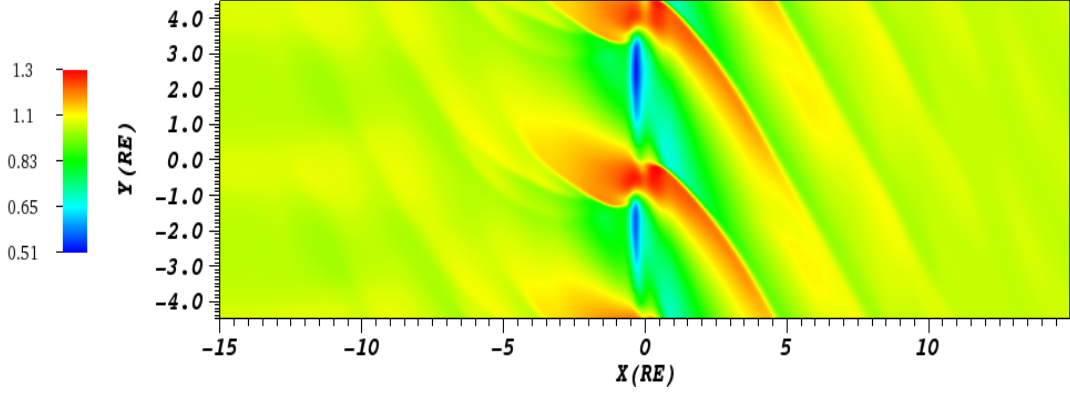
Figure 6.10: Density profile showing wave emission into both regions at normalized time $t/\tau_{A2} = 12.5$ obtained from FLASH code simulations where the linear perturbations corresponding $k_y \Delta_x = 0.42$ Figure 6.7 are used as initial perturbations.
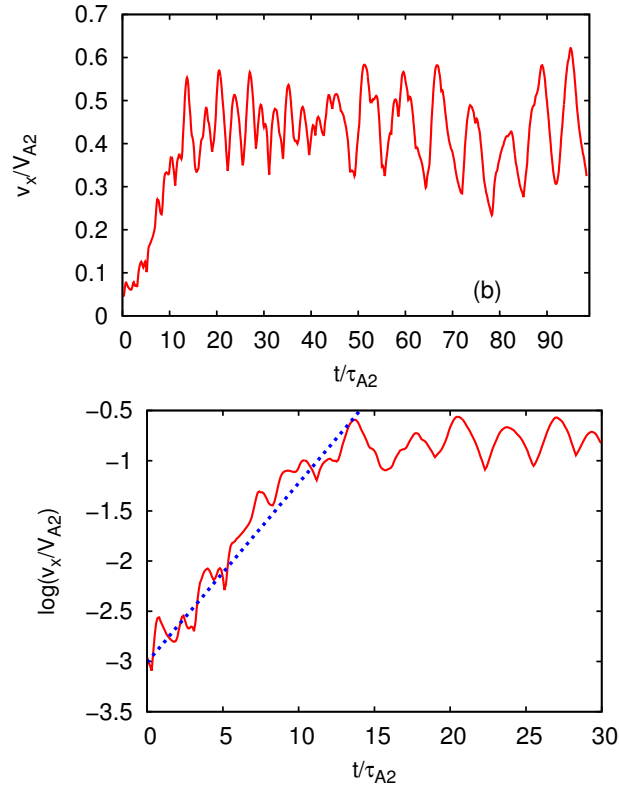
6.4.2 Nonlinear KHI and Magnetosonic Wave Emission with Arbitrary Initial Perturbation

In this section the same perturbation as in *Lai and Lyu* [2006] is used and evolution of KHI and magnetosonic wave emission from MHD shear flow boundaries is investigated. It is suggested in *Lai and Lyu* [2006] that these emitted waves were a result of nonlinearity, i.e. magnetosonic wave emission can only occur during nonlinear stages of the KHI. In chapter 5 of this thesis, emission of magnetosonic waves is shown to occur during linear stages of the KHI. Therefore, nonlinearity should not be a necessary condition for wave emission.

A 2-D model of a shear flow boundary is considered with a boundary layer thickness Δ_x with all zero order quantities varying only along the x-direction. Following hyperbolic tangent function is used to set up the background equilibrium across the boundary;

$$g_0(x) = \frac{g_{01} + g_{02}}{2} + \frac{g_{01} - g_{02}}{2} tanh\left(\frac{x}{a}\right),$$ (6.12)

where the variable $g_0(x)$ represents any background parameters such as $B_0(x), V_0(x), \rho_0(x)$, and a is proportional to the boundary thickness, $\Delta_x = 3a$. We assume the background velocity in region 1, V_{01} along y-direction and zero in region 2, $V_{02} = 0$. The background magnetic fields,

B_{01}, B_{02}, are assumed to lie in $y - z$ plane. All the background values are assumed to be uniform in y and z direction and only vary along x direction across the boundary. The background plasma pressure is chosen such that the total pressure is uniform across the boundary, which means $P_{01} + B_{01}^2/2 = P_{02} + B_{02}^2/2$ with the normalization used in FLASH code. The boundary conditions along y is set as *periodic*, wrap around, and along x is set as *outflow*, zero gradient.

Initial velocity which satisfies the condition that $\nabla \cdot \delta V = 0$ adapted from *Lai and Lyu* [2006] is given to FLASH code to trigger KHI. The initial velocity perturbation is described as;

$$\delta v_x = -\delta v_0 \, sech\left(\frac{x}{a}\right) sin\left(\frac{2\pi y}{\lambda_y}\right),\tag{6.13}$$

$$\delta v_y = \delta v_0 \frac{\lambda_y}{2\pi a} sech\left(\frac{x}{a}\right) tanh\left(\frac{x}{a}\right) cos\left(\frac{2\pi y}{\lambda_y}\right).\tag{6.14}$$

Above initial perturbation is periodic in the y-direction and finite extend in the x-direction. Wavelength is λ_y and perturbation decays along x with a spatial decay length a [*Lai and Lyu*, 2006].

The physical parameters chosen are applicable to various MHD shear flow boundaries; magnetosphere - magnetosheath boundary [*Nakai and Ueno*, 2011; *Hwang et al.*, 2011; *Agapitov et al.*, 2009; *Gnavi et al.*, 2009; *Foullon et al.*, 2008; *Hasegawa et al.*, 2006; *Owen et al.*, 2004, e.g.,], BBF flow channel boundaries in the central plasmasheet [e.g., *Angelopoulos et al.*, 1994; *Grigorenko et al.*, 2012; *Ma et al.*, 2012], and shear flow boundaries in the solar coronal regions [e.g., *Andries and Goossens*, 2001; *Foullon et al.*, 2013; *Ofman and Thompson*, 2011; *Nykyri and Foullon*, 2013; *Cécere et al.*, 2014]. We have chosen Flash code normalization parameters as $\varrho_0 = \rho_{02}$, $v_0 = V_{A2} = B_{02}/\sqrt{(\rho_{02}\mu_0)}$, and $\Re_0 = R_E$. Corresponding normalization parameters are then $P_0 = \rho_{02} V_{A2}^2$, $B_{02} = V_{A2}\sqrt{\rho_{02}\mu_0}$, and $\tau_{A2} = R_E/V_{A2}$. The wavenumber is normalized with the thickness of the transition layer Δ_x. With this normalization scheme the background plasma parameters are set as, $\rho_{01} = \rho_{02} = 1$, $B_{01} = 1.25$, $B_{02} = 1$. $P_{01} = 0.4$, $P_{02} = 0.7$, $\beta_1 = 0.5$, and $\beta_2 = 1.4$. Here, $\beta_{1,2} = P_{01,02}/(B_{01,02}^2/2\mu_0)$ are the plasma beta values in regions 1 and 2. The flow velocity in region 2 is set to zero, while different values of flow velocity in region 1 is considered. The direction of background magnetic fields is varied and emission of magnetosound with and without the effects of magnetic tension is investigated.

The results of the simulations show that nonlinearity is a sufficient but not a necessary condition for magnetosonic wave emission from an MHD shear flow boundary. We have considered

only flow velocities corresponding to $M_{F2} \geq 1$, since MHD wave emission is found to be possible for this range of flow speed values in chapter 5 of this thesis.

6.4.3 Wave Emission Due to KHI in the Absence of Magnetic Tension

In this section, we investigate the KHI and MHD wave emission under the condition that magnetic tension is zero. When the background magnetic fields are set along z-direction in both regions for the model described in the previous section, the effects of magnetic tension is removed from the boundary. Flow in region 1 V_{01} is set along y. We investigate the dependence of the KHI growth rates on the normalized wave number at four different flow speed values in region 1. Figure 6.11 displays the variation of the normalized growth rates with respect to $k_y \Delta_x$ for
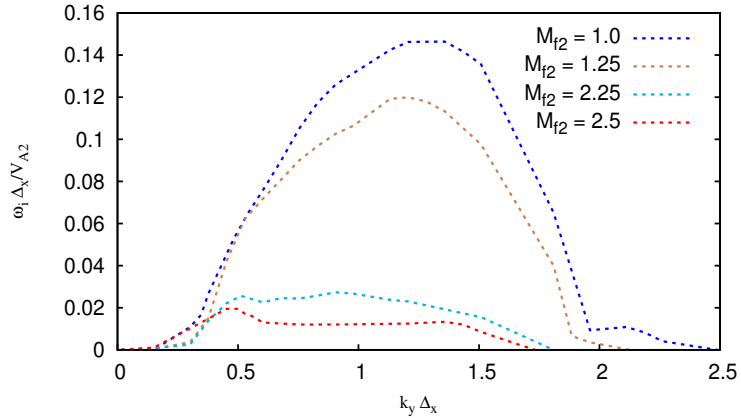
Figure 6.11: Growth rates vs $k_y \Delta x$, for M_{F2} varying from 0.75 - 2.5. Growth rate and wavelengths of the fastest growing modes decrease as M_{F2} increases. Flow speed values of $M_{F2} > 1$ is chosen since MHD wave emission is not found to be possible for smaller flow speeds. $k_y \Delta_x$ values at which the maximum growth occur decreases as M_{F2} increases.

M_{F2} values 1, 1.25, 2.25, and 2.5. The growth rates reach to a maximum and then decreases to zero for all shear flow values considered. Figure 6.11 displays that the growth rate and wavenumber of fastest growing modes decrease with increasing M_{F2}. These results agrees with linear results obtained in chapter 5. The wave emission starts for flow speed values corresponding to $M_{F2} \geq 2.25$. However, as M_{F2} increases beyond 2.5, wave emission process starts happening only at nonlinear stages. There is no growing mode after $M_{F2} = 6.5$.

For the flow speed values corresponding to $M_{F2} \leq 2.25$, wave propagation is not observed

both in linear and in nonlinear stages. Figure 6.12 shows the maximum value of perpendicular velocity change over the time for flow speed corresponding to $M_{F2} = 1$ and $k_y\Delta_x = 0.83$. It is seen on the Figure 6.12 that linear growth of v_x/V_{A2} saturates at normalized time $t/\tau_{A2} \simeq 55$ and magnetosonic wave emission is not present. If wave emission is existent, wavy structures would be seen on the profile of the v_x velocity component (see Figure 6.14 panel (a)). KHI growth rate form above graph is calculated as $\omega_i\Delta_x/V_{A2} = 0.13$.
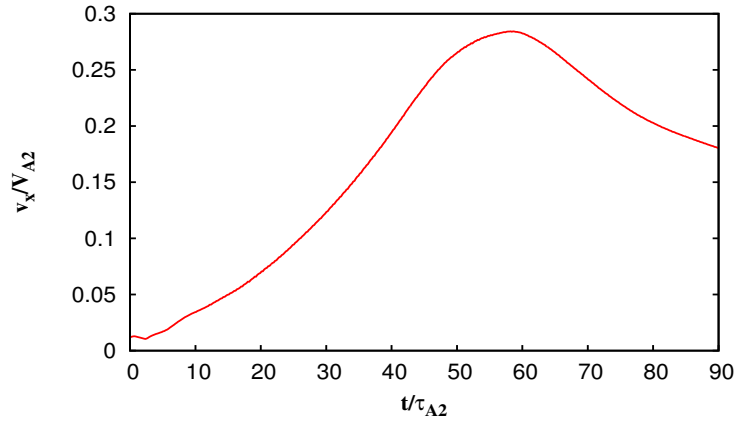
Figure 6.12: Growth of v_x component with t/τ_{A2} for $M_{F2} = 1.0$ and $k_y\delta_x = 0.83$. It is possible to conclude from this plot that MHD wave emission is not possible at any stages of the KHI. If present, emission of magnetosound would show wavy structures on the growth of v_x profile (see Figure 6.14).

Figure 6.13 shows density profile superposed with velocity vector at normalized time $t/\tau_{A2} = 51.35$. Only KHI vortices without any sign of emission of magnetosound are seen on Figure 6.13. We have investigated the process until normalized time $t/\tau_{A2} = 300$ and found that neither linear nor nonlinear stages produce wave emission. We have also investigated different $k_y\Delta_x$ and shear flow values where emission of magnetosound is found not to be possible as long as $M_{F2} < 2.25$.

KHI growth rates decrease with increasing flow speeds and wave emission becomes possible at $M_{F2} \geq 2.25$. Wave emission is found to be present at both linear and nonlinear stages of the KHI. Figure 6.14 show the growth of v_x velocity (panel (a)) and calculated growth rate with log linear fit (panel (b)) for $M_{F2} = 2.5$ and $k_y\Delta_x = 0.45$. Growth of v_x saturates at $t/\tau_{A2} = 180$ after which it decays and settles into a quasi steady oscillations. Sharp peak obtained at normalized
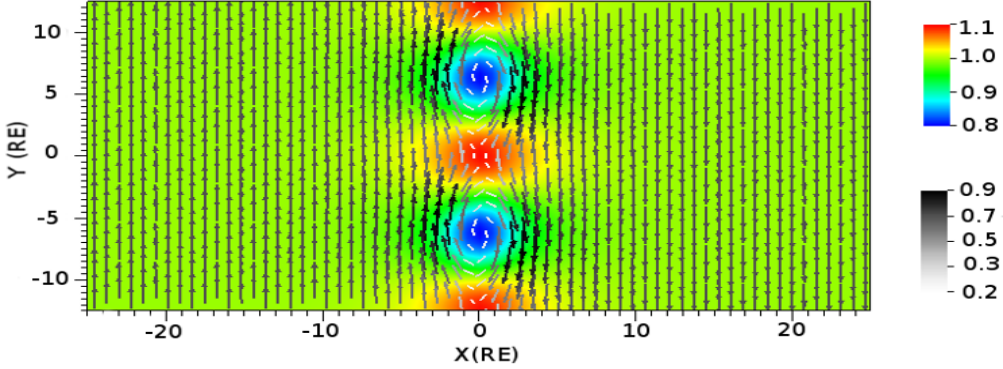
Figure 6.13: Superposed plot of density and total velocity at $t/\tau_{A2} = 51.5$ for flow speed value corresponding to $M_{F2} = 1.0$. KHI vortices are visible while wave emission is not present.

time $t/\tau_{A2} \simeq 25$ is possibly due to resonances which is out of the scope of this thesis. Normalized growth rate is calculated from log linear fit in panel (b) in Figure 6.14 as $\omega_i \Delta_x / V_{A2} = 0.02$. The small value of growth rate is due to MHD wave emission controlling the KHI evolution on the boundary. When the wave emission starts the KHI growth is hindered since energy available on the boundary is efficiently carried away with the magnetosonic waves emitted.

Figures 6.15 and 6.16 show density profile and vorticity at normalized time $t/\tau_{A2} = 139.5$. Figure 6.15 shows wave emission into both region with stronger emission into the region 1. Figure 6.16 shows that the vortices are not very strongly rolled up due to the wave emission process. Even at the nonlinear stages of the KHI, rolled up vortices are not found to be possible if wave emission is occurring along the boundary.

Plasma and magnetic pressure variations are shown in Figure 6.17 at the same normalized time as in Figure 6.15 at positions $x = -7.5 R_E$ (panel (a)), $x = 0 R_E$ (panel (b)), and $x = 7.5 R_E$ (panel (c)). These are corresponding region 1, along the boundary and region 2, respectively. Pressure variations are in phase in both regions implying that the emitted waves are fast MHD waves. This shows that the primary KHI is occurring on the shear flow boundary [*Turkakin et al.*, 2013]. An MHD shear flow boundary may also emit slow magnetosonic waves which would be due to the secondary KHI which is subject to future work.
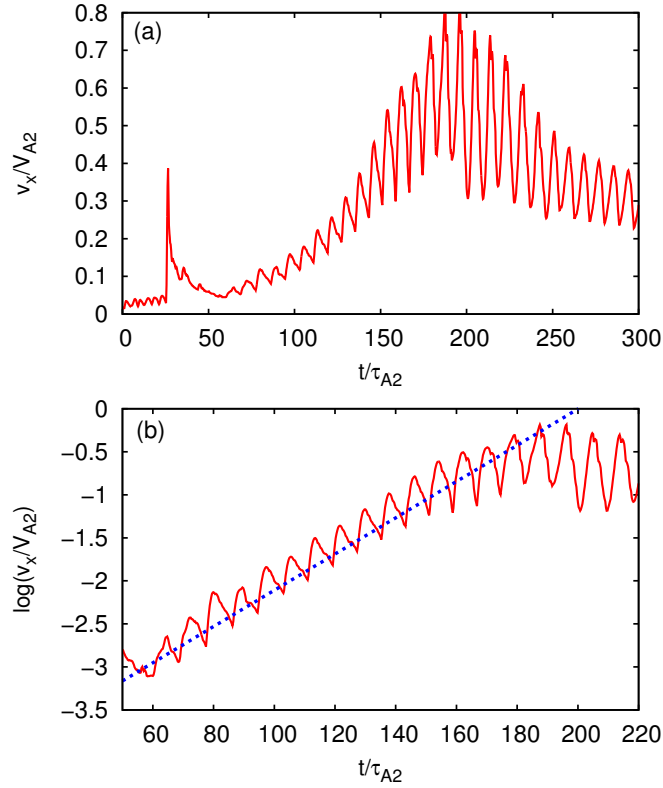
Figure 6.14: Growth of v_x component with t/τ_{A2} (panel (a)) and log linear fit (panel (b)) for $M_{F2} = 2.5$, and $k_y\Delta_x = 0.45$. Normalized growth rate is calculated from panel (b) is $\omega_i\Delta_x/V_{A2} = 0.02$.
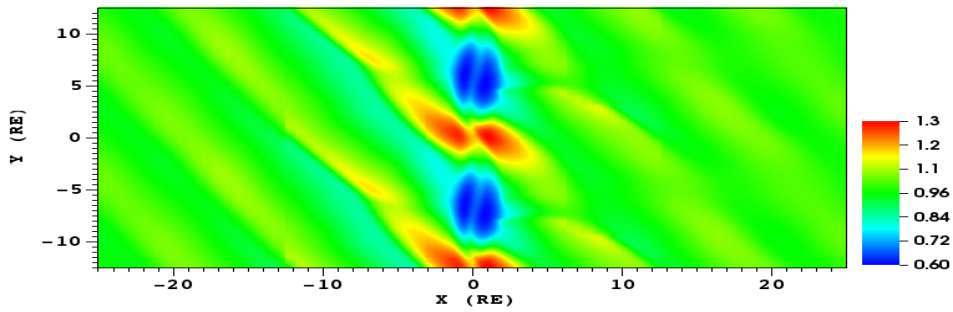
Figure 6.15: Density profile at $t/\tau_{A2} = 139.5$ for $\theta_1 = \theta_2 = 90°$, $M_{fast2} = 2.5$ and $k_y\Delta_x = 0.45$.
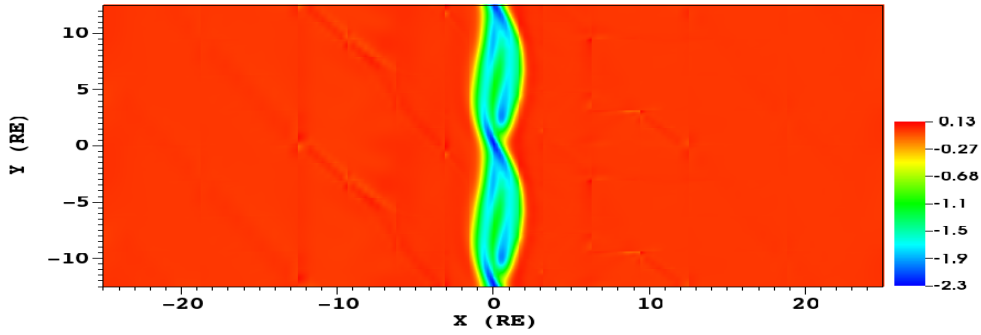
Figure 6.16: Vorticity at $t/\tau_{A2} = 139.5$ at the same time as Figure 6.15, $M_{fast2} = 2.5$.
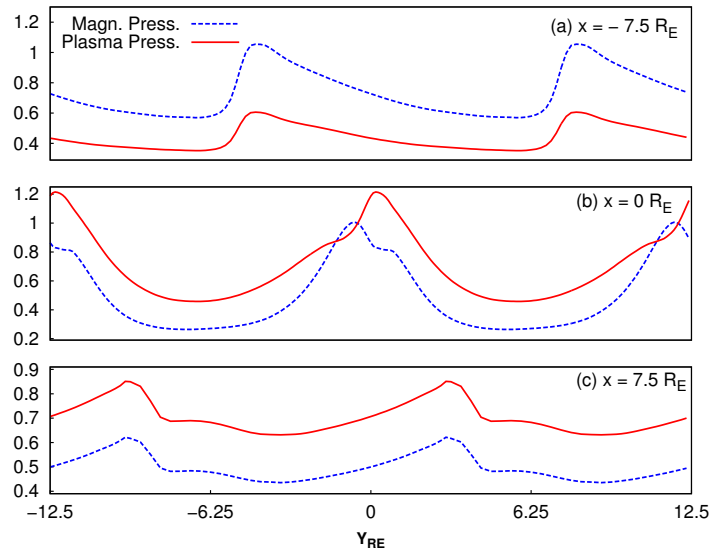
Figure 6.17: Pressure perturbations along y-direction at three different positions along x obtained from Figure 6.15. Panel (a) is for $x = -7.5$ in region 1, panel (b) is for $x = 0$, and panel (c) is for $x = 7.5$ in region 2. Variations of plasma and magnetic pressure are in phase implying that emitted waves are fast MHD waves in both regions.

As the flow speed increases, wave emission starts to happen closer to the nonlinear stages and only in nonlinear stages for $M_{F2} \geqq 3$. Figure 6.18 shows this fact for flow speed value corresponding to $M_{F2} = 3$.
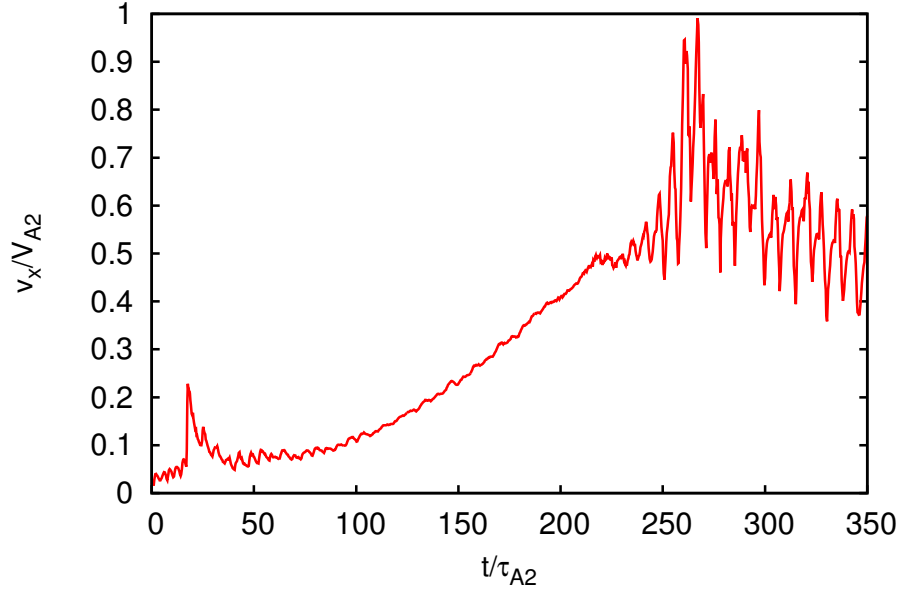
Figure 6.18: Growth of v_x component with t/τ_{A2} for flow speed corresponding to $M_{F2} = 3.0$. Spontaneous wave emission is not obtained in the linear stages of KHI for this flow speed value.

When we include a magnetic field component parallel to the boundary the KHI growth starts at a later time. Although the growth rate is not smaller than zero magnetic tension case, growth in amplitude is smaller. Figure 6.19 shows the growth of v_x, panel (a), and log linear fit, panel (b), for $M_{F2} = 2.5$, $\theta_1 = 60°, \theta_2 = 30°$, and $k_y \Delta_x = 0.45$. KHI growth rate is calculated as $wi\Delta_x/V_{A2} = 0.02$ and is quickly saturated due to the strong magnetic tension in both sides. Density profile at $t/\tau_{A2} = 204.5$ shows that strong wave emission is present in linear stages of the KHI for this configuration into both regions. This result agrees with the results obtained in chapter 5.
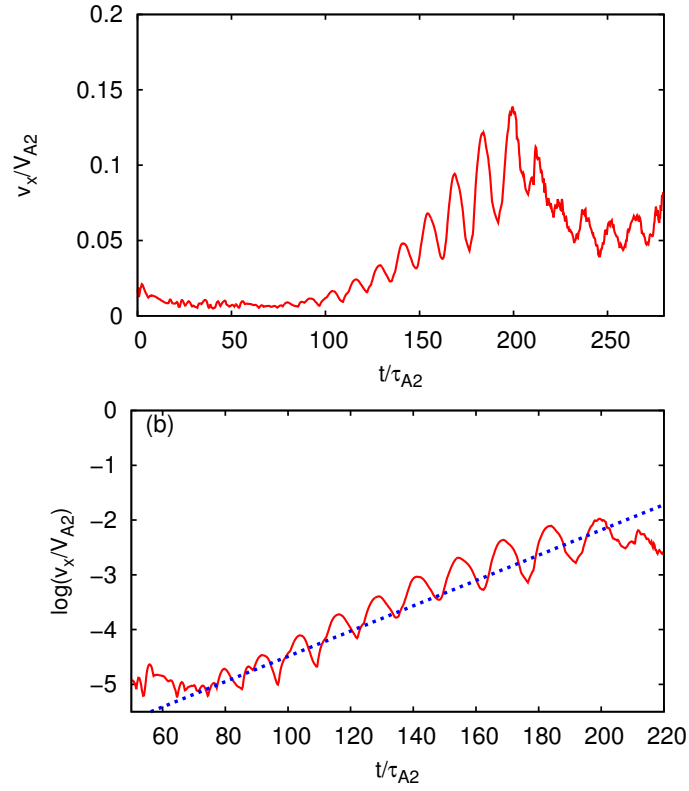
Figure 6.19: Growth of v_x component with t/τ_{A2} with parameters; $M_{F2} = 2.5$, $\theta_1 = 60°$, $\theta_2 = 30°$, and $k_y \Delta_x = 0.45$.
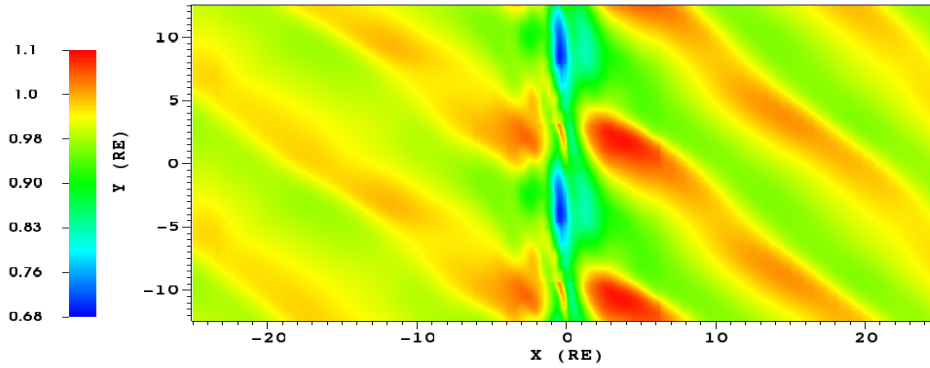
Figure 6.20: density at $t/\tau_{A2} = 204.5$ from runs with parameters in this section, $M_{fast2} = 2.5$ with angles changed to $\theta_1 = 60°$, $\theta_2 = 30°$.

We have also found not only the values of background parameters, but also the type of perturbations have significant effects on the growth of the KHI and emission of magnetosound from an MHD shear flow boundary. Not all type of perturbations evolve to give a result of KHI and emission of magnetosound. This fact is tested using the same perturbations as in *Rankin et al.* [1993] and *Waagan et al.* [2011] and with the background parameters above, for which MHD wave emission is obtained. The KHI growth is found to be possible depending on the shear flow speed, however, MHD wave emission is not obtained. This result is significant in showing that along the MHD shear flow boundaries in the solar-terrestrial environment and other remote astrophysical objects the KHI and magnetosonic wave emission is not possible for all type of initial perturbation.

6.5   Applications to Various MHD Shear Flow Boundaries

Kelvin-Helmholtz Instability (KHI) is often observed along shear flow boundaries in the solar atmosphere, in interplanetary space and planetary magnetospheres. It is also possible on the shear flow boundaries in remote astrophysical objects such as accretion disks, black holes and neutron stars. KHI controls physical processes such as plasma mixing, energy and momentum transfer in between two different media in both sides of these boundaries.

As studied in chapter 3 of this thesis, the KHI is generated due the velocity shear between magnetosheath and magnetosphere flows of the Earth and it plays momentous roles in many magnetospheric phenomena. Such are generation of geomagnetic pulsations [*Agapitov et al.*, 2009; *Villante*, 2007; *Rae et al.*, 2005; *Chen and Hasegawa*, 1993; *Miura and Pritchett*, 1982; *Walker*, 1981; *Southwood*, 1974], inducing magnetic reconnection and plasma mixing at the magnetopause during northward Interplanetary Magnetic Field(IMF) [*Nakai and Ueno*, 2011; *Pegoraro et al.*, 2008; *Nakamura et al.*, 2006; *Fairfield et al.*, 2000], causing momentum and energy transport across the magnetopause [*Hasegawa et al.*, 2006; *Kivelson and Chen*, 1995; *Miura*, 1984; *Pu and Kivelson*, 1983b], and initiating field line resonances [*Mann et al.*, 1999; *Mills and Wright*, 2000]. The KHI generated surface waves on the BBF boundaries in the inner plasmasheet, which is also studied in chapter 4 of this thesis, may also be a possible motive for the substorms expansion onsets which are key elements for solar wind interaction with the Earth's magnetosphere and the ionosphere [*Uberoi*, 2006; *Lui*, 2004; *Yoon et al.*, 1996; *Rae et al.*, 2005].

KHI on the MHD shear flow boundaries is also a significant tool for understanding many physical processes in solar atmosphere heliopause, and remote astrophysical objects such as accretion disks, galactic centers molecular clouds, and cometary tails. For instance, in the solar atmosphere KHI is a process that could lead to plume/interplume mixing, provide a source for Alfvénic fluctuations [*Andries and Goossens*, 2001; *Andries et al.*, 2000] and mixing of Coronal Mass Ejection (CME) regions with the outside region of the solar corona [*Foullon et al.*, 2011, 2013; *Nykyri and Foullon*, 2013; *Möstl et al.*, 2013]. On the heliopause, the boundary between the solar system and interstellar wind, the KHI can affect the energy transport from interstellar medium into the solar system [*Ruderman and Fahr*, 1993, 1995; *Taroyan and Ruderman*, 2011]. KHI is also possible along the boundary of cometary plasma tails which causes the mixing of the solar wind and cometary tail plasmas [e.g., *Ershkovich and Mendis*, 1986; *Niedner et al.*, 1983]. In protoplanetary disks, the KHI inhibits the settling of dust particles and stops planetary formation by mixing the dust with the gas [*Johansen et al.*, 2006; *Baranov*, 2009]. KHI is also suggested to be an efficient mechanism for mixing chemical elements in interstellar medium [e.g., *Berné and Matsumoto*, 2012] and deformation of the astrophysical jets [e.g., *Micono et al.*, 2000; *Lai and Lyu*, 2008].

We introduce emission of magnetosound due to the action of the KHI along MHD shear flow boundaries as a new efficient way of energy transport in between two media. Results shown may be applicable to all of the above mentioned shear flow boundaries.

Chapter 7

Conclusions and Future Work

7.1 Conclusions

In this thesis we have investigated the Kelvin-Helmholtz Instability (KHI) and emission of magnetosound due to KHI along various MHD shear flow boundaries in the solar-terrestrial environment and solar corona. Although parameters used are applicable to these environments, characteristic behavior of the KHI and MHD wave emission will be similar in remote astrophysical objects where KHI is also possible.

In chapter 1 we have introduced the background information about the solar-terrestrial environment, MHD approach for studying plasmas and MHD waves which are closely related to the KHI on MHD shear flow boundaries.

In chapter 2 we show background and theory for the KHI on MHD shear flow boundaries. Derivations for three different approaches for solving the KHI along MHD shear flow boundaries are shown in detail. First the linear development of the KHI where transition thickness between two plasma regions is assumed to be zero is considered and detailed derivations are shown. Two different boundary conditions are considered for zero transition thickness approximation, semi-infinite plasmas in both regions and a boundary is added in one of the regions while other plasma region is still assumed to be semi-infinite. Following, derivations for non-zero transition thickness with two semi-infinite plasmas on both sided of the boundary is shown. In this chapter a possible relation between the KHI and Negative Energy Waves (NEWs) is also discussed.

Chapter 3 shows the first paper published on the primary and secondary KHI along the

magnetopause boundary using bounded and unbounded models and a zero thickness boundary approach. We show that fast MHD waves generate the primary KHI and slow MHD waves generate the secondary KHI along the magnetopause boundary. It is found that at sufficiently high flow speed, a KHI unstable boundary separating two semi-infinite plasma regions is always ultimately stabilized to KHI growth at an upper cut-off velocity. If an inner boundary is included in one plasma region, however, this stabilization is removed. Phase velocity diagrams of fast and slow MHD waves that correspond to growing modes of the KHI are shown. These diagrams have shown that the KH unstable fast and slow MHD modes behave as expected on the near-Earth flanks. On the deeper flank and into the magnetotail, where magnetic fields in the magnetosphere and magnetosheath become more aligned, we have identified new intermediate-fast modes which can have phase speeds above the Alfvén speed and cannot propagate exactly perpendicularly to the magnetic field. In the plasma frame, the primary unstable KHI waves show fast MHD wave behavior in both the magnetosphere and magnetosheath, while secondary KHI waves show slow wave behavior in the magnetosphere and fast wave behavior in the magnetosheath. It is found that the secondary KHI occurs at slower flow speeds and grows more slowly than the primary KHI. Although the growth of the secondary KHI is only possible for a narrow range of angles between the magnetosphere and magnetosheath magnetic fields, it is found to be the most probable means of energy transportation on the dayside magnetosphere. This is due to the fact that the flow speed needed to generate primary KHI is usually not observed on the dayside. Further down the flanks and on the nightside magnetopause, both the primary and secondary KHI lower cut-off speeds can be reached and thus energy propagation into the magnetosphere from the magnetosheath can be possible due to both. Doppler shifted frequencies of the KHI waves have shown that both fast and slow KHI waves are also NEWs - they have negative Doppler shifted frequencies. This result suggests that, the same as NEWs, the KHI waves also extracts energy from the background flow through the work done by the Maxwell and Reynolds stresses.

Chapter 4 shows the second paper published on the KH unstable magnetotail flow channels. This work is significant in providing the first theoretical work which explains the link between Bursty Bulk Flow (BBFs), the KHI, and excitation of wave modes in the central plasma sheet which are often observed and referred to tail flapping. Our work is the first to consider emission of magnetosound due to KHI from the BBF channels towards the flanks of the magnetopause. We have investigated MHD oscillations of the channel in both kink and sausage modes for the KHI

and found that both the primary and the secondary KHI drive MHD waves. We have also shown that the yet unexplained flow channel breaking is likely the KHI where emitted magnetosonic waves (fast and slow MHD waves) remove the energy from the flow. MHD wave emission due to the KHI is found to occur at flow speed values past the peak growth rates when KHI surface waves develop into propagating modes.

In chapter 5 we investigated the KHI and emission of magnetosound from an MHD shear flow boundary with a finite thickness. We have assumed two semi-infinite plasmas on both sides of the MHD boundary. We have found that the KHI and emission of MHD waves are two competing processes and the fastest growing modes of the KHI surface waves do not coincide with efficient wave energy transport. Directions of the magnetic fields on both sides of the boundary are found to have significant impact on the development of the KHI and MHD wave emission. MHD wave emission is found to be weak when the growth rates of the KHI surface waves are maximum, which occurs when the ambient magnetic fields on both sides of the boundary are perpendicular to the shear flow boundary. The efficiency of the wave emission increases with increasing magnetic tension, with magnetic fields components parallel to the boundary. Application of the results to the various MHD shear flow boundaries is also discussed. We have concluded that emission of magnetosound dominates along the nightside magnetopause, within BBFs in the inner plasma sheet, and in Supra-Arcade Downflows (SADs) in the solar corona, while the growth of the KHI surface waves dominates along the dayside magnetopause and Coronal Mass Ejection (CME) boundaries.

In chapter 6 we have investigated the nonlinear evolution of the KHI and MHD wave emission from MHD shear flow boundaries using the FLASH code developed by University of Chicago/Alliance Flash Center. We have tested the efficiency of the code using the same parameter setup as is *Rankin et al.* [1993] and *Waagan et al.* [2011] and our results were in excellent agreement with the results obtained in these papers. Following, we have compared the linear results obtained in chapter 5 with the FLASH code simulation results by using the linear perturbations as initial seed for the growth of the KHI. The KHI growth rates obtained from FLASH simulations were in good agreement with the linear results. Development of the KHI and wave emission are then investigated using an arbitrary perturbation adapted from *Lai and Lyu* [2006]. We have investigated the effect of the magnetic tension by changing the direction of the ambient magnetic fields in the FLASH code simulations as well. Results were in agreement with the

linear results obtained in the chapter 5. We have shown that contrary to what is suggested in *Lai and Lyu* [2006], nonlinearity is a sufficient but not a necessary condition for the wave emission. Our results have shown that the emission of magnetosound is possible both in the linear and nonlinear stages of the KHI depending on the background parameters, specifically the flow speed strength. When the magnetic fields are perpendicular to the boundary in both regions and flow speed values corresponding to $M_{F2} = V_{01}/V_{fast2} < 2.25$ wave emission is not possible in either the linear or nonlinear stages. When flow speed reaches a value corresponding to $M_{F2} \geq 2.25$ MHD wave emission is found to be present in both linear and nonlinear stages. As we continue to increase the flow speed up to $M_{F2} \geq 3$ wave emission becomes mainly possible in the nonlinear stages. We have included magnetic tension by changing the direction of the ambient magnetic fields and found that the growth rates of the KHI wave did not change significantly. The time where the KHI surface wave growth starts is increased however, the KHI surface wave growth is saturated in a shorter time, and the growth of the wave amplitude is found to be smaller than in the zero magnetic tension case. The emission of magnetosound is found to be stronger than that of the zero magnetic tension case. This result suggests that strong wave emission may be the cause for the early saturation of the KHI growth. We have discussed the application of the results in this chapter to various shear flow boundaries in the solar-terrestrial environment and remote astrophysical objects.

Future works may include Using resistive MHD, including inhomogeneities in the plasma regions in both sides of the MHD shear flow boundaries and using two-fluid MHD approach which may have significant impacts on the KHI and emission of magnetosound from MHD shear flow boundaries. We have investigated the secondary KHI, which is generated by slow MHD waves, and wave emission due to the action of the secondary KHI only for the zero thickness boundary approach. Future work on the linear and nonlinear evolution of the secondary KHI for a finite thickness MHD boundary may provide a better understanding of the phenomenon.

Bibliography

Acheson, D. J., On over-reflexion, *J. Fl. Mech.*, *77*, 433–472, 1976.

Agapitov, O., K.-H. Glassmeier, F. Plaschke, H.-U. Auster, D. Constantinescu, V. Angelopoulus, W. Magnes, R. Nakamura, C. Carlson, S. Frey, and J. P. McFadden, Surface waves and field line resonances: A themis study, *J. Geop. Res.*, *114*, 2009.

Allan, W., and A. N. Wright, Large-m waves generated by small-m field line resonances via the nonlinear Kelvin-Helmholtz instability, *J. Geop. Res.*, *102*, 19,927–19,933, 1997.

Andries, J., and M. Goossens, Kelvin-Helmholtz instabilities and resonant flow instabilities for a coronal plume model with plasma pressure, *Astron. and Astrop.*, *368*, 1083–1094, 2001.

Andries, J., and M. Goossens, Energy considerations for linear instabilities of parallel magnetohydrodynamic flows, *Phys. of Pl.*, *9*, 2876–2884, 2002.

Andries, J., W. J. Tirry, and M. Goossens, Modified Kelvin-Helmholtz instabilities and resonant flow instabilities in a one-dimensional coronal plume model: Results for plasma $\beta = 0$, *Astrophys. J.*, *531*, 561–570, 2000.

Angelopoulos, V., W. Baumjohann, C. Kennel, F. Coroniti, M. Kivelson, R. Pellat, R. Walker, H. Lühr, and G. Paschmann, Bursty bulk flows in the inner central plasma sheet, *J. Geop. Res.*, *97*, 4027–4039, 1992.

Angelopoulos, V., C. Kennel, F. Coroniti, R. Pellat, H. Spence, M. Kivelson, R. Walker, C. Russel, W. Baumjohann, W. Feldman, and J. Gosling, Statistical characteristics of bursty bulk flow events, *J. Geop. Res.*, *99*, 21,257–21,280, 1994.

Angelopoulos, V., T. Phan, D. Larson, F. Mozer, R. Lin, K. Tsuruda, H. Hayakawa, T. Mukai, S. Kokubun, T. Yamamoto, D. Williams, R. McEntire, R. Lepping, G. Parks, M. Brittnacher,

G. Germany, J. Spann, H. Singer, and K. Yumoto, Magnetotail flow bursts: Assosiation to global magnetspheric circulation, relatioship to ionospheric activity and direct evidence for localization, *Geop. Res. Lett.*, *24*, 2271–2274, 1997.

Anninos, P., P. C. Fragile, J. Wilson, and S. D. Murray, Three-dimensional moving-mesh simulations of galactic center cloud g2, *Astrophys. J.*, *759*, 132–143, 2012.

Baranov, J. A., Three-dimensional of Kelvin-Helmholtz instability in settled dust layers in protoplanetary disks, *Astrophys. J.*, *691*, 907–921, 2009.

Barranco, J. A., Three-dimensional simulations of Kelvin-Helmholtz instbility in settled dust layers in protoplanetary disks, *Astrophys. J.*, *691*, 907–921, 2009.

Baumjohann, W., and R. A. Treumann, *Basic Space Plasma Physics*, 2nd ed., Imperial College Press, London, 1999.

Baumjohann, W., and R. A. Treumann, *Advanced Space Plasma Physics*, rewised ed., Imperial College Press, Londan, 2001.

Baumjohann, W., G. Paschmann, and H. Lühr, Characteristics of high-speed ion flows in the plasma sheet, *J. Geop. Res.*, *95*, 3801–3809, 1990.

Berné, O., and Y. Matsumoto, The Kelvin-Helmholtz instability on orion: A source of turbulance and chemical mixing, *Astrophys. J. Lett.*, *761*, L4 (5pp), 2012.

Bers, A., *Handbook of Plasma Physics*, North-Holland, Amsterdam, 1983.

Cairns, R. A., The role of negative energy waves in some instabilities of parallel flows, *J. Fl. Mech.*, *92*, 1–14, 1979.

Cécere, M., A. Zurbriggen, E.a nd Costa, and M. Scheneiter, 3D MHD simulation of post-flare Supra-Arcade Downflows in a turbulent current sheet medium, *Astro-ph.SR*, *1*, 2014.

Chandrasekhar, S., *Hydrodynamic and Hydromagnetic Stability*, pp. 481–514, Oxford Univ. Press, 1961.

Chen, S.-H., and A. Hasegawa, A theory of long-period magnetic pulsations: I. steady state excitation of field line resonances, *J. Geop. Res.*, *79*, 1024–1032, 1993.

Chen, S.-H., and M. G. Kivelson, On non-sinusoidal waves at the magnetopause, *Geop. Res. Lett.*, *20*, 2699, 1993.

Chen, Y., H. Song, L. Li, Z. Xia, H. Wu, and L. Xing, Streamer wave driven by Coronal Mass Ejections, *Astrophys. J.*, *714*, 644–651, 2010.

Contin, J. E., F. T. Gratton, and C. J. Farrugia, Theoretical results on the latitude dependence of the Kelvin-Helmholtz instability at the day-side magnetopause of northward interplanetary magnetic field, *J. Geop. Res.*, *108*, 2003.

Dubey, A., L. Reid, and R. Fisher, Introduction to flash 3.0, with application to supersonic turbulance, *Physica Scr.*, p. 014046, 2008.

Erkaev, N., V. Semenov, and H. Biernat, Magnetic double gradient mechanism for flapping oscillations of a current sheet, *Geop. Res. Lett.*, *35*, 2008.

Ershcovich, A. I., and A. A. Chernikov, Non-linear waves in type-1 comet tails, *Planet. Space Sci.*, *21*, 663–670, 1973.

Ershkovich, A. I., Kelvin-Helmholtz instability in type-1 comet tails and associated phenomena, *Space Sci. Rev.*, *25*, 3–34, 1979.

Ershkovich, A. I., and D. A. Mendis, The stability of the cometary plasma tail and rays, *Earth, Moon, and Planets*, *36*, 127–134, 1986.

Fairfield, D. H., A. Otto, S. Kokobun, R. P. Lepping, J. T. Steinberg, A. J. Lazarus, and T. Yamamoto, Geotail observation of Kelvin-Helmholtz instability at the equatorial magnetotail boundary for parallel northward fields, *J. Geop. Res.*, *105*, 21,159–21,173, 2000.

Farrugia, C. J., F. Gratton, L. Bender, H. Biernat, N. Erkaev, J. Quinn, R. Torbert, and V. Dennisenko, Charts of joint Kelvin-Helmholtz and Rayleigh-Taylor instabilities a the dayside magnetopause for strongly northward interplanetary magnetic field, *J. Geop. Res.*, *103*, 6703–6727, 1998.

Fejer, J. A., Hydromagnetic reflection and refraction at a fluid velocity discontinuity, *Phys. of Fl.*, *6*, 508–512, 1963.

Fejer, J. A., Hydromagnetic stability at a fluid velocity discontinuity between compressible fluids, *Phys. of Fl.*, *7*, 499–503, 1964.

Feng, L., B. Inhester, and W. Gan, Kelvin-Helmholtz instability of a coronal streamer, *Astrophys. J.*, *774*, 2013.

Forsyth, C., M. Lester, R. Fear, E. Lucek, I. Dandouras, A. Fazakerley, H. Singer, and T. Yeoman, Solar wind and substorm excitation of the wavy current sheet, *Ann. Geop.*, *27*, 2457–2474, 2009.

Foullon, C., C. J. Farrugia, A. N. Fazakerley, C. J. Owen, F. T. Gratton, and R. B. Torbert, Evolution of Kelvin-Helmholtz activity on the dusk flank magnetopause, *J. Geop. Res.*, *113*, 2008.

Foullon, C., C. J. Farrugia, C. J. Owen, A. N. Fazakerley, and F. R. Gratton, Kelvin-Helmholtz multi-spacecraft studies at the earth's magnetopause boundaries, *Twelweth Int. Solar Wind Conf*, *1216*, 367–370, 2010.

Foullon, C., E. Verwichte, V. Nakariakov, K. Nykyri, and C. Farrugia, Magnetic Kelvin-Helmholtz instability at the sun, *Astrophys. J. Lett.*, *729*, 2011.

Foullon, C., E. Verwichte, K. Nykyri, J. Markus, and I. G.H., Kelvin-Helmholtz instability of the CME reconnection outflow layer in the solar corona, *Astrophys. J.*, *767*, 2013.

Fujita, S., K.-H. Galssmeier, and K. Kamide, MHD waves generated by the Kelvin-Helmholtz instability in a nonuniform magnetosphere, *J. Geop. Res.*, *101*, 27,317–27,325, 1996.

Gnavi, G., F. T. Gratton, C. J. Farrugia, and L. E. Bilbao, Supersonic mixing layers: Stability of magnetospheric flanks models, *J. of Phys.:Conf. Series*, *166*, 2009.

Golovchanskaya, I., and Y. Maltsev, On the identification of plasma sheet flapping waves observed by cluster, *Geop. Res. Lett.*, *32*, 2005.

González, A. G., and J. Gratton, The role of a density jump in the Kelvin-Helmholtz instability of a compressible plasma, *J. Pl. Phys.*, *52*, 223–244, 1994.

González, A. G., J. Gratton, F. T. Gratton, and C. J. Farrugia, Compressible Kelvin-Helmholtz instability at the terrestrial magnetopause, *Brazillian Jour. of Phys.*, *32*, 945–963, 2002.

Gratton, F. T., G. Gnavi, C. J. Farrugia, and L. Bender, On the MHD boundary of Kelvin-Helmholtz stability diagram at large wavelengths, *Brezillian J. Phys.*, *34*, 1804–1813, 2004.

Grigorenko, E. E., R. Koleva, and J.-A. Sauvaud, On the problem of plasma sheet boundary layer indentification from plasma moments in earth's magnetotail, *Ann. Geop.*, *30*, 1331–1343, 2012.

Guillochon, J., M. Dan, E. Ramirez-Ruiz, and S. Rosswog, Surface detonations in double degenerate binary systems triggered by accreation stream instabilities, *Astrophys. J. Lett.*, *709*, L64–L69, 2010.

Gurnett, D., and A. Bhattacharjee, *Introduction to Plasma Physics*, pp. 75–85, Cambridge University Press, 2004.

Hasegawa, H., M. Fujitomo, T.-D. Phan, H. Réme, H. Balogh, M. W. Dunlop, C. Hashimoto, and R. TanDokoro, Transport of solar wind into earth's magnetosphere through rolled-up Kelvin-Helmholtz vortices, *Lett. to Nat.*, *430*, 755–758, 2004.

Hasegawa, H., M. Fujitomo, K. Takagi, Y. Saito, and Réme, Single-spacecraft detection of rolled-up Kelvin-Helmholtz vortices at the flank magnetopause, *J. Geop. Res.*, *111*, 2006.

Hwang, K.-J., M. M. Kuznetsova, F. Sahraoui, M. L. Goldstein, E. Lee, and G. K. Parks, Kelvin-Helmholtz waves under southward IMF, *J. Geop. Res.*, *116*, 2011.

Itoh, K., H. Nakamura, H. Kumamaru, and Y. Kukita, Internal-shear mode instabilities on high-speed liquid jet: I characteristics of linear solutions, *J. of Nucl. Sci. and Tech.*, *41*, 802–808, 2004.

Jean, R., and J. Laurent, The baroclinic secondary instability of the two-dimensional shear layer, *Phys. of Fl.*, *12*, 2489–2505, 2000.

Joarder, P. S., V. M. Nakariakov, and B. Roberts, A manifestation of negative energy waves in the solar atmosphere, *Solar Phys.*, *176*, 285–297, 1997.

Johansen, A., T. Henning, and H. Klahr, Dust sedimentation and self-sustained Kelvin-Helmholtz turbulence in protoplanetary disk midplanes, *Astrophys. J.*, *643*, 1219–1232, 2006.

Kamaya, H., Stability of small-scale Kelvin-Helmholtz instbility for two-component protogalaxies, *Astrophys. J.*, *506*, 289–291, 1998.

Kato, Y., M. Tajiri, and T. Taniuti, Propagation of hydromagnetic waves in collisionless plasma. 1, *J. of Phys. Soc. of japan*, *21*, 765–777, 1966.

Kivelson, M. G., and S.-H. Chen, The magnetopause: Surface waves and instabilities and their possible dynamical consequences, *Phys. of Magnetosp.*, *Geop. Monogr. 90*, 257–268, 1995.

Kivelson, M. G., and C. Russell, *Introduction to Space Physics*, pp. 329–331, Cambridge Unive. Press, 1995.

Kozlov, D. A., and A. S. Leonovich, Transformation and absorption of MHD oscillations in plane-stratified models of the Earth's magnetosphere, *Geomagn. and Aeron.*, *51*, 1165–1173, 2011.

Lai, S. H., and L. H. Lyu, Nonlinear evolution of MHD Kelvin-Helmholtz instability in a compressible plasma, *J. Geop. Res.*, *111*, 2006.

Lai, S. H., and L. H. Lyu, Nonlinear evolution of jet-flow-associated Kelvin-Helmholtz instability in MHD plasmas and the formation of mach-cone-like plane waves, *J. Geop. Res.*, *113*, 2008.

Landau, L. D., and E. M. Lifshitz, *Fluid Mechanics*, pp. 259–262, Pergamon, Oxford, 1987.

Lashmore-Davies, C. N., Negative energy waves, *J. Pl. Phys.*, *71*, 101–109, 2005.

Lavraud, B., and J. E. Borovsky, Altered solar wind-magnetosphere interaction at low mach numbers: Coronal Mass Ejection, *J. Geop. Res.*, *113*, 2008.

Lavraud, B., J. E. Borovsky, A. J. Ridley, E. W. Pogue, M. F. Thomsen, A. N. Réme, A. N. Fazakerley, and L. E. A., Strong bulk plasma acceleration in earth's magnetosheath: A magnetic slingshot effect?, *Geop. Res. Lett.*, *34*, 2007.

Lawrence, G. A., F. K. Browand, and L. G. Redekopp, The stability of a sheared density interface, *Phys. of Fl.*, *3*, 2360–2370, 1991.

Lee, A. T., E. Chiang, X. Asay-Davis, and J. Barranco, Forming planetesimals by gravitational instability. I. the role of richardson number in triggering the Kelvin-Helmholtz instbility, *Astrophys. J.*, *718*, 1367–1377, 2010a.

Lee, A. T., E. Chiang, X. Asay-Davis, and J. Barranco, Forming planetesimals by gravitational instability. II. how sudt settles to its marginal stable state, *Astrophys. J.*, *725*, 1938–1954, 2010b.

Lee, L. C., and J. V. Olson, Kelvin-Helmholtz instability and the variation of geomagnetic pulsation activity, *Geop. Res. Lett.*, *7*, 777–780, 1980.

Lerche, I., Validity of hydromagnetic approach in discussing instability of the magnetospheric boundary, *J. Geop. Res.*, *71*, 2365–2371, 1966.

Lindzen, R. S., and A. J. Rosendhal, Instabilities in a stratified fluid having one critical level: III. Kelvin-Helmholtz instabilities as overreflected waves, *J. Atm. Sci.*, *40*, 530–542, 1982.

Liu, W., and L. Ofmann, Advances in observing various coronal EUV waves in the SDO era and their seismological applications, *Solar Phys.*, *289*, 3233–3277, 2006.

Lui, A. T. Y., Potential plasma instabilities for the substorm expansion onset, *Space Sci. Rev.*, *113*, 127–206, 2004.

Ma, Y., C. Shen, V. Angelopoulos, A. T. Y. Lui, X. Li, H. U. Frey, M. Dunlop, H. U. Auster, J. P. McFadden, and D. Larson, Tailward leap of multiple expansion of plasmasheet during a moderately intense substorm: THEMIS observation, *J. Geop. Res.*, *117*, 2012.

Malik, M. R., F. Li, and C.-L. Chang, Cross-flow disturbances in three-dimensional boundary layers: Nonlinear development, wave interaction and secondary instability, *J. Fl. Mech.*, *268*, 1–36, 1994.

Mann, I. R., A. N. Wright, K. J. Mills, and V. M. Nakariakov, Excitation of magnetospheric waveguide modes by magnetosheath flows, *J. Geop. Res.*, *104*, 333–353, 1999.

McKenzie, D. E., and S. Savage, Quantitative examination of Supra-Arcade Downflows in eruptive solar flares, *Astrophys. J.*, *697*, 1569–1577, 2009.

McKenzie, J. F., Hydromagnetic wave interaction with the magnetopause and the bow shock, *J. Geop. Res.*, *18*, 1–23, 1970.

McPherron, R. L., T.-S. Hsu, J. Kissinger, X. Chu, and V. Angelopoulos, Characteristics of plasma flows at the inner edge of the plasma sheet, *J. Geop. Res.*, *116*, 2011.

Michikoshi, S., and S.-I. Inutsuka, A two-fluid analysis of the Kelvin-Helmholtz instability in the dusty layer of a protoplanetary disk: A possible path toward planetesimal formation through graviational instability, *Astrophys. J.*, *641*, 1131–1147, 2006.

Micono, M., G. Bodo, P. Rossi, and R. Ferrari, A.a nd Rosner, Kelvin-Helmholtz instability in three dimensional radiative jets, *Astron. and Astrop.*, *360*, 795–808, 2000.

Mills, K. J., and A. N. Wright, Azimuthal phase speeds of field line resonances driven by Kelvin-Helmholtz unstable waveguide modes, *J. Geop. Res.*, *104*, 22,667–22,677, 1999.

Mills, K. J., and A. N. Wright, Trapping and excitation of modes in the magnetotail, *Phys. of Pl.*, *7*, 1572, 2000.

Mills, K. J., A. N. Wright, and I. R. Mann, Kelvin-Helmholtz driven modes of the magnetosphere, *Phys. of Pl.*, *6*, 4070–4087, 1999.

Miura, A., Nonlinear evolutions of the magnetohydrodynamic Kelvin-Helmholtz instability, *Plasma Rev. Lett.*, *49*, 779, 1982.

Miura, A., Anamolous transport by magnetohydrodynamic Kelvin-Helmholtz instabilities in the solar wind-magnetosphere interactions, *J. Geop. Res.*, *89*, 801–818, 1984.

Miura, A., Dependence of the magnetopause Kelvin-Helmholtz instability on the orientation of the magnetosheath field, *Geop. Res. Lett.*, *22*, 2993–2996, 1995.

Miura, A., and P. L. Pritchett, Nonlocal stability analysis of the MHD Kelvin-Helmholtz instability in a compressible plasma, *J. Geop. Res.*, *87*, 7431–7444, 1982.

Möstl, U., M. Temmer, and M. Veronic, The Kelvin-Helmholtz instability at Coronal Mass Ejection boundaries in the solar corona: Observations and 2.5D MHD simulations, *Astrophys. J. Lett.*, *776*, 2013.

Nakai, H., and G. Ueno, Plasma structures of Kelvin-Helmholtz billows at the dusk-side flank of the magnetotail, *J. Geop. Res.*, *116*, 2011.

Nakamura, R., W. Baumjohann, C. Mouikis, L. Kistler, A. Runov, M. Volwerk, Y. Asano, Z. Vörös, T. Zhang, B. Klecker, H. Rème, and A. Balogh, Spatial scale of high-speed flows in the plasma sheet observed by Cluster, *Geop. Res. Lett.*, *31*, 2004.

Nakamura, T. K. M., M. Fujitomo, and A. Otto, Magnetic reconnection induced by Kelvin-Helmholtz instability and the formation of the low-latitude boundary layer, *Geop. Res. Lett.*, *33*, 2006.

Namikawa, T., and H. Hamabata, Propagation of the hydromagnetic waves through a collisionless heat-conducting plasma, *J. Pl. Phys.*, *26*, 95–121, 1981.

Niedner, M. B., A. I. Ershkovich, and J. C. Brandt, The effect of MHD instabilities on the flaring of cometary plasma tails, *Astrophys. J.*, *272*, 362–364, 1983.

Nykyri, K., and C. Foullon, First magnetic seismology of the CME reconnection outflow layer in the low corona with 2.5D MHD simulations of Kelvin-Helmholtz instability, *Geop. Res. Lett.*, *40*, 4154–4159, 2013.

Ofman, L., and B. Thompson, SDO/AIA observation of Kelvin-Helmholtz instability in the solar corona, *ajl*, *734*, 2011.

Ong, R. S. B., and N. Roderick, On the Kelvin-Helmholtz instability of the earth's magnetopause, *Planet. Space Sci.*, *20*, 1–10, 1972.

Ostrovskii, L. A., S. A. Rybak, and L. S. Tsimring, Negative energy waves in hydrodynamics, *Sov. Phys. Usp.*, *29*, 1040–1051, 1986.

Otto, A., and D. H. Fairfield, Kelvin-Helmholtz instability at the magnetotail boundary: MHD simulations and comparison with geotail observations, *J. Geop. Res.*, *105*, 21,175–21,190, 2000.

Owen, C. J., M. G. G. T. Taylor, I. C. Krauklis, A. N. Fazakerley, M. W. Dunlop, and J. M. Bosqued, Cluster observations of surface waves on the dawn flank magnetopause, *Ann. Geop.*, *22*, 971–983, 2004.

Pegoraro, F., M. Faganello, and F. Califano, Collisionless Kelvin-Helmholtz instability and vortex-induced reconnection in the external region of the earth magnetotail, *J. of Phys.:Conf. Series*, *133*, 2008.

Pertinec, S. M., and C. T. Russell, Near-earth magnetotail shape and size as determined from the magnetopause flaring angle, *J. Geop. Res.*, *101*, 137–152, 1996.

Pessah, M. D., Angular momentum transport in protoplanetary and black hole accretion disks: The role of parasitic modes in the saturation of mhd turbulance, *Astrophys. J.*, *716*, 1012–1027, 2010.

Powell, K. G., P. L. Roe, T. J. Linde, T. I. Gombosi, and D. L. Zeeuw, A solution-adaptive upwind scheme for ideal magnetohydrodynamics, *J. of Comp. Phys.*, *154*, 284–309, 1999.

Pu, Z.-Y., and M. G. Kivelson, Kelvin-Helmholtz instability at the magnetopause: Solution for compressible plasmas, *J. Geop. Res.*, *88*, 841–852, 1983a.

Pu, Z.-Y., and M. G. Kivelson, Kelvin-Helmholtz instability at the magnetopause: Energy flux into the magnetosphere, *J. Geop. Res.*, *88*, 853–861, 1983b.

Rae, I. J., E. F. Donnavan, I. R. Mann, F. R. Fenrich, C. E. J. Watt, D. K. Milling, M. Lester, B. Levraud, J. A. Wild, H. J. Singer, H. Réme, and A. Balogh, Evolution and characteristics of global Pc5 ULF waves during a high solar wind speed, *J. Geop. Res.*, *110*, 2005.

Rankin, R., B. Harrold, J. Samson, and P. Frycz, The nonlinear evolution of field line resonances in the earth's magnetosphere, *J. Geop. Res.*, *98*, 5839–5853, 1993.

Rankin, R., P. Frycz, and J. Samson, Shear flow vortices in magnetospheric plasmas, *Phys. of Pl.*, *4*, 829–840, 1997.

Ray, T., Kelvin-Helmholtz instabilities on cometary ion tails, *Planet. Space Sci.*, *30*, 245–250, 1982.

Roberts, B., *MHD Waves in the Sun*, pp. 105–133, Cambridge univ. Press, Cambridge, 1991.

Roediger, E., R. P. Kraft, M. E. Machacek, W. R. Forman, P. E. J. Nulsen, C. Jones, and S. S. Murray, Irregular sloshing cold fronts in the nearby merging groups NGC 7618 and UGC 12491: Evidence for Kelvin-Helmholtz instbilities, *Astrophys. J.*, *754*, 147–152, 2012.

Roediger, E., R. P. Kraft, W. R. Forman, P. E. J. Nulsen, and E. Churazov, Kelvin-Helmholtz instbilities at the sloshing cold fronts in the virgo cluster as a measure for the intracluster medium viscosity, *Astrophys. J.*, *764*, 60–74, 2013.

Rostoker, G., and T. Eastman, A boundary layer model for magnetospheric substorms, *J. Geop. Res.*, *92*, 12,187–12,201, 1987.

Ruderman, M. S., and A. N. Belov, Stability of MHD shear flows: Application to space physics, *J. of Phys.:Conf. Series*, *216*, 2010.

Ruderman, M. S., and H. Fahr, The effect of magnetic fields on the macroscopic instability of the heliopause - I. parallel interstellar magnetic fields, *Astron. and Astrop.*, *275*, 635–644, 1993.

Ruderman, M. S., and H. Fahr, The effect of magnetic fields on the macroscopic instability of the heliopause - II. inclusion of solar winde magnetic fields, *Astron. and Astrop.*, *299*, 258–266, 1995.

Ruderman, M. S., and M. Goossens, Surface alfén waves of negative energy, *J. of Phys.:Conf. Series*, *54*, 149–155, 1995.

Ruderman, M. S., and A. N. Wright, Excitation of resonant alfvén waves in the magnetosphere by negative energy surface waves on the magnetopause, *J. of Phys.:Conf. Series*, *103*, 26,573–26,584, 1998.

Runov, A. M., R. Nakamura, W. Baumjohann, T. Zhang, M. Volwerk, H.-U. Eichelberger, and A. Balogh, Cluster observation of a bifurcated current sheet, *Geop. Res. Lett.*, *30*, 1036, 2003.

Sen, A. K., Stability of hydromagnetic Kelvin-Helmholtz discontinuity, *Phys. of Fl.*, *6*, 1154–1163, 1963.

Sen, A. K., Effect of compressibility on Kelvin-Helmholtz instability in a plasma, *Phys. of Fl.*, *216*, 1293–1298, 1964.

Sen, A. K., Stability of magnetospheric boundary, *Planet. Space Sci.*, *13*, 131–141, 1965.

Sergeev, V., A. Runov, W. Baumjohann, R. Nakmura, T. Zhang, M. Volwerk, A. Balogh, H. Rème, J.-A. Sauvaud, M. André, and B. Klecker, Current sheet flapping motion and structure observed by Cluster, *Geop. Res. Lett.*, *30*, 2003.

Sergeev, V., A. Runov, W. Baumjohann, R. Nakmura, T. Zhang, A. Balogh, P. Louarnd, J. A. Sauvaud, and H. Rème, Orientation and propagation of current sheet oscillations, *Geop. Res. Lett.*, *31*, 2004.

Sergeev, V., R. Sormakov, S. Apatenkiv, W. Baumjohann, R. Nakmura, A. Runov, T. Mukai, and T. Nagai, Survey of large-amplitude flapping motions in the midtail current sheet, *Ann. Geop.*, *24*, 2015–2024, 2006.

Shiokawa, K., W. Baumjohann, and G. Haerendel, Braking of high-speed flows in the near-Earth tail, *Geop. Res. Lett.*, *24*, 1179–1182, 1997.

Shiryeava, S. O., Linear wave interaction at the charged fluid-fluid interface under tangential discontinuity of the velocity field, *Tech. Phys.*, *46*, 280–286, 2001.

Southwood, D. J., The hydromagnetic stability of the magnetospheric boundary, *Planet. Space Sci.*, *16*, 587–605, 1968.

Southwood, D. J., Some features of field line resonances in the magnetosphere, *Planet. Space Sci.*, *22*, 483–491, 1974.

Sutherland, B. R., *Internal Gravity Waves*, 1st ed., Cambridge University Press, Cambridge, 2010.

Swanson, D. G., *Plasma Waves*, 2nd ed., Academic Pr., Boston, 1989.

Tajiri, M., Propagation of hydromagnetic waves in collisionless plasma. II, kinetic approach, *J. of Phys. Soc. of japan*, *22*, 1482–1494, 1967.

Takagi, K., C. Hashimoto, H. Hasegawa, M. Fujitomo, and R. TanDokoro, Kelvin-Helmholtz instability in a magnetotail flank-like geometry: Three-dimensional MHD simulations, *J. Geop. Res.*, *111*, 2006.

Taroyan, Y., and R. Erdélyi, Resonant and Kelvin-Helmholtz instabilities on the magnetopause, *Phys. of Pl.*, *9*, 3121–3129, 2002.

Taroyan, Y., and R. Erdélyi, Resonant surface waves and instabilities in finite β plasmas, *Phys. of Pl.*, *10*, 266–276, 2003a.

Taroyan, Y., and R. Erdélyi, On resonantly excited MHD waves in the magnetotail, *J. Geop. Res.*, *108*, 2003b.

Taroyan, Y., and M. Ruderman, MHD waves and instabilities in space plasma flows, *Space Sci. Rev.*, *158*, 505–523, 2011.

Tirry, W. J., V. M. Čadež, R. Erdélyi, and M. Goossens, Resonant flow instability of MHD surface waves, *Astron. and Astrop.*, *332*, 786–794, 1998.

Turkakin, H., R. Rankin, and I. R. Mann, Primary and secondary compressible Kelvin-Helmholtz surface waves instabilities on the earth's magnetopause, *J. Geop. Res.*, *118*, 2013.

Turkakin, H., I. R. Mann, and R. Rankin, Kelvin-Helmholtz unstable magnetotail flow channels: Deceleration and radiation of MHD waves, *Geop. Res. Lett.*, *41*, 2014.

Uberoi, C., Surface waves induced magnetic reconnection and quantification of space weather phenomena, *Proceedings of ILWS Workshop*, 2006.

Villante, U., Ultra low frequency waves in the magnetosphere, *Handbook of the Solar-Terrestrial Environment*, pp. 397–422, 2007.

Volwerk, M., K.-H. Glassmeier, A. Runov, W. Baumjohann, R. Nakamura, T. Zhang, A. Klecker, B. .and Balogh, and H. Rème, Kink mode oscillation of the current sheet, *Geop. Res. Lett.*, *30*, 2003.

Volwerk, M., W. Baumjohann, K.-H. Glassmeier, R. Nakamura, T. Zhang, A. Runov, Z. Vörös, B. Klecker, R. Treumann, Y. Bogdanova, H.-U. Eichhelberger, A. Balogh, and H. Rème, Compressional waves in the Earth's neutral sheet, *Ann. Geop.*, *22*, 303–305, 2004.

Volwerk, M., T. Zhang, R. Nakamura, A. Runov, W. Baumjohann, K.-H. Glassmeier, T. Takada, H.-U. Eichhelberger, C. Carr, A. Balogh, B. Klecker, and H. Rème, Plasma flow channels with ULF waves observed by Cluster and Double Star, *Ann. Geop.*, *23*, 2929–2935, 2005.

Volwerk, M., K.-H. Glassmeier, R. Nakamura, T. Takada, W. Baumjohann, B. Klecker, H. Rème, T. Zhang, E. Lucek, and C. Carr, Flow burst-induced Kelvin-Helmholtz waves in the terrestrial magnetotail, *Geop. Res. Lett.*, *34*, 2007.

Volwerk, M., T. Zhang, K.-H. Glassmeier, A. Runov, W. Baumjohann, A. Balogh, B. Rème, H.and Klecker, and C. Carr, Study of waves in the magnetotail region with Cluster and DSP, *Advances in. Sp. Res.*, *41*, 1593–1597, 2008.

Waagan, K., C. Federrath, and C. Klingenberg, A robust numerical scheme for highly compressible magnetohydrodynamics: Nonlinear stability, implementatio and tests, *J. of Comp. Phys.*, *230*, 3331–3351, 2011.

Walker, A. D. M., The phase velocity, ray velocity and group velocity surfaces for a magneto-ionic medium, *J. Pl. Phys.*, *17*, 467–486, 1977.

Walker, A. D. M., Kelvin-Helmholtz instability in the low-latitude boundary layer, *Planet. Space Sci.*, *29*, 1119–1133, 1981.

Walker, A. D. M., Reflection and transmission at the boundary between two counter-streaming MHD plasmas-active boundaries or negative-energy waves, *J. Geop. Res.*, *63*, 203–219, 2000.

Walker, A. D. M., *Magnetohydrodynamic Waves in Geospace*, pp. 457–467, IOP Publishing Ltd., 2005.

Yoon, P.-H., J. F. Darake, and A. T. Y. Lui, Theory and simulation of Kelvin-Helmholtz instability in the geomagnetic tail, *J. Geop. Res.*, *101*, 27,327–27,339, 1996.

Zhang, T., W. Baumjohann, R. Nakamura, A. Balogh, and K.-H. Glassmeier, A wavy twisted neutral sheet observed by Cluster, *Geop. Res. Lett.*, *29*, 1899, 2002.

Zhang, T., R. Nakamura, M. Volwerk, A. Runov, W. Baumjohann, H. Eichelberger, C. Carr, A. Balogh, V. Sergeev, J. Shi, and K.-H. Fornacon, Double Star/Cluster observation of neutral sheet oscillations on 5 August 2004, *Ann. Geop.*, *23*, 2909–2914, 2005.